Towards the creation of an atlas of scaffold patterns

TOWARDS THE CREATION OF AN ATLAS OF

SCAFFOLD PATTERNS

Mapping out the influence of scaffold geometry in tissue engineering

By

Kenny Van Kampen

Towards the creation of an atlas of scaffold patterns: Mapping out the influence of scaffold geometry in tissue engineering

Kenny Antonius Geert Theodorus van Kampen

Towards the creation of an atlas of scaffold patterns: Mapping out the influence of scaffold geometry in tissue engineering

PhD Thesis, Maastricht University, Maastricht, The Netherlands

ISBN: 978-94-6483-963-0

Cover Art: Sidhant Sridhar

Printed by: Ridderprint, Alblasserdam

Towards the creation of an atlas of scaffold patterns: Mapping out the influence of scaffold geometry in tissue engineering

DISSERTATION

To obtain the degree of Doctor at Maastricht University,
on the authority of the Rector Magnificus, Prof. Dr. Pamela Habibović
in accordance with the decision of the Board of Deans, to be
defended in public on Tuesday 2nd of April 2024, at 16:00 hours.

By

Kenny Antonius Geert Theodorus van Kampen

Born on the 9th September 1992, in Nijmegen, the Netherlands

Supervisor:

Prof. Dr. Lorenzo Moroni

Co-supervisor:

Dr. Carlos Mota

Assessment committee:

Prof. Dr. Roman Truckenmüller (Chair, Maastrichtu University)

Prof. Dr. Carlijn V.C. Bouten (Eindhoven University, the Netherlands)

Dr. Barend M.E. Mees (Maastricht University)

Prof. Dr. Cecilia Sahlgren (Åbo Akademi University, Finland)

Prof. Dr. Tim J.M. Welting (Maastricht Univeristy)

The research described in this thesis was conducted at MERLN Institute for Technology Inspired Regenerative Medicine in Maastricht University. The work in this thesis was financially supported by the European Commission H2020 Program, call H2020-NMP-PILOTS-2015, Project FAST – Functionally graded Additive Manufacturing scaffolds by hybrid manufacturing and the ERC Cell Hybridge (GA n. 637308).

Table of Contents

Chapter 1

General introduction

General introduction

Every tissue found in the human body is a complex mixture of cells and extracellular matrix (ECM) components that are arranged in a specific way. Such arrangement is often related to the function of the tissue. Some examples are the collagen type II organization in articular cartilage to reduce the mechanical stress [1] or the specific cell orientation found in smooth muscle cells of larger arteries to facilitate contraction [2]. Researchers have attempted to recreate the complexity of tissues in the lab with the goal of replacing or repairing these tissues. The process of mimicking a tissue is called biomimicry and is defined as “the imitation of life or nature” [3]. This is an important aspect in tissue engineering and regenerative medicine with the ultimate goal of replacing a damaged or diseased tissue.

Many techniques in regenerative medicine have been developed over the past 2 decades and some of them are referred to as biofabrication techniques [4]. These techniques are important to recreate tissues on a larger scale, especially when the traditional method of culturing cells is largely performed in 2D. The creation of three-dimensional (3D) scaffolds with hierarchical and/or surface engineered properties capable of steering cell activity, can be produced by an additive manufacturing technology called fused deposition modeling (FDM), or variations of FDM such as 3D-fiber deposition and bioextrusion, among the most commonly used techniques in biofabrication. With FDM, a material is extruded through a nozzle in a molten form that solidifies directly after extrusion to form a filament. This process is repeated for each layer until a 3D scaffold is manufactured. FDM is compatible with a variety of materials, some of them are already FDA approved as material for drug delivery or medical devices [5]. This technique is flexible in creating on demand designs by converting any 3D reconstructions based on medical imaging techniques and converted it into a tool pathway for an FDM printer [6].

Even though any 3D design can be used in FDM, the infill patterns that are used in these scaffolds are limited. The infill pattern is generated through a software that “slices” a 3D design into layers. Each of these layers will get an infill pattern that is based on a parallel meandering line. The layers are then stacked on top of each other with the meandering lines offset at a different angle per layer. An infill pattern with fibers deposited perpendicular from each other, i.e. at a 0-90 angle, is often referred to as a woodpile pattern. Unfortunately, many of the studies using extrusion-based additive manufacturing technologies implement this woodpile pattern as a default design no matter what the final application is [7, 8]. This raises the question whether the woodpile pattern is the best design for every regenerative medicine application. In addition, it is known that cells respond to their environment and the design choice has an influence on the final biological outcome [9]. Therefore, there is a need to create more biomimicking patterns that can be used as infills for additive manufacturing technologies.

In this thesis, we aimed at investigating alternative patterns that can be fabricated through extrusion-based additive manufacturing. These were used to create more complex biomimicking scaffolds, which were explored for different tissue engineering applications, namely vascular and skeletal regeneration.

Chapter 2 focus on what biomimicry encompasses as the term is broadly used in regenerative medicine. This chapter will introduce three forms of biomimicry: mechanical biomimicry, morphological biomimicry and biological biomimicry. The chapter explores how each form of biomimicry is currently obtained with commonly used biofabrication techniques in regenerative medicine.

Chapter 3 is focused on establishing the methodology to create more biomimicking patterns for regenerative medicine. These patterns can be

based on various mathematical curves. In addition, the effect of different loading regimes is tested to study the influence of these different pore architectures on the mechanical behavior of the fabricated 3D scaffolds. Finally, I discuss how these patterns can be created and used for various regenerative medicine applications.

Chapter 4 demonstrates that scaffolds for cartilage tissue engineering can be fabricated using a hypotrochoidal design. This design applies a mechanical and morphological biomimicry approach to mimic the collagen type II fiber alignment found in articular cartilage.
Chapter 5 introduces a different approach to create complex scaffolds. Instead of creating FDM scaffolds in a traditional way with a flat collecting surface, a 4th axis is introduced to create tubular scaffolds that could potentially be used for tubular hollow tissues. This chapter showcases the technology and compares two possible scaffold designs that could not be manufactured through traditional means. In **Chapter 6**, the four-axis printer discussed in the previous chapter was used to mimic the mechanical properties of a large artery using a corrugated design. Here, we demonstrate that the choice of scaffolds' design can have a major influence on the mechanical properties of the resulting constructs.

In **Chapter 7**, melt spinning was combined with the four-axis FDM technique. The melt spinning technique can create thin fibers that are highly aligned. The aligned microfibers can mimic the tunica media of an artery. This chapter explores how well controlled these fibers can be deposited and predicted through a simple mathematical model. In addition, the influence of these fibers on cell morphology was studied and a co-culture with endothelial and smooth muscle cells was performed to create a morphological and biological mimicking scaffold.

In **Chapter 8**, the significant findings of this thesis are discussed in the broader context of the current state of the art in scaffold design for regenerative medicine. A future perspective on the knowledge that our results contribute to the field is also provided. Finally, **Chapter 9** discusses the potential impact of the results contained in this thesis for the application of tissue engineering to our society.

References

[1] F. Guilak, D.L. Butler, S.A. Goldstein, Functional tissue engineering: the role of biomechanics in articular cartilage repair, Clinical Orthopaedics and Related Research® 391 (2001) S295-S305.
[2] S. Rensen, P. Doevendans, G. Van Eys, Regulation and characteristics of vascular smooth muscle cell phenotypic diversity, Netherlands Heart Journal 15(3) (2007) 100-108.
[3] G. Zhang, Biomimicry in biomedical research, Taylor & Francis, 2012.
[4] K.A. van Kampen, R.G. Scheuring, M.L. Terpstra, R. Levato, J. Groll, J. Malda, C. Mota, L. Moroni, Biofabrication: From Additive Manufacturing to Bioprinting, in: R.L. Reis (Ed.), Encyclopedia of Tissue Engineering and Regenerative Medicine, Academic Press, Oxford, 2019, pp. 41-55.
[5] M.A. Woodruff, D.W. Hutmacher, The return of a forgotten polymer—Polycaprolactone in the 21st century, Progress in polymer science 35(10) (2010) 1217-1256.
[6] F. Rengier, A. Mehndiratta, H. Von Tengg-Kobligk, C.M. Zechmann, R. Unterhinninghofen, H.-U. Kauczor, F.L. Giesel, 3D printing based on imaging data: review of medical applications, International journal of computer assisted radiology and surgery 5(4) (2010) 335-341.
[7] K. Eichholz, F. Freeman, P. Pitacco, J. Nulty, D. Ahern, R. Burdis, D. Browe, O. Garcia, D. Hoey, D.J. Kelly, Scaffold microarchitecture regulates angiogenesis and the regeneration of large bone defects, Biofabrication (2022).
[8] S. Basile, E. Mathew, I. Genta, B. Conti, R. Dorati, D.A. Lamprou, Optimization of FDM 3D printing process parameters to produce haemodialysis curcumin-loaded vascular grafts, Drug Delivery and Translational Research (2021) 1-14.
[9] A. Di Luca, I. Lorenzo-Moldero, C. Mota, A. Lepedda, D. Auhl, C. Van Blitterswijk, L. Moroni, Tuning Cell Differentiation into a 3D Scaffold Presenting a Pore Shape Gradient for Osteochondral Regeneration, Advanced healthcare materials 5(14) (2016) 1753-63.

Chapter 2

A tissue engineering's guide to biomimicry

A tissue engineering's guide to biomimicry

Kenny A. van Kampen[1], Carlos Mota[1], Lorenzo Moroni[1]

[1]Department of Complex Tissue Regeneration, MERLN Institute for Technology-Inspired Regenerative Medicine, Maastricht University, Universiteitsingel 40, 6229ER Maastricht, The Netherlands

Abstract

Biomimicry is a broadly used term in many fields such as in architecture and industrial design to pharmacology and many others. Biomimicry tries to replicate a product or process that occurs in the natural environment. However, due to the broad use of the term biomimicry it becomes unclear what is exactly being mimicked. Specifically, in tissue engineering and regenerative medicine (TERM) where research is focussed on mimicking complex native tissues and organs, the term biomimicry is often used to designate a single aspect. Therefore, in TERM biomimicry can be clustered into to three different categories correlated to the aspect that is being mimicked: i) mechanical biomimicry - that has a focus on obtaining the correct mechanical properties of a tissue; ii) morphological biomimicry - that aims at recreating a scaffold having a similar morphology to its native counterpart; iii) biological biomimicry - that has a prime focus on recreating the biological microenvironment that is found in the targeted tissue. This review discusses the strategies and methods with which these different forms of biomimicry can be achieved with the current techniques available.

1. Introduction

The term “biomimicry” or “biomimetic” was first described by Otto Schmitt in 1957 when he attempted to mimic the electrical action of a nerve using a physical device [1]. Over the course of the years, scientists from different fields used the term to describe a product or process that tries to imitate a certain aspect from the natural environment, or taken more literally as the imitation of life and nature [2-5]. Biomimicry ranges from biomimicking furniture design from natural elements [6] to efficient car design [7] to improved platforms for toxicity studies [8]. In the field of tissue engineering and regenerative medicine (TERM) similar efforts were made to emulate the natural microenvironment [9, 10], ranging from mimicking the morphological [11], to physiological conditions such as electrical stimulation to improve muscle contractility [12] or the mechanical properties of a specific tissue [13].

Studies in regenerative medicine, where a biomimicry strategy is aimed for, often focus on only one single characteristic that researchers aim to mimic [14]. The different types of biomimicry can be classified into three main categories: 1) mechanical biomimicry, where researchers focus on obtaining mechanical properties similar to those of the target tissue [15]; 2) morphological biomimicry, where the aim is to create a scaffold that is morphologically similar to the native counterpart [16]; 3) biological biomimicry, where the prime focus is on recreating the exact biological environment that is found in the specific tissue [17].

Therefore, the aim of this review is to discuss strategies and methods to obtain the previously mentioned mechanical, morphological and biological biomimicry. We will focus on 3D tissue engineered scaffolds and hydrogels, which are relevant in the context of regenerative medicine, since other reviews have focused more on a specific tissue [18], single aspect of biomimicry [19], or two-dimensional (2D) substrates [20, 21].

2. Mechanical biomimicry

Each tissue is characterized by specific mechanical properties, from soft brain tissue in the range of 0,1-16 kPa [22] to stiff cortical bone with 19,3 GPa [23]. Mimicking the mechanical properties of a targeted tissue with a designed 3D environment has been the subject of many studies [24-26]. The reason to mimic the mechanical properties is to reduce the risk of a mechanical mismatch, which often leads to graft failure [27-29]. This is especially the case where the mechanical properties play a pivotal role in tissue development and homeostasis, such as the supporting capabilities of bone [30], the ability to withstand physiological pressure conditions and prevent stenosis in arteries [31] or the elasticity of skin [32]. Strategies to obtain mechanical properties of 3D scaffolds mimicking the tissue of interest can vary by choosing the right material [33], by varying the porosity or the architecture of the pore network [34, 35], by changing the crosslinkers to tailor the mechanical properties of the scaffold [36], or using fillers to create composite materials to improve its performance [37].

2.1 Bulk material

One major influence on the mechanical properties of a scaffold is the bulk material. The materials that are used in TERM can range from soft hydrogels to stiff metals. The range in stiffness can vary by as much as a factor 1,000,000 [38, 39] (Figure 1). Therefore, the mechanical bulk properties are often one of the reasons why to create a scaffold out of a certain material [33, 40]. For example, Janke et al. described how the mechanical properties of collagen type I scaffolds for ureteral tissue engineering improved significantly with the addition of poly(L-lactide-co-ε-caprolactone) (PLCL), poly(glycolide-co-ε-caprolactone) (PGCL) or (poly(p-dioxanone) (PDS) [41]. The requirements for the material was to be biocompatible and biodegradable. The ultimate tensile strength increased from 1.8 ± 0.8 kPa to 160 ± 20 kPa with the addition of PDS. In addition, the stress strain curve became "J"-shaped

displaying the toe-region, which is also observed in the native tissue. It is worth to note that even though the study of Janke et al. reported that the mass and compressive strength of PDS did not decrease after 48 days, a different study by Ping Ooi et al. showed both the strain and load at break in tension decreased over time even after 15 days of degradation [42]. To overcome the issue of degradation Yoon et al. used poly(ε-caprolactone) (PCL) to increase the mechanical properties [43]. PCL is known to be a slow degrading polymer and can hold its shape even after 2 years of implantation [44]. The study showed that the resilience of the scaffold increased by introducing an electrospun PCL mesh inside an alginate hydrogel. The PCL mesh also helped retaining the shape of the alginate hydrogel after crosslinking and compression tests. Besides the mechanical support, the mesh was still permeable for the cells to migrate through. A different application for PCL was found in skin regeneration, where Rad et al. combined PCL with Zein and gum Arabic (GA) in electrospun meshes [45]. During the study it was noted that the formulations with the highest concentration of PCL (20%) and a lower concentration of Zein (15%) had the highest tensile strength (2.9 MPa) while the samples with the lowest tensile strength (1.3 MPa) contained less PCL (15%) and more Zein (20%). Interestingly to note is that the presence of GA enhanced the hydrophilicity and gave the scaffold antibacterial properties. A different approach to alter the mechanical properties of a scaffold by adding materials was taken by Khalili et al. [46]. During the study elastin was added to electrospun meshes, which slightly decreased the Young's modulus, but significantly increased the elongation at break under tensile characterization, thus making this an ideal candidate for skin tissue engineering where skin is able to stretch up to 100% without break [47].

As mentioned earlier, the bulk material choice is pivotal for the mechanical properties of the final scaffold and is often the starting point of a study. However, the human body remodels biomaterials over time and materials can degrade resulting in a change in mechanical properties [48, 49]. To overcome

this, the degradation time of the material has to match the speed of which the biological tissue is regenerated. Another issue that might arise is that even though the material properties can be right from a mechanical biomimicry perspective, the material might not facilitate biological integration or even elicit an immune response [50, 51]. In summary, the choice of the bulk material is the major player in the mechanical properties of a scaffold and the first step in obtaining mechanical biomimicry.

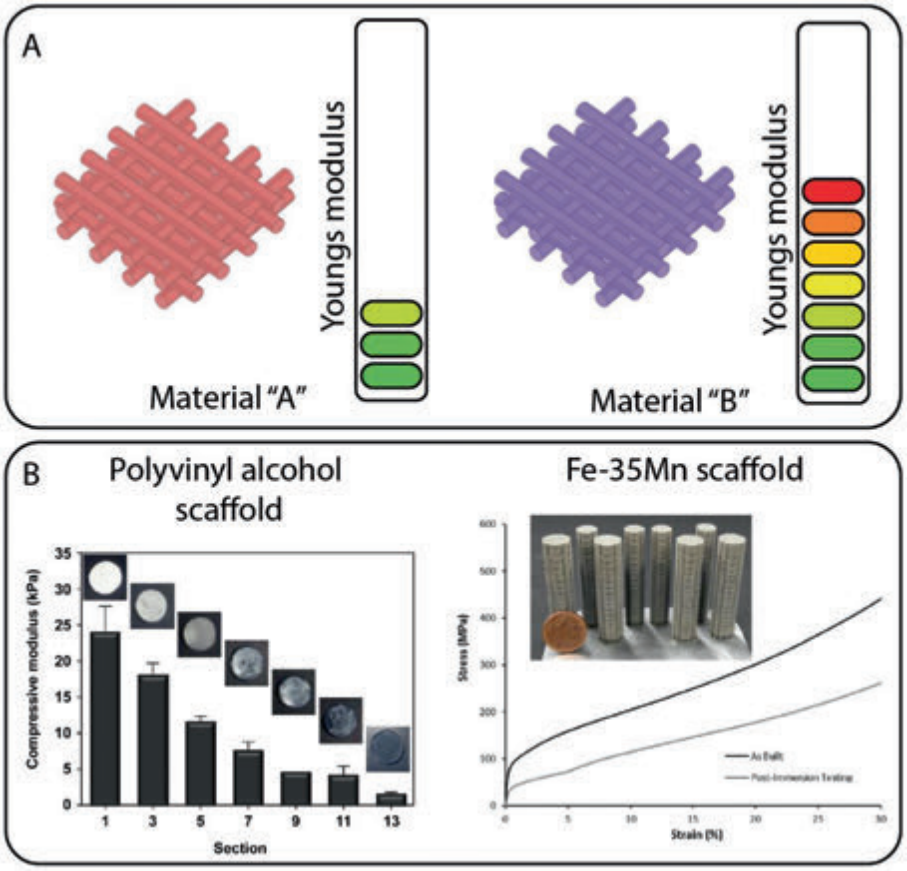

Figure 1. *Changing bulk material of a scaffold to match the mechanical properties of a native tissue. (A) Schematic illustration to describe the change in materials influencing the mechanical properties. (B) left panel; compressive modulus of a Polyvinyl alcohol for neural tissue engineering [38], right panel; stress-strain curve of a Fe-35Mn scaffold for load bearing bone tissue engineering [52].*

2.2 Scaffold design

Not only the choice of material has an influence, but also the geometrical design can play a pivotal role. For instance, the porosity of the scaffolds has a direct effect on their mechanical properties [53]. Melchels et al. showed that by varying the design within poly(D,L-lactide) (PDLLA) functionalized with methacrylate groups from a cube to a gyroid architecture the elastic modulus decreased from 324 MPa to 169 MPa, respectively [54]. The von Mises stress distribution was also improved with the gyroid design. This in turn could expose attached cells to a more equal mechanical stimulation throughout the whole scaffold. Other designs can introduce a negative Poisson's ratio (auxetic) as Jin et al. showed [55]. The auxetic properties were introduced by creating a periodic star-shaped re-entrant lattice structure on the scaffold through fused deposition modeling (FDM). This was combined with a melt-electrospun mesh to increase the surface area for cells to attach to. The Poisson's ratio could be varied by changing the angle of the unit cell. In addition, it was found that the elastic modulus in the scaffolds increased with the decreasing re-entrant angle of the unit cell from 100 MPa to 40 MPa with a 140° and 110° angle, respectively. Unfortunately only a static culture with cells was performed and the auxetic effect was not investigated in this study. A different study by Di Luca et al. used PCL to fabricate scaffolds in different designs [56]. By changing the deposition angle of the fibers, scaffolds were fabricated in a gradient pattern and compared to their non-gradient counterparts. The results showed that the gradient design were stiffer compared to a non-gradient scaffold. Instead of changing the deposition pattern, Huebner et al. showed that by varying the fiber spacing from 100 µm to 400 µm within the scaffolds, the elastic modulus after 4 weeks of implantation in a porcine model for meniscus regeneration was 380 kPa and 108 kPa respectively [57]. Yet, after 12 weeks of implantation the elastic modulus was similar between both conditions and the collagen alignment within the strands of the scaffold had a significant influence on the elastic modulus rather than the density of the deposited matrix. This demonstrates

that the mechanical properties can be precisely controlled pre-implantation, though after implantation there is little to no control over the scaffolds mechanical properties as degradation and tissue formation have a major influence. Besides proving the importance of design, Zamani et al. showed that the direction in which the scaffold was fabricated in a layer-by-layer fashion can change drastically the mechanical properties [58], especially if there is tension which is perpendicular to the fabrication direction of the scaffold. This results in an increased chance of delamination, which is also true if there is a compression collinear to the fabrication direction. An entirely different strategy described by Jing et al. used scaffold's design to prevent

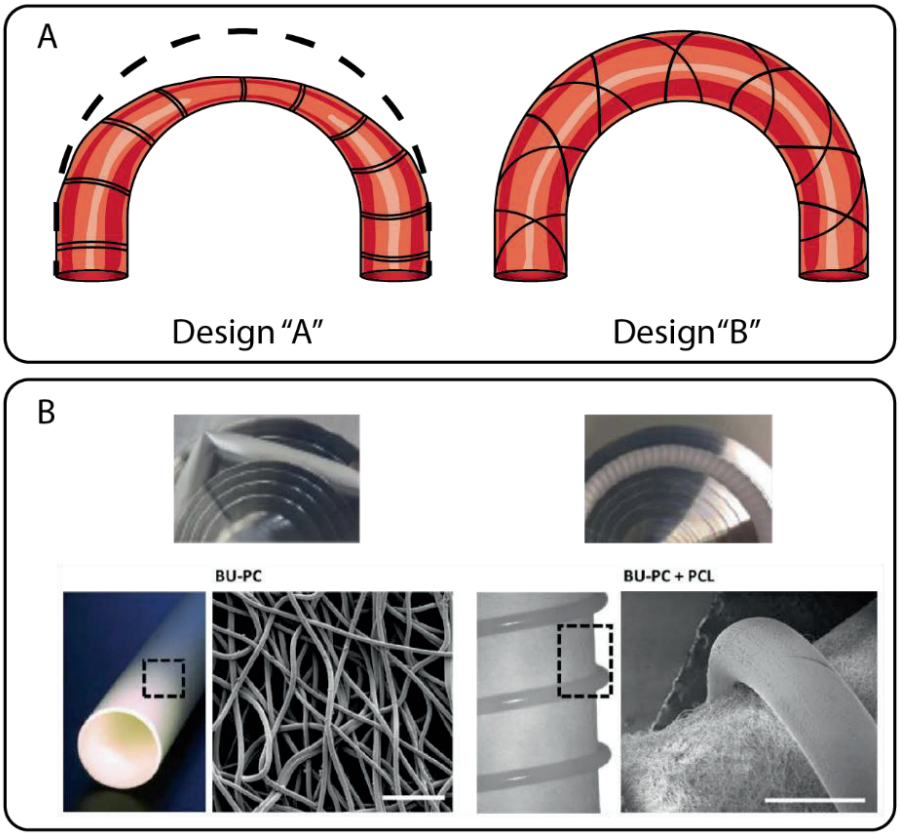

Figure 2. *Changing the scaffold design to match the mechanical behavior of a native tissue. (A) Illustrated example describe the change in design to prevent kinking of the scaffold when bent around a tight corner. (B) Bending test of polycarbonate bisurea scaffolds with two different designs around a radius of 30 mm [59].*

kinking of vascular grafts [59] (Figure 2). Testing various designs, having an outer spiral architecture on a tubular scaffolds had an improved effect on the retention of the scaffold's diameter compared to a ring or cross design. Even with a small bending radius of 4 mm, the spiral design prevented a major diameter reduction (< 20%).

As discussed in these studies, the mechanical properties can be tuned to a large extend depending on the design. This allows the use of the same material for a wider range of applications. For instance, the design of a scaffold can be changed for materials that have stiff bulk properties. In addition, with the relatively new field of meta-materials, complex mechanical properties can be introduced such as negative Poisson's ratio designs or origami-inspired meta-materials on materials that do not have those intrinsic properties [60, 61]. However, these meta-material designs require the unit cells to be relatively open and only display these properties when there is room for the design to bend or twist [62], which opens the question whether they would retain their properties when implanted in-vivo. As discussed earlier with the material choice, the design can change the mechanical properties on a scaffold level, but it cannot change the bulk material properties. This might result in a scaffold design with the right mechanical properties, but suboptimal biological properties (e.g. cell attachment and immune response) if the material chemistry is not adequate to allow cell-material interactions [50, 51]. In summary, scaffolds' design plays a key role in obtaining the right mechanical properties, whether it is to fine-tune the mechanical properties to match exactly those of the tissue or to prevent the collapse of a scaffold.

2.3 Crosslinkers

The crosslinking of materials is another method to modulate the mechanical properties of a scaffold, especially since the crosslinking density can drastically affect the mechanical properties. As described by Suo et al. [63], an interpenetrating network of gelatin methacryloyl (GelMA) and chitosan was

formed by covalent bonds and hydrophobic interactions through both photo-crosslinking and basification through sodiumhydroxide as crosslinking methods. The gelatin from GelMA was derived from porcine skin and had a methacrylation degree of 95% [64]. This resulted in a significant increase in tensile strength and compressive modulus compared to chitosan entrapped in the UV crosslinked GelMA network. The lowest compressive modulus of 3.4 kPa was with chitosan gels that were crosslinked through basification. The strongest gels with a compressive modulus of 116.1 kPa were made out of a GelMA-chitosan blend that was crosslinked through both photo-crosslinking and basification. In addition to the increased mechanical properties, the degradation time also increased with crosslinking. Whereas the non-crosslinked GelMA degraded within 48 hours, the crosslinked GelMA remained with about 75% of its mass after 4 days. Besides the increase in mechanical properties also the method of crosslinking has an influence. For instance, Martínez et al. compared three different crosslinking methods on Chitosan-collagen sponges [65]. A comparison between 1-ethyl-3-(3-dimethylaminopropyl) carbo-diimide hydrochloride (EDAC), sodium tripolyphosphate (TPP) and a combination of the two methods was made. The results showed, in line with the other papers, that the Young's modulus changed with the crosslinking conditions. The non-crosslinked scaffold had the lowest Young's modulus (4.5 ± 0.3 kPa) while the TPP crosslinked scaffold had the highest Young's modulus (20 ± 0.2 kPa). Interestingly, the combined crosslinking method resulted in the lowest Young's modulus of 7.7 ± 0.5 kPa with EDAC followed right after at 9.9 ± 0.4 kPa. The authors explained that specifically chitosan crosslinked more efficiently with TPP instead of EDAC, implying that the combination between material choice and crosslinking method matters. Besides the crosslinking method, the duration of crosslinking also influences mechanical properties as shown by Naghieh et al. [66], where printed alginate scaffolds were subjected to calcium chloride crosslinking for different periods (Figure 3). Directly after printing the Young's modulus was only 39.8 kPa, whereas after 1 day of crosslinking the Young's modulus

increased up to 273.4 kPa. In addition, the results showed that having a bigger crosslinker volume led to a higher Young's modulus due to the larger amount of calcium ions available. Though this method can increase the mechanical properties, long exposure to Ca^{2+} ions at high concentrations can lead to induced apoptosis [67].

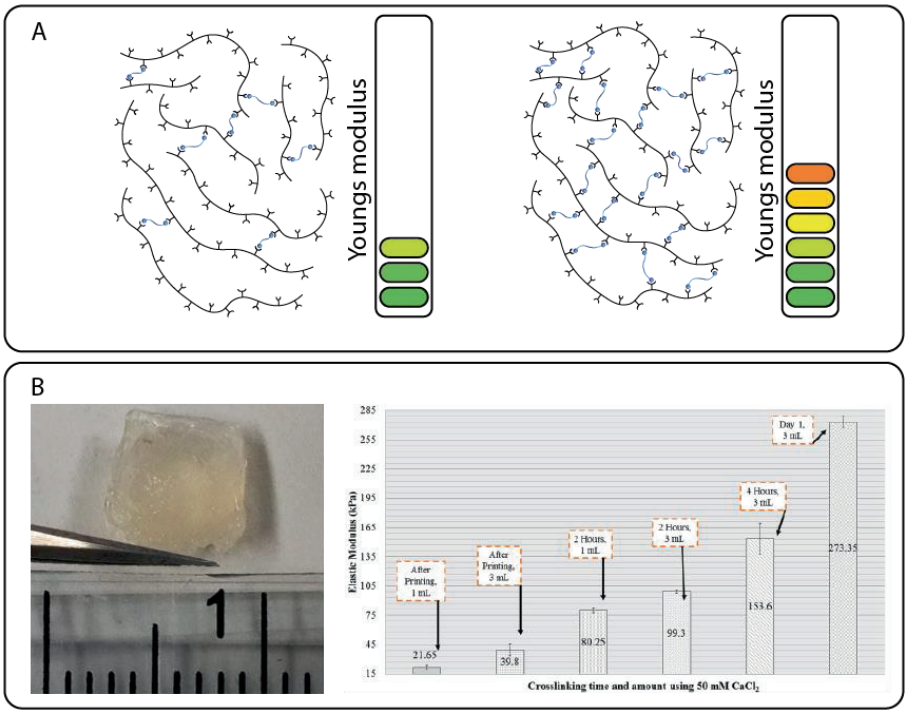

Figure 3. *Changing crosslinking density in a scaffold to match the mechanical properties of a native tissue. (A) Schematic illustration of increasing the crosslinker density to increase the stiffness. (B) Bioplotted bulk gel in the left panel and the effect of crosslinking duration and volume on the elastic modulus of the scaffold in the right panel [66].*

Certain crosslinkers, however, can be toxic especially when used in higher concentrations due to the increased amount of unreacted cytotoxic compounds [68, 69]. An alternative is to switch to non-toxic crosslinking system, which in turn can change the mechanical properties [65]. In addition, a tradeoff has to be made with hydrogels: on one side having a mechanically stable and stiff hydrogel that is easy to process and shape, while on the other side a softer hydrogel that allows cell proliferation but degrades within an

appropriate application-specific time frame [70]. A solution to this problem could be offered by reversible hydrogels that change mechanical properties with either light or temperature [71, 72]. In general, the mechanical properties of crosslinked hydrogels range from a storage modulus of less than 100 Pa [73] up to 300 MPa [74], which makes them suitable for soft tissues such as lung and brain [75], or hard ones such as cancellous bone, respectively [76]. In summary, using crosslinkers is one of the strategies to modulate the mechanical properties of a hydrogel to obtain mechanical biomimicry.

2.4 Fillers

There is a variety of reasons why the use of fillers inside a bulk material is investigated. One of them is to change the mechanical properties. For example, Janfada et al. described that when PCL was electrospun in combination with mesoporous silica particles the elastic modulus increased according to the amount of particles added [77] (Figure 4). The explanation given by the author is that the physical connection between the particles and the polymer restricts the movement of the polymeric chains, resulting in an increase in elastic modulus and ultimate strength. In addition, the ultimate tensile strength also increased. However, the strain at break significantly decreased, because of the brittleness of the ceramic particles that are included in the polymer. Similar findings were observed by Du et al. who used hydroxyapatite as a filler in a polyurethane composite scaffold [78]. Both compressive strength and elastic modulus increased significantly from 0.6 ± 0.1 MPa and 4.4 ± 0.4 MPa respectively without fillers, to 4.6 ± 0.3 MPa and 36.9 ± 8.7 MPa respectively when 40% wt hydroxyapatite was added. A solution to reduce the brittleness that occurs when using a high filler content is to create gradients in composition during scaffold fabrication [79]. This continuous hydroxyapatite composition gradient within a poly(ethylene oxide terephthalate)/poly(butylene terephthalate) (PEOT/PBT) resulted in scaffolds with an improvement of the strain at break by 50% compared to their discrete gradient counterpart. By having a discrete gradient, the difference in

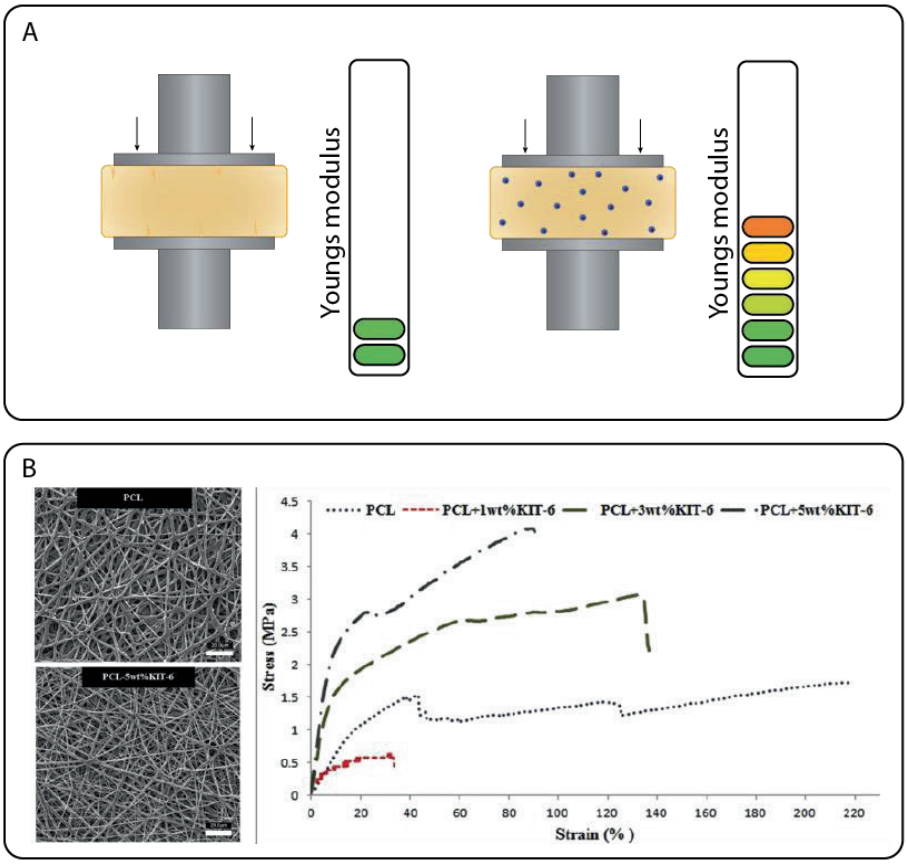

Figure 4. *Adding fillers inside a bulk material to match the mechanical properties of a native tissue. (A) Schematic illustration to describe the added effect of fillers on the Young's modulus of a scaffold. (B) SEM images of the PCL scaffold with and without mesoporous silica particles and the stress strain curves of the tested scaffolds [77].*

mechanical properties between layers is bigger compared to having a continuous gradient, which results in reduced stress at these interfaces. Increasing the amount of fillers does not always increase the mechanical properties. A study by Seyedsalehi et al. found that adding 0.5% wt reduced graphene oxide (rGO) in a 3D printed scaffold increased the compressive strength and modulus [80]. However, when a higher percentage rGO was added the compressive modulus significantly decreased even when compared to the PCL scaffold without rGO. An explanation for this was that increased rGO concentrations caused aggregation and re-stacking of the rGO

sheets, whereas at a lower concentration the rGO was dispersed homogenously throughout the polymer matrix contributing to the mechanical properties.

Introducing fillers to a material can increase the stiffness of a scaffold. However, not always does this lead to an increase in mechanical properties as discussed earlier. Adding more fillers might contribute to an increased Young's modulus, but it also causes the scaffold to be more brittle, which poses a problem when used for more flexible tissues such as cartilage, muscle or tendons [81, 82]. Another more practical issue with the use of fillers is the difficulty to work with them; mixing them inside the polymer matrix can be difficult, since the fillers are prone to form micrometer sized aggregates leading to a heterogeneous distribution [83, 84]. Replicating the anatomical features with precision requires high resolution biofabrication techniques. These techniques use nozzles that range in the micrometers. This in turn makes the use of fillers more prone to clogging of the needle resulting in producing heterogeneous scaffolds with defects [85, 86]. Nonetheless, the use of fillers can be ideal for stiffer tissues such as bone and dental applications, due to the mechanical properties of the filler and the inorganic component found in both the tissue and the filler that is used [87].

3. Morphological biomimicry

The morphology of a tissue is normally related to its function. In the trachea for example, the C-shaped rings of cartilaginous tissue have their opening facing the side of the esophagus [88]. The cartilage within these rings helps maintaining the tissue structural integrity, yet the opening is made out of flexible tissue that extends whenever food travels through the esophagus. Another example is the shape of the dental root, which can cause a difference in force distribution and in turn can impact alveolar bone resorption [89]. There are multiple strategies to obtain a morphological biomimicking scaffolds,

ranging from mimicking interfaces between tissues [90], to mimicking the hierarchical pore architecture that is present in various tissues [91], to using a decellularized tissue [92], or through templating techniques [93].

3.1 Interfaces between tissues

Biphasic or bilayered scaffolds are generally used in tissue engineering where there is a tissue transition, such as the interface between bone and cartilage [94]. Liu et al. described how a biomimetic biphasic osteochondral scaffold was made by fabricating a porous 3D plotted hydroxyapatite scaffold as the solid bone part and integrating it with a hyaluronic acid methacryloyl hydrogel as chondrogenic layer on top [95] (Figure 5). The results showed a higher expression of cartilage specific markers, such as collagen type II and aggrecan in the chondrogenic side of the scaffold, and an upregulated expression of osteogenic markers such as alkaline phosphatase (ALP) and Runt Related Transcription Factor 2 (Runx2) in the osteogenic side of the scaffold. In addition, by integrating a transition zone where both the hydrogel and solid scaffold were combined, both sides remained connected after two months of subcutaneous implantation. Instead of using a solid polymer and hydrogel combination, Mesallati et al. either used two hydrogels or a hydrogel combined with a self-assembled cell layer. The bone compartment was made out of alginate in both conditions while the chondral part was made out of agarose or a scaffold free cartilage layer of bone marrow derived mesenchymal stem cells (MSCs) [96]. A higher sulfated glycosaminoglycans (sGAG) and collagen amount was found in the self-assembled chondral layer compared to the agarose layer. Furthermore, the integration and stability between both bone and cartilage layers seemed to improve when a co-culture was performed with chondrocytes and bone marrow stem cells. This technique could also be easily scaled up to an anatomically shaped osteochondral construct, which covers an entire condyle. After 8 weeks *in vivo,* a layer of cartilage remained on the surface of the construct as was shown by collagen type II staining. However, the same histological analysis

also showed the presence of collagen type I or III. Collagen type I in cartilage is associated with osteoarthritis [97], while collagen type III indicates that the chondrocytes are dedifferentiated [98]. In addition, some degree of mineralization was found in the osseous part of the scaffold. Another example of an anatomically shaped osteochondral construct was made by Alhadlaq et al. [99]. Here, the mandibular condyle of an adult human cadaver was used to fabricate a mold out of acrylic. MSC derived chondrogenic cells were suspended in a polyethylene glycol diacrylate (PEGDA) hydrogel, the chondral part of the mold was filled with this hydrogel and photocrosslinked. Afterwards, MSC derived osteogenic cells were suspended in PEGDA and cast on top of the previous layer. The results showed a clear distinction between the cartilage part and the bone part of the hydrogel with collagen type II in the cartilage part and collagen type I in the bone part of the scaffold, mimicking the osteochondral tissue. Another more recent attempt to make an anatomically correct condyle shape was by Peiffer et al. [100]. In this study, a mesh fabricated through MEW was deposited on a curved surface that matched the curvature of the diarthrodial condyle. This mesh was then placed on top of an extrusion based PCL scaffold with similar curvature. The surface of the scaffold was seeded with articular cartilage progenitor cells while the bone part of the scaffold was left without cells. The study showed the presence of collagen type II in the chondral part and no cell infiltration in the bone part of the scaffold. However, the interaction between the osteo and chondral cells in their respective part of the scaffold was not known due to the lack of osteoprogenitor cells in the study. In addition, the adherence between the two different zones was not tested, which is a known problem [96].

The tendon-bone interface has similar challenges when it pertains to the integration between these two different tissues [101]. Instead of using 2 different hydrogels, Echave et al. applied magnetic alignment to create a biphasic gelatin hydrogel with anisotropic features [102]. The bone layer was

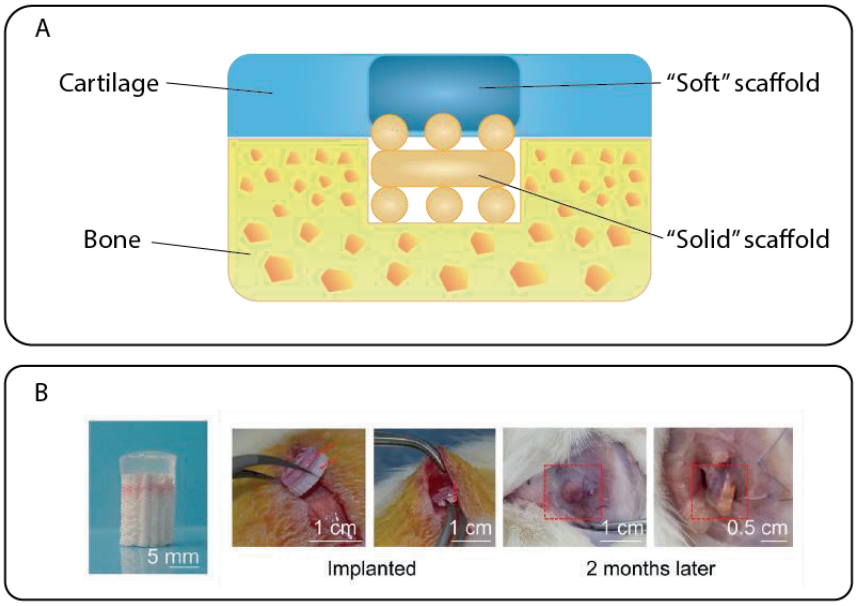

Figure 5. *Mimicking tissue interfaces such as the bone cartilage interface with a hydrogel and solid polymer combination. (A) Schematic illustration of a bilayered scaffold mimicking the morphology of the surrounding tissue. (B) Bilayered osteochondral scaffold on the left, before implantation and after 2 months subcutaneous implantation [95].*

loaded with hydroxyapatite (HA) microparticles to promote osteogenesis, while cellulose nanocrystals in a magnetic field were used to create aligned pores in the hydrogel for the tendon layer. The results showed the possibility to create an anisotropic hydrogel and the addition of HA significantly increase the Young's modulus from 17.4 ± 6.8 kPa to 38.4 ± 4.9 kPa, and stimulated the ALP activity and osteopontin (OPN) expression, which is beneficial for osteogenesis. In addition, the magnetically stimulated nano-cellulose crystals were able to orient in a controlled direction, which resulted in increased tendon-related marker Tenascin-C (TNC) expression. Even though the Young's modulus increased significantly with the addition of HA, the mechanical properties of bone are still several orders of magnitude higher [23]. In addition, the presence of HA does mimic the osseous part, but the

particles themselves do not show any hierarchical structure as seen in bone [103].

The morphology at interfaces of tissues has caught the attention of many researchers trying to replicate it. Because of the dissimilarity between these targeted tissues in terms of morphology, mechanical properties and extracellular matrix (ECM) composition, many attempts have been made to create a scaffold that is comprised of a stiff and a soft part made out of two materials [95, 104]. The disadvantage of this approach is that there is a risk of delamination at the interface of the scaffold [96, 105]. To overcome this challenge, these interface scaffolds could be made out of a single base material with one or both sides functionalized to promote the differentiation towards their end-goal application [106, 107]. However, in most interfaces, especially when bone is one of the tissues, the mechanical properties are several orders of magnitude different, which makes this approach of using a single material challenging from a mechanical point of view [23]. In addition, the ECM composition between the tissues at the interfaces are very dissimilar and complex, which raises the question whether adding or removing a single component on one side of the scaffold could lead to successful in-vivo integration [108, 109]. Future studies could focus on trying to create a better integration between the two dissimilar parts of the scaffold. In addition, in the specific case of skeletal articular tissues, the tidemark area is often an overlooked part of the interface that could be recreated. In spite of the challenges, biphasic scaffolds are an elegant strategy to create scaffolds suitable for interfaces of tissues.

3.2 Architecture of pores and porosity

Pore architecture, size and porosity in tissues are important properties to mimic. The range of pore sizes associated to a specific tissue are generally attributed to a specific function. For example, in bone the largest pore or cavity are called the medullary cavities, where the mesenchymal stem cells reside

and are produced, which can range between 4 mm up to 10.5 mm [110, 111]. The smaller pores come from the Harversian and Volkmann's canals that provide the blood supply for the osteon's with a size of around 200 µm; even smaller pores of around 7 µm called canaliculi, which spread out radially from the Haversian canals, are used by osteocytes to communicate with each other [112]. Observing this organization from a macro perspective, a gradient in porosity can be observed from a more dense and compact tissue outside to a more porous tissue inside [113]. With this observation in mind, Di Luca et al. fabricated a scaffold with a radial gradient with 3 distinct regions, ranging from the most porous medulla substitute part with a porosity of 77.6% ± 3.2% to the densest outer cortical mimicking bone part with 29.6% ± 5.0% [114]. The study showed an increase in ALP activity in the areas with pores of 1000 µm, yet not directly correlated to osteogenic differentiation of the seeded human MSCs. Additional findings showed that specific osteogenic markers Runx-2 and bone sialoprotein (BSP) were upregulated in the regions with smaller pores of 500 µm. Bittner et al. used a similar technique to create a gradient scaffolds out of PCL; instead of having a radial gradient, the gradient was created by increasing the spacing of each fiber after several layers ranging from 200 µm up to 900 µm [115]. In addition, each section of the gradient had a certain concentration of HA mixed inside the PCL scaffold, with highest concentration of 30% in the layers with the largest spacing. Though from a morphological point of view the scaffold mimics the porosity found at an osteochondral transition zone by having the largest pores at the center of the bone, from the previously discussed study having smaller pores of 500 µm instead of 1000 µm improved osteogenic gene expression. However, Bittner et al. did not show any *in vitro* work during this study. A different approach to create porosity described by Sola et al. [116] was by solvent-casting poly(methyl methacrylate) or polyurethane with NaCl or $NaHCO_3$ with a subsequent salt-leaching step. By varying the different ratios between the polymer and the salt, different size in pores could be obtained ranging from

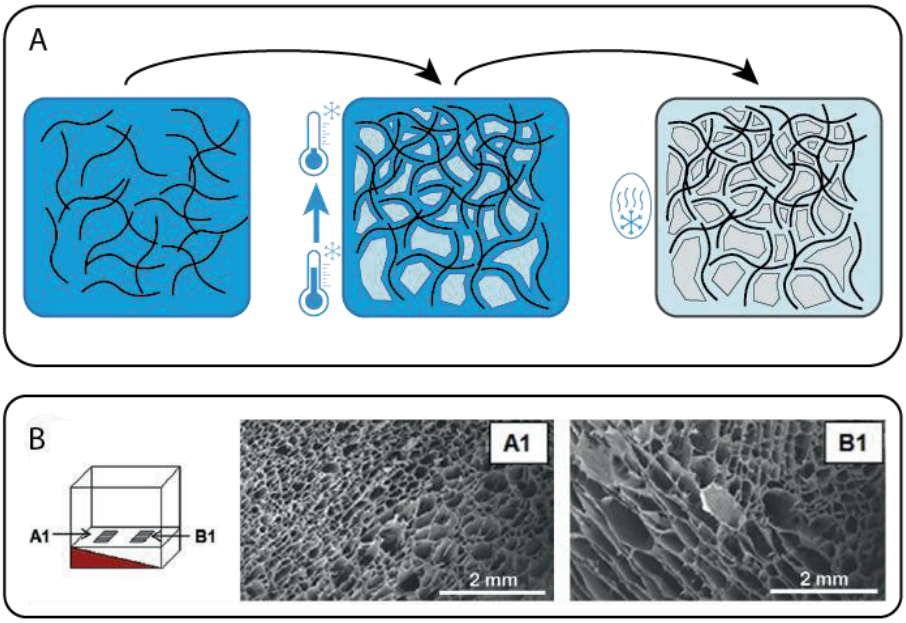

Figure 6. *(A) Schematic illustration of obtaining a porosity gradient to mimic the (B) SEM images of pore-gradient collagen type I scaffolds produced in a mould that creates a temperature gradient [118].*

600 µm up to 1000 µm. The resulting surface of the pores was irregular, which could be advantageous since that is known to enhance cellular attachment and proliferation [117]. Initial cell studies showed that some of the seeded cells managed to migrate in the central part of the scaffolds after 48 hours, though in limited number; furthermore, the long term effect of cell differentiation in these scaffolds has not been studied. Davidenko *et al.* demonstrated an alternative method to produce scaffolds with morphologically similar pores while avoiding the use of salts [118](Figure 6). During this study, a gradient in porosity was created through ice crystal formation by adding a collagen solution inside a custom-made mould that would create a gradient in temperature. The porosity of the scaffold was 98.9% ± 0.05, which corresponds to the 1 wt.% collagen suspension used. This resulted in a gradient in pores of between 70-100 µm and 130-180 µm when the solution was frozen and lyophilized. However, the cell response on these small pores was not studied, which might be too small and, together with their tortuosity

and incomplete interconnectivity and accessibility, is known to cause limited nutrient supply and oxygen availability at the center of the scaffold depending on the application [119].

Mimicking the porosity of a tissue is important not only for replicating the morphology of a tissue, but can dictate whether cells would differentiate towards their targeted tissue [114]. Populating in a uniform way a scaffold with cells depends on the seeding methods and the time in culture [120]. Having larger pores requires more time to entirely populate the scaffold; on the other hand having small pores might take less time but can cause a lack of oxygen and nutrient supply [119]. To tackle oxygen supply limitation, a possible solution is by incorporating oxygen-releasing materials, such as calcium peroxide incorporated in a polyurethane scaffold [121]. Another alternative could be by promoting vascularization prior and after implantation by including preformed vessels or incorporating VEGF in the scaffold respectively, which could solve both the nutrient and oxygen supply problems [122] [123]. In summary, having and controlling porosity is vital for morphological mimicry and ultimately nutrient supply and *de novo* tissue homeostasis.

3.3 Decellularized tissues

Using a decellularized tissue to retain extracellular matrix morphology has been an investigated strategy for many years, where these templates are typically seeded with cells from another host [124-126]. Certain decellularized products are already clinically applied such as pig heart valves [127], porcine and human dermis for rotator cuff repair [128, 129], and bovine decellularized bone for skeletal repair [130]. Pors et al. described how human ovarian tissue was decellularized and repopulated with human follicles and implanted in mice [131]. The results showed that the decellularized scaffolds were able to support the survival and promote the growth of human follicles both *in vitro* and *in vivo*. Similarly, Giraldo-Gomez et al. investigated a rapid

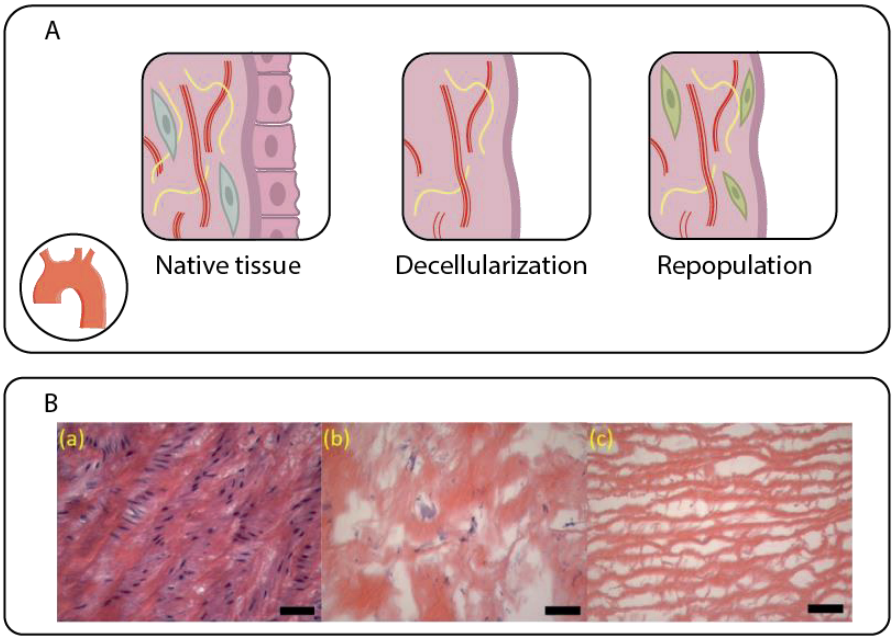

Figure 7. *(A) Schematic illustration of decellularizing a tissue to mimic the morphology of a native tissue. (B) Haematoxylin and Eosin stained section of a porcine aorta (a) before decellularization, (b) after SDS treatment and (c) after supercritical CO_2 treatment [134]. Scale bar represents 50 µm.*

decellularization process of a porcine trachea with guanidine, trypsin and ultrasounds [132]. Besides the architecture, also some essential ECM components, such as collagen type II and glycosaminoglycans, were preserved after the decellularization process. The decellularized scaffolds were recellularized with human adipose-derived mesenchymal stem cells and implanted in mice and checked for their immunogenicity. The results showed that although there was a presence of the inflammatory cytokine tumor necrosis factor alpha (TNF-α), this was also shown in the sham control group and in both groups the concentration decreased over time. In addition, some cells in the scaffold showed early differentiation towards chondrocytes by the presence of SRY-Box Transcription Factor 9 (SOX9) after 15 days of implantation. Even though the study used low concentrations, it is known that trypsin can cause ECM degradation [133]. Casali *et al.* proposed a different method where supercritical CO_2 was used in combination with sodium dodecyl

sulfate (SDS) for the decellularization of porcine aortas [134] (Figure 7). Whereas other methods mainly use harsh chemicals or physical treatments, supercritical CO_2 is relatively inert as the results showed that the combination with SDS resulted in a similar morphology as the native tissue, but without the presence of cells. However, the method still has to be optimized and tested *in vivo* to check whether it is biologically comparable to other methods. Besides animal or human organs, also decellularized plants are potential candidates for skeletal muscle tissue as studied by Cheng *et al.* [135]. During this study, several fruits and vegetables were decellularized and their morphology was evaluated with scanning electron microscopy (SEM). As final candidate, scaffolds produced from green onion were chosen, since the resulting decellularized structure presented highly aligned pores similar to those of the skeletal muscle tissue. Once seeded with human skeletal muscle cells, these aligned in the direction of the pores. Even though the availability and costs of green onions or any other vegetable is better compared to human or animal tissue, their use is somewhat limited to certain tissues and for now only limited to just a few cell layers thick tissue. Furthermore, the degradation of the cellulose present in vegetables pose a foreseeable problem due to the absence of cellulase in the human body.

Since there is almost no better way to exactly mimic a tissue morphologically than through the use of a decellularized tissue, researchers have tried for over 25 years to use this method to mimic the native tissue morphology [136]. However, some issues such as removal of chemical remnants in the decellularization process [137] and the immunogenic response that could be elicited by the presence of DNA, collagen type VI or galactose-α-1,3-galactose (α-Gal) [138], remain unsolved challenges. In addition, there is a trade-off where either valuable ECM components are lost or unwanted components, such as DNA, remain in the tissue after processing [139]. To summarize, using decellularized tissue for morphological biomimicry is a viable strategy when current techniques are unable to replicate the morphology of the tissue.

3.4 Templating

Another way to morphologically mimic a scaffold is by using a template for cells to grow in. These templating techniques have been the main strategy in creating conduits for nerve regeneration or vasculature [140, 141]. Especially in recent years smaller and more complex microstructures were developed [142, 143]. For example, Jenkins et al. described how a conduit with microchannels was created by electrospinning a blend of poly(serinol hexamethylene urea) and PCL onto sucrose fibers using a dual electrospinning setup [144]. The resulting fibers contained highly aligned microchannels of less than 500 µm, which had a similar morphology to a nerve and showed to stimulate neurite growth and extension by the presence of ß-III tubulin staining throughout the microchannels. A similar approach of using sugar as a template was performed by Wu et al., where sugar fibers were winded around a mandrel and dissolved afterwards to create circumferential oriented microchannels envisioning a vascular graft [145] (Figure 8). The size of the circumferentially aligned channels was approximately 56 µm and much like the native situation the seeded vascular smooth muscle cells showed a circumferential alignment. A different approach performed by Huling et al. was to make a negative template of the whole kidney vasculature [146]. This was done by injecting a rat kidney with PCL. After solidification, the renal tissue was digested leaving the PCL vasculature cast behind. That cast was coated in collagen and then washed with acetone to remove PCL leaving a hollow collagen microvascularized scaffold behind. SEM analysis showed the preservation of the delicate and complex structures, such as the glomerulus ultrastructure. The seeded cells inside the cast formed a uniform and complete monolayer in the channels. Gershlak et al. showed that templates for vasculature can also be made from spinach leaves, since it shares a similar branching structure [147]. Perfusion tests within the leave template showed that the vascular network remained intact and seeded human umbilical vein endothelial cells (HUVECs) were able to populate the network. The use of spinach leaves is a simple and cheap solution that could easily be up-scaled

for mass production to create templates, although plant vasculature does not have a venous system like mammalians do, which might present a drawback of such solution.

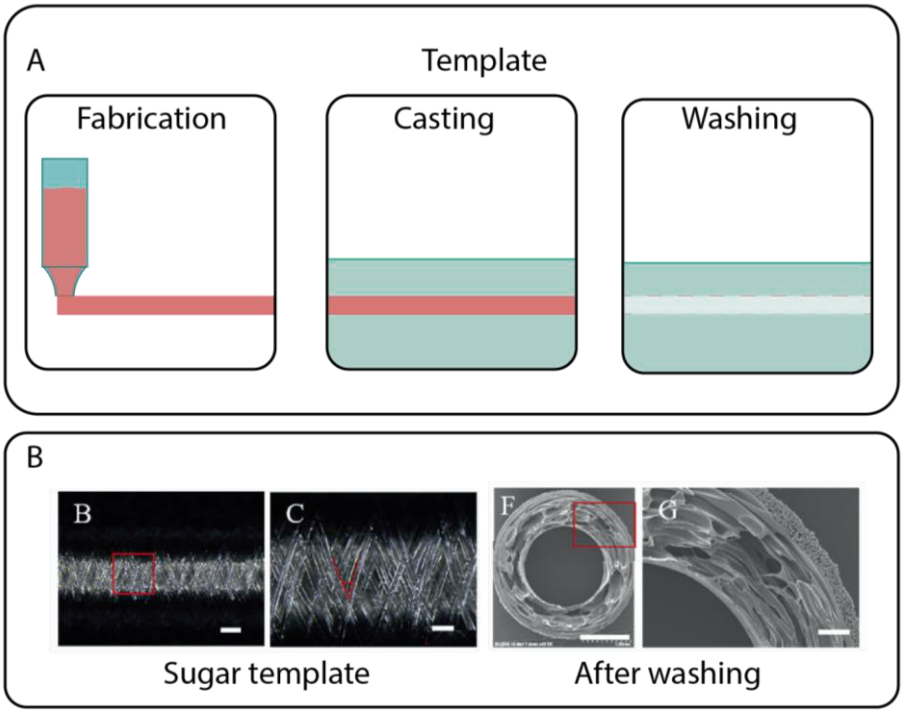

Figure 8. *(A) Creating a template that mimics the architecture of a tissue. (B) Resulting sugar fibers after being winded around a mandrel and the resulting scaffold after dissolving the sugar fibers [145]. Scale bar represents 1 mm in the overview images and 200 µm in the close-up images.*

Depending on what sacrificial material or solvent is used, there is always the chance that remnants of the template remain that can be cytotoxic or impartial dissolution that can block the template itself from being washed away from the scaffold [148, 149]. In addition, the majority of the published studies that use templating techniques are somewhat limited to the complex shapes that they can achieve, resulting in channels that run parallel or simple vascular network structures, which do not contain any micro capillaries [123, 150]. On the other hand, complex structures such as the kidney vasculature have been made through templating, showing the possibility to achieve this complexity [146].

Nonetheless, using templates to morphologically mimic organs remains a valuable and often pursued strategy.

4. Biological biomimicry

Many organs have a specific biological microenvironment. Examples are the low oxygen tension in cartilage [151], the electric conductivity of the atrioventricular bundle in the heart [152], the high blood pressure of the glomerular capsule in the kidney [153], or the presence of high amounts of growth factors in the bone marrow [154]. This natural environment for each of these organs is vital for their functioning. Therefore, it has also been a topic of many studies trying to replicate that specific biological environment. Strategies to obtain biological mimicry can range from improving cellular attachment by mimicking cellular anchoring points [155], conditioning the scaffold by placing it in a more naturally mimicking environment [156], adding growth factors in order to promote rapid growth and maturation of the tissue [157], or using decellularized organs as a base material for creating scaffolds [158].

4.1 Improving cellular attachment

The lack of cell attachment can have a great influence on the success of a scaffold [159]. High cell adhesion determines the initial amount of cells that attach right after seeding and has also a strong influence in the longer term when cell-seeded scaffolds are subjected to dynamic culturing conditions [160, 161]. Therefore, several studies aimed at increasing the cell attachment properties of scaffolds through various methods. Tsai et al. covalently crosslinked chitosan, a natural polymer known for its lack in cell attachment, through azide photocrosslinking to an Arginine, Glycine, and Aspartate (RGD) cell-binding peptide sequence for bone tissue engineering [162]. This resulted in an improved amount of cells attached from day 1, which led to increased calcium deposition after 14 days in culture. Another method studied by Kao et

al. used a polydopamine (PDA) coated PLA scaffold for bone tissue engineering [163]. The results showed that higher concentrations of PDA coating on the scaffold improved adipose derived stem cell attachment and stimulated proliferation. Besides the increased attachment, PDA coated membranes also stimulated angiogenesis as shown by the increased expression of angiogenesis related proteins angiopoietin-1 and von Willebrand factor. Instead of chemical treatments, plasma surface treatment can also be used to increase cell attachment as shown by Wang et al. [164]. PLA scaffolds were treated with cold atmospheric plasma for bone regeneration, resulting in improved cellular attachment. Atomic force microscopy analysis showed that the plasma treatment had an influence on the roughness of the fibers and that the contact angle decreased based on the duration of plasma exposure. A low contact angle indicates that the surface is hydrophilic. The hydrophilic surface in turn improved the MSC attachment. However, the contact angle increased from 25° at day 0 to 40° at day 10 as compared to 70° of the untreated scaffolds, indicating that the effect of plasma treatment decreases over time. A different approach without altering the structure or surface of the scaffold to increase the cell attachment was described by Cámara-Torres et al. [120] (Figure 9). Media density and viscosity were changed to counteract the gravitational force to which the cells are subjected when seeding on PEOT/PBT scaffolds. The results showed that the seeding efficiency was higher and a homogenous cell distribution throughout the scaffolds was obtained when either density or viscosity was changed compared to the conventional seeding method. This initial improvement in seeding efficiency led to increased mineralization in osteogenic differentiation conditions, suggesting a specific role of cell density in differentiation mechanisms.

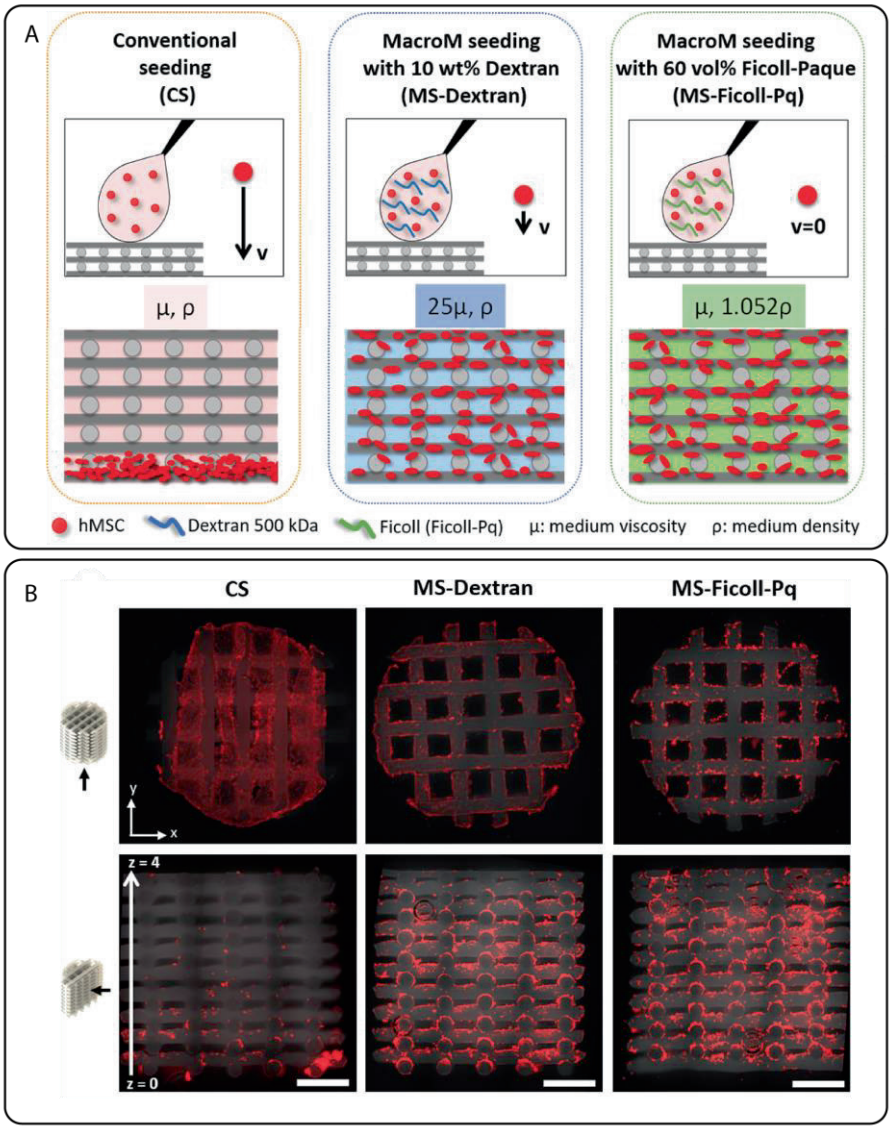

Figure 9. *(A) Schematic illustration of different seeding methods to improve seeding efficiency. (B) Fluorescent staining of cells in the bottom sides (top) and cross sections (bottom) of the scaffolds seeded with a conventional method (CS), with dextran to match the viscosity (MS-Dextran) or with Ficoll to match the density (MS-Ficoll-Pq) [120]. Scale bar represents 1mm.*

Adding RGD peptides to scaffolds is known to have a beneficial biological effect in terms of cell adhesion and differentiation, it is also observed that the addition of RGD could decrease the mechanical properties [165]. Wang et al. even observed that spacing RGD-motifs too tightly together at 37 nm can actually decrease proliferation, but increasing this spacing to 87 nm increased growth rate [166]. In summary, controlling the attachment of cells to a scaffold is important for the success of a tissue engineered graft and a valuable parameter for biologically mimicry.

4.2 Mimicking the cellular niche biophysical properties

Conventional culturing methods rely on mono culturing in a static manner on polystyrene plates with a steady supply of nutrients and oxygen. However, many organs are dynamic and have a specific biophysical environment specific to their function, which greatly differ from the stiff and flat environment offered by conventional culture plates. Examples comprise: i) an air-liquid interface characteristic of the lungs to control carbon dioxide and oxygen exchange from the inhaled air [167]; ii) the necessity to apply a load to bone, which is otherwise remodeled [168]; iii) the critical need for oxygen in the kidney with specifically the proximal tubule cells requiring large amounts of oxygen in order to facilitate sodium transport [169], to mention a few. Therefore, some studies aim at mimicking a specific local biophysical environment to maturate their scaffolds. For example, Munir et al. compared adipose-derived stromal cells cultured under 21% O_2 or 5% O_2 and confirmed that a reduced oxygen tension mimicking native cartilage conditions increased the deposition of cartilage specific markers such as SOX9 and collagen type II [170]. Besides, also the hypertrophic cartilage marker collagen type X decreased, indicating that the formed cartilage in reduced oxygen conditions is neither fibrocartilage nor hypertrophic. Doryab et al. mimicked the natural lung environment in multiple ways [171] (Figure 10). During the study, epithelial cells were cultured on top of a PCL gelatin membrane, which was lifted to create an air-liquid interface. The resulting membrane was then

stretched to mimic also the natural condition in the lung. The results showed that under dynamic physiological culturing the formation of cell-cell tight junctions was increased compared to static culture conditions, as shown by the presence of Zonula occludens-1 (ZO-1). Stretching the samples beyond physiological conditions led to a decrease in tight junction formation, as well as an increase in apoptosis because of a lower cell number after stimulation. A different study performed by Pennings et al. used a custom-made bioreactor to mature a bioengineered vascular graft [172]. The results showed that under dynamic culturing conditions the endothelial cells had a higher expression of the endothelial markers vascular endothelial cadherin (VE-cadherin) and cluster of differentiation 31 (CD31). Shear stress-induced genes cyclooxygenase-2 (COX-2) and Krüppel-like Factor 2 (KLF2) were also highly expressed when subjected to flow. A recent study, however, showed that dynamically overstimulating scaffolds increased the expression of inflammatory markers [173]. Takeda et al, dynamically stimulated cartilage cells in a collagen hydrogel, which was entrapped in a collagen sponge, and found that inflammatory and cartilage matrix-degrading enzymes ADAM Metallopeptidase With Thrombospondin Type 1 Motif 4 (ADAMTS4), Interleukin 1 (IL-1) and matrix metalloproteinase-3 (MMP3) were upregulated when the cyclic load was at a physiological load of 40 kPa or 10% deformation as compared to the no loading or only 20 kPa loading. In addition, reactive oxygen species accumulation was observed when samples were dynamically loaded. When the antioxidant pyrrolidine dithiocarbamate (PDTC) was administered during mechanical loading, the upregulation of ADAMTS4 and IL-1 receptor was no longer observed, thus partially compensating for the overloading conditions.

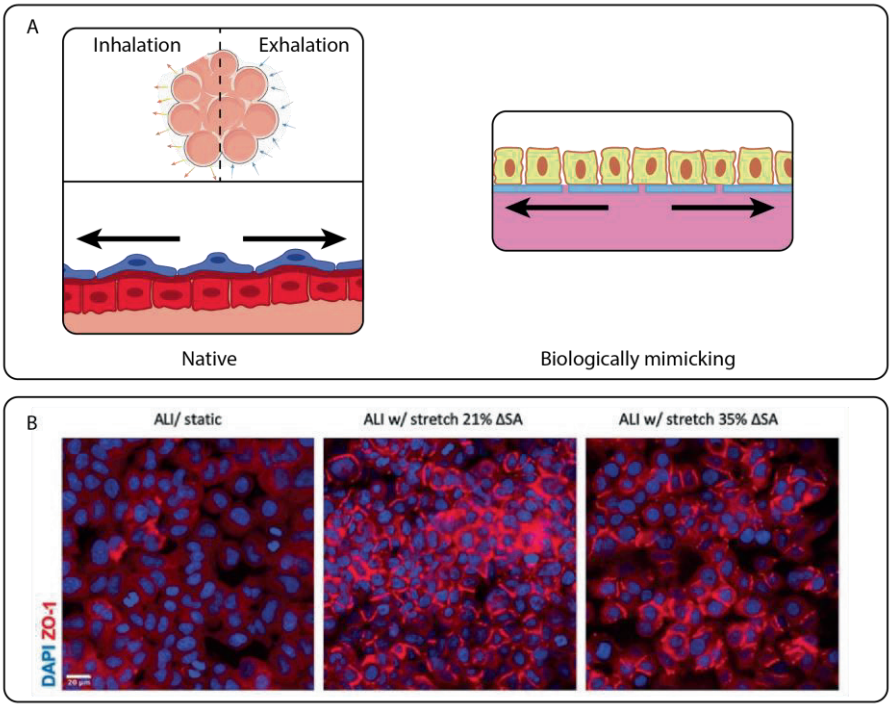

Figure 10. *(A) Schematic illustration of mimicking the natural environment of a lung by stretching the scaffold and using an air-liquid interface to further maturate the cells. (B) ZO-1 expression in respiratory epithelial cells in (left) static condition, (middle) cyclic stretch at 21% strain and (right) cyclic stretch at 35% strain [171]. Scale bar represents 20 µm.*

Mimicking a complex environment of a tissue is not an easy task, since multiple elements could play a role in the environment. For example, in articular cartilage a complex anisotropic loading plays an important role besides low oxygen tension and different osmolarity of the local microenvironment [174] [175]. In vascular networks, the blood flow through the vessel lumen is regulated dynamically by the autonomic nervous system to contract or dilate [176]. Mimicking the local biophysical conditions and properties of the microenvironment of a tissue plays a key role in biological biomimicry and can help further tissue maturation.

4.3 Growth factors

Growth factors are important in the natural regeneration process and are therefore widely used in regenerative medicine [177]. The general use for these growth factors is to enhance the natural healing process or to stimulate the differentiation of cells towards the targeted tissue (or organ) of interest. For example, Li et al. used nerve growth factor (NGF) to promote peripheral nerve regeneration [178]. Heparin was used to load NGF in chitosan scaffolds, resulting in an increase in initial Schwann cell attachment and proliferation after 5 days of culture. In addition, the number of neurites formed by the Schwann cells was increased in the presence of NGF. Instead of using heparin to load growth factors via electrostatic interactions, Park et al. chemically immobilized a Bone morphogenetic protein 2 (BMP-2) mimetic peptide in a click-crosslinked hyaluronic hydrogel [179] (Figure 11). The bioactivity of the biomimetic BMP-2 peptide showed similar results to BMP-2 supplemented medium condition, as seen by ALP and bone specific markers osteonectin and osteocalcin expression. Because of the chemical immobilization, the release of BMP-2 was more controlled over a longer period of time instead of an initial burst release. This in turn led to a more effective osteogenic differentiation. A different strategy was applied by Rezaii et al., who used curcumin nanoparticles incorporated in collagen-chitosan scaffolds to regulate the release of Transforming growth factor beta 1 (TGF-β1) and Smad7 for wound healing [180]. TGF-β1 is known to enhance extracellular matrix production and Smad7 is an inhibitor of the TGF-β family. The results of the *in vivo* study showed that with the addition of the curcumin nanoparticles, the mRNA expression of TGF-β1 and Smad7 were upregulated after 3 days. This upregulation was no longer observed after 15 days and the wound area was significantly reduced. TGF-β1 expression is known to decrease when the wound is closed, indicating that the particles decreased the duration of wound closing [181].

The addition of growth factors to promote regeneration is not valid for all cases. This was shown by Pan et al. by blocking a growth factor receptor to promote meniscus fibrocartilage formation [182]. During the study, an epidermal growth factor receptor (EGFR) inhibitor was injected *in vivo* at the implantation site of a collagen type I scaffold. After 16 weeks, the scaffolds injected with the EGFR inhibitor showed a similar matrix to that of a healthy meniscus, as observed from Safranin-O staining for GAG production. In addition, there was more collagen type II expression in the scaffolds with EGFR inhibitor and had a lower Mankin's score, which is used to grade osteoarthritis.

Growth factors are vital in normal tissue morphogenesis and function, which makes adding them an interesting approach for biological biomimicry. However, uncontrolled or prolonged release of growth factors are associated with multiple forms of cancer [183-185]. Another issue is that simply adding the growth factors to a scaffold *in vivo* would result in a systemic response. Therefore, growth factors controlled release or immobilization is needed in designing bioactive scaffolds [186]. Even though the addition and release profile of growth factors to a scaffold is complex to control, it remains a viable strategy for biological biomimicry.

4.4 Decellularized tissue for hydrogels

Unlike the previously discussed use of decellularized ECM to mimic the tissue morphology, in this section decellularized ECM is discussed as bulk material for hydrogels and bioinks to mimic the biological microenvironment. For example, Seo et al. exploited a supercritical CO_2 ethanol (EtOH) treatment to decellularize heart tissue, which was then combined with collagen type I and used as an injectable hydrogel [187]. As comparison for the supercritical CO_2 EtOH, a common SDS Triton X-100 detergent based method was used. Both methods proved to remove the DNA, but hematoxylin and eosin staining showed that the supercritical CO_2 EtOH treatment was better at retaining the

collagen bundles of the native tissue. GAG and Collagen contents were better preserved, in addition to retaining Fibroblast growth factors (FGF), vascular endothelial growth factor B (VEGF-B) and platelet factors. The decellularized ECM was able to form a gel. Finally, subcutaneous injection for 3 days showed that the supercritical CO_2 EtOH treated gels improved neovascularization as compared to the detergent based gels. Another study by Lewis et al. used decellularized liver ECM to create hydrogels for bile duct regeneration [188]. The results showed that increasing the concentration of decellularized liver ECM also increased the stiffness of the gels from less than 50 Pa at a concentration of 2 mg/mL to just below 1000 Pa at 20 mg/mL. Cholangiocytes cultured in the 2 mg/mL gels showed the highest amount of branchingstructures, thus indicating that the soft hydrogels allowed the infiltration and migration of cells, in turn resulting in better tissue morphogenesis. A lower concentration, however, could not be obtained due to the mechanical stability of the gel. In addition, the cholangiocytes were capable of forming complex duct formations after 7 days of culture. A different approach performed by Toprakhisar et al, was to use decellularized tendon to form a bioink for bioprinting [189]. The decellularization process proved to be successful in removing 97% of the DNA. The decellularized ECM was composed mostly out of collagen type I, whereas other proteins such as fibromodulin and prolargin at much smaller concentrations. In addition, during the decellularization process the collagen band patterns remained intact and could be used as a bioink for bioprinting. An additional bioprinting approach done by Ali et al. used decellularized kidney that was photo-crosslinkable [190] (Figure 12). The decellularized kidney ECM was chemically modified through a methacrylate reaction that allowed the ECM to crosslink under ultraviolet light exposure. The results showed that growth factors such as BMP-7, epidermal growth factor (EGF), NGF-1 and TGF-β1 remained active even after methacrylation. The results showed that the bioink was able to create a 16-layered scaffold that did not dissolve after 7 days unlike the unmethacrylated decellularized ECM, which dissolved within 1 day after

printing. Even after 2 weeks of culture bioprinted primary human kidney cells maintained their tubular marker Aquaporin-1 (AQP1).

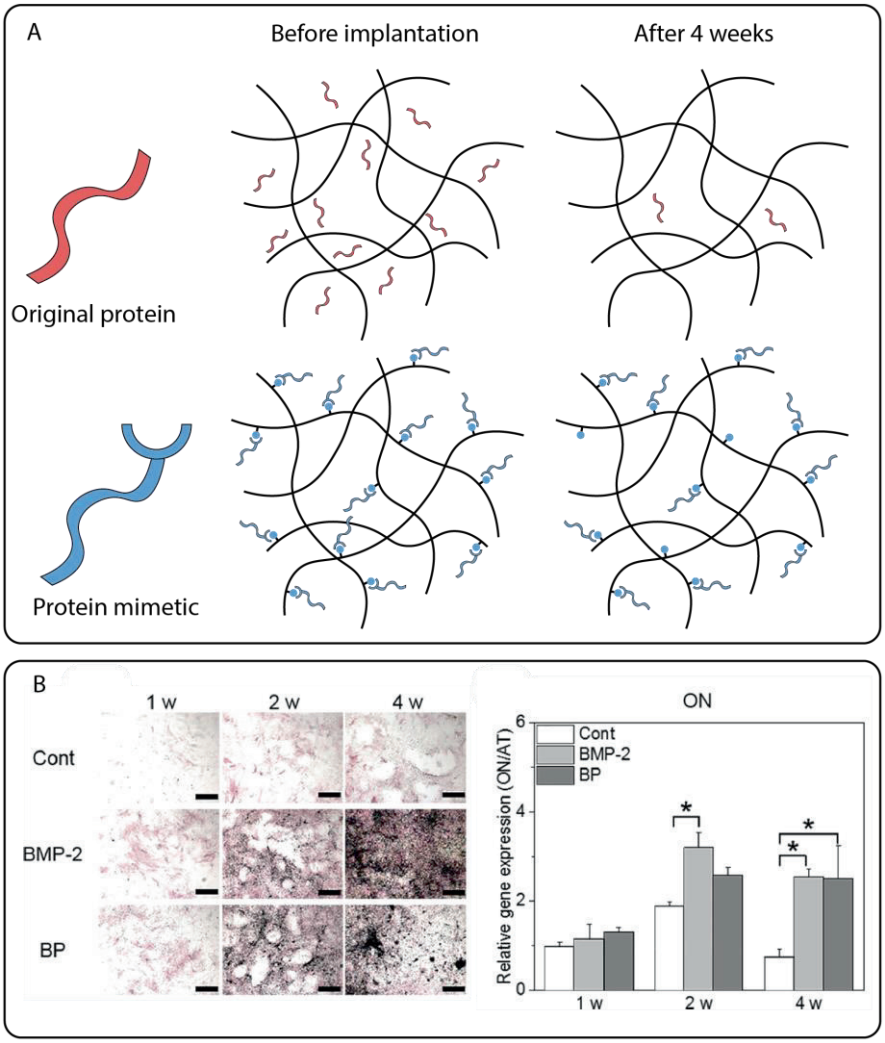

Figure 11. *(A) Schematic of using a mimetic protein that attaches to a hydrogel. Adding growth factors to boost the growth of a newly implanted scaffold. (B) ALP staining during the osteogenic differentiation of stem cells (left) in culture medium (control) or osteogenic medium containing BMP-2 or biomimetic BMP-2 (BP) and Osteonectin expression (right) [179]. Scale bar represents 500 µm.*

Using decellularized tissue as hydrogels or bioinks to recreate the targeted tissue biological microenvironment is a topic that many researchers pursue [191-193]. However, as mentioned earlier, some challenges need still to be

tackled when using decellularized ECM, such as the removal of chemical remnants and the immunogenic response and the possible loss of valuable ECM components [137-139]. In addition, the ECM of various tissues is highly complex, organized and anisotropic, which when pulverized and blended to make an homogenous hydrogel will most likely lose this organization [194-196]. Summarizing, using decellularized tissue as bulk material is a valuable strategy to biologically mimic the complex cellular microenvironment, though an exquisite balance between retaining the ECM structural properties and bioactivity is needed.

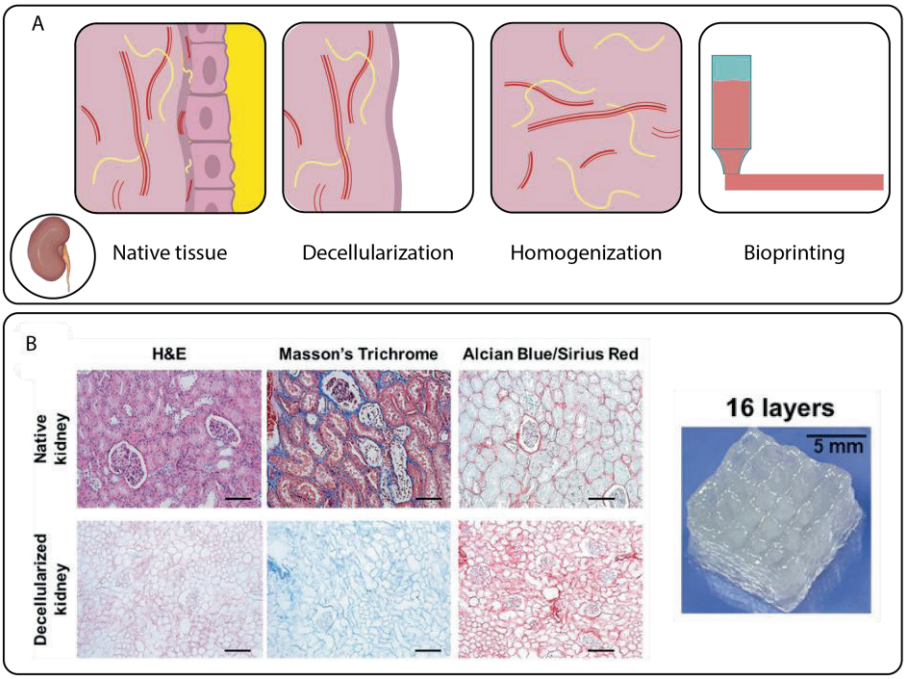

Figure 12. *Using decellularized ECM as base material for scaffolds to mimic the natural environment. (B) Histological sections of a native porcine kidney before and after the decellularization process (left) and the scaffold printed with the ECM based bioink (right) [190]. Scale bar represents 200 µm.*

5. Future outlook

This review provides an overview of the biomimicry strategies used in tissue engineering. Three main categories on which biomimicry criteria are pursued when designing scaffolds for tissue regeneration: mechanical, morphological and biological biomimicry. Each of these categories are important on their own and understanding how to mimic one aspect can give valuable insights on successfully regenerating a tissue. It is important to note that these subdivisions are not mutually exclusive to each other. Certain strategies or changing a single parameter can influence multiple forms of biomimicry. For example, the mechanical properties are influenced by changing the bulk material. Likewise, a different biological response would be implicitly expected [197]. Another example comes from decellularized tissues where the morphology is retained, but can also trigger a biological response due to growth factors or ECM components left after the decellularization process [132].

Strategies for mechanical biomimicry have undergone a lot of development over the last years. New materials have been created or modified to alter the mechanical properties [198, 199], the geometrical complexity of the scaffolds have been increased [200] and complex mechanical behavior has been introduced and studied [201, 202]. Future development for mechanical biomimicry should focus, in our opinion, on four subjects that when combined could create a successful mechanically mimicking scaffold. First, new materials should be developed and characterized, thus leading to expanding the palette of potential candidates for scaffold fabrication. The second focus point is the development of new biofabrication techniques that allow the creation of higher resolution scaffolds and more complex designs. In line with this, thirdly the role of scaffold design with respect to the mechanical properties of the scaffold should be studied more in depth and correlated to the biological effects that are observed. Finally, researchers should focus on

what happens to the mechanical properties of the scaffolds, and consequently of the biological constructs, over time. The scaffold will be remodeled over time and little is known of what happens to the mechanical properties after longer periods of *in vivo* culture and post *in vivo* implantation. Combining this knowledge could ultimately lead to the development of scaffolds that are tailored to the specific patient needs with a combination between the biomaterial used and the structural design that mimics the mechanical properties of the native tissue.

Also morphological biomimicry has undergone a lot of advances in terms of morphology [203, 204], improved decellularization protocols [205], better templating techniques [150], improved biofabrication techniques such as single cell bioprinting that can accurately deposit single cells [206]. This could lead to the fabrication of small tissues mimicking the cellular organization of the native tissue. Future developments could look into how to create large-scale biological constructs, specifically on how to vascularize and innervate them with the final goal of improving tissue integration and homeostasis after implantation. Many of the currently fabricated scaffolds, and hence biological constructs, are made on small scale. This brings a potential problem since the vascularization of small scaffolds is often neglected and not needed, although for clinically relevant defects it is the main requirement for success. Working out these obstacles would prove beneficial in creating a morphologically mimicking scaffold.

Many of the strategies that focus on biological biomimicry have improved, such as providing alternatives to static cultures [207, 208], improved understanding of the dynamic environment [209, 210] and enhancing cell scaffold interactions [211, 212]. Future development for biological mimicry should be focused on the dynamic culturing of scaffolds to standardize testing conditions. Further developments on bioreactors to make them more readily available at affordable costs should aid in creating a standardized dynamic

culture protocol for each tissue. Cell-material interactions should be further studied to increase the level of communication between synthetic and biological matters in order to reach a better functionality of the engineered tissue. In relation to decellularized ECM, it will be also important to achieve decellularization protocols able to avoid an immune response while keeping the ECM components. Solving these issues all together could aid in the fabrication of a scaffold that biologically mimics the native environment.

A future roadmap for the development of a fully biomimicking scaffold should not just focus on a single aspect of biomimicry. A more holistic approach towards biomimicry should be already conceived from the material development stage. We should also focus on how to get the morphology right, how to create a scaffold that is on scale of the native tissue, taking into consideration the multiscale properties of the targeted tissue, and how to tackle vascularization and innervation. In addition, to further mature and minimize the gap between *in vitro* and *in vivo,* the dynamicity of the local cellular environment should be recreated *in vitro* as close as possible to that of the native tissue. It is important to note that a lot of progress has been made in the development of a biomimicking scaffold and certain strategies are already at the preclinical evaluation stage in several animal models [213, 214].

A contradicting question arises whether how important it is to create a scaffold that fully mimics all aspects which after implantation are remodeled over time, or in other words how close should a scaffold mimic a tissue to achieve an optimal repair after implanted. If we learn from autologous tissue transplants, such as the reconstruction of the pharynx of cervical esophagus using the jejunum with success rates between 80 and 90% [215]. Though, the epithelial cells of the jejunum have a different function [216] and the general morphology is different [217, 218]. A similar example is transplanting the saphenous vein for arterial reconstruction, it seems that only a resemblance is needed [219]. Yet, the saphenous vein has weaker mechanical properties compared to an

artery [220], has a thinner tunica media layer and not a smooth tunica intima [221] and the pressure and flow under physiological conditions is much lower [222], which account for a 58% survival rate in patients 5 years post-implantation. Despite the tremendous advances achieved so far, there is still a lot of room for improvement. One of these improvements could be a graft or scaffold that better mimics the original tissue. This was also shown in a coronary artery bypass graft [223]. In this study the replacement of the coronary artery with the radial artery had an improved outcome over the saphenous vein as revealed by the meta analyses, indicating that it is important to mimic the original tissue as close as possible for the best outcome.

6. Conclusion

Mimicking only one aspect of biomimicry proofs to be a challenge, whether it is to obtain the correct mechanical properties for a mechanically complex tissue such as bone [224], mimicking the exact structure and organization of a liver [225], or replicating the complex kidney environment for each kidney cell type [226]. To fully mimic all these aspects presents an outstanding challenge unattainable with our current knowledge. However, over the years research on biomimicry has improved from the early reports from Otto Schmitt in 1957 to biologically mimic the electrical action of a nerve [227] to complex hydrogel yarns that align cells, mimicking the native architecture of tendons [228]. For regenerative medicine, biomimicry is important in order to manufacture a fully functioning tissue or organ. Whenever a strategy successfully employs mechanical, morphological and biological biomimicry, a fully functioning regenerated tissue should be expected.

References

[1] J.F. Vincent, O.A. Bogatyreva, N.R. Bogatyrev, A. Bowyer, A.-K. Pahl, Biomimetics: its practice and theory, Journal of the Royal Society Interface 3(9) (2006) 471-482.
[2] M. Pawlyn, Biomimicry in architecture, Routledge2019.
[3] R. Esfand, D.A. Tomalia, Poly(amidoamine) (PAMAM) dendrimers: from biomimicry to drug delivery and biomedical applications, Drug Discovery Today 6(8) (2001) 427-436.
[4] L. Eadie, T.K. Ghosh, Biomimicry in textiles: past, present and potential. An overview, Journal of the royal society interface 8(59) (2011) 761-775.
[5] G. Zhang, Biomimicry in biomedical research, Taylor & Francis, 2012.
[6] F. Tavsan, E. Sonmez, Biomimicry in furniture design, Procedia-social and behavioral sciences 197 (2015) 2285-2292.
[7] H. Chowdhury, R. Islam, M. Hussein, M. Zaid, B. Loganathan, F. Alam, Design of an energy efficient car by biomimicry of a boxfish, Energy Procedia 160 (2019) 40-44.
[8] S.L. Chia, C.Y. Tay, M.I. Setyawati, D.T. Leong, Biomimicry 3D gastrointestinal spheroid platform for the assessment of toxicity and inflammatory effects of zinc oxide nanoparticles, Small 11(6) (2015) 702-712.
[9] D. Qu, C.Z. Mosher, M.K. Boushell, H.H. Lu, Engineering complex orthopaedic tissues via strategic biomimicry, Annals of biomedical engineering 43(3) (2015) 697-717.
[10] D. Huh, Y.-s. Torisawa, G.A. Hamilton, H.J. Kim, D.E. Ingber, Microengineered physiological biomimicry: organs-on-chips, Lab on a Chip 12(12) (2012) 2156-2164.
[11] S. Minardi, B. Corradetti, F. Taraballi, M. Sandri, J. Van Eps, F.J. Cabrera, B.K. Weiner, A. Tampieri, E. Tasciotti, Evaluation of the osteoinductive potential of a bio-inspired scaffold mimicking the osteogenic niche for bone augmentation, Biomaterials 62 (2015) 128-137.
[12] S. Ahadian, S. Ostrovidov, V. Hosseini, H. Kaji, M. Ramalingam, H. Bae, A. Khademhosseini, Electrical stimulation as a biomimicry tool for regulating muscle cell behavior, Organogenesis 9(2) (2013) 87-92.
[13] T. Jiang, D. Kai, S. Liu, X. Huang, S. Heng, J. Zhao, B.Q.Y. Chan, X.J. Loh, Y. Zhu, C. Mao, Mechanically cartilage-mimicking poly (PCL-PTHF urethane)/collagen nanofibers induce chondrogenesis by blocking NF–kappa B signaling pathway, Biomaterials 178 (2018) 281-292.
[14] J.Y. Oh, Y.S. Kim, Y. Jung, S.J. Yang, C.R. Park, Preparation and exceptional mechanical properties of bone-mimicking size-tuned graphene oxide@ carbon nanotube hybrid paper, ACS nano 10(2) (2016) 2184-2192.
[15] S. Ma, Q. Tang, Q. Feng, J. Song, X. Han, F. Guo, Mechanical behaviours and mass transport properties of bone-mimicking scaffolds consisted of gyroid structures manufactured using selective laser melting, Journal of the mechanical behavior of biomedical materials 93 (2019) 158-169.
[16] A. Mellati, C.M. Fan, A. Tamayol, N. Annabi, S. Dai, J. Bi, B. Jin, C. Xian, A. Khademhosseini, H. Zhang, Microengineered 3D cell-laden thermoresponsive hydrogels for mimicking cell morphology and orientation in cartilage tissue engineering, Biotechnology and bioengineering 114(1) (2017) 217-231.
[17] A. Skardal, M. Devarasetty, H.-W. Kang, I. Mead, C. Bishop, T. Shupe, S.J. Lee, J. Jackson, J. Yoo, S. Soker, A hydrogel bioink toolkit for mimicking native tissue biochemical and mechanical properties in bioprinted tissue constructs, Acta biomaterialia 25 (2015) 24-34.
[18] O.A. Bolonduro, B.M. Duffy, A.A. Rao, L.D. Black, B.P. Timko, From biomimicry to bioelectronics: Smart materials for cardiac tissue engineering, Nano Research 13(5) (2020) 1253-1267.
[19] J.Y. Ng, S. Obuobi, M.L. Chua, C. Zhang, S. Hong, Y. Kumar, R. Gokhale, P.L.R. Ee, Biomimicry of microbial polysaccharide hydrogels for tissue engineering and regenerative medicine–A review, Carbohydrate polymers 241 (2020) 116345.
[20] A. Marino, C. Filippeschi, V. Mattoli, B. Mazzolai, G. Ciofani, Biomimicry at the nanoscale: current research and perspectives of two-photon polymerization, Nanoscale 7(7) (2015) 2841-2850.
[21] S. Kumari, S. Vermeulen, B. Van Der Veer, A. Carlier, J. De Boer, D. Subramanyam, Shaping cell fate: influence of topographical substratum properties on embryonic stem cells, Tissue Engineering Part B: Reviews 24(4) (2018) 255-266.
[22] W.J. Tyler, The mechanobiology of brain function, Nature Reviews Neuroscience 13(12) (2012) 867-878.

[23] T. Hoc, L. Henry, M. Verdier, D. Aubry, L. Sedel, A. Meunier, Effect of microstructure on the mechanical properties of Haversian cortical bone, Bone 38(4) (2006) 466-474.
[24] Y. Chen, J.E. Frith, A. Dehghan-Manshadi, H. Attar, D. Kent, N.D.M. Soro, M.J. Bermingham, M.S. Dargusch, Mechanical properties and biocompatibility of porous titanium scaffolds for bone tissue engineering, Journal of the mechanical behavior of biomedical materials 75 (2017) 169-174.
[25] F. Zhang, Y. Xie, H. Celik, O. Akkus, S.H. Bernacki, M.W. King, Engineering small-caliber vascular grafts from collagen filaments and nanofibers with comparable mechanical properties to native vessels, Biofabrication 11(3) (2019) 035020.
[26] H. Rogan, F. Ilagan, X. Tong, C.R. Chu, F. Yang, Microribbon-hydrogel composite scaffold accelerates cartilage regeneration in vivo with enhanced mechanical properties using mixed stem cells and chondrocytes, Biomaterials 228 (2020) 119579.
[27] P.D. Ballyk, C. Walsh, J. Butany, M. Ojha, Compliance mismatch may promote graft–artery intimal hyperplasia by altering suture-line stresses, Journal of biomechanics 31(3) (1997) 229-237.
[28] Q.-H. Zhang, A. Cossey, J. Tong, Stress shielding in bone of a bone-cement interface, Medical engineering & physics 38(4) (2016) 423-426.
[29] J.L. Forman, R.W. Kent, The effect of calcification on the structural mechanics of the costal cartilage, Computer methods in biomechanics and biomedical engineering 17(2) (2014) 94-107.
[30] E.A. Zimmermann, R.O. Ritchie, Bone as a structural material, Advanced healthcare materials 4(9) (2015) 1287-1304.
[31] N.F. Renna, N. De Las Heras, R.M. Miatello, Pathophysiology of vascular remodeling in hypertension, International journal of hypertension 2013 (2013).
[32] C.C. Finnerty, M.G. Jeschke, L.K. Branski, J.P. Barret, P. Dziewulski, D.N. Herndon, Hypertrophic scarring: the greatest unmet challenge after burn injury, The Lancet 388(10052) (2016) 1427-1436.
[33] C.G. Jeong, S.J. Hollister, A comparison of the influence of material on in vitro cartilage tissue engineering with PCL, PGS, and POC 3D scaffold architecture seeded with chondrocytes, Biomaterials 31(15) (2010) 4304-4312.
[34] R. Gauvin, Y.-C. Chen, J.W. Lee, P. Soman, P. Zorlutuna, J.W. Nichol, H. Bae, S. Chen, A. Khademhosseini, Microfabrication of complex porous tissue engineering scaffolds using 3D projection stereolithography, Biomaterials 33(15) (2012) 3824-3834.
[35] L. Moroni, J.R. de Wijn, C.A. van Blitterswijk, 3D fiber-deposited scaffolds for tissue engineering: Influence of pores geometry and architecture on dynamic mechanical properties, Biomaterials 27(7) (2006) 974-985.
[36] F. Ruini, C. Tonda-Turo, V. Chiono, G. Ciardelli, Chitosan membranes for tissue engineering: comparison of different crosslinkers, Biomedical materials 10(6) (2015) 065002.
[37] D. Pierantozzi, A. Scalzone, S. Jindal, L. Stīpniece, K. Šalma-Ancāne, K. Dalgarno, P. Gentile, E. Mancuso, 3D printed Sr-containing composite scaffolds: Effect of structural design and material formulation towards new strategies for bone tissue engineering, Composites Science and Technology 191 (2020) 108069.
[38] T.H. Kim, D.B. An, S.H. Oh, M.K. Kang, H.H. Song, J.H. Lee, Creating stiffness gradient polyvinyl alcohol hydrogel using a simple gradual freezing–thawing method to investigate stem cell differentiation behaviors, Biomaterials 40 (2015) 51-60.
[39] C.N. Kelly, J. Francovich, S. Julmi, D. Safranski, R.E. Guldberg, H.J. Maier, K. Gall, Fatigue behavior of As-built selective laser melted titanium scaffolds with sheet-based gyroid microarchitecture for bone tissue engineering, Acta biomaterialia 94 (2019) 610-626.
[40] A. Abdal-Hay, M. Bartnikowski, S. Hamlet, S. Ivanovski, Electrospun biphasic tubular scaffold with enhanced mechanical properties for vascular tissue engineering, Materials Science and Engineering: C 82 (2018) 10-18.
[41] H. Janke, J. Bohlin, R. Lomme, S. Mihaila, J. Hilborn, W. Feitz, E. Oosterwijk, Bioinspired coupled helical coils for soft tissue engineering of tubular structures–Improved mechanical behavior of tubular collagen type I templates, Acta biomaterialia 59 (2017) 234-242.
[42] C. Ping Ooi, R.E. Cameron, The hydrolytic degradation of polydioxanone (PDSII) sutures. Part I: Morphological aspects, Journal of biomedical materials research 63(3) (2002) 280-290.
[43] Y. Yoon, C.H. Kim, J.E. Lee, J. Yoon, N.K. Lee, T.H. Kim, S.-H. Park, 3D bioprinted complex constructs reinforced by hybrid multilayers of electrospun nanofiber sheets, Biofabrication 11(2) (2019) 025015.

[44] H. Sun, L. Mei, C. Song, X. Cui, P. Wang, The in vivo degradation, absorption and excretion of PCL-based implant, Biomaterials 27(9) (2006) 1735-1740.
[45] Z.P. Rad, J. Mokhtari, M. Abbasi, Fabrication and characterization of PCL/zein/gum arabic electrospun nanocomposite scaffold for skin tissue engineering, Materials Science and Engineering: C 93 (2018) 356-366.
[46] S. Khalili, S.N. Khorasani, S.M. Razavi, B. Hashemibeni, A. Tamayol, Nanofibrous scaffolds with biomimetic composition for skin regeneration, Applied biochemistry and biotechnology 187(4) (2019) 1193-1203.
[47] G. Wilkes, I. Brown, R. Wildnauer, The biomechanical properties of skin, CRC critical reviews in bioengineering 1(4) (1973) 453-495.
[48] Y. Hong, A. Huber, K. Takanari, N.J. Amoroso, R. Hashizume, S.F. Badylak, W.R. Wagner, Mechanical properties and in vivo behavior of a biodegradable synthetic polymer microfiber–extracellular matrix hydrogel biohybrid scaffold, Biomaterials 32(13) (2011) 3387-3394.
[49] M. Baldassarri, E. Bonfante, M. Suzuki, C. Marin, R. Granato, N. Tovar, P.G. Coelho, Mechanical properties of human bone surrounding plateau root form implants retrieved after 0.3–24 years of function, Journal of Biomedical Materials Research Part B: Applied Biomaterials 100(7) (2012) 2015-2021.
[50] S. Franz, S. Rammelt, D. Scharnweber, J.C. Simon, Immune responses to implants–a review of the implications for the design of immunomodulatory biomaterials, Biomaterials 32(28) (2011) 6692-6709.
[51] R. Strehl, T. Tallheden, E. Sjögren-Jansson, W.W. Minuth, A. Lindahl, Long-term maintenance of human articular cartilage in culture for biomaterial testing, Biomaterials 26(22) (2005) 4540-4549.
[52] D. Carluccio, C. Xu, J. Venezuela, Y. Cao, D. Kent, M. Bermingham, A.G. Demir, B. Previtali, Q. Ye, M. Dargusch, Additively manufactured iron-manganese for biodegradable porous load-bearing bone scaffold applications, Acta biomaterialia 103 (2020) 346-360.
[53] B. Ostrowska, A. Di Luca, L. Moroni, W. Swieszkowski, Influence of internal pore architecture on biological and mechanical properties of three-dimensional fiber deposited scaffolds for bone regeneration, Journal of biomedical materials research Part A 104(4) (2016) 991-1001.
[54] F.P. Melchels, K. Bertoldi, R. Gabbrielli, A.H. Velders, J. Feijen, D.W. Grijpma, Mathematically defined tissue engineering scaffold architectures prepared by stereolithography, Biomaterials 31(27) (2010) 6909-6916.
[55] Y. Jin, C. Xie, Q. Gao, X. Zhou, G. Li, J. Du, Y. He, Fabrication of multi-scale and tunable auxetic scaffolds for tissue engineering, Materials & Design 197 (2021) 109277.
[56] A. Di Luca, I. Lorenzo-Moldero, C. Mota, A. Lepedda, D. Auhl, C. Van Blitterswijk, L. Moroni, Tuning Cell Differentiation into a 3D Scaffold Presenting a Pore Shape Gradient for Osteochondral Regeneration, Advanced healthcare materials 5(14) (2016) 1753-63.
[57] P. Huebner, P.B. Warren, D. Chester, J.T. Spang, A.C. Brown, M.B. Fisher, R.A. Shirwaiker, Mechanical properties of tissue formed in vivo are affected by 3D-bioplotted scaffold microarchitecture and correlate with ECM collagen fiber alignment, Connective tissue research 61(2) (2020) 190-204.
[58] Y. Zamani, G. Amoabediny, J. Mohammadi, H. Seddiqi, M.N. Helder, B. Zandieh-Doulabi, J. Klein-Nulend, J.H. Koolstra, 3D-printed poly (Ɛ-caprolactone) scaffold with gradient mechanical properties according to force distribution in the mandible for mandibular bone tissue engineering, Journal of the mechanical behavior of biomedical materials 104 (2020) 103638.
[59] D.J. Wu, K. Van Dongen, W. Szymczyk, P.J. Besseling, R.M. Cardinaels, G. Marchioli, M.H. Van Genderen, C.V. Bouten, A.I. Smits, P.Y. Dankers, Optimization of anti-kinking designs for vascular grafts based on supramolecular materials, Frontiers in Materials 7 (2020) 220.
[60] J. Dagdelen, J. Montoya, M. de Jong, K. Persson, Computational prediction of new auxetic materials, Nature Communications 8 (2017) 323.
[61] K. Bertoldi, V. Vitelli, J. Christensen, M. Van Hecke, Flexible mechanical metamaterials, Nature Reviews Materials 2(11) (2017) 1-11.
[62] H. Kolken, K. Lietaert, T. van der Sloten, B. Pouran, A. Meynen, G. Van Loock, H. Weinans, L. Scheys, A.A. Zadpoor, Mechanical performance of auxetic meta-biomaterials, journal of the mechanical behavior of biomedical materials 104 (2020) 103658.

[63] H. Suo, D. Zhang, J. Yin, J. Qian, Z.L. Wu, J. Fu, Interpenetrating polymer network hydrogels composed of chitosan and photocrosslinkable gelatin with enhanced mechanical properties for tissue engineering, Materials Science and Engineering: C 92 (2018) 612-620.
[64] H. Suo, K. Xu, X. Zheng, Using glucosamine to improve the properties of photocrosslinked gelatin scaffolds, Journal of biomaterials applications 29(7) (2015) 977-987.
[65] A. Martínez, M. Blanco, N. Davidenko, R. Cameron, Tailoring chitosan/collagen scaffolds for tissue engineering: Effect of composition and different crosslinking agents on scaffold properties, Carbohydrate polymers 132 (2015) 606-619.
[66] S. Naghieh, M.R. Karamooz-Ravari, M. Sarker, E. Karki, X. Chen, Influence of crosslinking on the mechanical behavior of 3D printed alginate scaffolds: Experimental and numerical approaches, Journal of the mechanical behavior of biomedical materials 80 (2018) 111-118.
[67] Y. Ladilov, C. Schäfer, A. Held, M. Schäfer, T. Noll, H.M. Piper, Mechanism of Ca2+ overload in endothelial cells exposed to simulated ischemia, Cardiovascular research 47(2) (2000) 394-403.
[68] J. Berger, M. Reist, J.M. Mayer, O. Felt, R. Gurny, Structure and interactions in chitosan hydrogels formed by complexation or aggregation for biomedical applications, European Journal of Pharmaceutics and Biopharmaceutics 57(1) (2004) 35-52.
[69] C.H. Jeong, D.H. Kim, J.H. Yune, H.C. Kwon, D.-M. Shin, H. Sohn, K.H. Lee, B. Choi, E.S. Kim, J.H. Kang, E.K. Kim, S.G. Han, In vitro toxicity assessment of crosslinking agents used in hyaluronic acid dermal filler, Toxicology in Vitro 70 (2021) 105034.
[70] C. Wang, X. Tong, F. Yang, Bioengineered 3D brain tumor model to elucidate the effects of matrix stiffness on glioblastoma cell behavior using PEG-based hydrogels, Molecular pharmaceutics 11(7) (2014) 2115-2125.
[71] A.M. Rosales, S.L. Vega, F.W. DelRio, J.A. Burdick, K.S. Anseth, Hydrogels with reversible mechanics to probe dynamic cell microenvironments, Angewandte Chemie International Edition 56(40) (2017) 12132-12136.
[72] D.C. Lin, B. Yurke, N.A. Langrana, Mechanical properties of a reversible, DNA-crosslinked polyacrylamide hydrogel, J. Biomech. Eng. 126(1) (2004) 104-110.
[73] B.A. Juliar, J.A. Beamish, M.E. Busch, D.S. Cleveland, L. Nimmagadda, A.J. Putnam, Cell-mediated matrix stiffening accompanies capillary morphogenesis in ultra-soft amorphous hydrogels, Biomaterials 230 (2020) 119634.
[74] N. Rauner, M. Meuris, M. Zoric, J.C. Tiller, Enzymatic mineralization generates ultrastiff and tough hydrogels with tunable mechanics, Nature 543(7645) (2017) 407-410.
[75] T.R. Cox, J.T. Erler, Remodeling and homeostasis of the extracellular matrix: implications for fibrotic diseases and cancer, Disease models & mechanisms 4(2) (2011) 165-178.
[76] L.V. Burgin, R.M. Aspden, Impact testing to determine the mechanical properties of articular cartilage in isolation and on bone, Journal of Materials Science: Materials in Medicine 19(2) (2008) 703-711.
[77] A. Janfada, A. Asefnejad, M.T. Khorasani, M.D. Joupari, Reinforcement of electrospun polycaprolacton scaffold using KIT-6 to improve mechanical and biological performance, Polymer Testing 84 (2020) 106391.
[78] J. Du, Y. Zuo, L. Lin, D. Huang, L. Niu, Y. Wei, K. Wang, Q. Lin, Q. Zou, Y. Li, Effect of hydroxyapatite fillers on the mechanical properties and osteogenesis capacity of bio-based polyurethane composite scaffolds, Journal of the mechanical behavior of biomedical materials 88 (2018) 150-159.
[79] R. Sinha, M. Cámara-Torres, P. Scopece, E. Verga Falzacappa, A. Patelli, L. Moroni, C. Mota, A hybrid additive manufacturing platform to create bulk and surface composition gradients on scaffolds for tissue regeneration, Nature Communications 12(1) (2021) 500.
[80] A. Seyedsalehi, L. Daneshmandi, M. Barajaa, J. Riordan, C.T. Laurencin, Fabrication and characterization of mechanically competent 3D printed polycaprolactone-reduced graphene oxide scaffolds, Scientific reports 10(1) (2020) 1-14.
[81] J.S. Petrofsky, M. Laymon, H. Lee, Effect of heat and cold on tendon flexibility and force to flex the human knee, Medical science monitor: international medical journal of experimental and clinical research 19 (2013) 661.
[82] R.J. McCormick, The flexibility of the collagen compartment of muscle, Meat Science 36(1-2) (1994) 79-91.

[83] M. Degli Esposti, F. Chiellini, F. Bondioli, D. Morselli, P. Fabbri, Highly porous PHB-based bioactive scaffolds for bone tissue engineering by in situ synthesis of hydroxyapatite, Materials Science and Engineering: C 100 (2019) 286-296.
[84] D. Morselli, F. Bondioli, M. Sangermano, M. Messori, Epoxy networks reinforced with TiO2 generated by nonhydrolytic sol–gel process: A comparison between in situ and ex situ syntheses to obtain filled polymers, Polymer Engineering & Science 55(7) (2015) 1689-1697.
[85] K.A. van Kampen, R.G. Scheuring, M.L. Terpstra, R. Levato, J. Groll, J. Malda, C. Mota, L. Moroni, Biofabrication: From Additive Manufacturing to Bioprinting, in: R.L. Reis (Ed.), Encyclopedia of Tissue Engineering and Regenerative Medicine, Academic Press, Oxford, 2019, pp. 41-55.
[86] J. Saroia, Y. Wang, Q. Wei, M. Lei, X. Li, Y. Guo, K. Zhang, A review on 3D printed matrix polymer composites: its potential and future challenges, The International Journal of Advanced Manufacturing Technology 106(5) (2020) 1695-1721.
[87] H. Zhou, J. Lee, Nanoscale hydroxyapatite particles for bone tissue engineering, Acta biomaterialia 7(7) (2011) 2769-2781.
[88] J. Russo, R. Robinson, M.J. Oldham, Effects of cartilage rings on airflow and particle deposition in the trachea and main bronchi, Medical engineering & physics 30(5) (2008) 581-589.
[89] K. Choy, E.-K. Pae, Y. Park, K.-H. Kim, C.J. Burstone, Effect of root and bone morphology on the stress distribution in the periodontal ligament, American Journal of Orthodontics and Dentofacial Orthopedics 117(1) (2000) 98-105.
[90] G. Chen, T. Sato, J. Tanaka, T. Tateishi, Preparation of a biphasic scaffold for osteochondral tissue engineering, Materials Science and Engineering: C 26(1) (2006) 118-123.
[91] N. Reznikov, M. Bilton, L. Lari, M.M. Stevens, R. Kröger, Fractal-like hierarchical organization of bone begins at the nanoscale, Science 360(6388) (2018).
[92] P.J. Schaner, N.D. Martin, T.N. Tulenko, I.M. Shapiro, N.A. Tarola, R.F. Leichter, R.A. Carabasi, P.J. DiMuzio, Decellularized vein as a potential scaffold for vascular tissue engineering, Journal of vascular surgery 40(1) (2004) 146-153.
[93] T. Gros, J.S. Sakamoto, A. Blesch, L.A. Havton, M.H. Tuszynski, Regeneration of long-tract axons through sites of spinal cord injury using templated agarose scaffolds, Biomaterials 31(26) (2010) 6719-6729.
[94] K. Shimomura, Y. Moriguchi, C.D. Murawski, H. Yoshikawa, N. Nakamura, Osteochondral tissue engineering with biphasic scaffold: current strategies and techniques, Tissue Engineering Part B: Reviews 20(5) (2014) 468-476.
[95] X. Liu, Y. Wei, C. Xuan, L. Liu, C. Lai, M. Chai, Z. Zhang, L. Wang, X. Shi, A Biomimetic Biphasic Osteochondral Scaffold with Layer-Specific Release of Stem Cell Differentiation Inducers for the Reconstruction of Osteochondral Defects, Advanced healthcare materials 9(23) (2020) 2000076.
[96] T. Mesallati, E. Sheehy, T. Vinardell, C. Buckley, D. Kelly, Tissue engineering scaled-up, anatomically shaped osteochondral constructs for joint resurfacing, Eur Cell Mater 30 (2015) 163-85.
[97] N. Miosge, M. Hartmann, C. Maelicke, R. Herken, Expression of collagen type I and type II in consecutive stages of human osteoarthritis, Histochemistry and cell biology 122(3) (2004) 229-236.
[98] L.J. Sandell, T. Aigner, Articular cartilage and changes in arthritis: cell biology of osteoarthritis, Arthritis Research & Therapy 3(2) (2001) 1-7.
[99] A. Alhadlaq, J.J. Mao, Tissue-engineered osteochondral constructs in the shape of an articular condyle, JBJS 87(5) (2005) 936-944.
[100] Q.C. Peiffer, M. de Ruijter, J. van Duijn, D. Crottet, E. Dominic, J. Malda, M. Castilho, Melt electrowriting onto anatomically relevant biodegradable substrates: Resurfacing a diarthrodial joint, Materials & design 195 (2020) 109025.
[101] W. Balestri, R.H. Morris, J.A. Hunt, Y. Reinwald, Current advances on the regeneration of musculoskeletal interfaces, Tissue Engineering Part B: Reviews (2021).
[102] M.C. Echave, R.M. Domingues, M. Gómez-Florit, J.L. Pedraz, R.L. Reis, G. Orive, M.E. Gomes, Biphasic hydrogels integrating mineralized and anisotropic features for interfacial tissue engineering, ACS applied materials & interfaces 11(51) (2019) 47771-47784.
[103] P. Fratzl, Biomimetic materials research: what can we really learn from nature's structural materials?, Journal of the Royal Society Interface 4(15) (2007) 637-642.

[104] M. Bartnikowski, A.R. Akkineni, M. Gelinsky, M.A. Woodruff, T.J. Klein, A hydrogel model incorporating 3D-plotted hydroxyapatite for osteochondral tissue engineering, Materials 9(4) (2016) 285.
[105] W. Zhang, Q. Lian, D. Li, K. Wang, D. Hao, W. Bian, Z. Jin, The effect of interface microstructure on interfacial shear strength for osteochondral scaffolds based on biomimetic design and 3D printing, Materials Science and Engineering: C 46 (2015) 10-15.
[106] Y.P. Singh, J.C. Moses, B.K. Bhunia, S.K. Nandi, B.B. Mandal, Hierarchically structured seamless silk scaffolds for osteochondral interface tissue engineering, Journal of Materials Chemistry B 6(36) (2018) 5671-5688.
[107] M. Sartori, S. Pagani, A. Ferrari, V. Costa, V. Carina, E. Figallo, M. Maltarello, L. Martini, M. Fini, G. Giavaresi, A new bi-layered scaffold for osteochondral tissue regeneration: In vitro and in vivo preclinical investigations, Materials Science and Engineering: C 70 (2017) 101-111.
[108] A.I. Alford, K.M. Kozloff, K.D. Hankenson, Extracellular matrix networks in bone remodeling, The international journal of biochemistry & cell biology 65 (2015) 20-31.
[109] T.J. McKee, G. Perlman, M. Morris, S.V. Komarova, Extracellular matrix composition of connective tissues: a systematic review and meta-analysis, Scientific reports 9(1) (2019) 1-15.
[110] G.S. Travlos, Normal structure, function, and histology of the bone marrow, Toxicologic pathology 34(5) (2006) 548-565.
[111] G. Windisch, H. Clement, W. Grechenig, N.P. Tesch, W. Pichler, A morphometrical study of the medullary cavity of the ulna referred to intramedullary nailing, Surgical and Radiologic Anatomy 29(1) (2007) 47-53.
[112] J.D. Black, B.J. Tadros, Bone structure: from cortical to calcium, Orthopaedics and Trauma 34(3) (2020) 113-119.
[113] D. Cooper, C. Kawalilak, K. Harrison, B. Johnston, J. Johnston, Cortical bone porosity: what is it, why is it important, and how can we detect it?, Current osteoporosis reports 14(5) (2016) 187-198.
[114] A. Di Luca, A. Longoni, G. Criscenti, C. Mota, C. van Blitterswijk, L. Moroni, Toward mimicking the bone structure: design of novel hierarchical scaffolds with a tailored radial porosity gradient, Biofabrication 8(4) (2016) 045007.
[115] S.M. Bittner, B.T. Smith, L. Diaz-Gomez, C.D. Hudgins, A.J. Melchiorri, D.W. Scott, J.P. Fisher, A.G. Mikos, Fabrication and mechanical characterization of 3D printed vertical uniform and gradient scaffolds for bone and osteochondral tissue engineering, Acta biomaterialia 90 (2019) 37-48.
[116] A. Sola, J. Bertacchini, D. D'Avella, L. Anselmi, T. Maraldi, S. Marmiroli, M. Messori, Development of solvent-casting particulate leaching (SCPL) polymer scaffolds as improved three-dimensional supports to mimic the bone marrow niche, Materials Science and Engineering: C 96 (2019) 153-165.
[117] V. Karageorgiou, D. Kaplan, Porosity of 3D biomaterial scaffolds and osteogenesis, Biomaterials 26(27) (2005) 5474-5491.
[118] N. Davidenko, T. Gibb, C. Schuster, S. Best, J. Campbell, C. Watson, R. Cameron, Biomimetic collagen scaffolds with anisotropic pore architecture, Acta biomaterialia 8(2) (2012) 667-676.
[119] N. Kamboj, J. Kazantseva, R. Rahmani, M.A. Rodríguez, I. Hussainova, Selective laser sintered bio-inspired silicon-wollastonite scaffolds for bone tissue engineering, Materials Science and Engineering: C 116 (2020) 111223.
[120] M. Cámara-Torres, R. Sinha, C. Mota, L. Moroni, Improving cell distribution on 3D additive manufactured scaffolds through engineered seeding media density and viscosity, Acta Biomaterialia 101 (2020) 183-195.
[121] P.A. Shiekh, A. Singh, A. Kumar, Oxygen-releasing antioxidant cryogel scaffolds with sustained oxygen delivery for tissue engineering applications, ACS applied materials & interfaces 10(22) (2018) 18458-18469.
[122] T.U. Esser, K. Roshanbinfar, F.B. Engel, Promoting vascularization for tissue engineering constructs: current strategies focusing on HIF-regulating scaffolds, Expert opinion on biological therapy 19(2) (2019) 105-118.
[123] S. Li, K. Wang, X. Jiang, Q. Hu, C. Zhang, B. Wang, Rapid Fabrication of Ready-to-Use Gelatin Scaffolds with Prevascular Networks Using Alginate Hollow Fibers as Sacrificial Templates, ACS Biomaterials Science & Engineering 6(4) (2020) 2297-2311.

[124] W. Sheridan, G.P. Duffy, B. Murphy, Mechanical characterization of a customized decellularized scaffold for vascular tissue engineering, Journal of the mechanical behavior of biomedical materials 8 (2012) 58-70.
[125] M. Ozeki, Y. Narita, H. Kagami, N. Ohmiya, A. Itoh, Y. Hirooka, Y. Niwa, M. Ueda, H. Goto, Evaluation of decellularized esophagus as a scaffold for cultured esophageal epithelial cells, Journal of Biomedical Materials Research Part A 79(4) (2006) 771-778.
[126] G. Mazza, K. Rombouts, A.R. Hall, L. Urbani, T.V. Luong, W. Al-Akkad, L. Longato, D. Brown, P. Maghsoudlou, A.P. Dhillon, Decellularized human liver as a natural 3D-scaffold for liver bioengineering and transplantation, Scientific reports 5(1) (2015) 1-15.
[127] A.W. Godehardt, R.R. Tönjes, Xenotransplantation of decellularized pig heart valves—regulatory aspects in Europe, Xenotransplantation 27(3) (2020) e12609.
[128] E.S. Lederman, A.P. Toth, G.P. Nicholson, R.J. Nowinski, G.K. Bal, G.R. Williams, J.P. Iannotti, A prospective, multicenter study to evaluate clinical and radiographic outcomes in primary rotator cuff repair reinforced with a xenograft dermal matrix, Journal of Shoulder and Elbow Surgery 25(12) (2016) 1961-1970.
[129] V. Agrawal, Healing rates for challenging rotator cuff tears utilizing an acellular human dermal reinforcement graft, International journal of shoulder surgery 6(2) (2012) 36.
[130] D.N. Bracey, N.E. Cignetti, A.H. Jinnah, A.V. Stone, B.M. Gyr, P.W. Whitlock, A.T. Scott, Bone xenotransplantation: A review of the history, orthopedic clinical literature, and a single-center case series, Xenotransplantation 27(5) (2020) e12600.
[131] S. Pors, M. Ramløse, D. Nikiforov, K. Lundsgaard, J. Cheng, C.Y. Andersen, S. Kristensen, Initial steps in reconstruction of the human ovary: survival of pre-antral stage follicles in a decellularized human ovarian scaffold, Human Reproduction 34(8) (2019) 1523-1535.
[132] D.M. Giraldo-Gomez, S.J. García-López, L. Tamay-de-Dios, R. Sánchez-Sánchez, J. Villalba-Caloca, A. Sotres-Vega, M.L. Del Prado-Audelo, K.K. Gómez-Lizárraga, D. Garciadiego-Cázares, M.C. Piña-Barba, Fast cyclical-decellularized trachea as a natural 3D scaffold for organ engineering, Materials Science and Engineering: C 105 (2019) 110142.
[133] C. Rao, Y.Y. Liu, C.L. Peavey, D.T. Woodley, Novel extracellular matrix-associated serine proteinase inhibitors from human skin fibroblasts, Archives of biochemistry and biophysics 317(1) (1995) 311-314.
[134] D.M. Casali, R.M. Handleton, T. Shazly, M.A. Matthews, A novel supercritical CO2-based decellularization method for maintaining scaffold hydration and mechanical properties, The Journal of Supercritical Fluids 131 (2018) 72-81.
[135] Y.-W. Cheng, D.J. Shiwarski, R.L. Ball, K.A. Whitehead, A.W. Feinberg, Engineering aligned skeletal muscle tissue using decellularized plant-derived scaffolds, ACS Biomaterials Science & Engineering 6(5) (2020) 3046-3054.
[136] J.P. Hodde, S.F. Badylak, A.O. Brightman, S.L. Voytik-Harbin, Glycosaminoglycan content of small intestinal submucosa: a bioscaffold for tissue replacement, Tissue engineering 2(3) (1996) 209-217.
[137] R. Ackbar, H. Ainoedhofer, M. Gugatschka, A.K. Saxena, Decellularized ovine esophageal mucosa for esophageal tissue engineering, Technology and Health Care 20(3) (2012) 215-223.
[138] J. Tan, Q.-Y. Zhang, L.-P. Huang, K. Huang, H.-Q. Xie, Decellularized scaffold and its elicited immune response towards the host: the underlying mechanism and means of immunomodulatory modification, Biomaterials Science (2021).
[139] P.M. Crapo, T.W. Gilbert, S.F. Badylak, An overview of tissue and whole organ decellularization processes, Biomaterials 32(12) (2011) 3233-3243.
[140] J. Wang, Y. Cheng, H. Wang, Y. Wang, K. Zhang, C. Fan, H. Wang, X. Mo, Biomimetic and hierarchical nerve conduits from multifunctional nanofibers for guided peripheral nerve regeneration, Acta Biomaterialia 117 (2020) 180-191.
[141] J.S. Miller, K.R. Stevens, M.T. Yang, B.M. Baker, D.-H.T. Nguyen, D.M. Cohen, E. Toro, A.A. Chen, P.A. Galie, X. Yu, Rapid casting of patterned vascular networks for perfusable engineered three-dimensional tissues, Nature materials 11(9) (2012) 768-774.
[142] S. Sämfors, K. Karlsson, J. Sundberg, K. Markstedt, P. Gatenholm, Biofabrication of bacterial nanocellulose scaffolds with complex vascular structure, Biofabrication 11(4) (2019) 045010.

[143] X. Chen, Y. Yao, S. Liu, Q. Hu, An integrated strategy for designing and fabricating triple-layer vascular graft with oriented microgrooves to promote endothelialization, Journal of biomaterials applications (2021) 08853282211001006.
[144] P.M. Jenkins, M.R. Laughter, D.J. Lee, Y.M. Lee, C.R. Freed, D. Park, A nerve guidance conduit with topographical and biochemical cues: potential application using human neural stem cells, Nanoscale research letters 10(1) (2015) 1-7.
[145] P. Wu, L. Wang, W. Li, Y. Zhang, Y. Wu, D. Zhi, H. Wang, L. Wang, D. Kong, M. Zhu, Construction of vascular graft with circumferentially oriented microchannels for improving artery regeneration, Biomaterials 242 (2020) 119922.
[146] J. Huling, I.K. Ko, A. Atala, J.J. Yoo, Fabrication of biomimetic vascular scaffolds for 3D tissue constructs using vascular corrosion casts, Acta biomaterialia 32 (2016) 190-197.
[147] J.R. Gershlak, S. Hernandez, G. Fontana, L.R. Perreault, K.J. Hansen, S.A. Larson, B.Y. Binder, D.M. Dolivo, T. Yang, T. Dominko, Crossing kingdoms: Using decellularized plants as perfusable tissue engineering scaffolds, Biomaterials 125 (2017) 13-22.
[148] K.R. Phipps, B. Danielewska-Nikiel, J. Mushonganono, N. Baldwin, Reproductive and developmental toxicity screening study of an acetone extract of rosemary, Regulatory Toxicology and Pharmacology 120 (2021) 104840.
[149] J.F. Patrick, K.R. Hart, B.P. Krull, C.E. Diesendruck, J.S. Moore, S.R. White, N.R. Sottos, Continuous self-healing life cycle in vascularized structural composites, Advanced materials 26(25) (2014) 4302-4308.
[150] N.C. Negrini, M. Bonnetier, G. Giatsidis, D.P. Orgill, S. Farè, B. Marelli, Tissue-mimicking gelatin scaffolds by alginate sacrificial templates for adipose tissue engineering, Acta biomaterialia 87 (2019) 61-75.
[151] R. Rajpurohit, C.J. Koch, Z. Tao, C.M. Teixeira, I.M. Shapiro, Adaptation of chondrocytes to low oxygen tension: relationship between hypoxia and cellular metabolism, Journal of cellular physiology 168(2) (1996) 424-432.
[152] H. Watson, D. Emslie-Smith, K. Lowe, The intracardiac electrocardiogram of human atrioventricular conducting tissue, American heart journal 74(1) (1967) 66-70.
[153] U.D. Mathisen, T. Melsom, O.C. Ingebretsen, T.G. Jenssen, I. Njølstad, M.D. Solbu, I. Toft, B.O. Eriksen, Ambulatory blood pressure is associated with measured glomerular filtration rate in the general middle-aged population, Journal of hypertension 30(3) (2012) 497-504.
[154] M. Korf-Klingebiel, T. Kempf, T. Sauer, E. Brinkmann, P. Fischer, G.P. Meyer, A. Ganser, H. Drexler, K.C. Wollert, Bone marrow cells are a rich source of growth factors and cytokines: implications for cell therapy trials after myocardial infarction, European heart journal 29(23) (2008) 2851-2858.
[155] M. Zhou, A.M. Smith, A.K. Das, N.W. Hodson, R.F. Collins, R.V. Ulijn, J.E. Gough, Self-assembled peptide-based hydrogels as scaffolds for anchorage-dependent cells, Biomaterials 30(13) (2009) 2523-2530.
[156] D. Seliktar, R.A. Black, R.P. Vito, R.M. Nerem, Dynamic mechanical conditioning of collagen-gel blood vessel constructs induces remodeling in vitro, Annals of biomedical engineering 28(4) (2000) 351-362.
[157] Y.H. Shen, M.S. Shoichet, M. Radisic, Vascular endothelial growth factor immobilized in collagen scaffold promotes penetration and proliferation of endothelial cells, Acta biomaterialia 4(3) (2008) 477-489.
[158] J. Jang, T.G. Kim, B.S. Kim, S.-W. Kim, S.-M. Kwon, D.-W. Cho, Tailoring mechanical properties of decellularized extracellular matrix bioink by vitamin B2-induced photo-crosslinking, Acta biomaterialia 33 (2016) 88-95.
[159] S. Schlie, M. Gruene, H. Dittmar, B.N. Chichkov, Dynamics of cell attachment: adhesion time and force, Tissue Engineering Part C: Methods 18(9) (2012) 688-696.
[160] F.P. Melchels, B. Tonnarelli, A.L. Olivares, I. Martin, D. Lacroix, J. Feijen, D.J. Wendt, D.W. Grijpma, The influence of the scaffold design on the distribution of adhering cells after perfusion cell seeding, Biomaterials 32(11) (2011) 2878-2884.
[161] M.T. Raimondi, S. Bertoldi, S. Caddeo, S. Farè, C. Arrigoni, M. Moretti, The effect of polyurethane scaffold surface treatments on the adhesion of chondrocytes subjected to interstitial perfusion culture, Tissue engineering and regenerative medicine 13(4) (2016) 364-374.

[162] W.-B. Tsai, Y.-R. Chen, H.-L. Liu, RGD-conjugated crosslinked chitosan scaffolds for culture and osteogenic differentiation of mesenchymal stem cells, Journal of the Taiwan Institute of Chemical Engineers 44(1) (2013) 1-7.
[163] C.-T. Kao, C.-C. Lin, Y.-W. Chen, C.-H. Yeh, H.-Y. Fang, M.-Y. Shie, Poly (dopamine) coating of 3D printed poly (lactic acid) scaffolds for bone tissue engineering, Materials Science and Engineering: C 56 (2015) 165-173.
[164] M. Wang, P. Favi, X. Cheng, N.H. Golshan, K.S. Ziemer, M. Keidar, T.J. Webster, Cold atmospheric plasma (CAP) surface nanomodified 3D printed polylactic acid (PLA) scaffolds for bone regeneration, Acta biomaterialia 46 (2016) 256-265.
[165] F.C.S. de Oliveira, R.J.F.C. do Amaral, L.E.C. Dos Santos, C. Cummins, M.M. Morris, C.J. Kearney, A. Heise, Versatility of unsaturated polyesters from electrospun macrolactones: RGD immobilization to increase cell attachment, Journal of Biomedical Materials Research Part A (2021).
[166] X. Wang, K. Ye, Z. Li, C. Yan, J. Ding, Adhesion, proliferation, and differentiation of mesenchymal stem cells on RGD nanopatterns of varied nanospacings, Organogenesis 9(4) (2013) 280-286.
[167] A. Bangham, C. Morley, M. Phillips, The physical properties of an effective lung surfactant, Biochimica et Biophysica Acta (BBA)-Lipids and Lipid Metabolism 573(3) (1979) 552-556.
[168] E.F. Eriksen, Cellular mechanisms of bone remodeling, Reviews in Endocrine and Metabolic Disorders 11(4) (2010) 219-227.
[169] A. Deng, C.M. Miracle, M. Lortie, J. Satriano, F.B. Gabbai, K.A. Munger, S.C. Thomson, R.C. Blantz, Kidney oxygen consumption, carbonic anhydrase, and proton secretion, American Journal of Physiology-Renal Physiology 290(5) (2006) F1009-F1015.
[170] S. Munir, C.B. Foldager, M. Lind, V. Zachar, K. Søballe, T.G. Koch, Hypoxia enhances chondrogenic differentiation of human adipose tissue-derived stromal cells in scaffold-free and scaffold systems, Cell and tissue research 355(1) (2014) 89-102.
[171] A. Doryab, M.B. Taskin, P. Stahlhut, A. Schröppel, D.E. Wagner, J. Groll, O. Schmid, A biomimetic, copolymeric membrane for cell-stretch experiments with pulmonary epithelial cells at the air-liquid interface, Advanced functional materials 31(10) (2021) 2004707.
[172] I. Pennings, E.E. van Haaften, T. Jungst, J.A. Bulsink, A.J. Rosenberg, J. Groll, C.V. Bouten, N.A. Kurniawan, A.I. Smits, D. Gawlitta, Layer-specific cell differentiation in bi-layered vascular grafts under flow perfusion, Biofabrication 12(1) (2019) 015009.
[173] Y. Takeda, Y. Niki, Y. Fukuhara, Y. Fukuda, K. Udagawa, M. Shimoda, T. Kikuchi, S. Kobayashi, K. Harato, T. Miyamoto, Compressive mechanical stress enhances susceptibility to interleukin-1 by increasing interleukin-1 receptor expression in 3D-cultured ATDC5 cells, BMC musculoskeletal disorders 22(1) (2021) 1-13.
[174] S. Sieber, M. Michaelis, H. Gühring, S. Lindemann, A. Gigout, Importance of osmolarity and oxygen tension for cartilage tissue engineering, BioResearch open access 9(1) (2020) 106-115.
[175] J. Jurvelin, M. Buschmann, E. Hunziker, Mechanical anisotropy of the human knee articular cartilage in compression, Proceedings of the Institution of Mechanical Engineers, Part H: Journal of Engineering in Medicine 217(3) (2003) 215-219.
[176] L. Wilding, D. Howlett, H. Anderson, P. Sangle, N. Violaris, G. Evans, Extracranial internal carotid artery aneurysm presenting as symptomatic hypoglossal and glossopharyngeal nerve paralysis, The Journal of Laryngology & Otology 118(2) (2004) 150-152.
[177] L. Maddaluno, C. Urwyler, S. Werner, Fibroblast growth factors: key players in regeneration and tissue repair, Development 144(22) (2017) 4047-4060.
[178] G. Li, Q. Xiao, L. Zhang, Y. Zhao, Y. Yang, Nerve growth factor loaded heparin/chitosan scaffolds for accelerating peripheral nerve regeneration, Carbohydrate polymers 171 (2017) 39-49.
[179] S.H. Park, J.Y. Park, Y.B. Ji, H.J. Ju, B.H. Min, M.S. Kim, An injectable click-crosslinked hyaluronic acid hydrogel modified with a BMP-2 mimetic peptide as a bone tissue engineering scaffold, Acta biomaterialia 117 (2020) 108-120.
[180] M. Rezaii, S. Oryan, A. Javeri, Curcumin nanoparticles incorporated collagen-chitosan scaffold promotes cutaneous wound healing through regulation of TGF-β1/Smad7 gene expression, Materials Science and Engineering: C 98 (2019) 347-357.
[181] M.K. Lichtman, M. Otero-Vinas, V. Falanga, Transforming growth factor beta (TGF-β) isoforms in wound healing and fibrosis, Wound Repair and Regeneration 24(2) (2016) 215-222.

[182] Z. Pan, Y. Wu, X. Zhang, Q. Fu, J. Li, Y. Yang, D. Yu, Y. Xu, X. Lu, H. Sun, Delivery of epidermal growth factor receptor inhibitor via a customized collagen scaffold promotes meniscal defect regeneration in a rabbit model, Acta biomaterialia 62 (2017) 210-221.
[183] J.R. Flynn, L. Wang, D.L. Gillespie, G.J. Stoddard, J.K. Reid, J. Owens, G.B. Ellsworth, K.L. Salzman, A.Y. Kinney, R.L. Jensen, Hypoxia-regulated protein expression, patient characteristics, and preoperative imaging as predictors of survival in adults with glioblastoma multiforme, Cancer 113(5) (2008) 1032-1042.
[184] A.M. Steitz, A. Steffes, F. Finkernagel, A. Unger, L. Sommerfeld, J.M. Jansen, U. Wagner, J. Graumann, R. Müller, S. Reinartz, Tumor-associated macrophages promote ovarian cancer cell migration by secreting transforming growth factor beta induced (TGFBI) and tenascin C, Cell death & disease 11(4) (2020) 1-15.
[185] A.M. Mahecha, H. Wang, The influence of vascular endothelial growth factor-A and matrix metalloproteinase-2 and-9 in angiogenesis, metastasis, and prognosis of endometrial cancer, OncoTargets and therapy 10 (2017) 4617.
[186] Z. Wang, Z. Wang, W.W. Lu, W. Zhen, D. Yang, S. Peng, Novel biomaterial strategies for controlled growth factor delivery for biomedical applications, NPG Asia Materials 9(10) (2017) e435-e435.
[187] Y. Seo, Y. Jung, S.H. Kim, Decellularized heart ECM hydrogel using supercritical carbon dioxide for improved angiogenesis, Acta biomaterialia 67 (2018) 270-281.
[188] P.L. Lewis, J. Su, M. Yan, F. Meng, S.S. Glaser, G.D. Alpini, R.M. Green, B. Sosa-Pineda, R.N. Shah, Complex bile duct network formation within liver decellularized extracellular matrix hydrogels, Scientific reports 8(1) (2018) 1-14.
[189] B. Toprakhisar, A. Nadernezhad, E. Bakirci, N. Khani, G.A. Skvortsov, B. Koc, Development of bioink from decellularized tendon extracellular matrix for 3D bioprinting, Macromolecular bioscience 18(10) (2018) 1800024.
[190] M. Ali, A.K. Pr, J.J. Yoo, F. Zahran, A. Atala, S.J. Lee, A photo-crosslinkable kidney ECM-derived bioink accelerates renal tissue formation, Advanced healthcare materials 8(7) (2019) 1800992.
[191] A. Abaci, M. Guvendiren, Designing Decellularized Extracellular Matrix-Based Bioinks for 3D Bioprinting, Advanced healthcare materials 9(24) (2020) 2000734.
[192] A.J. Vernengo, S. Grad, D. Eglin, M. Alini, Z. Li, Bioprinting tissue analogues with decellularized extracellular matrix bioink for regeneration and tissue models of cartilage and intervertebral discs, Advanced Functional Materials 30(44) (2020) 1909044.
[193] M.M. De Santis, H.N. Alsafadi, S. Tas, D.A. Bölükbas, S. Prithiviraj, I.A. Da Silva, M. Mittendorfer, C. Ota, J. Stegmayr, F. Daoud, Extracellular-matrix-reinforced bioinks for 3D bioprinting human tissue, Advanced Materials 33(3) (2021) 2005476.
[194] A. Remuzzi, S. Conti, B. Ene-Iordache, S. Tomasoni, P. Rizzo, A. Benigni, G. Remuzzi, Role of ultrastructural determinants of glomerular permeability in ultrafiltration function loss, JCI insight 5(13) (2020).
[195] D. Park, E. Wershof, S. Boeing, A. Labernadie, R.P. Jenkins, S. George, X. Trepat, P.A. Bates, E. Sahai, Extracellular matrix anisotropy is determined by TFAP2C-dependent regulation of cell collisions, Nature materials 19(2) (2020) 227-238.
[196] X. Lin, S. Patil, Y.-G. Gao, A. Qian, The bone extracellular matrix in bone formation and regeneration, Frontiers in pharmacology 11 (2020) 757.
[197] L. Di Silvio, Cellular response to biomaterials, Elsevier2008.
[198] W. Wang, G. Jia, Q. Wang, H. Huang, X. Li, H. Zeng, W. Ding, F. Witte, C. Zhang, W. Jia, The in vitro and in vivo biological effects and osteogenic activity of novel biodegradable porous Mg alloy scaffolds, Materials & Design 189 (2020) 108514.
[199] L. Zhou, Y.-M. Zhai, M.-B. Yang, W. Yang, Flexible and tough cellulose nanocrystal/polycaprolactone hybrid aerogel based on the strategy of macromolecule cross-linking via click chemistry, ACS Sustainable Chemistry & Engineering 7(18) (2019) 15617-15627.
[200] B. Zhang, X. Pei, C. Zhou, Y. Fan, Q. Jiang, A. Ronca, U. D'Amora, Y. Chen, H. Li, Y. Sun, The biomimetic design and 3D printing of customized mechanical properties porous Ti6Al4V scaffold for load-bearing bone reconstruction, Materials & Design 152 (2018) 30-39.
[201] K. Cui, Y.N. Ye, C. Yu, X. Li, T. Kurokawa, J.P. Gong, Stress relaxation and underlying structure evolution in tough and self-healing hydrogels, ACS Macro Letters 9(11) (2020) 1582-1589.

[202] S. Nam, R. Stowers, J. Lou, Y. Xia, O. Chaudhuri, Varying PEG density to control stress relaxation in alginate-PEG hydrogels for 3D cell culture studies, Biomaterials 200 (2019) 15-24.
[203] A. D'Amore, S.K. Luketich, G.M. Raffa, S. Olia, G. Menallo, A. Mazzola, F. D'Accardi, T. Grunberg, X. Gu, M. Pilato, Heart valve scaffold fabrication: Bioinspired control of macro-scale morphology, mechanics and micro-structure, Biomaterials 150 (2018) 25-37.
[204] M. Zhang, R. Lin, X. Wang, J. Xue, C. Deng, C. Feng, H. Zhuang, J. Ma, C. Qin, L. Wan, 3D printing of Haversian bone–mimicking scaffolds for multicellular delivery in bone regeneration, Science advances 6(12) (2020) eaaz6725.
[205] Y.S. Kim, M. Majid, A.J. Melchiorri, A.G. Mikos, Applications of decellularized extracellular matrix in bone and cartilage tissue engineering, Bioengineering & translational medicine 4(1) (2019) 83-95.
[206] J. Zhang, P. Byers, A. Erben, C. Frank, L. Schulte-Spechtel, M. Heymann, D. Docheva, H.P. Huber, S. Sudhop, H. Clausen-Schaumann, Single Cell Bioprinting with Ultrashort Laser Pulses, Advanced Functional Materials 31(19) (2021) 2100066.
[207] K. Theodoridis, E. Aggelidou, M. Manthou, E. Demiri, A. Bakopoulou, A. Kritis, Assessment of cartilage regeneration on 3D collagen-polycaprolactone scaffolds: Evaluation of growth media in static and in perfusion bioreactor dynamic culture, Colloids and Surfaces B: Biointerfaces 183 (2019) 110403.
[208] R. Daum, D. Visser, C. Wild, L. Kutuzova, M. Schneider, G. Lorenz, M. Weiss, S. Hinderer, U.A. Stock, M. Seifert, Fibronectin adsorption on electrospun synthetic vascular grafts attracts endothelial progenitor cells and promotes endothelialization in dynamic in vitro culture, Cells 9(3) (2020) 778.
[209] N. Jourde-Chiche, F. Fakhouri, L. Dou, J. Bellien, S. Burtey, M. Frimat, P.-A. Jarrot, G. Kaplanski, M. Le Quintrec, V. Pernin, Endothelium structure and function in kidney health and disease, Nature Reviews Nephrology 15(2) (2019) 87-108.
[210] V. Schwach, R. Passier, Native cardiac environment and its impact on engineering cardiac tissue, Biomaterials science 7(9) (2019) 3566-3580.
[211] T.H. Qazi, D.J. Mooney, G.N. Duda, S. Geissler, Niche-mimicking interactions in peptide-functionalized 3D hydrogels amplify mesenchymal stromal cell paracrine effects, Biomaterials 230 (2020) 119639.
[212] C. Aronsson, M. Jury, S. Naeimipour, F.R. Boroojeni, J. Christoffersson, P. Lifwergren, C.-F. Mandenius, R. Selegård, D. Aili, Dynamic peptide-folding mediated biofunctionalization and modulation of hydrogels for 4D bioprinting, Biofabrication 12(3) (2020) 035031.
[213] S.H. Kim, J.H. Park, J.S. Kwon, J.G. Cho, K.G. Park, C.H. Park, J.J. Yoo, A. Atala, H.S. Choi, M.S. Kim, NIR fluorescence for monitoring in vivo scaffold degradation along with stem cell tracking in bone tissue engineering, Biomaterials 258 (2020) 120267.
[214] Z. Wu, Q. Li, S. Xie, X. Shan, Z. Cai, In vitro and in vivo biocompatibility evaluation of a 3D bioprinted gelatin-sodium alginate/rat Schwann-cell scaffold, Materials Science and Engineering: C 109 (2020) 110530.
[215] M.E. Couch, Laryngopharyngectomy with reconstruction, Otolaryngologic Clinics of North America 35(5) (2002) 1097-1114.
[216] A.L. Brown Jr, Microvilli of the human jejunal epithelial cell, The Journal of cell biology 12(3) (1962) 623-627.
[217] J.J. Disa, A.L. Pusic, B.J. Mehrara, Reconstruction of the hypopharynx with the free jejunum transfer, Journal of surgical oncology 94(6) (2006) 466-470.
[218] R. Hyland, A. Chalmers, CT features of jejunal pathology, Clinical radiology 62(12) (2007) 1154-1162.
[219] A.B.H. Bhatti, F.S. Dar, A.I. Qureshi, S. Haider, N.A. Khan, Saphenous vein conduits for hepatic arterial reconstruction in living donor liver transplantation, Langenbeck's archives of surgery 404(3) (2019) 293-300.
[220] G. Konig, T.N. McAllister, N. Dusserre, S.A. Garrido, C. Iyican, A. Marini, A. Fiorillo, H. Avila, W. Wystrychowski, K. Zagalski, Mechanical properties of completely autologous human tissue engineered blood vessels compared to human saphenous vein and mammary artery, Biomaterials 30(8) (2009) 1542-1550.
[221] S.F. Hashmi, B. Krishnamoorthy, W.R. Critchley, P. Walker, P.W. Bishop, R.V. Venkateswaran, J.E. Fildes, N. Yonan, Histological and immunohistochemical evaluation of human saphenous vein harvested by endoscopic and open conventional methods, Interactive cardiovascular and thoracic surgery 20(2) (2015) 178-185.

[222] W. Stooker, M. Gök, P. Sipkema, H.W. Niessen, A. Baidoshvili, N. Westerhof, E.K. Jansen, C.R. Wildevuur, L. Eijsman, Pressure-diameter relationship in the human greater saphenous vein, The Annals of thoracic surgery 76(5) (2003) 1533-1538.
[223] C. Cao, C. Manganas, M. Horton, P. Bannon, S. Munkholm-Larsen, S.C. Ang, T.D. Yan, Angiographic outcomes of radial artery versus saphenous vein in coronary artery bypass graft surgery: a meta-analysis of randomized controlled trials, The Journal of thoracic and cardiovascular surgery 146(2) (2013) 255-261.
[224] J.-Y. Rho, L. Kuhn-Spearing, P. Zioupos, Mechanical properties and the hierarchical structure of bone, Medical engineering & physics 20(2) (1998) 92-102.
[225] E. Wisse, F. Braet, D. Luo, R. De Zanger, D. Jans, E. Crabbe, A. Vermoesen, Structure and function of sinusoidal lining cells in the liver, Toxicologic pathology 24(1) (1996) 100-111.
[226] C. Rouiller, General anatomy and histology of the kidney, The kidney, Elsevier1969, pp. 61-156.
[227] J.M. Harkness, In Appreciation¶ A Lifetime of Connections: Otto Herbert Schmitt, 1913-1998, Physics in Perspective 4(4) (2002) 456-490.
[228] J. Costa, M. Ghilardi, V. Mamone, V. Ferrari, J.J. Busfield, A. Ahluwalia, F. Carpi, Bioreactor with electrically deformable curved membranes for mechanical stimulation of cell cultures, Frontiers in bioengineering and biotechnology 8 (2020) 22.

Chapter 3

Scaffolds with atypical space-filling curves for tissue engineering

Scaffolds with atypical space-filling curves for tissue engineering

Kenny A. van Kampen[1], Carlos Mota[1], Lorenzo Moroni[1]

[1]Department of Complex Tissue Regeneration, MERLN Institute for Technology-Inspired Regenerative Medicine, Maastricht University, Universiteitssingel 40, 6229ER Maastricht, The Netherlands

Abstract

The goal of tissue engineering and regenerative medicine (TERM) is to repair damaged organs or tissue, thus restoring functionality and biological activity. As the recreation of this complex environment is highly tissue dependent, strategies aiming at creating a biological construct that could mimic this environment, including the extracellular matrix architecture, are highly desired. While biofabrication technologies have been able to mimic tissue organization, the majority of biofabrication approaches present a woodpile or honeycomb structure design regardless of the final tissue application. This woodpile filling pattern is a result of a slicing software that generates lines of machine language called G-code. Ultimately the G-code dictates how the scaffold is built up. Expanding upon such simple architectures would enable a higher degree of biomimicry that can be tailored to the specific needs of a targeted tissue. This study focused on creating a methodology to create complex printing patterns based on fractal designs, Penrose tilings and Cartesian coordinate equations. In addition, the effects of different loading regimes within each design were tested and explored to replicate potential suturing positions within the scaffolds. Seven different patterns in multiple configurations and loading regimes were tested. The mechanical properties of the fabricated scaffolds ranged from flexible patterns with a Young's modulus

of 1 MPa suitable for skin tissue engineering to stiff patterns with a Young's modulus of 100 MPa suitable for bone tissue engineering. In addition, the results showed that different loading regimes can have a major influence on the stress-strain curve of the architected scaffolds as well as on the morphology of the scaffolds during mechanical stimulation. These results highlight that with simple G-code editing, it is possible to create a whole variety of new patterns for multiple applications such as skin, heart, tendon and bone.

1. Introduction

The ultimate goal of tissue engineering and regenerative medicine (TERM) is to restore the function of a damaged or diseased organ [1]. In order to achieve this goal, a combination of cells, biocompatible materials or biochemical cues is typically applied to create a tissue substitute. Many researchers have attempted to recreate the microenvironment of a tissue or organ by tweaking materials to mimic the mechanical properties of the targeted native tissues [2, 3] or by designing three-dimensional (3D) scaffolds that could offer suitable supports to cells with appropriate mechanical properties by varying, for instance, their architecture [4]. Examples comprise tendon, skin, muscle or interfacial tissues, among others [5-7]. However, biomimetic constructs remain a challenge due to the biological, physicochemical, and mechanical complexity and various structural differences between tissues and organs of our body [8, 9]. Specifically, the mechanical properties can vary significantly from soft and flexible tissues, such as skin, to stiff tissues, such as bone [10, 11]. Therefore the scaffold design should be tailored to the specific application. It is known that having a mismatch in mechanical properties often leads to graft failure [12, 13]. In addition, cells sense and are influenced by mechanical cues, which might actively steer tissue regeneration by providing dynamic mechanical loading [14]. The mechanical cues of the scaffolds are also influenced by the design [15]. In addition, these scaffolds have to be transplanted *in vivo*, the majority of which by sutures [16], which in turn can

also have an influence on the loading regime on the scaffolds [17]. Therefore, creating a scaffold that has the right mechanical properties and gives the correct mechanical cues to stimulate cell activity is essential in TERM.

Many biofabrication technologies able to create complex scaffolds are available. One such is fused deposition modeling (FDM), a technique within the additive manufacturing (AM) pool of technologies that has existed for decades and is widely used in TERM [18-20]. The basic principle of FDM is that a material is extruded through a nozzle and deposited in the form of fibres on a collecting plate [21]. The first step in the manufacturing of a three-dimensional (3D) object is to generate a 3D model using computer-aided design (CAD) software [22]. This model is then processed in a slicing software that converts the 3D object into layers with outer boundaries [23]. These outer boundaries will limit the filling pattern generated for each layer, in which the default and sometimes only option is the continuous meandering of parallel lines. When stacked with a rotation of 90 degrees, these lines result in a woodpile structure. All filling patterns calculated for each layer are then converted into G-code, which is the machine language for most FDM systems [24]. The majority of the G-code is a list of numerical coordinates that the tool head will follow line by line and is similar for every system [25]. This limited pattern generation restricts the freedom required to replicate the different morphologies present in each tissue [26-28]. It is known that cells react to different scaffold architectures and respective mechanical behaviour, which stresses the need for the creation of complex patterns capable of mimicking the aimed tissue architecture and of influencing cell activity while new tissue is formed [29, 30]. Hence, the fabrication of scaffolds with more complex designs able to better mimic the biomechanical microenvironment of our tissues remains limited. Recent advances made it possible to both print fibres of less than 100 μm [31] and use different collecting surfaces [32, 33]. The technique allows the freedom to print almost any kind of pattern that is available. Yet, the majority of studies for the fabrication of scaffolds in TERM

utilizes a woodpile or honeycomb design based on parallel meandering lines stacked in a different angle per layer regardless of the final application [3, 34].

As a promising alternative, scaffold architecture can be modulated by editing the G-code of the chosen AM system, where more complex shapes with different morphology and mechanical properties could be fabricated [35]. The possibility to create more complex patterns requires the development of custom computational scripts to generate ad-hoc deposition or filling patterns. The resulting patterns can be generated through multiple methods such as creating space-filling fractals using the Lindenmayer system (e.g. Hilbert's curve, Moore's curve, Peano's curves, Sierpiński's curve and Gosper curves), alternative tilling methods such as the Penrose tilling or Cartesian coordinate equations. Each of these could potentially replicate natural patterns observed in several tissues in the body, such as the fractal organization of bone [36], the concentric circle patterns of intervertebral discs [37], the spiral organization of the muscle bands in the myocardium [38, 39] or the sine-wave collagen fibril bundles of the tendon [40].

The Lindenmayer system or L-system is often used to generate fractal-based scaffolds [41]. The L-system generates a string of letters that can be converted into a set of commands for a moving object to follow. By communicating the current position of that moving object, the Cartesian coordinates can be extracted to generate a printing pathway. Another method is to convert the Ammann bars formed when lines are drawn on tiles, all connecting in sets of parallel lines in order to create the correct tiling. Amman bars of any tiling set, such as Penrose tiling, can be converted into G-code [42]. A final method is by knowing the Cartesian coordinate equations to generate both X and Y coordinates [43]. Successful examples to generate these structures are spirals, circles and sine waves [44].

The aim of the study was to develop a simple methodology that could be largely adopted to generate more complex printing patterns using the aforementioned methods. The final printed patterns were characterised by morphology and mechanical properties. A finite element model was used to simulate the stress distribution through the designed scaffolds. Finally, the effect of different loading regimes was tested to replicate potential suturing positions within the scaffolds. We found that all designs were printable, with the 0-90 woodpile design having the highest Young's modulus and the Gosper curve the lowest with a factor 100. Together, our observations argue that a whole new series of patterns can be created using the methods described in this study.

2. Materials and methods

2.1 Scaffold Fabrication

Poly(ε-caprolactone) (PCL) (Mn 45.000, Sigma-Aldrich, USA) was used to fabricate scaffolds via FDM using a Bioscaffolder (SysENG, Germany). Briefly, pellets of PCL were placed in a stainless-steel syringe and heated to 110 °C. Nitrogen with 4 bar of pressure was used to force the molten polymer to the extrusion screw, which was set at a constant rotation speed of 45 rpm. A 25G nozzle (260 µm internal diameter) was used for extrusion. The layer thickness and speed was kept constant at 180 µm and 400 mm/min, respectively. Gripping extensions were printed on all the scaffolds for mechanical analyses.

2.2 Fractal-based scaffold design

A script was written in Rhino 7 Grasshopper (Rhino 7, Version 7.22) that produces fractal patterns using an L-system. The variables, axiom, production rules, fractal generation, rotation of each layer and the number of layers could be varied in the script. The parameters for each design depended on the fractal (Figure 1). The scripts gave as output a set of polylines that were

converted using a second script into G-code that was compatible with the printer. In total, five different fractal designs were used to print six different scaffolds, as the Hilbert curve can be stacked in two different configurations. As a reference, a 0-90 woodpile structure was printed, where each meandering layer is rotated at a 90° angle. The fiber distance was set at 800 µm for both the fractals and 0-90 woodpile structure.

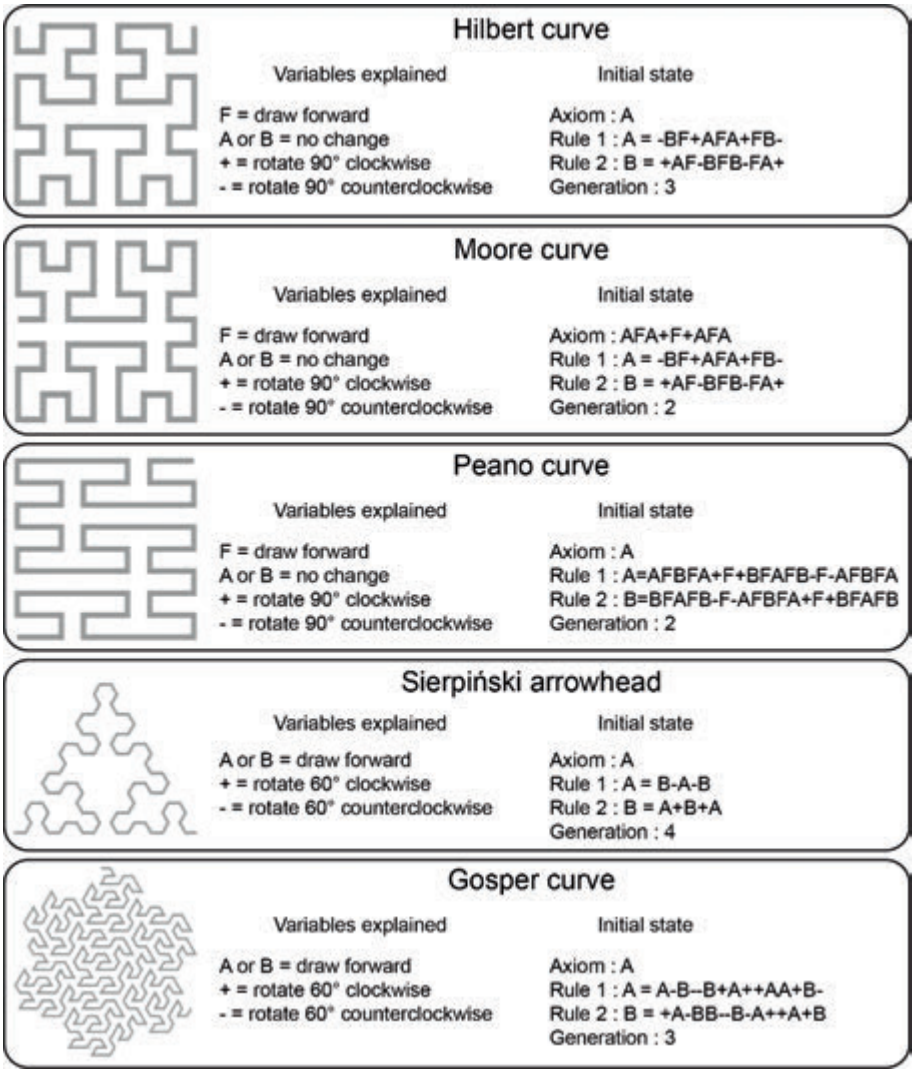

Figure 1. *Overview of the design parameters of the 5 fractal-based scaffolds.*

2.3 Penrose tiling pattern design

The Penrose kite and dart tilling pattern with predefined Ammann bars were created (Figure 2A) using a Grasshopper written script. The Ammann bars on each individual kite and dart tile have to be connected in order to form an infinite Penrose tiling pattern. The Ammann bars that are generated form parallel lines with five different slopes. A set of Ammann bars from the same layer with the same slope was highlighted and connected with each other creating a meander with a different pattern of fiber spacing between each other. There are numerous variations of spacing patterns but for this study only three were selected and studied. The spacing ratio between the long (L) and short (S) spacing was equal to the golden ratio ($\varphi \approx 1.62$). A pentagonal outline was projected around the fibers as boundary condition. Five layers of each design were printed, stacked on top of each other, rotated 72° between each subsequent layer. Three different versions were created, denoted by L or S spacing between fibers, and tested (Figure 2B–D).

2.4 Cartesian coordinate scaffold design

Cartesian coordinate equations were used to generate a spiral (Eq. 1 and 2) using a Python 3.7 script, with r being a multiplier for the radius of the spiral and φ the angle that the spiral makes. Each spiral was then rotated 45° until eight spiral arms were generated (Figure 3). Finally, a fiber was generated to connect the spiral arms for mechanical stability. These connections were made after every defined iterations of both X and Y coordinates of the spiral. A small number of iterations results into an abundance of supporting fibers and thus a loss of porosity while a large number of iterations translates in fewer supporting fibers and thus a loss of support for the next layers. In this example, 30 connections were chosen to maintain porosity while still providing a support for the next layers.

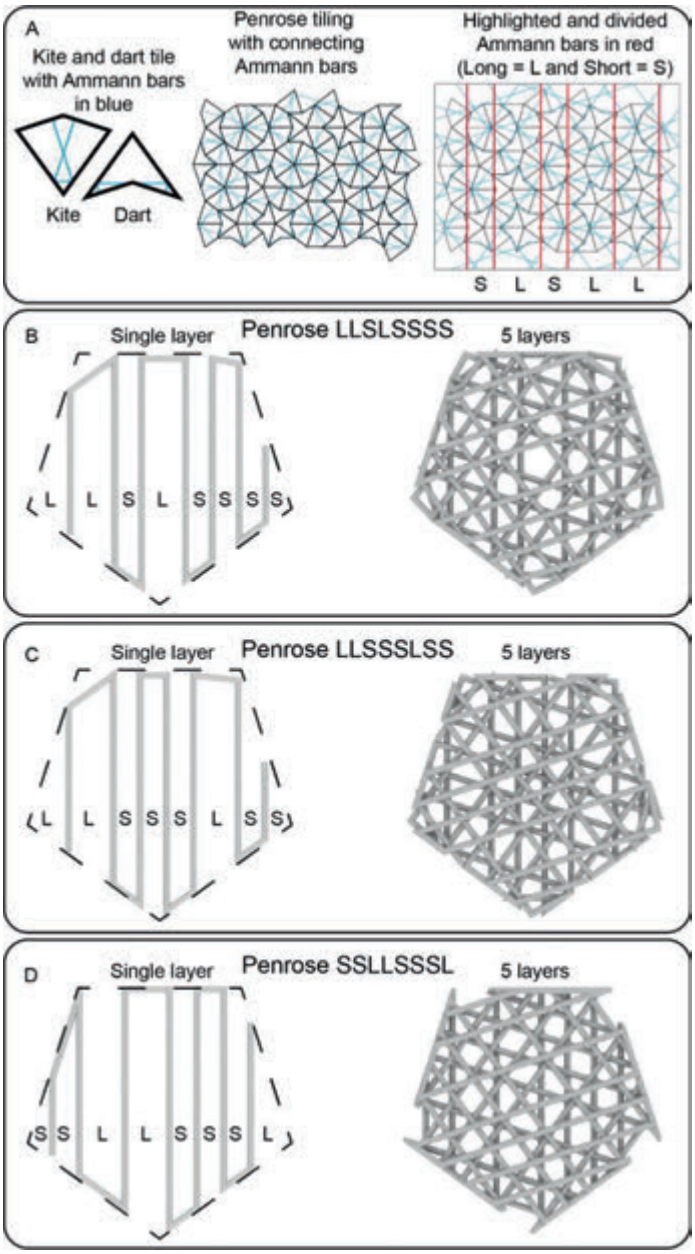

Figure 2. *Schematic overview of the generation of the Penrose tilling pattern with long (L) and short (S) spacing between the fibers of each layer (A). (B–D) Three different designs of Penrose tiling, LLSLSSSS (B), LLSSSLSS (C), SSLLSSSL (D), with the single layer design showing the distances between fibers on the left and a rendered version of the full scaffolds on the right.*

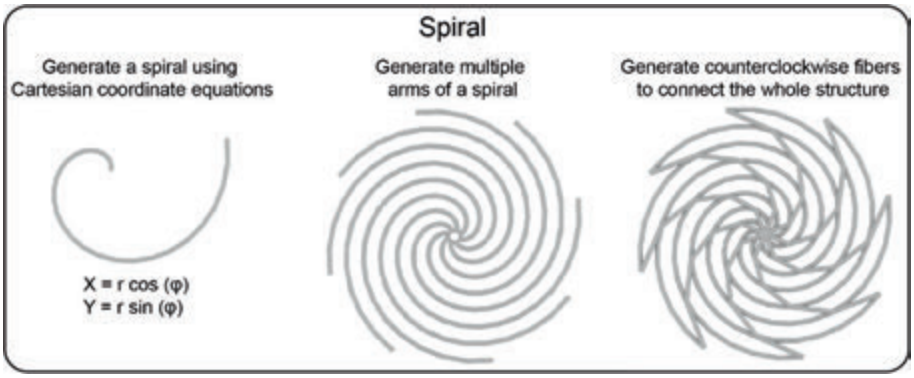

Figure 3. *Generation of the spiral pattern using Cartesian coordinate equations. On the left panel a single spiral arm, the middle panel 8 arms of the spiral and the right panel the full scaffold with connecting fibers.*

Equation 1. $X = r\ cos(\varphi)$
Equation 2. $Y = r\ sin(\varphi)$

2.5 Scaffold characterization

Stereomicroscopy (SMZ25, Nikon instruments) with a dark field illuminator (Nikon instruments) was used to analyse the manufactured scaffolds. In addition, the fibre diameter was measured and the morphology of the scaffolds was assessed (Table 1). The data from the fibre measurements were used to generate an equivalent 3D model of the scaffold to calculate the bulk volume. The volume of the scaffolds was calculated by measuring the weight and using the density of PCL. The porosity of the scaffolds was calculated by subtracting the volume of the scaffolds from the bulk volume.

2.6 Mechanical characterization

Mechanical characterization was performed on a mechanical tester (ElectroForce, TA instruments) with a 45 N load cell (ElectroForce). Custom-made clamps were used to match the shape of the scaffolds during tensile test. These custom clamps were fabricated using a milling machine (Roland SRM-20) using polycarbonate. Parafilm® M (Heathrow Scientific) was used

at the clamps to prevent slippage during the test. Due to the various lengths of the designs, each tensile test was performed up to a total of 100% strain or until failure with a rate of 1% strain per second. The tensile tests were recorded with a camera (DMC-G3, Panasonic, The Netherlands) with a macro-lens (Panagor 90mm f2.8, Komine, Japan). Images and videos were analysed using ImageJ (Version 1.52p, NIH) and Adobe Premiere Pro (Version 12.0, Premiere Pro CC 2018). The obtained force displacement values from the mechanical tester were converted to stress and strain. The Young's modulus was defined as the linear part of the stress-strain curve. The yield strain and strength were calculated where the stress-strain curve were no longer elastic. The resilience was defined as the area under the curve until the yield point and the ultimate strength was set at the maximum force failure. The ultimate strain was calculated at the failure point and the toughness was defined as the area under the curve until this failure point. If the scaffolds did not fully break before 100% strain, then these values were not calculated.

2.7 Finite element modelling

3D CAD models were generated with Rhino 7 based on the G-code. The CAD models were imported in a finite element model software (COMSOL Multiphysics, Version 6.0). The model was fixed at one extremity of the scaffold and at the opposite extremity was strained up to 100%, and simulations were performed in steps of 5% strain. The von Mises stress were plotted along with the displacement.

2.8 Statistics

Statistical analyses was performed with GraphPad Prism 8.1.2. Significant differences were tested using an ANOVA test with a Tukey post-hoc test. The tests were considered significant when $p<0.05$.

3. Results

3.1 Scaffold design and printing

Seven different designs were printed (Figure 1–3). Briefly, the scaffolds were fabricated through FDM using a nozzle of 260 µm in diameter with PCL as printing material. The morphology of each scaffold design was assessed (Table 1), which showed that they all had similar porosity.

3.2 Tensile testing

Additional gripping extensions were printed at the edges of the scaffolds for tensile tests. The position of the clamps were varied within the scaffold to simulate different loading regimes and assess whether the location made a difference in mechanical behaviour. The mechanical assessment was performed in the X or Y plane of the scaffold.

3.1 0-90 Woodpile structure

The woodpile design has been the main design by many studies that use any FDM system [45-47], likely because it is either the default or the only design in many of the slicing software available. In addition, from a fabrication point of view, it is also one of the simpler design to create as the straight fibres are the longest with the fewest turns possible per layer. This feature is important as some materials require more time for a constant flow rate directly after deposition [48, 49]. The main parameter that can be adjusted within this design is that the angle of each layer is changed [50]. Each layer of the woodpile structure is generated by creating a set of parallel lines with equal distance between them. The layers are stacked and rotated from each other by a given angle and repeated until the full scaffold is fabricated. This study focussed on the woodpile design that was created by rotating each subsequent layer by 90° (0–90 woodpile). As expected, stereomicroscopy images revealed that the square shaped pores were all equal in size

throughout the scaffold (0.29 ± 0.01 mm^2) (Figure 4A). The fibre diameter was consistent through the scaffold at 266.4 ± 7.0 µm and the porosity was 73.3 ± 0.1%. Three different sets of gripping extensions were fabricated; (1) over the entire length of the scaffold (full), (2) at the centre of the scaffold (inner) and (3) at the edge of the scaffold (outer). The mechanical data revealed that the Young's modulus, yield strain, yield strength and resilience were significantly higher with the full clamps (Figure 4B, Table 1). The scaffolds with the inner and outer gripping broke at the clamping sites, while the other scaffold areas remained intact. This observation was also confirmed by the finite element

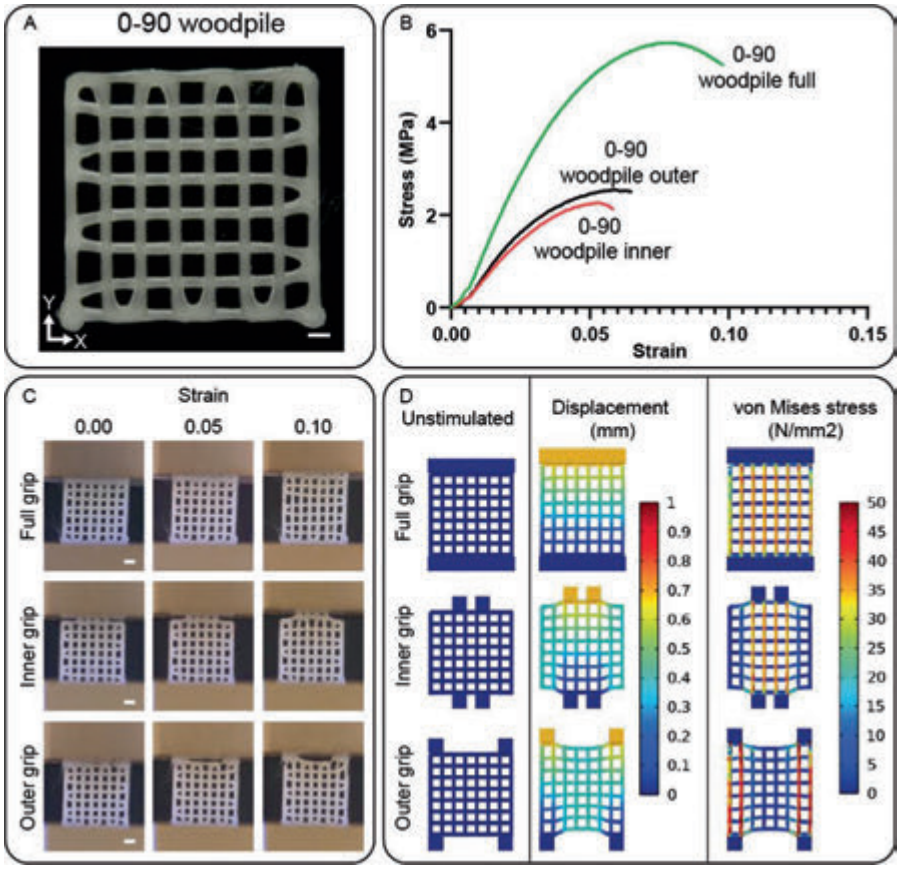

Figure 4. *0-90 woodpile design. Stereomicroscopy image of the 0-90 woodpile design (A). Representative stress-strain curve (B). Time-lapsed snapshots of the tensile test (C). Finite element model with the left panels the unstimulated scaffold, the middle panel and right panel the displacement and von Mises stress respectively and 10% strain (D). Scale bar represents 500 µm.*

model where the edges and the centre of the scaffolds showed no stress in the inner and outer clamped scaffolds, respectively (Figure 4D). This trend is most likely due to the stress being focused at the gripping positions and limited fusion area between the gripper and the scaffold. The shape of the pores deformed from square to rectangular with increasing strain, which was especially noticeable in the scaffolds with the full clamp.

Table 1. *Mechanical properties of the 0-90 woodpile structure with various clamping positions. Values represent average ± standard deviation. * Statistical significance $p<0.05$ compared to the other two conditions. $^{+}$ No standard deviation available as this is based on a single sample.*

Scaffold	Gripping position	Young's modulus (MPa)	Yield strain (mm/mm)	Yield strength (MPa)	Resilience ($N \cdot mm^{-2}$)	Ultimate Strain (mm/mm)	Toughness ($N \cdot mm^{-2}$)
0-90 woodpile	Full	131.5 ± 11.3*	0.030 ± 0.011	3.3 ± 0.6*	0.047 ± 0.018*	No failure	No failure
	Inner	75.9 ± 2.9	0.019 ± 0.005	1.6 ± 0.1	0.019 ± 0.002	0.49 ± 0.22	1.34 ± 0.76
	Outer	80.1 ± 5.0	0.014 ± 0.001	1.6 ± 0.1	0.019 ± 0.001	0.58^{+}	1.58^{+}

The 0-90 woodpile design was also one of the stiffer designs tested as the fibres were fully stretched and directed parallel to the applied strain. Other studies also revealed that the 0-90 woodpile structure display a stiff pattern [50, 51]. These studies, however, often performed compression tests in the Z direction.

3.2 Fractal-based scaffolds

The printing pathway for space-filling, fractal-based scaffolds was generated through an L-system, which uses a simple set of rules to generate a fractal design, and depending on the rules, the base fractal changes. In this study, Grasshopper was used to generate the printing fillings. Other software such as Python could also be used to generate strings of text using an L-system [52].

3.2.1 Hilbert 90

The Hilbert curve is the most commonly used space-filling fractal [53]. In this study, a 3rd generation Hilbert curve was used and each layer was stacked at a 90° angle. Analysing the morphology of the scaffolds revealed that the pore sizes were not equal throughout the scaffolds (Figure 5A). Four large rectangular pores were located at the edges of the scaffolds and faced towards the centre (0.20 ±0.02 mm2) while a three by three grid of small pores were located at the corners (0.05 ±0.04 mm2). Fibre diameter throughout the scaffolds was 293.8 ± 39.4 µm and the porosity was 73.8 ± 0.6%. The stress strain curves revealed that the samples with a full grip and an outer grip were similar, while the inner grip extension was different with an additional inflection point at around 0.02 strain (Figure 5B). For this case, the fibres present in the middle of the scaffolds failed primarily followed by the ones farther from the centre of the scaffolds as shown in the time-lapsed snapshots (Figure 5C). This observation was further confirmed by the modelling as the middle fibres take up most of the von Mises stresses (Figure 5D). Samples with an inner grip extension also showed significantly lower Young's modulus and yield strength as well as lower (but not significant) resilience (Table 2). The yield strain between the different conditions was similar.

Table 2. *Mechanical properties of the Hilbert 90 design with various gripping positions. Values represent average ± standard deviation. * Statistical significance p<0.05.*

Scaffold	Gripping position	Young's modulus (MPa)	Yield strain (mm/mm)	Yield strength (MPa)	Resilience ($N \cdot mm^{-2}$)	Ultimate Strain (mm/mm)	Toughness ($N \cdot mm^{-2}$)
Hilbert 90	Full	113.3 ± 3.9*	0.017 ± 0.001	2.3 ± 0.1	0.027 ± 0.001	No failure	No failure
	Inner	69.8 ± 1.3	0.015 ± 0.004	1.4 ± 0.1*	0.017 ± 0.001	No failure	No failure
	Outer	89.4 ± 14.1	0.021 ± 0.008	2.2 ± 0.3	0.031 ± 0.011	No failure	No failure

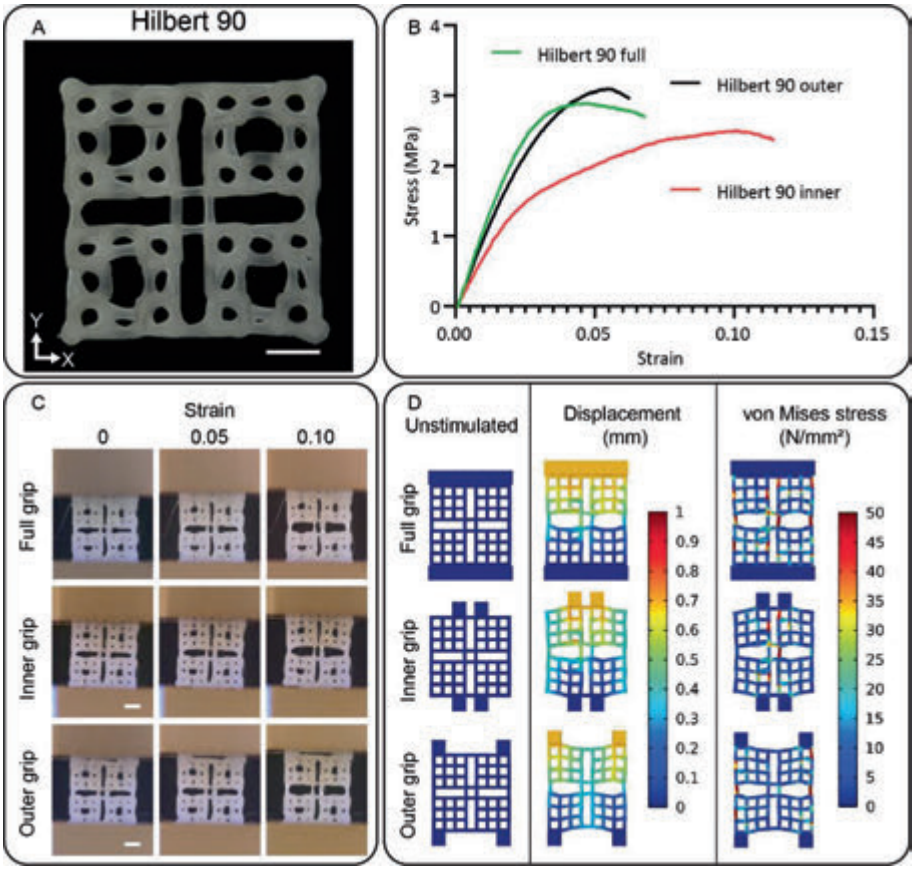

Figure 5. *Hilbert 90. Stereomicroscopy image of the Hilbert 90 design (A). Representative stress-strain curve (B). Time-lapsed snapshots of the tensile test (C). Finite element model with the left panels the unstimulated scaffold, the middle panel and right panel the displacement and von Mises stress respectively and 10% strain (D). Scale bar represents 500 µm.*

3.2.2 Hilbert 180

The Hilbert curve with a layer rotation of 180 degrees can be mounted in the X direction (Hilbert 180X) and Y direction (Hilbert 180Y). The X and Y direction both had the same architecture with a long stretching pore (2.05 ± 0.12 mm^2) right through the middle of the scaffolds dividing the scaffolds in half and another set of large pores (1.03 ± 0.08 mm^2) that separate those halves in quarters (0.11 ± 0.02 mm^2), effectively creating three different pore types (Figure 6A and E). The porosity for both configurations was 75.1 ± 0.7% with

an average fibre diameter of 287.4 ± 64.7 µm. Even though the morphology was the same between the Hilbert 180X and 180Y, the outer grips for the 180X and the inner grip for the 180Y samples created a rotation in each of the quadrants (Figure 6D and G). This rotation was most likely caused by the fact that the gripping position was not in the same line as the fibres that connected the halves of the scaffolds. This effect was not present when the gripping position was in line with the connecting fibres. This resulted in the 180X gripped clamped and the 180Y outer gripped samples to have similar mechanical properties as the full gripped versions. The full gripping position for both configurations had almost identical mechanical properties. An explanation could be that the total amount of fibres that contribute to the load was identical, highlighting that this is a key parameter for the mechanical properties within a scaffold. The stress strain curves of the Hilbert 180X design revealed that the outer clamped samples were substantially different from the inner and full clamps. For the Hilbert 180Y scaffolds, those with an inner gripping position had an additional inflection point in the stress-strain curves, right at the point where the large pore in the middle started to open up (Figure 6G). For both Hilbert 180X outer and 180Y inner samples, the Young's modulus and yield strength were significantly lower compared to their respective other clamped samples (Table 3). Resilience for 180X outer grips was also significantly lower. The simulations also revealed that the quadrants started to rotate in the 180X outer clamped samples, mitigating the von Mises stresses (Figure 6D). The finite element model also indicated that the 180Y scaffolds with inner gripping had an improved stress distribution with the lowest von Mises stress (Figure 6H).

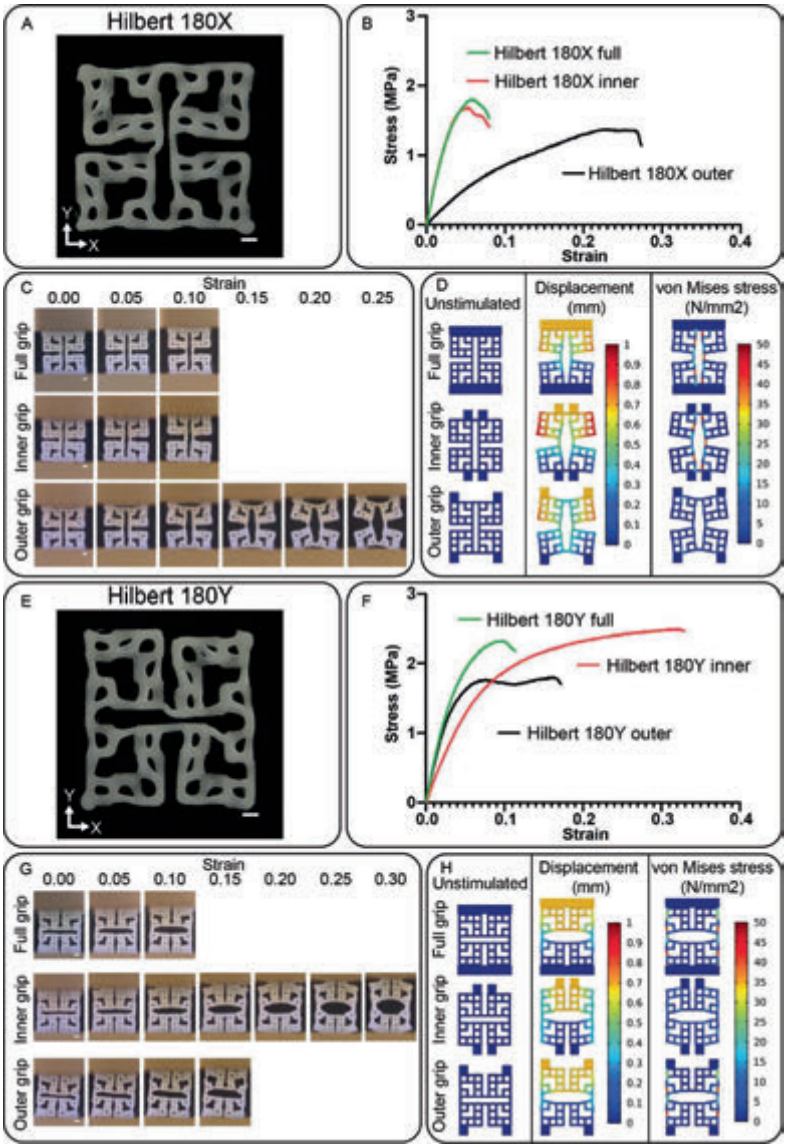

Figure 6. *Hilbert 180 design. Stereomicroscopy image of the Hilbert 180X design (A). Representative stress-strain curve (B). Time-lapsed snapshots of the tensile test (C). Finite element model with the left panels the unstimulated scaffold, the middle panel and right panel the displacement and von Mises stress respectively and 10% strain (D). Stereomicroscopy image of the Hilbert 180Y design (E). Representative stress-strain curve (F). Time-lapsed snapshots of the tensile test (G). Finite element model with the left panels the unstimulated scaffold, the middle panel and right panel the displacement and von Mises stress respectively and 10% strain (H). Scale bar represents 500 µm.*

Table 3. *Mechanical properties of the Hilbert 180X and 180Y design with various gripping positions. Values represent average ± standard deviation. * Statistical significance p<0.05.*

Scaffold	Gripping position	Young's modulus (MPa)	Yield strain (mm/mm)	Yield strength (MPa)	Resilience ($N \cdot mm^{-2}$)	Ultimate Strain (mm/mm)	Toughness ($N \cdot mm^{-2}$)
Hilbert 180X	Full	54.0 ± 1.3	0.016 ± 0.002	1.1 ± 0.0	0.014 ± 0.001	No failure	No failure
	Inner	54.3 ± 1.5	0.013 ± 0.001	1.1 ± 0.0	0.014 ± 0.001	No failure	No failure
	Outer	10.1 ± 1.4*	0.018 ± 0.003	0.2 ± 0.1*	0.003 ± 0.001*	No failure	No failure
Hilbert 180Y	Full	54.6 ± 1.3	0.016 ± 0.002	1.2 ± 0.0	0.014 ± 0.001	No failure	No failure
	Inner	30.1 ± 0.8*	0.019 ± 0.004	0.8 ± 0.1*	0.010 ± 0.002	No failure	No failure
	Outer	40.2 ± 12.1	0.016 ± 0.001	1.1 ± 0.1	0.010 ± 0.003	No failure	No failure

3.2.3 Moore curve

The Moore curve is a different variant of the Hilbert curve with the start and end point at different positions [54]. Unlike the Hilbert curve, the Moore curve can only be stacked at an angle of 90° while still maintaining side porosity as the 180° stacking resulted in scaffolds with identical layers. Here, we investigated a 2nd generation Moore curve. The morphology of the Moore curve scaffolds revealed that there were large pores in the shape of a cross through the middle of the scaffolds (1.95 ± 0.10 mm^2) (Figure 7A). The edges and the middle of the scaffolds had small pores (0.23 ± 0.04 mm^2) that were separated by a ring of larger pores (2.09 ± 0.08 mm^2). The average fibre diameter was 246.5 ± 34.7 µm and the porosity was 75.0 ± 0.1%. The stress strain curves showed that the full gripping position had a steeper slope compared to the inner and outer gripped conditions (Figure 7B). The Young's modulus, yield strength and resilience were significantly higher in the full gripped samples (Table 4). Interestingly, the fibres failed in different places depending on the gripping position (Figure 7C and Figure S1): fibres that connected the top and bottom halves of the scaffolds failed in the full gripping condition, whereas only the outer and middle fibres failed with the outer and inner grippers, respectively. This observation was confirmed by modelling as

the stress was distributed across all the connecting fibres with the full gripping position while it was focused in outer and middle fibres for the outer and inner gripping position, respectively.

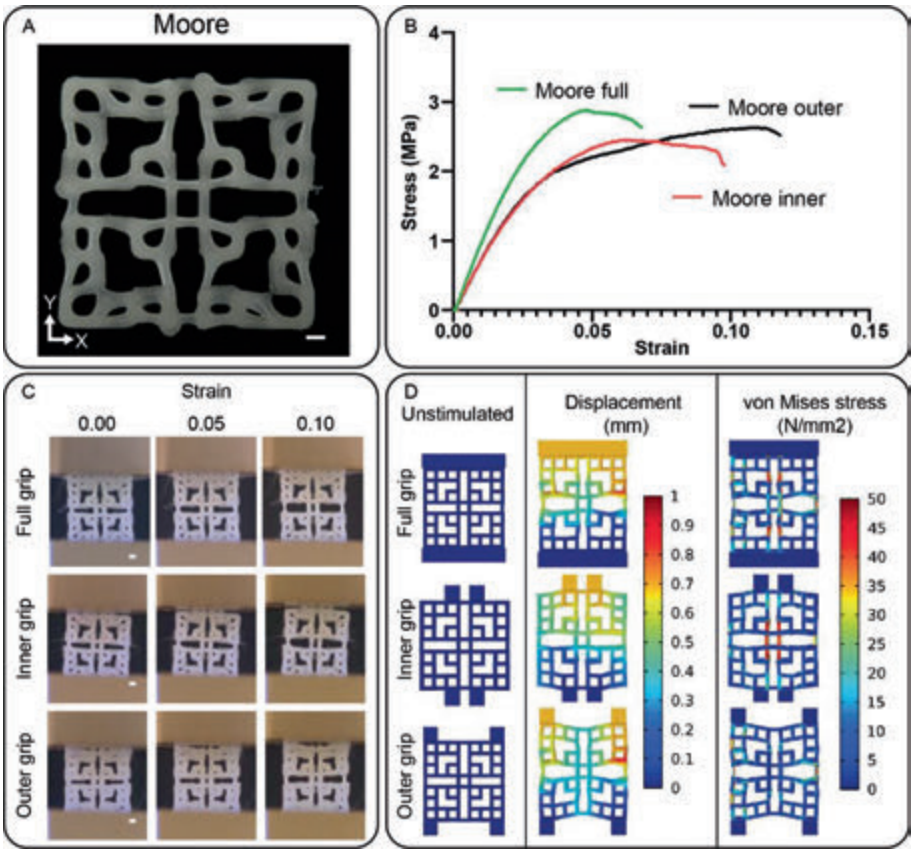

Figure 7. *Moore design. Stereomicroscopy image of the Moore design (A). Representative stress-strain curve (B). Time-lapsed snapshots of the tensile test (C). Finite element model with the left panels the unstimulated scaffold, the middle panel and right panel the displacement and von Mises stress respectively and 10% strain (D). Scale bar represents 500 µm.*

3.2.4 Peano curve

The Peano curve is the first known space-filling fractal and has a similar origin as the Hilbert curve [54]. A second-generation Peano curve was investigated in this study. The morphology of the scaffolds showed that the Peano curve can be divided in nine segments (Figure 8A). Each segment consists of a square of four small pores (0.62 ± 0.03 mm^2) that were separated by larger

pores (4.29 ± 0.42 mm^2). The average fibre diameter was 254.0 ± 22.1 µm and the porosity was 74.7 ± 0.3%. The stress-strain curves revealed that the full and outer gripped samples were similar in mechanical properties except the samples with the outer grips failed at a lower strain (Figure 8B). The inner gripped samples showed significantly lower Young's modulus, yield strength and resilience but significantly higher yield strain (Table 5). All samples

Table 4. *Mechanical properties of the Moore design with various gripping positions. Values represent average ± standard deviation. * Statistical significance p<0.05.*

Scaffold	Gripping position	Young's modulus (MPa)	Yield strain (mm/mm)	Yield strength (MPa)	Resilience ($N \cdot mm^{-2}$)	Ultimate Strain (mm/mm)	Toughness ($N \cdot mm^{-2}$)
Moore	Full	100.9 ± 5.3*	0.018 ± 0.001	2.1 ± 0.1*	0.025 ± 0.001*	No failure	No failure
	Inner	65.9 ± 3.8	0.014 ± 0.002	1.4 ± 0.1	0.016 ± 0.001	No failure	No failure
	Outer	73.3 ± 2.1	0.014 ± 0.003	1.5 ± 0.0	0.018 ± 0.000	No failure	No failure

showed a rotating middle segment with increasing applied strain (Figure 8C). This rotation was also confirmed by modelling, where also some of the larger pores opened (Figure 8D). The modelling also revealed that the inner gripped samples had a lower von Mises stress compared to the other conditions. This could be an explanation for the lower Young's modulus and the higher yield strain in this condition. In another study, the orientation of the curve in a Peano curve was reported to influence the mechanical properties of the resulting polymer scaffold [55]. However, since the layers in our study were stacked at a 90° angle, the morphology of the scaffolds in both X and Y direction were similar. It is possible to stack the scaffold at 180° and get a difference in morphology in the X and Y direction, but this design results in a scaffold with identical layers and no side porosity.

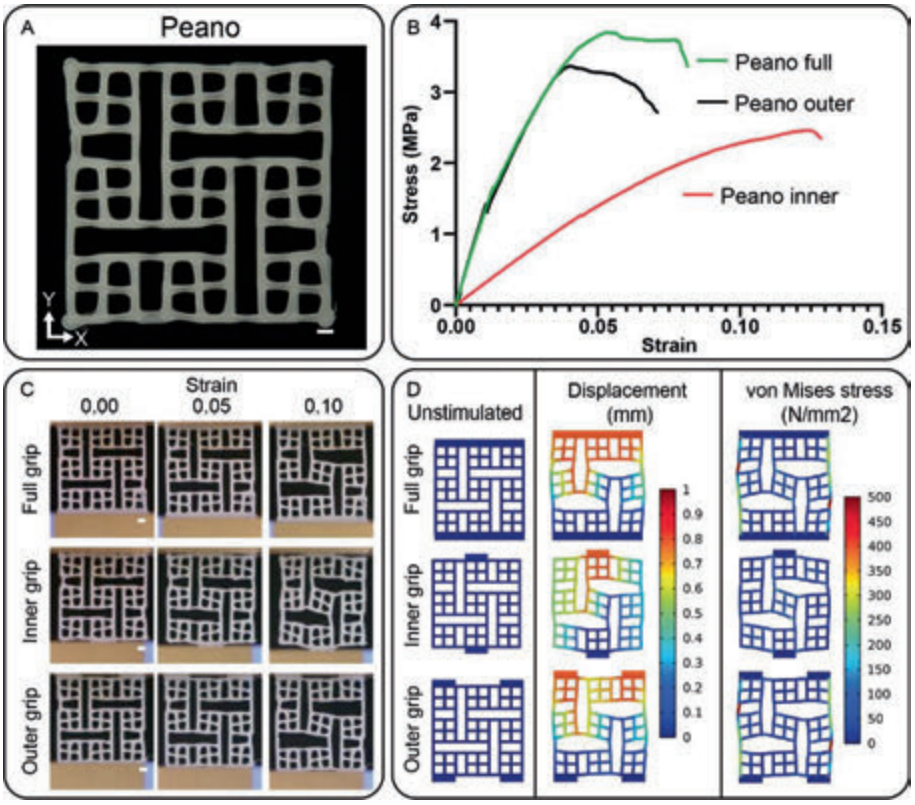

Figure 8. *Peano design. Stereomicroscopy image of the Peano design (A). Representative stress-strain curve (B). Time-lapsed snapshots of the tensile test (C). Finite element model with the left panels the unstimulated scaffold, the middle panel and right panel the displacement and von Mises stress respectively and 10% strain (D). Scale bar represents 500 µm.*

Table 5. *Mechanical properties of the Peano design with various Gripping positions. Values represent average ± standard deviation. * Statistical significance p<0.05. [+]Based on 2 samples out of 5.*

Scaffold	Gripping position	Young's modulus (MPa)	Yield strain (mm/mm)	Yield strength (MPa)	Resilience ($N \cdot mm^{-2}$)	Ultimate Strain (mm/mm)	Toughness ($N \cdot mm^{-2}$)
Peano	Full	79.0 ± 2.1	0.034 ± 0.002	3.0 ± 0.2	0.058 ± 0.006	0.41 ± 0.05[+]	0.48 ± 0.04[+]
	Inner	26.2 ± 5.0*	0.045 ± 0.001*	1.1 ± 0.2*	0.027 ± 0.007*	0.77 ± 0.18	1.08 ± 0.31
	Outer	81.0 ± 3.3	0.035 ± 0.002	3.1 ± 0.1	0.060 ± 0.004	0.72 ± 0.12[+]	1.11 ± 0.11[+]

3.2.5 Sierpiński arrowhead

The Sierpiński arrowhead is a space-filling fractal with the outer contour of the curve resembling an isosceles triangle [56]. A fourth-generation Sierpiński arrowhead curve was used with each stacked layer rotated at 120°. The stereomicroscopy images revealed that the resulted triangular fractal scaffolds could be divided in 4 smaller triangles with the middle triangle being an open pore (8.66 ± 0.14 mm^2) (Figure 9A). This division could be continued for each triangle until the smallest pores were reached (0.17 ± 0.05 mm^2). The fibre diameter was 243.8 ± 11.2 µm and the porosity was 81.4 ± 0.7%. The stress-strain curves revealed that there was a difference in mechanical properties depending on the gripping position (Figure 9B and Table 6). This was a general observation with all of the tested designs. Both the Young's modulus and yield strength were significantly higher in the scaffolds with inner gripped positions while the yield strain was significantly lower. Whereas the inner grippers caused one of the bases of the triangle to protrude, the outer grippers caused the whole shape to extend. The finite element model confirmed this observation and showed that the stress distribution was different between scaffolds with different gripping positions. The scaffolds with inner grippers caused a higher stress in the two upper triangles while the bottom triangle was unaffected. The scaffolds with outer grippers focussed the stress on the thinnest section between the triangles.

Table 6. *Mechanical properties of the Sierpiński arrowhead design with various gripping positions. Values represent average ± standard deviation. * Statistical significance p<0.05. [+]No standard deviation available as this is based on a single sample.*

Scaffold	Gripping position	Young's modulus (MPa)	Yield strain (mm/mm)	Yield strength (MPa)	Resilience ($N \cdot mm^{-2}$)	Ultimate Strain (mm/mm)	Toughness ($N \cdot mm^{-2}$)
Sierpiński	Inner	68.2 ± 10.6*	0.033 ± 0.001*	2.4 ± 0.4*	0.044 ± 0.009	No failure	No failure
	Outer	24.2 ± 11.9	0.052 ± 0.017	1.2 ± 0.4	0.032 ± 0.014	0.89[+]	2.12[+]

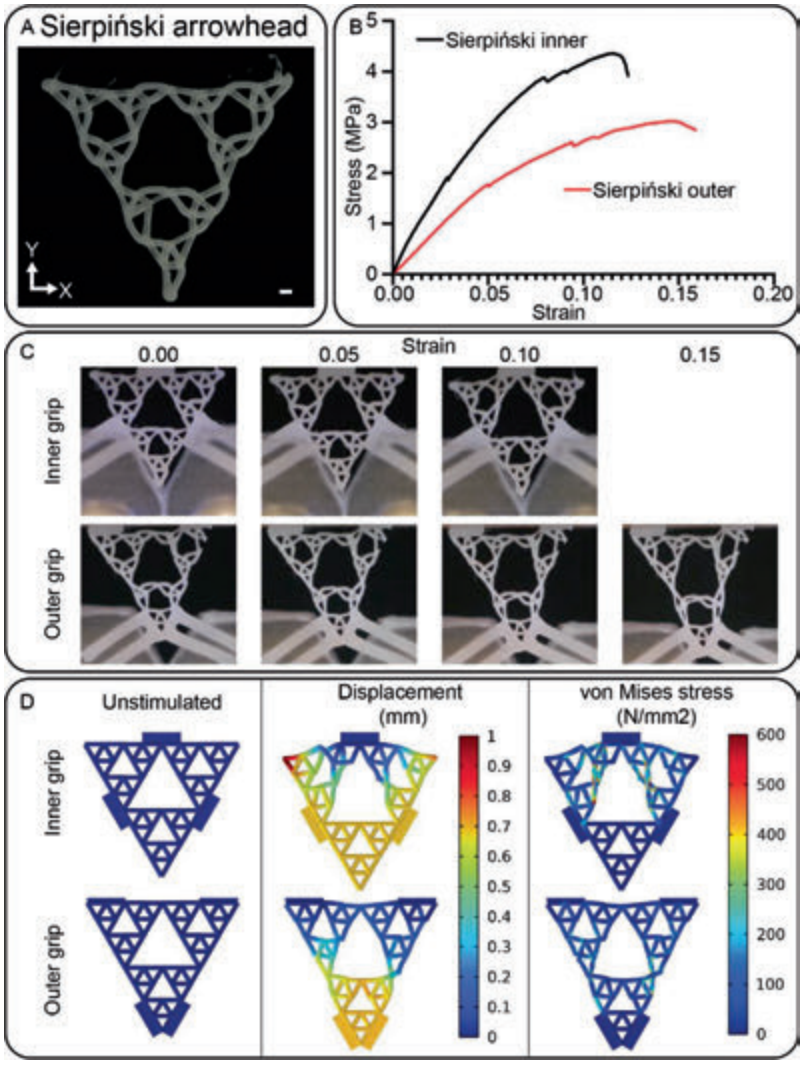

Figure 9. *Sierpiński arrowhead design. Stereomicroscopy image of the Sierpiński arrowhead design (A). Representative stress-strain curve (B). Time-lapsed snapshots of the tensile test (C). Finite element model with the left panels the unstimulated scaffold, the middle panel and right panel the displacement and von Mises stress respectively and 10% strain (D). Scale bar represents 500 μm.*

3.2.6 Gosper curve

The Gosper space filling fractal is a curve that can be divided into 7 hexagons with one at the centre being completely surrounded by six other hexagons [57]. In this study a third-generation Gosper curve with each layer stacked at 120° was investigated. The Gosper curve could not be stacked at a 60° rotation as this resulted in large overhanging parts, which could not be manufactured without a supporting material. The layers of the scaffolds were almost identical except for three lines that can be drawn from the centre hexagon to three outer hexagons of the scaffolds. Consequently, the scaffolds only had side porosity within those specific hexagons. The average fibre diameter was 277.8 ± 20.1 µm and the porosity was 78.9 ± 0.2%. The grippers for the scaffolds were set at two different places; (1) at the edge of the hexagons where there was side porosity (inner), and (2) at the edge of the hexagons where there was no side porosity (outer). The stress strain curves revealed that the scaffolds with the inner grippers had a much steeper slope (Figure 10B). The Young's modulus, yield strength and resilience were significantly higher in the inner gripped samples, while the yield strain was significantly lower (Table 7). The inner gripped scaffolds unfolded and expanded in the orthogonal direction with increasing strain (Figure 10C). Only two segments of the outer gripped samples expanded. This observation was confirmed by the modelling where the displacement was focused in only a single segment of the scaffolds (Figure 10D). The stress distribution between the samples was also different as the von Mises stress on the outer gripped samples was lower compared to the inner gripped samples.

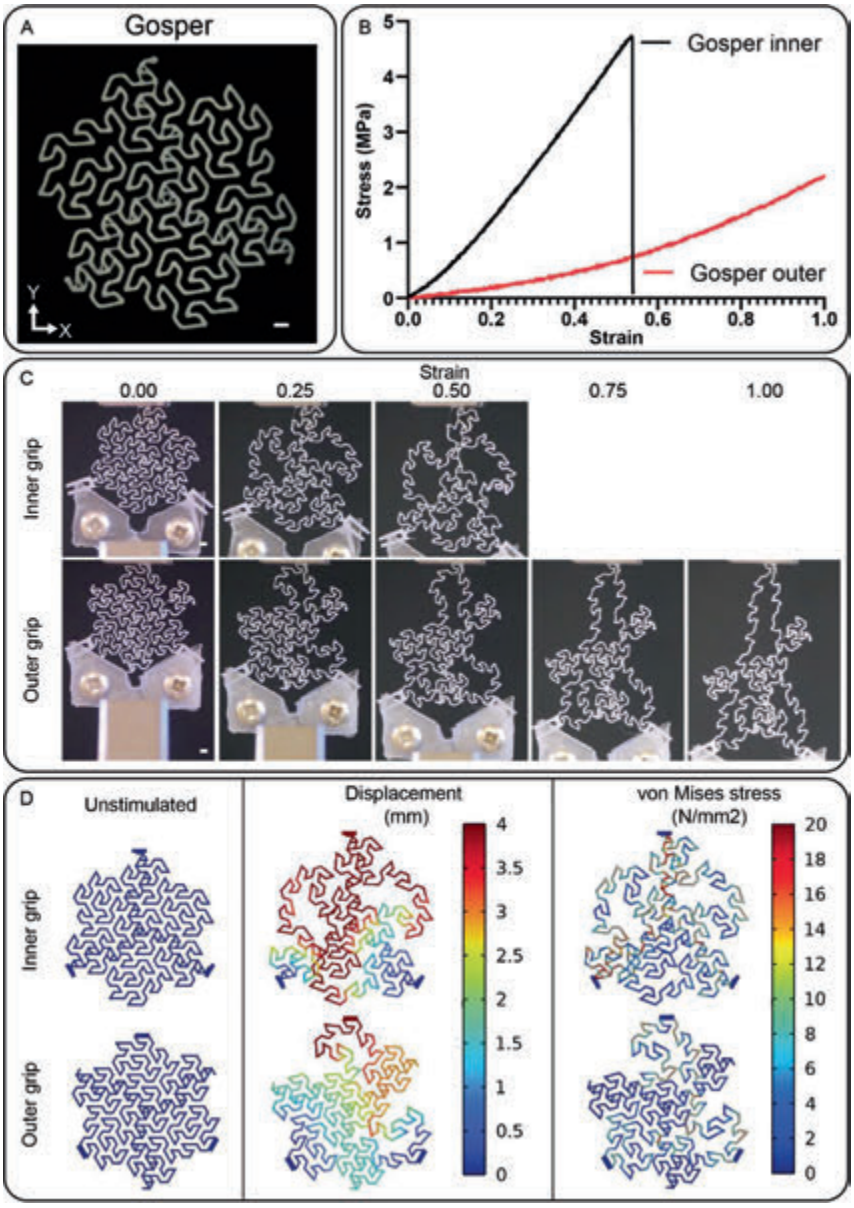

Figure 10. *Gosper design. Stereomicroscopy image of the Gosper design (A). Representative stress-strain curve (B). Time-lapsed snapshots of the tensile test (C). Finite element model with the left panels the unstimulated scaffold, the middle panel and right panel the displacement and von Mises stress respectively and 25% strain. (D). Scale bar represents 500 µm.*

Table 7. *Mechanical properties of the Gosper design with various gripping positions. Values represent average ± standard deviation. * Statistical significance p<0.05.*

Scaffold	Gripping position	Young's modulus (MPa)	Yield strain (mm/mm)	Yield strength (MPa)	Resilience ($N \cdot mm^{-2}$)	Ultimate Strain (mm/mm)	Toughness ($N \cdot mm^{-2}$)
Gosper	Inner	8.9 ± 1.2	0.474 ± 0.041	3.7 ± 0.4	0.724 ± 0.165	0.52 ± 0.07	0.92 ± 0.17
	Outer	1.4 ± 0.4*	0.243 ± 0.068*	0.2 ± 0.1*	0.029 ± 0.015*	No failure	No failure

3.3 Penrose tiling

The Penrose tiling is an infinite pattern that is generated by two different tiles containing predefined Ammann bars [58]. The only condition for tiling the pattern is that the Ammann bars are always connected because it is impossible to create an infinite pattern without this connection. The Ammann bars that are generated form parallel lines with five different slopes. The gaps between the lines with the same slope can be short or long. Observing a finite area of the infinite pattern reveals that the ratio of short and long gaps between lines approaches the golden ratio. A random set of these lines was taken and connected together to form a layer. Each layer was rotated 72° until five layers were created. The names of the scaffolds was based on the sequence of long and short gaps between the fibres and three different patterns were tested (LLSLSSSS, LLSSSLSS and SSLLSSSL). The morphology between the LLSLSSSS, LLSSSLSS and SSLLSSSL design was different even though the theoretical porosity was nearly the same (76.6 ± 0.3%, 74.9 ± 0.4% and 74.5 ± 0.1% respectively) (Figure 11A). The average fibre diameter for LLSLSSSS, LLSSSLSS and SSLLSSSL was 252.6 ± 22.6 µm, 257.3 ± 22.9 µm and 262.9 ± 26.6 µm respectively. If the short gaps were in the centre of the sequence, the final scaffolds had a denser core and *vice versa*. The stress-strain curves were nearly identical with the SSLLSSSL samples having a significantly lower Young's modulus, yield strength and resilience (Figure 11B and Table 8), which can be explained an open edge that contributes only partially to the mechanical properties. In addition, the finite element model revealed that the maximum von Mises stress in this particular sample was higher while the other

two were similar (Figure 11D). The other two variations had a nearly identical Young's modulus, yield strength, yield strain and resilience (Table 8) while having a different morphology (Figure 11A).

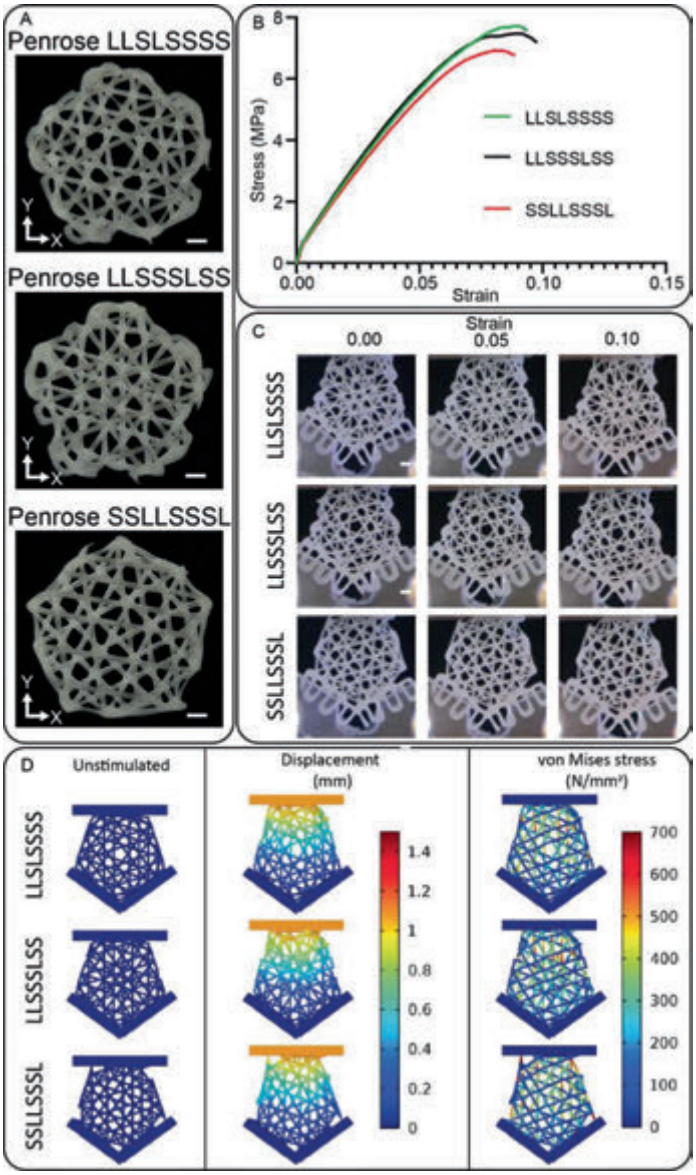

Figure 11. *Penrose tilling design. Stereomicroscopy image of three different Penrose tilling designs, LLSLSSS, LLSSSLSS and SSLLSSSL (A). Representative stress-strain curve (B). Time-lapsed snapshots of the tensile test (C). Finite element model with the left panels the unstimulated scaffold, the middle panel and right panel the displacement and von Mises stress respectively and 10% strain (D). Scale bar represents 500 μm.*

Table 8. *Mechanical properties of three different variations of the Penrose tilling design with various clamping positions. Values represent average ± standard deviation. * Statistical significance p<0.05. ⁺Based on 2 out of 5 samples. ⁼Based on 3 out of 5 samples.*

Scaffold	Young's modulus (MPa)	Yield strain (mm/mm)	Yield strength (MPa)	Resilience ($N \cdot mm^{-2}$)	Ultimate Strain (mm/mm)	Toughness ($N \cdot mm^{-2}$)
LLSLSSS	105.9 ± 6.1	0.045 ± 0.001	5.3 ± 0.3	0.134 ± 0.007	No Failure	No failure
LLSSSLS	106.7 ± 2.8	0.044 ± 0.003	5.3 ± 0.2	0.129 ± 0.012	0.40 ± 0.06⁺	0.96 ± 0.12⁺
SSLLSSL	94.9 ± 4.1*	0.044 ± 0.001	4.6 ± 0.2*	0.111 ± 0.006*	0.44 ± 0.23⁼	1.34 ± 0.43⁼

3.4 Cartesian-based spirals

The spiral architecture was generated through Cartesian coordinate equations (Equation 1 and 2). The spiral generated here was an Archimedean spiral. Each arm of the spiral was rotated 45° until eight arms were generated. Afterwards, a layer of connecting fibres was printed for mechanical stability. The stereomicroscopy images revealed that the distance between the arms of the spirals remained similar (Figure 12A). In addition, there were four different pore sizes detected; the smallest pores (0.97 ± 0.06 mm^2) at the centre of the spiral, intermediate sized pores (2.18 ± 0.13 mm^2) that were directly connected, another set of slightly larger pores (3.29 ± 0.11 mm^2) connecting the previous set and finally the largest at the edges of the scaffold (4.45 ± 0.27 mm^2). The average fibre diameter was 264.9 ± 31.0 µm and the porosity was 82.9 ± 0.6%. The mechanical data revealed that the Young's modulus was only 3.0 ± 0.2 MPa and the yield strength was very low at 0.25 ± 0.11 MPa, compared to the previously tested designs. The yield strain, however, was higher compared to any of the other designs at 0.08 ± 0.04 mm/mm. The outer segments close to the clamps expanded upon higher strain while the segments in the middle contracted (Figure 12C). The scaffold broke at the connecting fibre layer. The finite element model also confirmed this observation (Figure 12D). In addition, the model showed that the highest von

Mises stress was noted in the connecting fibre layer, which also coincides with the breaking point during the mechanical test.

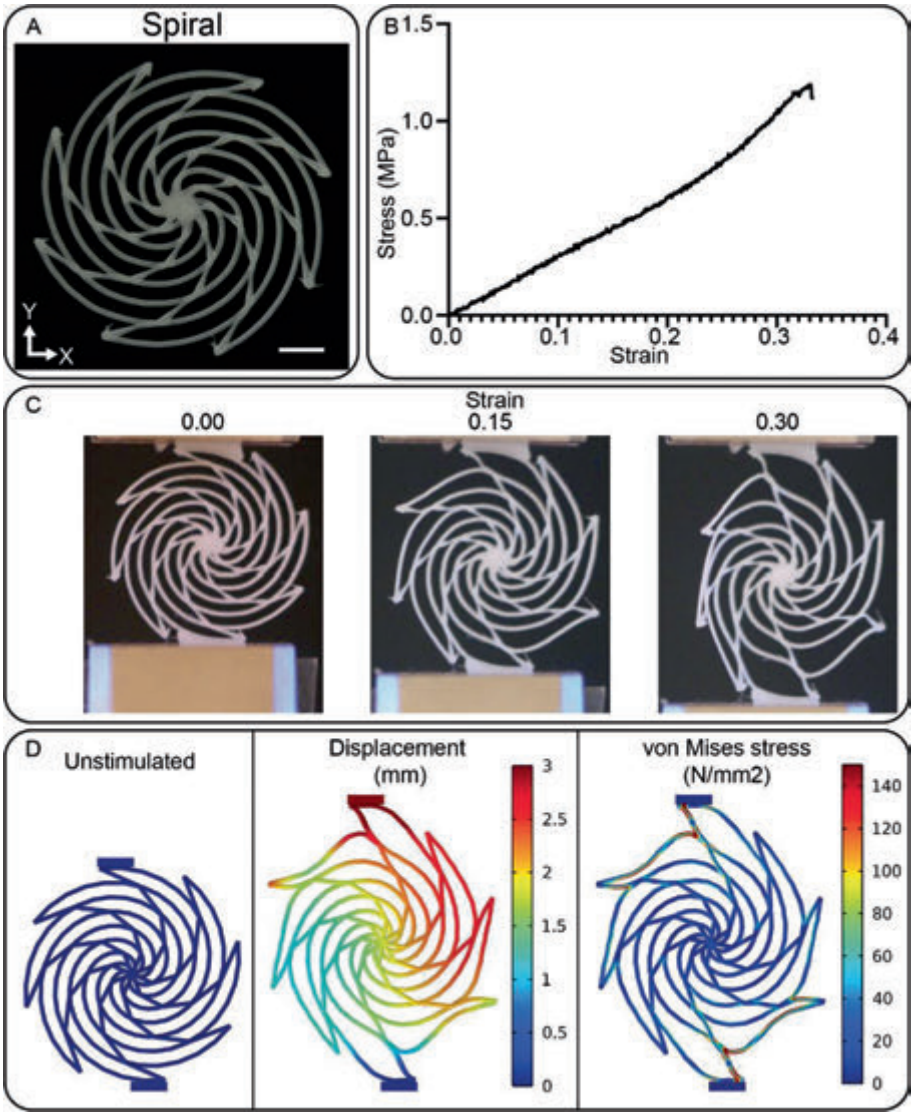

Figure 12. *Spiral design. Stereomicroscopy image of the Spiral design (A). Representative stress-strain curve (B). Time-lapsed snapshots of the tensile test (C). Finite element model with the left panels the unstimulated scaffold, the middle panel and right panel the displacement and von Mises stress respectively and 15% strain (D). Scale bar represents 500 µm.*

Table 9. *Mechanical properties of the spiral design with various clamping positions. Values represent average ± standard deviation. * Statistical significance p<0.05. [+]Based on 3 out of 5 samples.*

Scaffold	Young's modulus (MPa)	Yield strain (mm/mm)	Yield strength (MPa)	Resilience ($N \cdot mm^{-2}$)	Ultimate Strain (mm/mm)	Toughness ($N \cdot mm^{-2}$)
Spiral	3.0 ± 0.2	0.08 ± 0.04	0.25 ± 0.11	0.012 ± 0.010	0.91 ± 0.03[+]	1.09 ± 0.16[+]

3.5 Young's modulus and apparent density

Comparing the Young's modulus and apparent density from all of the tested designs revealed that in general a higher density, calculated by measuring both the weight and volume of the scaffold, correlated to a higher Young's modulus (Figure 13), as the 0-90 woodpile design has both the highest Young's modulus and apparent density. In addition, the spiral scaffolds, which had the lowest apparent density, also had one of the lowest Young's modulus with only the Gosper curve having a lower Young's modulus. This trend was also observed in other studies where scaffolds with different porosities were compared [59, 60].

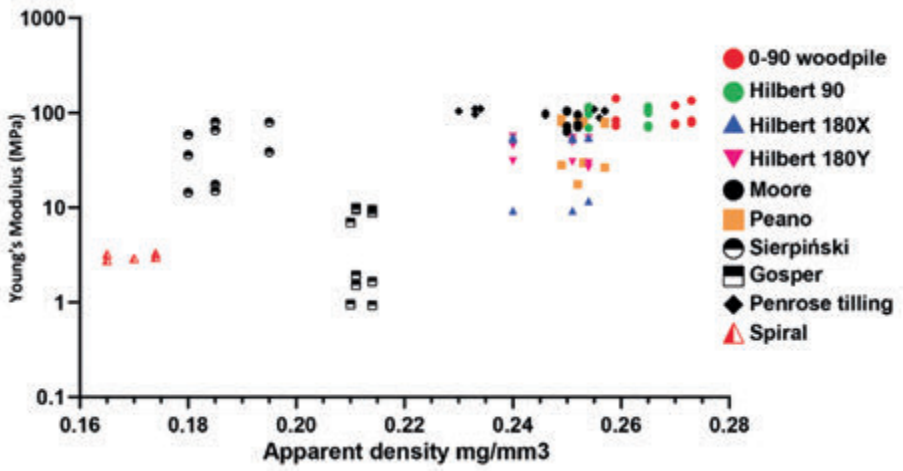

Figure 13. *Apparent density plotted against the calculated Young's modulus of all the tested designs.*

4. Discussion

Scaffold architecture is of paramount importance for the mechanical and biological outcome during tissue or organ regeneration. In this study, a broad range of space-filling curves and other filling patterns were manufactured with custom-generated G-codes, to obtain a variety of scaffolds with architectures inspired by biomimicry principles. The scaffolds obtained presented a similar porosity (Table 1) but showed different mechanical behaviour that spans from very flexible patterns such as the Gosper curve to stiff and dense patterns such as the Penrose tiling. These patterns can therefore expand the palette of possible biomechanical applications of an otherwise stiff polymer such as PCL.

The scripts generated allow the creation of G-codes, which generally have a simple syntax that includes coordinate points and machine instructions such as the extrusion control for the FDM systems. The majority of the lines consists of X, Y and Z coordinates that are universal with the exception being the start and final commands. The creation of coordinate points to manufacture complex printing fillings is generally limited in the printer software that is commercially available. Free software such as Python, Notepad or even the macros function within FIJI can potentially be used to generate a list of coordinates that can be drawn from a simple image. If combined with the specific printer commands, then a fully functional printing pathway can be created.

One limitation for custom G-code creation is that certain designs cannot be fabricated. Examples of these designs are cases where the printing pathway goes through previously deposited fibres or if multiple layers are added, the pattern needs a solid support underneath it to prevent sagging. To overcome the first problem, classical FDM could be replaced by a robotic arm that can avoid potential collisions with the printed objects, something that a traditional

FDM system cannot execute due to its layer-by-layer principle [61]. To address the second problem, selecting a material that quenches fast enough after leaving the nozzle [62] can prevent sagging, circumventing the need for a support. Some careful considerations have to be made when using fractal patterns as stacking them in different orientations could hinder the folding or unfolding capabilities of the scaffolds. This hindrance is due to the fact that the second layer will lock certain parts of the previously deposited layer, which was observed in all fractal patterns but clearly evident in the Gosper curve.

The loading regime or the interface position with the surrounding tissue (simplified with the gripping position) of the scaffolds mattered, as was shown by the results of this study. When tensile tests were performed, all of the samples that had similar morphologies but received different loading regimes showed variation in stress-strain curves or morphology during the test. Although the type of grippers can influence the stress-strain curve [63, 64], none of the studies reported that applying a partial load could have an influence. The loading regime is of importance especially considering that these scaffolds have to be sutured when implanted. Suturing solid polymer scaffolds could prove difficult as the needle has to go through the pores of the scaffolds [16]. Both a high amount of suture material and suture slack could hinder healing [65, 66], therefore a scaffold should be tightly sutured at specific (minimal) locations, resulting in the scaffold being loaded in certain regimes. Having a partially loaded scaffold can give skewed results, such as failing at the clamping site (e.g., representing suturing points with surrounding tissue) of the scaffold as was shown by the 0-90 woodpile design in both the inner and outer clamped positions. Therefore it is required to have reinforced suturing points in order to avoid these possible skewed results. Our results also showed that different loading regimes can have a significant effect on the stress-strain curve or morphology during the test as was shown by the Hilbert 180X, Peano and Gosper curves.

Our mechanical data were generated under a controlled *in vitro* testing environment, which differs from the *in vivo* loading of a scaffold [67]. Furthermore, the scaffolds in this study were only tested in tension and in the X and Y direction, which has an influence on the mechanical properties. Therefore, replicating these studies with different mechanical loading patterns, different tests, and in different directions could give valuable insight about how these scaffolds behave mechanically *in vivo*. In addition, these scaffolds should be cultured with cells to provide a dynamic environment since cells are known to respond differently to mechanical stimuli [68]. These scaffolds in combination with hMSCs could be used to study the effect of mechanical stimulation and different pore sizes on cell differentiation, decoupling mechanical from architecture and chemical properties [50]. Future studies could aim at investigating whether mechanically stimulating a scaffold with different loading regimes could have an effect on cell fate. For example, the stress distribution within the Moore curve with the inner loading regime was focused on the middle section of the scaffolds, while the outer edges of the scaffolds were unaffected. This scaffold could be used to study the effect of local stress on cells as this is known to alter cellular behaviour [69]. In addition, this design could be interesting to study the effect of porosity and cell growth [70] as increasing the generation of the Moore curves results in rings of alternating high and low porosity.

The variation in mechanical behaviour from our designs can be deployed to generate appropriate scaffolds for targeted tissue engineering applications. For example, the stiff and dense characteristic of 0-90 woodpile design makes it a potential candidate for load-bearing tissues such as bone and articular cartilage [50, 71]. The Hilbert curve scaffolds, with the same Young's modulus and a similar apparent density, could be a suitable alternative to the 0-90 woodpile design for softer tissues such as cartilage or tendon [72, 73]. Gosper curve showed a Young's modulus two orders of magnitude lower compared to the 0-90 woodpile structure, most likely due to limited interconnections

between fibres. This low interconnectivity from the Gosper curve allowed it to unfold and resulted in greater flexibility. Thus, the Gosper curve could be used to study contractile effects of certain cell types such as smooth muscle cells [74, 75]. The spiral and the Peano curve, with a lower Young's modulus and a higher yield strain, could be suitable for more flexible tissues such as the skin [76].

It was also noted that the tensile strength of the Hilbert curve pattern was lower compared to the 0-90 woodpile structure. However, a direct comparison with other studies was not possible as the Hilbert curve was not rotated for every layer, which could have an influence on the mechanical properties. The Young's modulus was lower in the Peano and Hilbert 180X and Y curve compared to the 0-90 woodpile design, while the yield strain was higher.

Penrose tiling, with different spacing order between fibres per layer, could be used to create a porosity gradient in scaffolds. Other studies also attempted to create a gradient in porosity by changing the fibre distance for each layer [77]. However, this resulted in a gradient in the Z direction of the scaffolds and not radial porosity. An approach to achieve a radial gradient is to fabricate multiple toroidal shaped scaffolds with different fibre spacing and fit them into each other [78]. However, the mechanical properties were lower due to the discontinuity of the different parts of the scaffolds. Even though the morphology of the scaffolds varied, the mechanical properties were similar. This is unlike the other patterns that were measured in this study and it could be useful to study and decouple the influence of morphology on a scaffold from the mechanical properties.

Spiral patterns have already been used in other studies [79, 80]. However, often a sheet of a single material is made and then rolled up to form a spiral, which was previously not done using FDM. Another approach using DLP is to print a spiral pattern in the Z-direction creating a tubular structure [81].

Although a good approach to create a tubular structure, porous non-tubular structures cannot be constructed with this method. In addition, this was done using an FDM system which has a wider range of materials available to use. We showcased here that it is possible by adding a second layer that connects the arms of each spiral. Cartesian equations are not only limited to spiral patterns. Other patterns can be created once the equations are known for both the X and Y coordinate. The most simple one is a circle, but other more complex curves such as sinusoidal waves have already been achieved [43].

The number of patterns available to print is infinite. Other space-filling fractals not explored here and variations thereof [55, 82] could be designed, printed and systematically characterised, as we did here. These patterns could be used to study cell contractility or cellular growth. Additionally, they could be used to study cellular behaviour during mechanical stimulation [83]. For TERM applications, we recommend that the target tissue characteristics be taken into account when fabricating a specific pattern.

5. Conclusion

This study provides an overview of the complex patterns that can potentially be generated in G-code for any extrusion-based AM system. The patterns studied here were characterized morphologically, mechanically and through finite element modelling. In addition, this study showed that the scaffold loading regime can have a significant difference in mechanical properties. The library of patterns showcased here could serve as a guideline for other researchers to use more complex and relevant patterns in their scaffold design.

References

[1] F. Berthiaume, T.J. Maguire, M.L. Yarmush, Tissue engineering and regenerative medicine: history, progress, and challenges, Annual review of chemical and biomolecular engineering 2 (2011) 403-430.
[2] X. Song, W. He, H. Qin, S. Yang, S. Wen, Fused Deposition Modeling of Poly (lactic acid)/Macadamia Composites—Thermal, Mechanical Properties and Scaffolds, Materials 13(2) (2020) 258.
[3] C.G. Kim, K.S. Han, S. Lee, M.C. Kim, S.Y. Kim, J. Nah, Fabrication of biocompatible polycaprolactone–hydroxyapatite composite filaments for the FDM 3D printing of bone scaffolds, Applied Sciences 11(14) (2021) 6351.
[4] S.M. Giannitelli, D. Accoto, M. Trombetta, A. Rainer, Current trends in the design of scaffolds for computer-aided tissue engineering, Acta Biomaterialia 10(2) (2014) 580-594.
[5] M. Silva, F.N. Ferreira, N.M. Alves, M.C. Paiva, Biodegradable polymer nanocomposites for ligament/tendon tissue engineering, Journal of Nanobiotechnology 18 (2020) 1-33.
[6] M. Talikowska, X. Fu, G. Lisak, Application of conducting polymers to wound care and skin tissue engineering: A review, Biosensors and Bioelectronics 135 (2019) 50-63.
[7] M.E. Carnes, G.D. Pins, Skeletal muscle tissue engineering: biomaterials-based strategies for the treatment of volumetric muscle loss, Bioengineering 7(3) (2020) 85.
[8] Y. Yeni, C. Brown, Z. Wang, T. Norman, The influence of bone morphology on fracture toughness of the human femur and tibia, Bone 21(5) (1997) 453-459.
[9] R. Beeuwkes III, The vascular organization of the kidney, Annual Review of Physiology 42(1) (1980) 531-542.
[10] P.G. Agache, C. Monneur, J.L. Leveque, J. De Rigal, Mechanical properties and Young's modulus of human skin in vivo, Archives of dermatological research 269(3) (1980) 221-232.
[11] D.T. Reilly, A.H. Burstein, The mechanical properties of cortical bone, JBJS 56(5) (1974) 1001-1022.
[12] Q.-H. Zhang, A. Cossey, J. Tong, Stress shielding in bone of a bone-cement interface, Medical engineering & physics 38(4) (2016) 423-426.
[13] J.L. Forman, R.W. Kent, The effect of calcification on the structural mechanics of the costal cartilage, Computer methods in biomechanics and biomedical engineering 17(2) (2014) 94-107.
[14] L. Jiang, Z. Sun, X. Chen, J. Li, Y. Xu, Y. Zu, J. Hu, D. Han, C. Yang, Cells sensing mechanical cues: stiffness influences the lifetime of cell–extracellular matrix interactions by affecting the loading rate, ACS nano 10(1) (2016) 207-217.
[15] K.A. van Kampen, E. Olaret, I.-C. Stancu, D.F. Duarte Campos, H. Fischer, C. Mota, L. Moroni, Hypotrochoidal scaffolds for cartilage regeneration, bioRxiv (2022) 2022.11.29.518172.
[16] L. Ruiz-Cantu, A. Gleadall, C. Faris, J. Segal, K. Shakesheff, J. Yang, Characterisation of the surface structure of 3D printed scaffolds for cell infiltration and surgical suturing, Biofabrication 8(1) (2016) 015016.
[17] S. Todros, S. Spadoni, E. Maghin, M. Piccoli, P.G. Pavan, A novel bioreactor for the mechanical stimulation of clinically relevant scaffolds for muscle tissue engineering purposes, Processes 9(3) (2021) 474.
[18] P. Jain, H. Kathuria, N. Dubey, Advances in 3D bioprinting of tissues/organs for regenerative medicine and in-vitro models, Biomaterials 287 (2022) 121639.
[19] D.W. Hutmacher, K.W. Ng, C. Kaps, M. Sittinger, S. Kläring, Elastic cartilage engineering using novel scaffold architectures in combination with a biomimetic cell carrier, Biomaterials 24(24) (2003) 4445-4458.
[20] C. Mota, D. Puppi, F. Chiellini, E. Chiellini, Additive manufacturing techniques for the production of tissue engineering constructs, Journal of Tissue Engineering and Regenerative Medicine 9(3) (2015) 174-190.
[21] L. Moroni, T. Boland, J.A. Burdick, C. De Maria, B. Derby, G. Forgacs, J. Groll, Q. Li, J. Malda, V.A. Mironov, Biofabrication: a guide to technology and terminology, Trends in biotechnology 36(4) (2018) 384-402.
[22] K. Łukaszewicz, Use of CAD software in the process of virtual prototyping of machinery, Procedia Engineering 182 (2017) 425-433.
[23] F.M. Mwema, E.T. Akinlabi, Basics of fused deposition modelling (FDM), fused deposition modeling, Springer2020, pp. 1-15.

[24] S.-J. Shin, S.-H. Suh, I. Stroud, Reincarnation of G-code based part programs into STEP-NC for turning applications, Computer-Aided Design 39(1) (2007) 1-16.
[25] J. Bryła, A. Martowicz, Study on the Importance of a Slicer Selection for the 3D Printing Process Parameters via the Investigation of G-Code Readings, Machines 9(8) (2021) 163.
[26] E. Wisse, F. Braet, D. Luo, R. De Zanger, D. Jans, E. Crabbe, A. Vermoesen, Structure and function of sinusoidal lining cells in the liver, Toxicologic pathology 24(1) (1996) 100-111.
[27] R. Müller, Hierarchical microimaging of bone structure and function, Nature Reviews Rheumatology 5(7) (2009) 373-381.
[28] C. Waugh, T. Alktebi, A. De Sa, A. Scott, Impact of rest duration on Achilles tendon structure and function following isometric training, Scandinavian journal of medicine & science in sports 28(2) (2018) 436-445.
[29] D. Martínez-Moreno, G. Jiménez, C. Chocarro-Wrona, E. Carrillo, E. Montañez, C. Galocha-León, B. Clares-Naveros, P. Gálvez-Martín, G. Rus, J. de Vicente, Pore geometry influences growth and cell adhesion of infrapatellar mesenchymal stem cells in biofabricated 3D thermoplastic scaffolds useful for cartilage tissue engineering, Materials Science and Engineering: C 122 (2021) 111933.
[30] P.A. Janmey, C.A. McCulloch, Cell mechanics: integrating cell responses to mechanical stimuli, Annu. Rev. Biomed. Eng. 9 (2007) 1-34.
[31] S. Anand, T. Stoppe, M. Lucena, T. Rademakers, M. Neudert, S. Danti, L. Moroni, C. Mota, Mimicking the human tympanic membrane: The significance of scaffold geometry, Advanced healthcare materials 10(11) (2021) 2002082.
[32] A. Guerra, A. Roca, J. de Ciurana, A novel 3D additive manufacturing machine to biodegradable stents, Procedia Manufacturing 13 (2017) 718-723.
[33] K.A. van Kampen, E. Olaret, I.-C. Stancu, L. Moroni, C. Mota, Controllable four axis extrusion-based additive manufacturing system for the fabrication of tubular scaffolds with tailorable mechanical properties, Materials Science and Engineering: C 119 (2021) 111472.
[34] K. Eichholz, F. Freeman, P. Pitacco, J. Nulty, D. Ahern, R. Burdis, D. Browe, O. Garcia, D. Hoey, D.J. Kelly, Scaffold microarchitecture regulates angiogenesis and the regeneration of large bone defects, Biofabrication (2022).
[35] B. Starly, W. Sun, Internal scaffold architecture designs using Lindenmayer Systems, Computer-Aided Design and Applications 4(1-4) (2007) 395-403.
[36] W. Geraets, P. Van Der Stelt, Fractal properties of bone, Dentomaxillofacial Radiology 29(3) (2000) 144-153.
[37] L.M. Benneker, P.F. Heini, S.E. Anderson, M. Alini, K. Ito, Correlation of radiographic and MRI parameters to morphological and biochemical assessment of intervertebral disc degeneration, European spine journal 14(1) (2005) 27-35.
[38] F. Torrent-Guasp, M.J. Kocica, A.F. Corno, M. Komeda, F. Carreras-Costa, A. Flotats, J. Cosin-Aguillar, H. Wen, Towards new understanding of the heart structure and function, European journal of cardio-thoracic surgery 27(2) (2005) 191-201.
[39] B. Marino, A.F. Corno, Spiral pattern: universe, normal heart, and complex congenital defects, The Journal of Thoracic and Cardiovascular Surgery 126(4) (2003) 1225-1226.
[40] P.P. Provenzano, R. Vanderby Jr, Collagen fibril morphology and organization: implications for force transmission in ligament and tendon, Matrix Biology 25(2) (2006) 71-84.
[41] J. Mishra, S. Mishra, L-system Fractals, Elsevier2007.
[42] T. Fernique, C. Porrier, A General approach to Ammann bars for aperiodic tilings, arXiv preprint arXiv:2205.13973 (2022).
[43] J.C. McCaw, E. Cuan-Urquizo, Curved-layered additive manufacturing of non-planar, parametric lattice structures, Materials & Design 160 (2018) 949-963.
[44] S. Ji, M. Guvendiren, 3D printed wavy scaffolds enhance mesenchymal stem cell osteogenesis, Micromachines 11(1) (2019) 31.
[45] E. Cuan-Urquizo, A. Bhaskar, Flexural elasticity of woodpile lattice beams, European Journal of Mechanics-A/Solids 67 (2018) 187-199.
[46] T. Serra, M. Ortiz-Hernandez, E. Engel, J.A. Planell, M. Navarro, Relevance of PEG in PLA-based blends for tissue engineering 3D-printed scaffolds, Materials Science and Engineering: C 38 (2014) 55-62.
[47] J. Babilotte, B. Martin, V. Guduric, R. Bareille, R. Agniel, S. Roques, V. Héroguez, M. Dussauze, M. Gaudon, D. Le Nihouannen, Development and characterization of a PLGA-HA

composite material to fabricate 3D-printed scaffolds for bone tissue engineering, Materials Science and Engineering: C 118 (2021) 111334.
[48] B.N. Turner, R. Strong, S.A. Gold, A review of melt extrusion additive manufacturing processes: I. Process design and modeling, Rapid prototyping journal (2014).
[49] C. Duty, C. Ajinjeru, V. Kishore, B. Compton, N. Hmeidat, X. Chen, P. Liu, A.A. Hassen, J. Lindahl, V. Kunc, What makes a material printable? A viscoelastic model for extrusion-based 3D printing of polymers, Journal of Manufacturing Processes 35 (2018) 526-537.
[50] A. Di Luca, I. Lorenzo-Moldero, C. Mota, A. Lepedda, D. Auhl, C. Van Blitterswijk, L. Moroni, Tuning Cell Differentiation into a 3D Scaffold Presenting a Pore Shape Gradient for Osteochondral Regeneration, Advanced healthcare materials 5(14) (2016) 1753-63.
[51] Z. Liu, Q. Lei, S. Xing, Mechanical characteristics of wood, ceramic, metal and carbon fiber-based PLA composites fabricated by FDM, Journal of Materials Research and Technology 8(5) (2019) 3741-3751.
[52] B.R. Bielefeldt, G.W. Reich, P.S. Beran, D.J. Hartl, Development and validation of a genetic L-System programming framework for topology optimization of multifunctional structures, Computers & Structures 218 (2019) 152-169.
[53] D. Hilbert, Über die stetige Abbildung einer Linie auf ein Flächenstück, Dritter Band: Analysis· Grundlagen der Mathematik· Physik Verschiedenes, Springer1935, pp. 1-2.
[54] L. Antoniotti, F. Caldarola, M. Maiolo, Infinite numerical computing applied to Hilbert's, Peano's, and Moore's curves, Mediterranean Journal of Mathematics 17(3) (2020) 1-19.
[55] C. Wu, T.T. Do, P. Tran, Mechanical properties of polyjet 3d-printed composites inspired by space-filling peano curves, Polymers 13(20) (2021) 3516.
[56] W. Warchalowski, M.J. Krawczyk, Line graphs for fractals, Communications in Nonlinear Science and Numerical Simulation 44 (2017) 506-512.
[57] R. Kumar, S. Singh, Multiband antenna design based on Gosper fractal for implantable biomedical devices, International Journal of Microwave and Wireless Technologies (2021) 1-11.
[58] S. Akiyama, K. Imai, The corona limit of Penrose tilings is a regular decagon, International Workshop on Cellular Automata and Discrete Complex Systems, Springer, 2016, pp. 35-48.
[59] X. Wang, Y. Li, J. Xiong, P.D. Hodgson, Porous TiNbZr alloy scaffolds for biomedical applications, Acta biomaterialia 5(9) (2009) 3616-3624.
[60] D.A. Shimko, V.F. Shimko, E.A. Sander, K.F. Dickson, E.A. Nauman, Effect of porosity on the fluid flow characteristics and mechanical properties of tantalum scaffolds, Journal of Biomedical Materials Research Part B: Applied Biomaterials: An Official Journal of The Society for Biomaterials, The Japanese Society for Biomaterials, and The Australian Society for Biomaterials and the Korean Society for Biomaterials 73(2) (2005) 315-324.
[61] I. Ishak, J. Fisher, P. Larochelle, Robot arm platform for additive manufacturing: Multi-plane printing, Proceedings of the 2016 Florida conference on recent advances in robotics (FCRAR 2016), 2016.
[62] M. Gelber, G. Hurst, T. Comi, R. Bhargava, Model-guided design and characterization of a high-precision 3D printing process for carbohydrate glass, Additive Manufacturing 22 (2018) 38-50.
[63] A. Hrouda, R. Jirkovec, J. Safka, M. Vanierschot, K. Denis, L. Capek, Standardized tensile testing of electrospun PA6 membranes via the use of a 3D printed clamping system, Textile Research Journal (2022) 00405175221077046.
[64] S. Knecht, C. Erggelet, M. Endres, M. Sittinger, C. Kaps, E. Stüssi, Mechanical testing of fixation techniques for scaffold-based tissue-engineered grafts, Journal of Biomedical Materials Research Part B: Applied Biomaterials: An Official Journal of The Society for Biomaterials, The Japanese Society for Biomaterials, and The Australian Society for Biomaterials and the Korean Society for Biomaterials 83(1) (2007) 50-57.
[65] G.H. Ballantyne, The experimental basis of intestinal suturing: effect of surgical technique, inflammation, and infection on enteric wound healing, Diseases of the colon & rectum 27 (1984) 61-71.
[66] M. Dragovic, M. Pejovic, J. Stepic, S. Colic, B. Dozic, S. Dragovic, M. Lazarevic, N. Nikolic, J. Milasin, B. Milicic, Comparison of four different suture materials in respect to oral wound healing, microbial colonization, tissue reaction and clinical features—randomized clinical study, Clinical oral investigations 24 (2020) 1527-1541.

[67] P. Zhang, X. Liu, P. Guo, X. Li, Z. He, Z. Li, M.J. Stoddart, S. Grad, W. Tian, D. Chen, Effect of cyclic mechanical loading on immunoinflammatory microenvironment in biofabricating hydroxyapatite scaffold for bone regeneration, Bioactive materials 6(10) (2021) 3097-3108.
[68] Y. Zhang, P. Habibovic, Delivering mechanical stimulation to cells: state of the art in materials and devices design, Advanced Materials (2022) 2110267.
[69] J. Sadoshima, S. Izumo, The cellular and molecular response of cardiac myocytes to mechanical stress, Annual review of physiology 59(1) (1997) 551-571.
[70] A. Aarvold, J.O. Smith, E.R. Tayton, S.A. Lanham, J.B. Chaudhuri, I.G. Turner, R.O. Oreffo, The effect of porosity of a biphasic ceramic scaffold on human skeletal stem cell growth and differentiation in vivo, Journal of Biomedical Materials Research Part A: An Official Journal of The Society for Biomaterials, The Japanese Society for Biomaterials, and The Australian Society for Biomaterials and the Korean Society for Biomaterials 101(12) (2013) 3431-3437.
[71] B.E. Grottkau, Z. Hui, Y. Yao, Y. Pang, Rapid fabrication of anatomically-shaped bone scaffolds using indirect 3D printing and perfusion techniques, International Journal of Molecular Sciences 21(1) (2020) 315.
[72] Y. Liu, G. Zhou, Y. Cao, Recent progress in cartilage tissue engineering—our experience and future directions, Engineering 3(1) (2017) 28-35.
[73] J.T. Shearn, K.R. Kinneberg, N.A. Dyment, M.T. Galloway, K. Kenter, C. Wylie, D.L. Butler, Tendon tissue engineering: progress, challenges, and translation to the clinic, Journal of musculoskeletal & neuronal interactions 11(2) (2011) 163.
[74] B. Nedelec, A. Ghahary, P.G. Scott, E.E. Tredget, Control of wound contraction: basic and clinical features, Hand clinics 16(2) (2000) 289-302.
[75] J. Ribeiro-Silva, A. Miyakawa, J.E. Krieger, Focal adhesion signaling: Vascular smooth muscle cell contractility beyond calcium mechanisms, Clinical Science 135(9) (2021) 1189-1207.
[76] P. Chang, S. Li, Q. Sun, K. Guo, H. Wang, S. Li, L. Zhang, Y. Xie, X. Zheng, Y. Liu, Large full-thickness wounded skin regeneration using 3D-printed elastic scaffold with minimal functional unit of skin, Journal of Tissue Engineering 13 (2022) 20417314211063022.
[77] S.M. Bittner, B.T. Smith, L. Diaz-Gomez, C.D. Hudgins, A.J. Melchiorri, D.W. Scott, J.P. Fisher, A.G. Mikos, Fabrication and mechanical characterization of 3D printed vertical uniform and gradient scaffolds for bone and osteochondral tissue engineering, Acta biomaterialia 90 (2019) 37-48.
[78] A. Di Luca, A. Longoni, G. Criscenti, C. Mota, C. van Blitterswijk, L. Moroni, Toward mimicking the bone structure: design of novel hierarchical scaffolds with a tailored radial porosity gradient, Biofabrication 8(4) (2016) 045007.
[79] O.S. Manoukian, A. Aravamudhan, P. Lee, M.R. Arul, X. Yu, S. Rudraiah, S.G. Kumbar, Spiral layer-by-layer micro-nanostructured scaffolds for bone tissue engineering, ACS biomaterials science & engineering 4(6) (2018) 2181-2192.
[80] J. Wang, C.M. Valmikinathan, W. Liu, C.T. Laurencin, X. Yu, Spiral-structured, nanofibrous, 3D scaffolds for bone tissue engineering, Journal of Biomedical Materials Research Part A: An Official Journal of The Society for Biomaterials, The Japanese Society for Biomaterials, and The Australian Society for Biomaterials and the Korean Society for Biomaterials 93(2) (2010) 753-762.
[81] P. Zhuang, W.L. Ng, J. An, C.K. Chua, L.P. Tan, Layer-by-layer ultraviolet assisted extrusion-based (UAE) bioprinting of hydrogel constructs with high aspect ratio for soft tissue engineering applications, PLoS One 14(6) (2019) e0216776.
[82] X. Liu, Four alternative patterns of the Hilbert curve, Applied mathematics and computation 147(3) (2004) 741-752.
[83] N. Fahy, M. Alini, M.J. Stoddart, Mechanical stimulation of mesenchymal stem cells: Implications for cartilage tissue engineering, Journal of Orthopaedic Research® 36(1) (2018) 52-63.

Supplementary Information

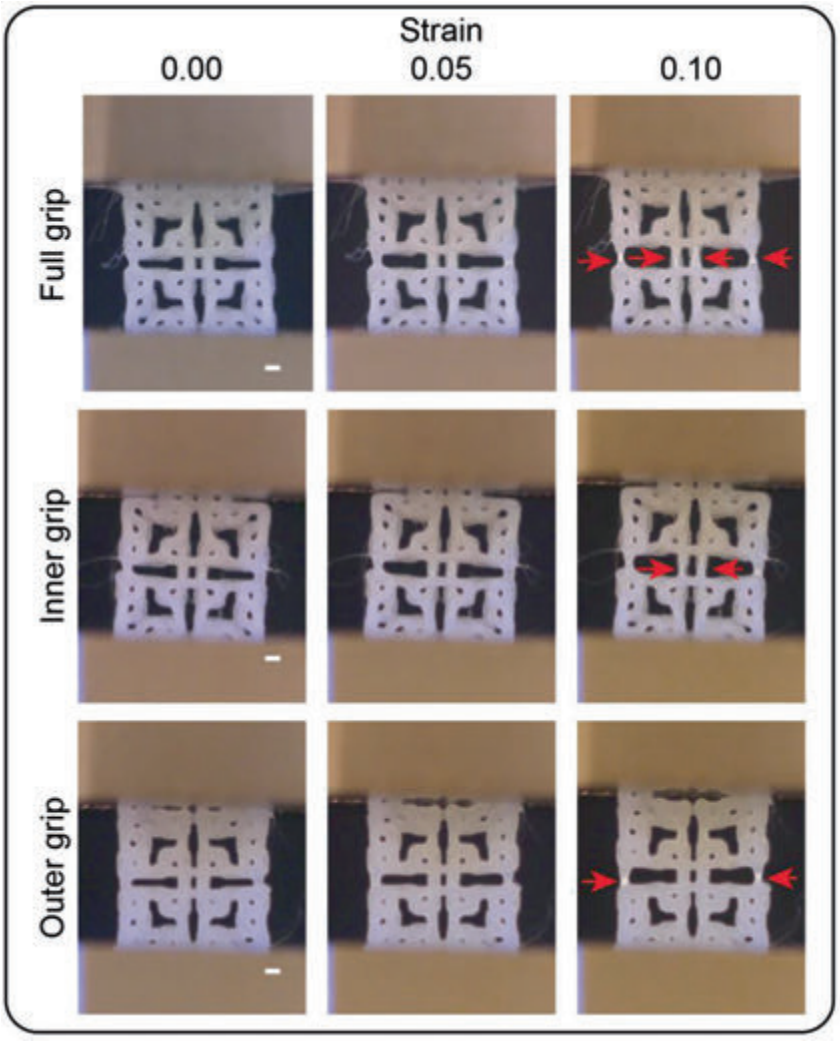

Figure S1. *Time-lapsed snapshots of the tensile test. Scale bar represents 500 μm. Red arrows indicate points of failure.*

Chapter 4

Hypotrochoidal scaffolds for cartilage regeneration

Hypotrochoidal scaffolds for cartilage regeneration*

Kenny A. van Kampen[1], Elena Olaret[2], Izabela-Cristina Stancu[2], Daniela F. Duarte Campos[3], Horst Fischer[4], Carlos Mota[1], Lorenzo Moroni[1]

[1]Department of Complex Tissue Regeneration, MERLN Institute for Technology-Inspired Regenerative Medicine, Maastricht University, Universiteitssingel 40, 6229ER Maastricht, The Netherlands

[2]Advanced Polymer Materials Group, University Politehnica of Bucharest, 1-7 Gh. Polizu Street, 011061, Bucharest, Romania

[3]Bioprinting & Tissue Engineering Group, Center for Molecular Biology Heidelberg (ZMBH), Heidelberg University, Germany

[4]Department of Dental Materials and Biomaterials Research, RWTH Aachen University Hospital, Aachen, Germany

***Chapter published in Materials Today Bio 2023, DOI: 10.1016/j.mtbio.2023.100830**

Abstract

The main function of articular cartilage is to provide a low friction surface and protect the underlying subchondral bone. The extracellular matrix composition of articular cartilage mainly consists of glycosaminoglycans and collagen type II, specifically the collagen type II fibers have an arch-like organization that can be mimicked with segments of a hypotrochoidal curve. In this study, a script was developed that allowed the fabrication of scaffolds with a hypotrochoidal design. This design was investigated and compared to a regular 0-90 woodpile design. The mechanical analyses revealed that the hypotrochoidal design had a lower component Young's modulus while the toughness and strain at yield were higher compared to the woodpile design. Fatigue tests showed that the hypotrochoidal design lost more energy per cycle due to the damping effect of the unique microarchitecture. In addition,

data from cell culture under dynamic stimulation demonstrated that the collagen type II deposition was improved and collagen type X reduced in the hypotrochoidal design. Finally, Alcian blue staining revealed that the areas where the stress was higher during the stimulation produced more glycosaminoglycans. Our results highlight a new and simple scaffold design based on hypotrochoidal curves that could be used for cartilage tissue engineering.

1. Introduction

Articular cartilage is an avascular tissue that is located in the joints.[1] The main function of cartilage is to protect the underlying subchondral bone from compressive loads and to provide a low-friction surface.[2] Injury or damage to cartilage can hamper this function and could lead to osteoarthritis.[3] Unfortunately, articular cartilage has a poor regenerative capacity due to the avascular and scarce cell density nature within the tissue.[4] Chondrocytes are the main cell population in articular cartilage and are responsible for synthesizing the extracellular matrix (ECM).[5] The ECM of articular cartilage mainly consists of collagen type II, aggrecan and other proteoglycans.[6] The organization of the ECM is important in cartilage, specifically the collagen type II fibers have a particular organization which helps to improve the mechanical properties.[7] Cartilage is characterized by three distinct zones; (1) the superficial zone which has collagen fibers oriented parallel to the surface, (2) the intermediate zone where there is no predominant orientation and (3) the deep zone which shows a high orientation with fibers perpendicular to the underlying bone.[8, 9] Each of these zones have a different composition in ECM and cell density,[10] which contributes to the unique properties of articular cartilage.

Hypotrochoidal scaffolds for cartilage regeneration

The organization of the collagen type II fibers could be mathematically described with arches or arch-like structures. A hypotrochoid is one of type of curve that could be used to describe an arch-like structure. This geometric curve that is generated by tracing a point that is linked to a smaller circle, which is rolling inside a larger circle.[11, 12] The hypotrochoidal curve is used to describe in a simplified way the satellite orbits around a planet in a solar system[13] and can be drawn using a tool called Spirograph.[14] The hypotrochoid is characterized by a closed outer surface with the outer shape being round in most cases. Depending on the parameters used, the hypotrochoidal curve can have a dense outer part with lines running parallel to the circle. These parallel lines, in combination with a more porous inner core with lines that run perpendicular to the surface of the circle, make it an interesting geometry that can be used to mimic cartilage ECM architecture. The generated arch-like structure resembles the collagen type II organization, especially if a segment on the top of the curve is taken. In addition, the complex arch-like structure should be able to distribute the forces through the whole scaffold more evenly.[15, 16]

Additive manufacturing (AM) techniques such as fused deposition modeling (FDM) and bioprinting have been widely used to fabricate scaffolds for cartilage regeneration.[17, 18] The main advantage of AM techniques is the possibility to tailor the design and porosity of the scaffold.[19] Many scaffold fabrication approaches focus on matching the mechanical properties of native cartilage with a common strategy of changing geometry or by adding materials to the scaffold.[20, 21] While techniques such as FDM do pose the ability to produce complex shapes, in most cases a woodpile design is used where each layer is a composition of parallel running lines stacked in different angles with each layer.[22] Some efforts have been made to introduce complexity in the design, such as introducing gradients by increasing the spacing between the fibers in each layer[23, 24] or using different periodic infilling patterns.[25] However, none of these studies take a biomimicking approach from both a

morphological and a mechanical point of view in the design of the scaffold. This could both be achieved by using a hypotrochoidal design.

In this study, we propose a new strategy to fabricate additive manufactured scaffolds with a hypotrochoidal pore network architecture. The mechanical properties of several hypotrochoidal designs were compared to a classical 0-90 woodpile structure. To reduce the influence of material properties Polycaprolactone (PCL) as inert biomaterial was chosen to study the effect of the architecture. In addition, a finite element model was used to simulate the stress distribution through the scaffold. Finally, the effect of the hypotrochoidal design on cellular behavior was studied in both static and dynamic culture conditions.

2. Results

2.1 Scaffold fabrication and morphology

The nomenclature and fabrication parameters are shown in figure 1. Briefly, the full hypotrochoid was sectioned by boundaries to mimic the collagen type II alignment. The scaffolds were fabricated through FDM after digital sectioning. The final scaffolds were divided in three distinct zones based on literature, deep (25%), middle (55%) and superficial zone (20%) (supplementary information, Figure S1).[26] For the hypotrochoidal designs, parameters R, d and the boundaries were kept the same while r varied between 0.17 and 0.68. As control a 0-90 design was compared to the hypotrochoidal designs.

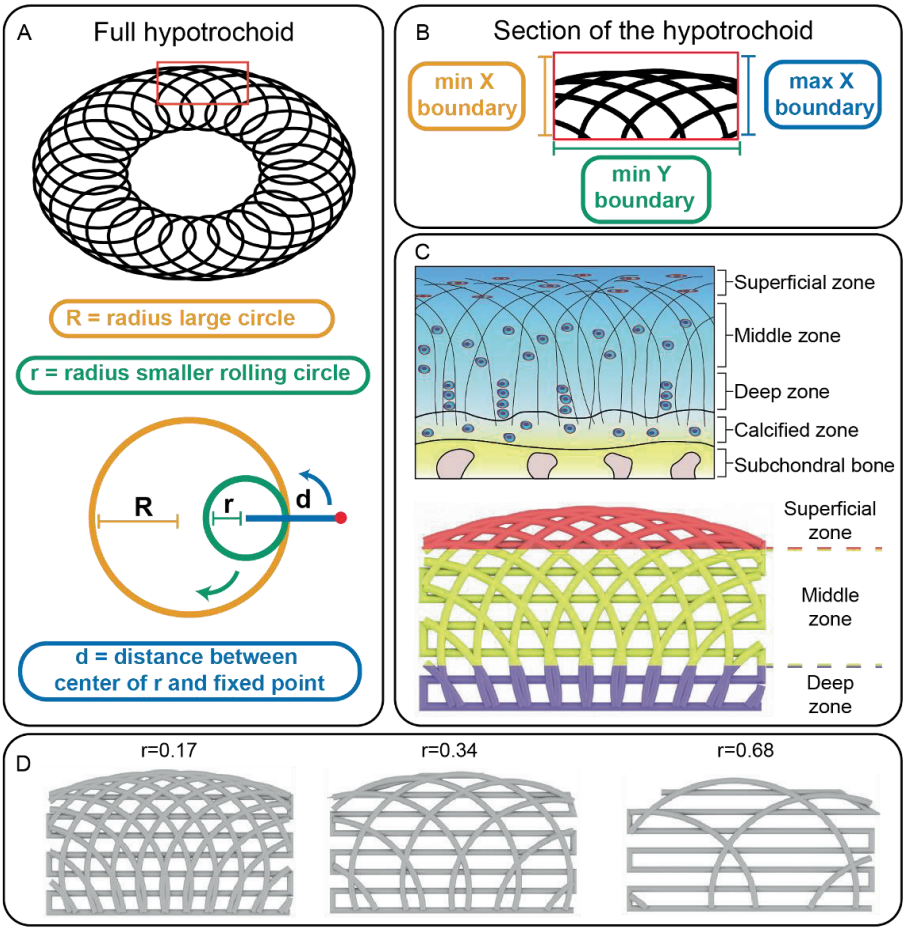

***Figure 1**. Nomenclature of the hypotrochoidal scaffold (A). Section of the hypotrochoidal scaffold (B). Different zones of the hypotrochoidal scaffold representing the different zones in articular cartilage, the fiber diameter in the scaffold is in the micron range while the bundles of collagen fibers is in the sub-micron range (C). Rendered images of the three tested designs with different r values (D).*

As seen from both stereomicroscopy and micro-CT images the hypotrochoidal designs were successfully fabricated (Figure 2). The hypotrochoidal scaffolds had a curved top surface due to the way a hypotrochoid was generated. The meandering layers between the hypotrochoidal layers served as a support during the fabrication process. Signs of fiber collapse were noted in the designs that were more porous, due to the lack of support for the fabricated

Table 1. *Volumetric micro-CT data of the different tested designs. Each condition contained n=3 samples. Values represent average ± standard deviation.*

Sample	Scaffold Volume (mm^3)	Surface area (mm^2)	Surface area/ Volume (1/mm)	Superficial zone radius (mm)
r=0.68	40.0 ± 0.4	636.8 ± 14.5	15.9 ± 0.5	13.32
r=0.34	61.9 ± 3.1	804.7 ± 114.8	16.3 ± 1.3	13.66
r=0.17	65.0 ± 2.4	919.3 ± 79.7	14.2 ± 1.3	13.83
0-90	42.4 ± 1.2	722.0 ± 40.3	17.0 ± 0.5	13.83

fiber that had to span in air multiple millimeters (Figure S2). The pores in all of the tested designs were interconnected. In the hypotrochoidal design, a gradient in pore size was observed with the smallest pores in the superficial zone and the largest pores in the deep zone. The volumetric analyses revealed that the solid scaffold volume of the hypotrochoidal design increased from 40.0 ± 0.4 mm^3 to 65.0 ± 2.4 mm^3 with a lower r value (r=0.68 and r=0.17 respectively) (table 1). A similar observation was made with the available surface area, increasing from 636.8 ± 14.5 mm^2 to 919.3 ± 79.7 mm^2 in the r=0.68 and r=0.17 samples respectively while the surface area to volume ratio remained similar between the hypotrochoidal conditions. The 0-90 structure was similar in volume to the r=0.68 scaffold (42.4 ± 1.2 mm^3 and 40.0 ± 0.4 mm^3 respectively) while having a higher surface area (722.0 ± 40.3 mm^2 and 636.8 ± 14.5 mm^2 respectively). The 0-90 structure, however, showed a higher surface area to volume ratio compared to the hypotrochoidal designs. The curvature of the different designs was shown in table 1 with minimal differences in radius between the scaffolds. The curvature for the 0-90 structure was set equal to the r=0.17 design.

2.2 Mechanical testing and Finite element modeling

The mechanical properties of the hypotrochoidal designs were tested via compression and fatigue tests. CAD models of the scaffolds were also imported in finite element software and a compression test was simulated. The compression tests revealed that the Young's modulus in the 0-90

structure was significantly higher compared to the r=0.17 hypotrochoidal designs (21.0 ± 1.8 MPa and 14.1 ± 1.8 MPa, respectively) (Figure 3A). In addition, the increase in r caused a decrease in Young's modulus from 14.1 ± 1.8 MPa to 1.4 ± 0.1 MPa for r=0.17 and r=0.68 samples respectively. The differences in yield strain between hypotrochoidal designs was small ranging from 7.9 ± 0.0% and 11.0 ± 2.6% strain in the r=0.34 and r=0.68 respectively (figure 3B). The yield strain in the 0-90 design was significantly lower at 4.2 ± 0.4% compared to the hypotrochoidal designs. The yield strength in the

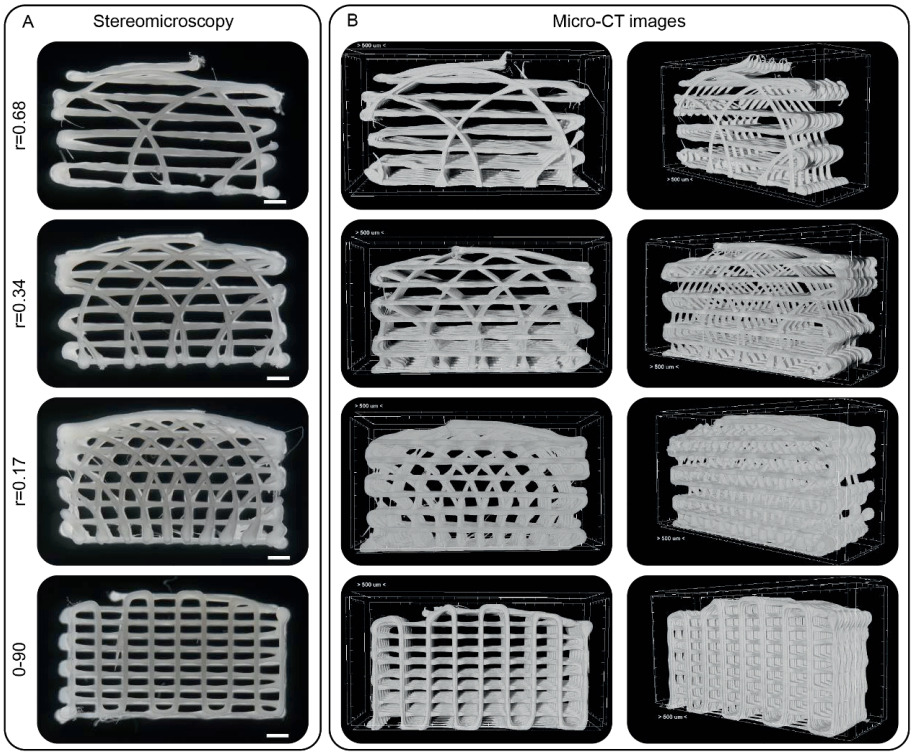

Figure 2. *Overview of the tested designs. (A) Stereomicroscopy images of the frontal view of the tested designs. (B) The micro-CT images of the scaffolds, the frontal view in the left panels and the perspective view in the right panels. Scale bar represents 500 µm.*

hypotrochoidal designs decreased significantly with the increase in r from 36.9 ± 2.2 N to 5.9 ± 2.6 N (Figure 3C). The 0-90 design had a yield strength that was significantly different, between the r=0.17 and r=0.34 design (21.8 ± 3.6 N, 36.9 ± 2.2 N and 10.9 ± 0.6 N respectively). The toughness in the r=0.17 was significantly higher at 0.035 ± 0.001 $N \cdot mm^2$ compared to the other tested design at 0.008 ± 0.002 $N \cdot mm^2$, 0.011 ± 0.001 $N \cdot mm^2$ and 0.006 ± 0.004 $N \cdot mm^2$ for the 0-90, r=0.34 and r=0.68 design respectively (Figure 3D). The stress strain curves showed that the stress in 0-90 structure after the yield point decreased, while in all of the hypotrochoidal designs kept increasing (Figure 3E). Time lapsed snapshots showed that near the yield point 0-90 structure buckled in the middle of the scaffold and the square pore shape became rhomboidal (Figure 3F, supplemental video S1). However, the hypotrochoidal designs did not show this behavior. Instead, the top pores collapsed while the bottom pores remained intact, even far beyond the yield point (Figure S3). This was also confirmed during the compression test and micro-CT analyses where the 0-90 structure buckled in the top half of the scaffold, while the hypotrochoidal designs collapsed inward (Figure S4). Even at 25% strain the bottom part of the hypotrochoidal scaffolds showed interconnected pores (Figure S5).

A finite element model simulated up to 10% strain on the scaffolds with increments of 2% was performed. The model revealed that the vertical fibers in the 0-90 design endured the highest von Mises stress while the horizontal fibers were unaffected (Figure S6). The displacement in the scaffold was evenly distributed from the bottom to the top of the scaffold. The stress distribution in the hypotrochoidal designs was improved compared to the 0-90 design, where the arches distribute the stress throughout the scaffolds and even in the meandering layer there was an increase in von Mises stresses. The highest stress was found in the superficial part of the scaffold (Figure S6).

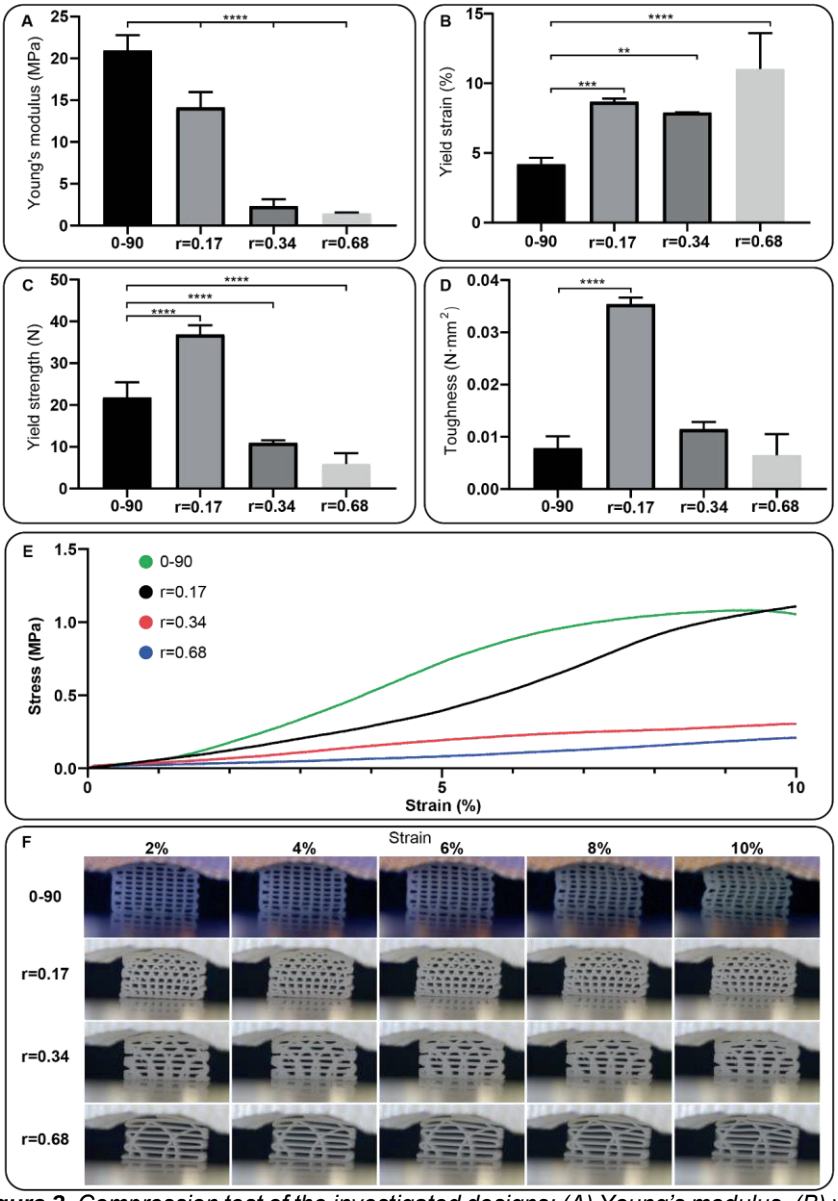

Figure 3. *Compression test of the investigated designs: (A) Young's modulus, (B) yield strain, (C) yield strength, (D) toughness, (E) representative stress strain curve, and (F) time-lapsed snapshots during the compression test. Each condition contained n=5 samples and values represent average ± standard deviation. Statistical significance: * p<0.05, ** p<0.01, *** p<0.005, **** p<0.0001.*

Based on the results from the compression test, a fatigue test of 100 cycles at 1 Hz with a fixed 2.5% strain was performed. The data from the fatigue test showed that the hysteresis loop was the steepest in the 0-90 design compared to the hypotrochoidal designs (Figure 4A). The percentage energy lost per cycle, however, was significantly higher in the r=0.34 and the r=0.68 design compared to r=0.17 and 0-90 design (4.7 ± 0.5%, 6.0 ± 0.5% and 3.8 ± 0.5% respectively) (Figure 4B). The peak force in all of the samples decreased by a small amount in the initial cycles and stabilized after that initial decrease (Figure 6C). The average peak force in the 0-90 structure was the highest stabilizing around 12N while in the r=0.68 it was the lowest at around 2N.

2.3 Dynamic cell culture

Cell culture experiments were performed on the r=0.17 design and the 0-90 woodpile structure to assess the cellular behavior on the hypotrochoidal design. Initially the r=0.34 design was tested, however after 28 days of static culture the scaffolds' pores remained open, resulting in low GAG synthesis (Figure S7), despite cell proliferation and good adhesion (Figure S8). Therefore, r=0.17 design was chosen since the pore size of the r=0.34 and the r=0.68 design were too large and would likely not be closed by sufficient regenerated tissue after the culture period. The fraction of the pore volume based on the micro-CT data in both the 0-90 woodpile structure and the r=0.17 design was similar for each zone (Figure 5A, Table S1). The scaffolds were seeded with ATDC5 cells and some of the scaffolds were transferred to a bioreactor after 7 days. A day 1 DNA quantification was done to asses if the scaffolds contained similar amount of cells. A dynamic culture was performed by applying a mechanical stimulation for 2 hours every day at 1Hz and 2.5% strain until 28 days. The DNA in the samples was normalized against the pore volume. There was no difference found between the amount of DNA found at day 1 between the 0-90 woodpile and r=0.17 design (13.5 ± 1.3 ng and 12.7

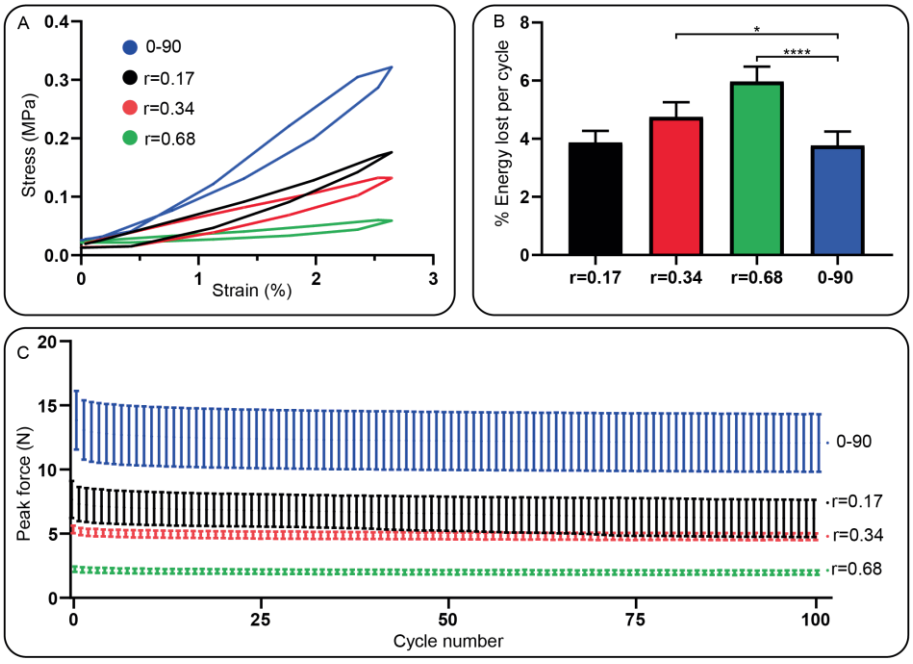

Figure 4. *Fatigue test data with a frequency of 1 Hz until a strain of 2.5%. (A) Hysteresis loop of a single cycle during the fatigue test. (B) Average energy lost per cycle during the fatigue test. (C) Average peak force of each cycle. Each condition contained n=5 samples and values represent average ± standard deviation. Statistical significance: * p<0.05, ** p<0.01, *** p<0.005, **** p<0.0001.*

± 1.2 ng respectively). A division was made based on the fraction of the pore volume found in each zone with the assumption that the cells were equally distributed throughout the scaffold (Figure S9). The dynamic stimulation increased the DNA per pore volume in the r=0.17 samples from 4.6 ± 1.0 μg/mm^3 to 5.9 ± 0.4 μg/mm^3 respectively while there was a slight decrease observed in the 0-90 woodpile design from 6.2 ± 1.3 μg/mm^3 to 5.8 ± 0.8 μg/mm^3 (Figure 5B). Between the tested designs it was noted that the DNA per pore volume was approximately similar. The GAG/DNA per pore volume remained similar in all of the tested conditions (Figure 5C). Dynamic stimulation did increase the collagen/DNA per pore volume in the 0-90 woodpile design (15.6 ± 2.2 ng/μg/mm^3 and 16.7 ± 0.8 ng/μg/mm^3 respectively), while in the r=0.17 design it remained similar. Comparable

values were observed if the values were corrected by the available surface area instead of the pore volume (Figure S10).

Alcian blue staining revealed that there was GAG deposition through the entire scaffold in all of the conditions (Figure 6). More pores in the 0-90 woodpile static condition seemed to be open compared to the dynamically stimulated samples. The intensity of the staining however was stronger in the static samples. The majority of the pores in r=0.17 hypotrochoidal design were open in both the static and dynamic samples, except for the smaller pores that were mainly located in the superficial zone of the scaffold. The r=0.17 dynamically stimulated samples showed darker areas with more GAG deposition that correlated with areas that should have received less stress during the culture located in the deep zone of the scaffold.

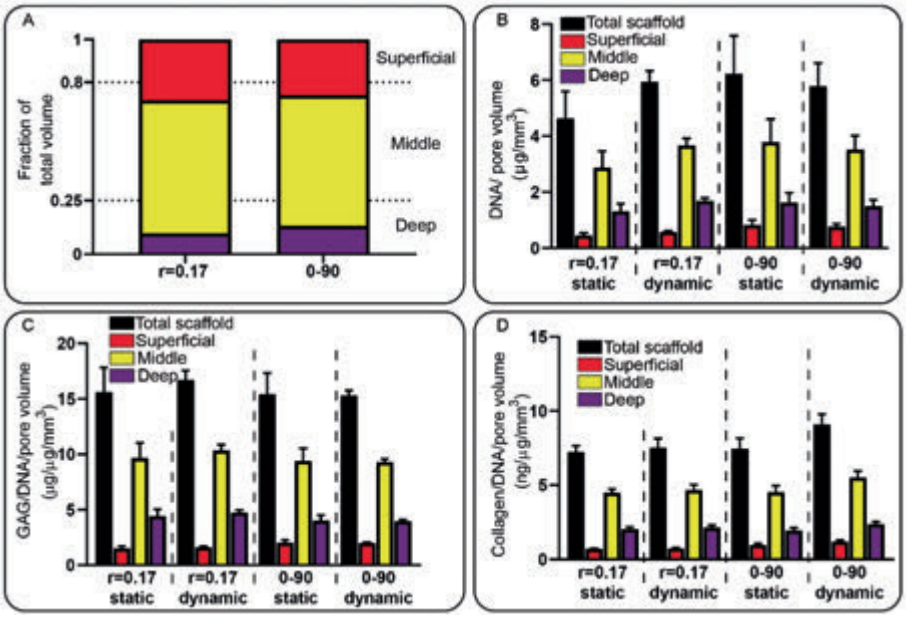

***Figure* 5.** *DNA, GAG and collagen analyses of the tested scaffolds after 28 days of culture. (A) Volumetric analyses of the pore volume as a fraction of the total volume. (B) DNA content normalized against the pore volume. (C) GAG per DNA content normalized against the pore volume. (D) Collagen per DNA content normalized against the pore volume. Each condition contained n=3 samples and values represent average ± standard deviation.*

Fluorescent images from the dynamic culture revealed a reduced collagen type X expression in the hypotrochoidal scaffolds compared to the 0-90 woodpile design (Figure 7). Combining the experimental data with the computational data from the finite element model revealed that in both scaffolds design the areas where there was more von Mises stress the amount of collagen type X expression was higher. Interestingly, in the hypotrochoidal design higher collagen type II expression was observed in the areas where the von Mises stress was increased, whereas there was almost no collagen type II expression in the 0-90 woodpile design. In the static conditions there was no collagen type II expression observed (Figure S11). The expression of collagen type X was comparable throughout the scaffold.

3. Discussion

In this study, a scaffold was created from a hypotrochoidal deposition pattern. The morphology of the hypotrochoidal scaffold resembled that of the collagen fiber architecture in articular cartilage.[8] In addition, micro-CT analyses revealed that the hypotrochoidal scaffold had a fully interconnected pore network, which is necessary to have a proper access to nutrients.[27] The mechanical tests showed that the hypotrochoidal design had a lower Young's modulus while having a significantly higher yield strain and higher toughness. In addition, the finite element model demonstrated that the stress distribution was improved with the hypotrochoidal design compared to the 0-90 woodpile structure. Further mechanical analysis from the fatigue test revealed that the hypotrochoidal design dissipated more energy per compression cycle. Finally, the dynamic culture demonstrated that the hypotrochoidal design had improved collagen type II deposition. Hence, the hypotrochoidal design could potentially be used for cartilage tissue regeneration.

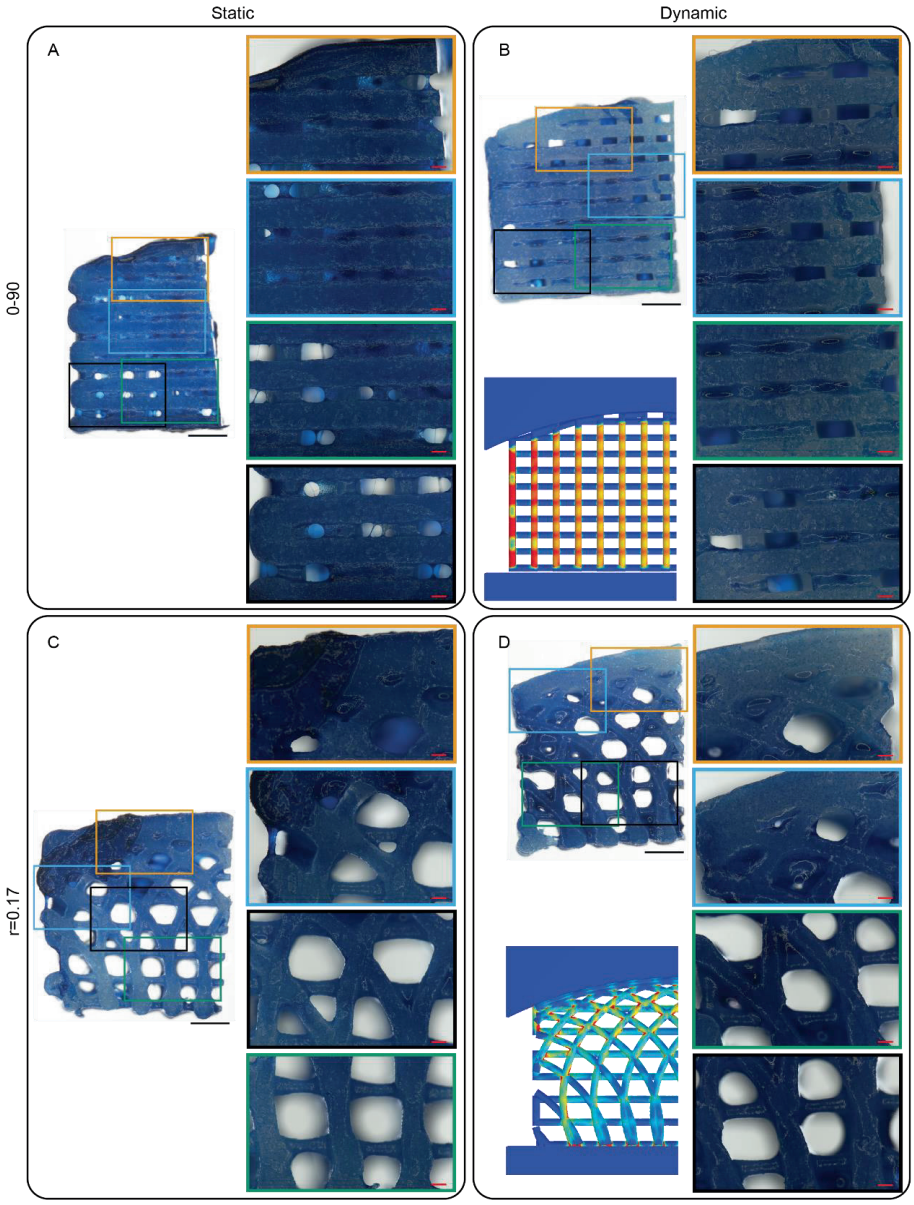

Figure 6. *Alcian blue staining of the tested scaffold after 28 days of culture. The left panels show a stained scaffold and in the right panels a close up of selected areas. A finite element model with the von Mises stress as a reference in the dynamic samples. (A) 0-90 woodpile design after static culture. (B) 0-90 woodpile design after dynamic culture. (C) r=0.17 hypotrochoidal design after static culture. (D) r=0.17 hypotrochoidal design after dynamic culture. Scale bar in the left panels represents 1 mm; in the close up panels 200 µm.*

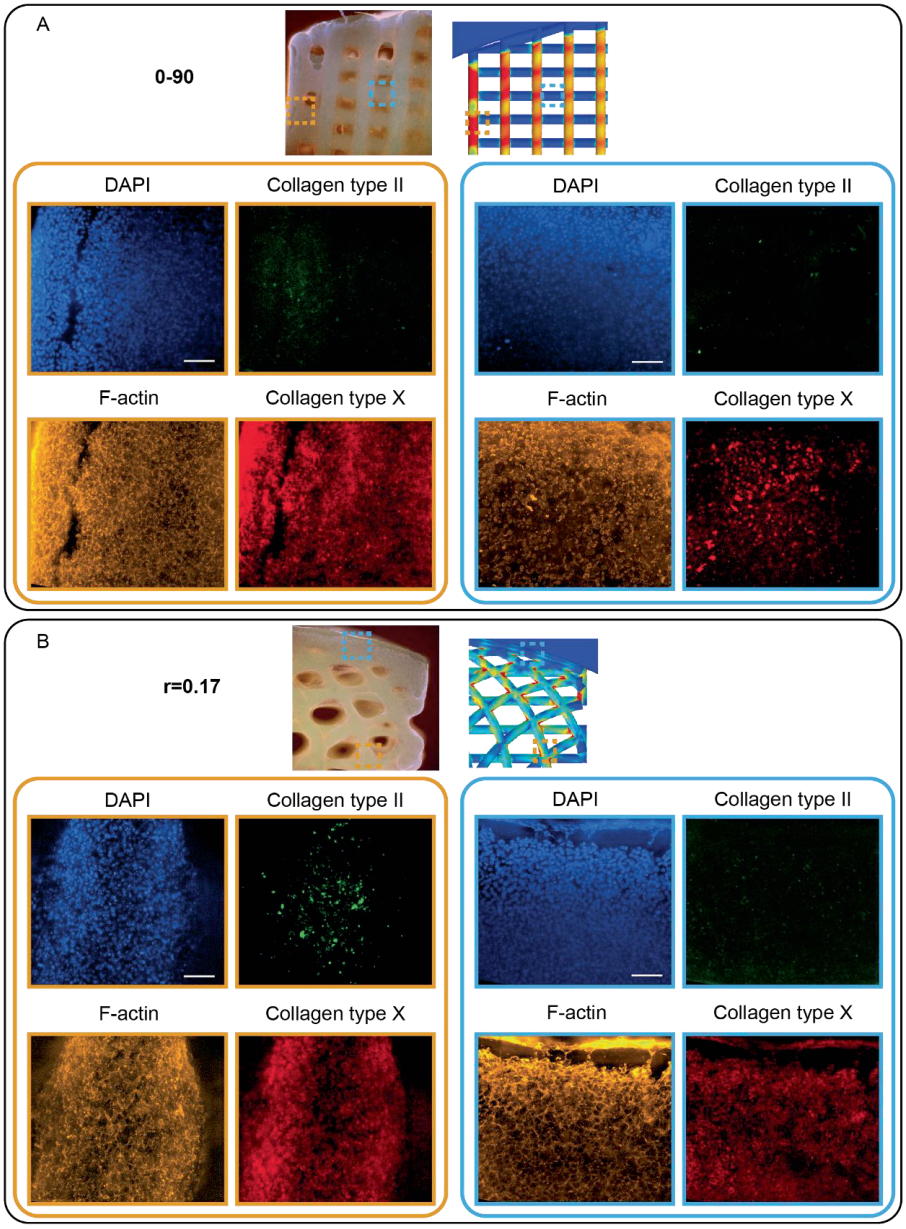

Figure 7. *Cells after 28 days in dynamic culture. On top of the panel an overview image of the scaffold with the finite element model as reference. The left panel set with orange boundaries an area with a high amount of von Mises stress and the right panel set with blue boundaries an area with a low amount of von Mises stress. (A) 0-90 woodpile design. (B) r=0.17 hypotrochoidal design. Scale bars represent 500 µm in the overview panel and 200 µm in the close up.*

The micro-CT analysis revealed that there was a pore gradient in the hypotrochoidal design, where the smallest pores resided in the top part of the scaffold and the largest pores in the bottom. This gradient can be beneficial since the structure of articular cartilage is heterogeneous, resulting in different regions of cartilage having a different range in mechanical properties.[10] Due to how a hypotrochoid is generated, the superficial zone of the scaffold always has a curved surface. The surface of healthy articular cartilage, however, is not perfectly round and is almost flat.[28] A solution to this could be to have R at least a factor 1000 bigger compared to r. This is also evident from equation 3 when R becomes so much larger the radius of the zone increases. This would approximate a flat surface while still creating a hypotrochoidal design. The hypotrochoidal design consists of parameters r, R and d. These parameters have no constrains and therefore give an infinite amount of possible hypotrochoidal designs. A programmed macro-function can offer the possibility to simulate what kind of final hypotrochoidal design is generated with the given parameters. Another option to investigate could be to edit the formula to generate a different hypotrochoidal pattern. An example of this could be to add another sine function within the equation for the Y-coordinate to create a concave surface that could be useful for other type of cartilages, for example similar to the meniscus.[29] The chondrocytes in the superficial zone are responsible for the synthesis of superficial zone protein and hyaluronan that acts as a lubricant.[30] Due to the “circular” design of the hypotrochoid, it creates fibers along the superficial surface, which in turn could decrease the friction when sliding against the other joint. Yet, as the hypotrochoidal curve is a closed curve, the hypotrochoidal design always lead to a non-porous surface. Therefore, adding a single layer of a woodpile structure could be a strategy to introduce some porosity in the surface, which may facilitate the migration of cells to the surface of the scaffold to secrete superficial zone protein. In addition, mechanical stimulation improved hyaluronan synthesis which could further decrease the friction in the

scaffold.[31] As the relatively rough surface of PCL filaments could affect the lubricity of the scaffold.

It was noted that the surface area to volume ratio in the hypotrochoidal design was lower compared to the 0-90 woodpile structure. An explanation for this could be that the fibers in the 0-90 design have the least amount of overlap in fibers due to a fiber angle of 90°, while the fiber angle in the hypotrochoidal design vary with every fiber. Having a lower surface area to volume ratio could interfere with transportation of nutrients and vasculature.[32] However, for cartilage this could be less important since it is avascular and relies on nutrients through diffusion.[33]

The mechanical properties for a tissue such as cartilage are important.[34] The Young's modulus of articular cartilage ranges from 10.6 – 18.6 MPa in the ankle joint to 5,5 – 11.8 MPa in the knee.[35] Specifically the r=0.17 design resulted within this range with an average of 14.1 MPa while the 0-90 woodpile design was slightly above the maximum range with 21 MPa. Even though the 0-90 woodpile structure is stiffer, it can absorb less energy before permanently deforming as was shown by the compression test. The contribution of the arches in the hypotrochoidal design could be the reason why the 0-90 woodpile design is less tough and stiffer. The arch architecture of the hypotrochoidal design can distribute the force through the scaffolds, as was shown in the finite element models. Similar findings from Chen et al. showed that a pillar design caused a higher stress more focused on the pillars compared to an octet design with more curved features.[36] The arch architecture in the hypotrochoidal design also showed that the collapse behavior was different. While the vertical fibers in the 0-90 woodpile structure buckled, the hypotrochoidal scaffold collapsed gradually, with the superficial zone collapsing before the deeper zone. Similar to articular cartilage, after impact the superficial zone is the first zone to receive permanent damage.[37] Besides compressive forces, articular cartilage is also subjected to shear

forces.[38] The hypotrochoidal design could prove beneficial as it is known that arches can distribute the shear forces through the entire structure.[39] Another observation that was made is that the energy lost per cycle in the fatigue test was higher in the r=0.34 and r=0.68 hypotrochoidal design compared to the 0-90 woodpile structure, indicating that having less arches in the scaffold resulted in a higher energy loss. It is reported that articular cartilage behaves as an elastic material during hysteresis, with a relative energy loss of 28%.[40] The same study also found that a higher energy loss is also linked to cartilage damage. All the tested designs were below 10% energy loss, which is well below the relative energy loss in articular cartilage. This value can change however, depending on the magnitude of the strain applied.[41, 42] A 2.5% strain for the dynamic culture was chosen based on the yield strain the 0-90 woodpile design had. The physiological relevant strain for articular cartilage in humans is 10% or more [43], which is what could be achieved with the r=0.68 design. Other options to improve this could involve changing the material or further exploring other hypotrochoidal designs.

GAG content is important for cartilage as it retains the water in the cartilage that can act as a lubricant.[44, 45] Our results showed that the GAG content per DNA remained similar in all of the conditions. It is important to note that the GAG content from the biochemical assay is performed on the entire scaffold, averaging the results from all the zones. This is rather a technical limitation of extracting the tissue on such a small scale without accidently removing parts of or adding unwanted parts of interest. The division of the zones was based on the micro-CT analyses with the assumption that the cells were distributed equally through the scaffolds. However, it could be that local areas that experienced more stress can contain higher amounts of GAG. This was demonstrated by histological analysis where certain areas were darker for Alcian Blue staining, thus possibly containing more GAGs. Specifically in the deeper zone of the hypotrochoidal scaffold, the intensity of the Alcian blue staining was higher. This correlates with a native hyaline cartilage tissue

where GAG content is higher in the deeper zone compared to the middle and superficial zone,[10, 46] Possibly due to GAG content being linked to improved mechanical properties and its deposition increased during mechanical loading.[47] Similar observations could be made for collagen content quantification, as also the collagen content is different for each zone with the highest amount of collagen found in the superficial surface.[5] The total collagen content was increased with the dynamic stimulation in the 0-90 woodpile structure. While the dynamic stimulation had no effect on the hypotrochoidal design. Examining immunostaining, however, revealed that the collagen that was deposited in the 0-90 woodpile design was collagen type X, which is a known hypertrophic marker.[48] ATDC5 cells are known to be hypertrophic and deposit collagen type X.[49] A study by Shukunami et al. shows that collagen type X deposition starts after 21 days in 2D.[50] In this study, the collagen type X deposition was primarily deposited in the areas where the von Mises stress was the highest according to the finite element model. The fibers within the samples that were unstimulated had a lower collagen type X deposition. Another method to decrease the amount of collagen type X is to use inhibitors such as parathyroid hormone [51] or using other polymers that showed to reduce hypertrophic differentiation [52, 53], the latter could also enhance collagen type II production. Finally, cells that are not intrinsically hypertrophic, such as human mesenchymal stem cells (hMSCs), could serve as an alternative to reduce collagen type X[54], providing also a better route towards clinical applications. Interestingly, collagen type II expression was increased in the hypotrochoidal design, specifically in the areas where the von Mises stress were high. The von Mises stress in the hypotrochoidal design were not as high as in the 0-90 structure indicating that collagen type II deposition can be enhanced by modulating the von Mises stress. Another method to increase collagen type II deposition for this study is to extend the dynamic stimulation until 4 weeks, as was shown with primary chondrocytes.[55] Culturing the scaffolds under a lower oxygen concentration in combination with the dynamic stimulation could be an additional step that

might be considered in future studies, since a lower oxygen concentration is known to improve collagen type II expression.[56, 57] An alternative would be to change the cell type that is known to produce more collagen type II such as primary chondrocytes or mesenchymal stem cells. [58] Finally, design the not limited to a certain material. Other less inert materials could be explored following this design.

Generally, bundles of collagen fibers have a diameter ranging from 0.7 to 5 µm.[59, 60] The diameter of the fibers produced in this study are two orders of magnitude bigger. Therefore, mimicking the collagen fiber arrangement could prove challenging with a technique such as FDM. However, the hypotrochoidal design could serve as a blueprint for collagen fiber deposition as collagen is synthesized intra-cellular and assembled extracellular into fibrils by chondrocytes.[61] The cells that attach to the fibers of the scaffold could start secreting pro-collagen and assemble it into collagen fibrils following the hypotrochoidal pattern. An alternative is to embed chondrocytes in a hydrogel within the hypotrochoidal design. This better represents the natural environment of chondrocytes.[62] Other techniques such as single cell acoustic patterning already allow cells to be arranged in a way that mimics the deep zone of cartilage.[63] The combination of cell patterning and having a template for the cells to follow could be worth exploring. The manufacturing of hypotrochoidal design scaffolds is not limited to FDM systems. Since the equations to generate X and Y coordinates are known, any system that uses an XY gantry could fabricate hypotrochoidal designs. Some alternative methods to produce these scaffolds might be with bioprinting or melt electrowriting systems (Figure S12). Specifically with melt electrowriting smaller fiber diameter can be obtained reaching the diameter of the collagen fiber bundles.[64] The hypotrochoidal design could potentially be used for other tissues where a gradient occurs such as long bones,[65] due to the empty inner circle in the hypotrochoid that resembles the medullary cavity and the dense outer structure resembling the compact bone (Figure S12).[66] Our

findings indicate that the hypotrochoidal design outperformed the 0-90 woodpile design both mechanically and biologically. However, it would be interesting to determine in future studies if this effect endures in vivo.

4. Conclusion

Here, we showcased a hypotrochoidal design for cartilage tissue engineering. Such scaffolds mimic the morphological architecture of collagen fibers in articular cartilage, despite being still an order of magnitude larger than native collagen. It was shown that the hypotrochoidal design had an improved toughness compared to a 0-90 woodpile design. In addition, the stress distribution in the hypotrochoidal was improved due to the arched architecture that was introduced. The dynamic culture showed that the collagen deposition was improved and the hypotrochoidal design showed synthesis of collagen type II deposition in the specific areas of the scaffolds with a higher amount of stress.

5. Materials and methods

5.1 Scaffold fabrication

Poly(ε-caprolactone) (PCL) (M_n 45.000, Sigma-Aldrich,USA) was used to fabricated scaffolds via FDM using a Bioscaffolder (SysENG, Germany). Briefly, pellets of PCL were placed in a stainless steel syringe and heated up to 110 °C. A pressure of 4 bar was used to force the molten polymer to the extrusion screw, which was set at a constant rotational speed of 45 rpm. A 25G nozzle (260 µm internal diameter) was used for extrusion. The layer thickness and speed was kept constant at 180 µm and 400 mm/min, respectively.

A custom written python script (Python Software Foundation, Version 3.7.0) was developed to generate the deposition pattern for extrusion. Using a hypotrochoidal function both X and Y coordinates were calculated (Equation

1 and Equation 2 respectively). R = the radius of the large circle, r = the radius of the rolling circle and d = the distance between the center of the rolling circle and the point which is traced. Afterwards, cut off values were set to mark the boundaries of the scaffold. The hypotrochoidal scaffold followed the equation R = 10 and d = 4 with cutoff values between -5 and 5 in the X and bigger than 8 in the Y direction. As a variable parameter for the mechanical characterization, r was changed between 0.17 and 0.68. After each hypotrochoidal layer, two meandering layers that matched the outline of the scaffold were deposited with a fixed strand distance of 800 µm. The radius of this surface can be calculated with R = the radius of the large circle, r = the radius of the rolling circle and d = the distance between the center of the rolling circle and the point which is traced (Equation 3). As control, the hypotrochoidal layer was replaced with a meandering woodpile layer of similar tool pathway length but with a 90° rotation between layers (0-90). The final scaffolds were 10 mm wide, 3 mm deep and 6 mm high at the top of the superficial zone.

Equation 1 $\mathrm{X}(\theta) = (R - r)\cos\theta + \mathrm{d}\cos\left(\frac{R-r}{r}\theta\right)$

Equation 2 $\mathrm{Y}(\theta) = (R - r)\sin\theta + \mathrm{d}\sin\left(\frac{R-r}{r}\theta\right)$

Equation 3 $\text{Superficial zone radius} = (\mathrm{R} - r) + \mathrm{d}$

5.2 Scaffold characterization

Scaffold geometry and architecture was characterized by Stereomicroscopy (SMZ25, Nikon instruments) with a dark field illuminator (Nikon instruments). MicroCT was used to qualitatively and quantitatively investigate the 3D structure, volume and available surface area. The obtained micrographs were reconstructed using Nrecon software (Version 1.7.1.6., Bruker MicroCT). The scanning parameters were set as follows: 2452x1640 camera resolution, 6.5 µm pixel size, source voltage and current of 50 kV and 130 µA respectively, 0.2 degree rotation step and 4 averaged frames. Pore shape was visualised using Ctvox (Version 3.3.0r1403, Bruker MicroCT) software and the quantitative data was analysed through Ctan software (1.18.4.0+, Bruker

MicroCT). The scaffold was divided in three different sections based on the three zones found in articular cartilage,[26] the deep, middle and superficial zone set at 25%, 55% and 20% of the scaffold, respectively. The fraction of the pore volume in each zone was derived from Equation 4.

Equation 4 $Pore\ volume\ fraction = \left(1 - \frac{V_{Solid(zone)}}{V_{total}}\right) * 100\%$

Where $V_{solid(zone)}$ from each zone was obtained from the micro-CT analysis. V_{total} was calculated based on an equivalent solid block that was generated with computer-assisted design (CAD) (Rhino 6, Robert McNeel Associates, Version 6.19) with the dimension of the full scaffold. Moreover, for samples 0-90 and 0-17 the total volume of pore space (for the superficial, middle, and deep zone) was obtained by the manual selection of the region of interest (ROI) using CTAn software (version 1.18.4.0+, Bruker, Kontich, Belgium). However, these results should be carefully considered since the manual selection might include errors.

5.3 Mechanical characterization

A custom designed adapter made of aluminum was used with a matching curvature of the scaffolds to maintain full contact area of the surface during mechanical testing (ElectroForce 3230, TA instruments, USA). Compression tests were performed using a 45 N load cell (ElectroForce) and the compression rate was set at 1% strain/s with a limit to 30%. A camera (DMC-G3, Panasonic) with macro lens (Panagor 90mm f2.8, Komine) was used for video acquisition during the compression test to observe the deformation. The Young's Modulus was calculated from the linear part of the stress strain curves. A pre-load of 1 Newton was applied before the mechanical test was initiated. The yield strain and strength were determined from the yield point that was set at the intersection between the stress-strain curve and the linear line drawn from the Young's modulus with a 0.2% offset. The toughness of the scaffold was calculated as the area under the stress/strain curve up until the

yield point. The maximum strain for the fatigue test was set at 2.5% based on the data obtained from the compression test. During that test 100 cycles were performed with a frequency of 1Hz. A single cycle of the hysteresis curve was plotted and the amount of energy lost per cycle was calculated as the difference in area under the curve between the loading and unloading part of the hysteresis. This was normalized against the total amount of energy to correct for differences between the scaffold designs.

5.4 Finite element modeling

A custom written script in Rhino grasshopper was used to convert the G-code of the hypotrochoidal design from the printer into a 3D CAD model. The CAD files of the tested designs were imported in finite element modeling software (COMSOL Multiphysics, COMSOL B.V. Version 6.0). The model was fixed at the bottom part and a concave fixture was made in the software to match the curvature of the scaffold. The radius of this curvature was based on equation 3. The contacts between the scaffolds and the fixture were fixated and a boundary condition was set to constrain the scaffold from falling forward during the simulation. A strain of 10% was simulated in steps of 2% and the Von Mises stress along with the displacement were plotted.

5.5 Cell culture

ATDC5 (RIKEN cell bank), a teratocarcinoma derived chondrogenic cell line, was used to test the effect of the hypotrochoidal design on cells. Cells were trypsinized before reaching 80% confluence and 75.000 cells were seeded per scaffold. The cells were brought to a concentration of 2,500,000 cells / ml and a 30 µl cell suspension was dropped on the side of the scaffold. After 2 hours the scaffold was flipped and after a total of 4 hours of attachment, the scaffolds were transferred into Dulbecco's Modified Eagle Medium: nutrient mixture F-12 (DMEM-F12) (Sigma-Aldrich) expansion media supplemented with 5% fetal bovine serum (FBS) (Sigma-Aldrich) and 1% Penicillin Streptomycin (Thermo Fisher Scientific). After 1 day, the media was switched

to differentiation media, which consisted of DMEM-F12 supplemented with 5% FBS, 1% Insuline, Transferin, sodium and Selenite (ITS) (Thermo Fisher Scientific), and 1% Penicillin Streptomycin. After 7 days, some of the scaffolds were transferred to a custom made bioreactor for dynamic stimulation. The bioreactor was powered by a DC-motor that was powered externally by a power supply. The DC-motor rotated a camshaft with a wedge shape cam at the end. The cam pushed a block that compresses the scaffold. The strain applied on the scaffold was determined by the shape of the cam. The stimulation was performed for 2 hours per day at 1Hz and 2.5% strain. The scaffolds were kept for a total of 28 days with media changes every other day.

5.6 Microscopy and cell analysis

Scaffolds were harvested after 28 days and used to analyze DNA, glycosaminoglycans (GAG) and collagen content or fixated for histological evaluation. A plate reader (CLARIOstar, BMG labtech) was used to quantify the biochemical assays. Scaffolds that were used for quantification were freeze/thawed 3 times before being submerged in 1 mg/ml proteinase K Tris/EDTA buffer solution. Samples were freeze/thawed again for three times after an overnight incubation at 56 °C in proteinase K solution. A part of the lysate solution was used to analyze DNA content through a DNA analysis kit (CyQUANT™ Cell Proliferation Assay Kit, Thermo Fischer Scientific) according to the manufacturer's protocol. The samples were excited at 480 nm and emission was measured at 520 nm. The amount of DNA present in the sample was calculated from a known bacteriophage λ DNA standard. Another part of the solution was used to perform a GAG assay with 1,9-dimethylmethylene blue (DMMB) (Sigma-Aldrich) dye. The absorbance was measured both at 525 nm and 595 nm. The amount of GAGs in the sample was calculated by the difference in absorbance from both wavelengths and compared to a known chondroitin sulfate standard. The final part portion of the lysate was used to quantify the collagen content according to a hydroxyproline assay (Sigma-Aldrich). The absorbance was measured at 570

nm and the collagen content in the sample was determined from a hydroxyproline standard.

The scaffolds used for microscopy were fixed with 4% Paraformaldehyde (PFA) (VWR) for 1 hour and subsequently placed in PBS until further processing. Cells were stained with 1/250 dilution (0.23 µg/ml) DAPI (Sigma-Aldrich), 1/200 (0.5 µM) Phalloidin (Thermo Fisher Scientific), 1/400 dilution Collagen type II (Anti-Collagen type II, ab34712, Abcam) and 1/200 dilution Collagen type X (Anti-Collagen type X, ab49945, Abcam). The scaffolds were stained with an Alcian blue staining (Sigma-Aldrich) with a Nuclear red counterstaining (Sigma-Aldrich) to check the presence of GAGs. Fluorescent images were taken (Nikon Eclipse Ti-e) and the bright field images were acquired with the stereomicroscope (SMZ25, Nikon instruments).

5.7 Statistics

Statistical analyses were performed with GraphPad Prism 8.1.2. Significant differences were tested using an ANOVA test with a Dunnett multiple comparisons test and a student's t-test to compare among two groups. The tests were considered significant when $p<0.05$.

Acknowledgements

This work was supported by H2020 FAST (NMP-7, GA n. 685825), the ERC Cell Hybridge (GA n. 637308). The microCT analyses was supported by the European Regional Development Fund (6695072), through Competitiveness Operational Program 2014-2020, Priority axis 1, ID P_36_611, MySMIS code 107066, INOVABIOMED, Romania. IC Stancu and E Olaret acknowledge the project Integrating mechanically-tunable 3D printing with new bioactive multi(nano)materials for next functional personalized bone regenerative scaffolds, PN-III-P4-PCE-2021-1240, no. PCE 88/2022. We also gratefully acknowledge Dr. J. Fernández-Pérez for the supervision during the hydroxyproline assay, A. Chandrakar for the melt electro written scaffold, Dr. M. Decarli for the bioprinting of the hypotrochoidal scaffold.

References

[1] J. Buckwalter, H. Mankin, Articular cartilage: part I, Journal of Bone and joint surgery 79(4) (1997) 600.
[2] A.J. Sophia Fox, A. Bedi, S.A. Rodeo, The basic science of articular cartilage: structure, composition, and function, Sports health 1(6) (2009) 461-468.
[3] L. Sharma, Osteoarthritis of the knee, New England Journal of Medicine 384(1) (2021) 51-59.
[4] D.J. Huey, J.C. Hu, K.A. Athanasiou, Unlike bone, cartilage regeneration remains elusive, Science 338(6109) (2012) 917-921.
[5] H. Muir, P. Bullough, A. Maroudas, The distribution of collagen in human articular cartilage with some of its physiological implications, The Journal of bone and joint surgery. British volume 52(3) (1970) 554-563.
[6] M. Ulrich-Vinther, M.D. Maloney, E.M. Schwarz, R. Rosier, R.J. O'Keefe, Articular cartilage biology, JAAOS-Journal of the American Academy of Orthopaedic Surgeons 11(6) (2003) 421-430.
[7] F. Guilak, D.L. Butler, S.A. Goldstein, Functional tissue engineering: the role of biomechanics in articular cartilage repair, Clinical Orthopaedics and Related Research® 391 (2001) S295-S305.
[8] R.M. Aspden, D.W. Hukins, Collagen organization in articular cartilage, determined by X-ray diffraction, and its relationship to tissue function, Proceedings of the Royal Society of London. Series B, Biological sciences 212(1188) (1981) 299-304.
[9] R. Minns, F. Steven, The collagen fibril organization in human articular cartilage, Journal of anatomy 123(Pt 2) (1977) 437.
[10] T. Klein, B. Schumacher, T. Schmidt, K. Li, M. Voegtline, K. Masuda, E.-M. Thonar, R. Sah, Tissue engineering of stratified articular cartilage from chondrocyte subpopulations, Osteoarthritis and cartilage 11(8) (2003) 595-602.
[11] J.D. Lawrence, A catalog of special plane curves, Courier Corporation2013.
[12] M. Bouthillier, Representations of Epitrochoids and Hypotrochoids, (2018).
[13] K. Nakanishi, H. Kojima, T. Watanabe, Trajectories of in-plane periodic solutions of tethered satellite system projected on van der Pol planes, Acta Astronautica 68(7-8) (2011) 1024-1030.
[14] C. Goldstein, J. Gray, J. Ritter, L'Europe mathématique/Mathematical Europe: Histoires, mythes, identités, Les Editions de la MSH1996.
[15] B. Glisic, New in Old: Simplified Equations for Linear-elastic Symmetric Arches and Insights on Their Behavior, Journal of the International Association for Shell and Spatial Structures 61(3) (2020) 227-240.
[16] C. Zhao, Y. Liu, P. Wang, M. Jiang, J. Zhou, X. Kong, Y. Chen, F. Jin, Wrapping and anchoring effects on CFRP strengthened reinforced concrete arches subjected to blast loads, Structural Concrete 22(4) (2021) 1913-1926.
[17] H.-J. Yen, C.-S. Tseng, S.-h. Hsu, C.-L. Tsai, Evaluation of chondrocyte growth in the highly porous scaffolds made by fused deposition manufacturing (FDM) filled with type II collagen, Biomedical microdevices 11(3) (2009) 615-624.
[18] M.E. Hoque, Y.L. Chuan, I. Pashby, Extrusion based rapid prototyping technique: an advanced platform for tissue engineering scaffold fabrication, Biopolymers 97(2) (2012) 83-93.
[19] L. Moroni, J.R. de Wijn, C.A. van Blitterswijk, 3D fiber-deposited scaffolds for tissue engineering: Influence of pores geometry and architecture on dynamic mechanical properties, Biomaterials 27(7) (2006) 974-985.
[20] K.-C. Hung, C.-S. Tseng, L.-G. Dai, S.-h. Hsu, Water-based polyurethane 3D printed scaffolds with controlled release function for customized cartilage tissue engineering, Biomaterials 83 (2016) 156-168.
[21] M.A. Shamekhi, H. Mirzadeh, H. Mahdavi, A. Rabiee, D. Mohebbi-Kalhori, M.B. Eslaminejad, Graphene oxide containing chitosan scaffolds for cartilage tissue engineering, International journal of biological macromolecules 127 (2019) 396-405.
[22] W. Kosorn, M. Sakulsumbat, P. Uppanan, P. Kaewkong, S. Chantaweroad, J. Jitsaard, K. Sitthiseripratip, W. Janvikul, PCL/PHBV blended three dimensional scaffolds fabricated by fused deposition modeling and responses of chondrocytes to the scaffolds, Journal of Biomedical Materials Research Part B: Applied Biomaterials 105(5) (2017) 1141-1150.
[23] S.M. Bittner, B.T. Smith, L. Diaz-Gomez, C.D. Hudgins, A.J. Melchiorri, D.W. Scott, J.P. Fisher, A.G. Mikos, Fabrication and mechanical characterization of 3D printed vertical uniform

and gradient scaffolds for bone and osteochondral tissue engineering, Acta biomaterialia 90 (2019) 37-48.
[24] A. Di Luca, I. Lorenzo-Moldero, C. Mota, A. Lepedda, D. Auhl, C. Van Blitterswijk, L. Moroni, Tuning Cell Differentiation into a 3D Scaffold Presenting a Pore Shape Gradient for Osteochondral Regeneration, Advanced healthcare materials 5(14) (2016) 1753-63.
[25] J. Baena, G. Jiménez, E. López-Ruiz, C. Antich, C. Griñán-Lisón, M. Perán, P. Gálvez-Martín, J. Marchal, Volume-by-volume bioprinting of chondrocytes-alginate bioinks in high temperature thermoplastic scaffolds for cartilage regeneration, Experimental Biology and Medicine 244(1) (2019) 13-21.
[26] M. Uhl, C. Ihling, K. Allmann, J. Laubenberger, U. Tauer, C. Adler, M. Langer, Human articular cartilage: in vitro correlation of MRI and histologic findings, European radiology 8(7) (1998) 1123-1129.
[27] Q.L. Loh, C. Choong, Three-dimensional scaffolds for tissue engineering applications: role of porosity and pore size, Tissue Engineering Part B: Reviews 19(6) (2013) 485-502.
[28] R. Sayles, T. Thomas, J. Anderson, I. Haslock, A. Unsworth, Measurement of the surface microgeometry of articular cartilage, Journal of Biomechanics 12(4) (1979) 257-267.
[29] P. Łuczkiewicz, K. Daszkiewicz, W. Witkowski, J. Chróścielewski, W. Zarzycki, Influence of meniscus shape in the cross sectional plane on the knee contact mechanics, Journal of biomechanics 48(8) (2015) 1356-1363.
[30] S.M. McNary, K.A. Athanasiou, A.H. Reddi, Transforming growth factor β-induced superficial zone protein accumulation in the surface zone of articular cartilage is dependent on the cytoskeleton, Tissue Engineering Part A 20(5-6) (2014) 921-929.
[31] G. Dowthwaite, A. Ward, J. Flannely, R. Suswillo, C. Flannery, C. Archer, A. Pitsillides, The effect of mechanical strain on hyaluronan metabolism in embryonic fibrocartilage cells, Matrix Biology 18(6) (1999) 523-532.
[32] S. Mohanty, L.B. Larsen, J. Trifol, P. Szabo, H.V.R. Burri, C. Canali, M. Dufva, J. Emnéus, A. Wolff, Fabrication of scalable and structured tissue engineering scaffolds using water dissolvable sacrificial 3D printed moulds, Materials science and engineering: C 55 (2015) 569-578.
[33] S. Roberts, J.P. Urban, H. Evans, S.M. Eisenstein, Transport properties of the human cartilage endplate in relation to its composition and calcification, Spine 21(4) (1996) 415-420.
[34] C.J. Little, N.K. Bawolin, X. Chen, Mechanical properties of natural cartilage and tissue-engineered constructs, Tissue Engineering Part B: Reviews 17(4) (2011) 213-227.
[35] D.E. Shepherd, B.B. Seedhom, The 'instantaneous' compressive modulus of human articular cartilage in joints of the lower limb, Rheumatology (Oxford, England) 38(2) (1999) 124-32.
[36] H. Chen, Y. Liu, C. Wang, A. Zhang, B. Chen, Q. Han, J. Wang, Design and properties of biomimetic irregular scaffolds for bone tissue engineering, Computers in Biology and Medicine 130 (2021) 104241.
[37] J.E. Jeffrey, D.W. Gregory, R.M. Aspden, Matrix damage and chondrocyte viability following a single impact load on articular-cartilage, Archives of biochemistry and biophysics 322(1) (1995) 87-96.
[38] L.T. Brody, Knee osteoarthritis: clinical connections to articular cartilage structure and function, Physical Therapy in Sport 16(4) (2015) 301-316.
[39] F. Tahmasebinia, Y. Ma, K. Joshua, S.M.E. Sepasgozar, Y. Yu, J. Li, S. Sepasgozar, F.A. Marroquin, Sustainable architecture creating arches using a bamboo grid shell structure: Numerical analysis and design, Sustainability 13(5) (2021) 2598.
[40] F. Malekipour, C. Whitton, D. Oetomo, P.V.S. Lee, Shock absorbing ability of articular cartilage and subchondral bone under impact compression, Journal of the mechanical behavior of biomedical materials 26 (2013) 127-135.
[41] B.M. Lawless, H. Sadeghi, D.K. Temple, H. Dhaliwal, D.M. Espino, D.W. Hukins, Viscoelasticity of articular cartilage: Analysing the effect of induced stress and the restraint of bone in a dynamic environment, Journal of the Mechanical Behavior of Biomedical Materials 75 (2017) 293-301.
[42] A. Weizel, T. Distler, D. Schneidereit, O. Friedrich, L. Bräuer, F. Paulsen, R. Detsch, A. Boccaccini, S. Budday, H. Seitz, Complex mechanical behavior of human articular cartilage and hydrogels for cartilage repair, Acta Biomaterialia 118 (2020) 113-128.

[43] D.D. Chan, L. Cai, K.D. Butz, S.B. Trippel, E.A. Nauman, C.P. Neu, In vivo articular cartilage deformation: noninvasive quantification of intratissue strain during joint contact in the human knee, Scientific reports 6(1) (2016) 19220.
[44] A. Sharma, L.D. Wood, J.B. Richardson, S. Roberts, N.J. Kuiper, Glycosaminoglycan profiles of repair tissue formed following autologous chondrocyte implantation differ from control cartilage, Arthritis Research & Therapy 9(4) (2007) R79.
[45] T.E. Hardingham, A.J. Fosang, Proteoglycans: many forms and many functions, The FASEB journal 6(3) (1992) 861-870.
[46] P. Bansal, N.S. Joshi, V. Entezari, M. Grinstaff, B.D. Snyder, Contrast enhanced computed tomography can predict the glycosaminoglycan content and biomechanical properties of articular cartilage, Osteoarthritis and cartilage 18(2) (2010) 184-191.
[47] S. Treppo, H. Koepp, E.C. Quan, A.A. Cole, K.E. Kuettner, A.J. Grodzinsky, Comparison of biomechanical and biochemical properties of cartilage from human knee and ankle pairs, Journal of Orthopaedic Research 18(5) (2000) 739-748.
[48] G. Shen, The role of type X collagen in facilitating and regulating endochondral ossification of articular cartilage, Orthodontics & craniofacial research 8(1) (2005) 11-17.
[49] H. Akiyama, C. Shukunami, T. Nakamura, Y. Hiraki, Differential expressions of BMP family genes during chondrogenic differentiation of mouse ATDC5 cells, Cell structure and function 25(3) (2000) 195-204.
[50] C. Shukunami, K. Ishizeki, T. Atsumi, Y. Ohta, F. Suzuki, Y. Hiraki, Cellular hypertrophy and calcification of embryonal carcinoma-derived chondrogenic cell line ATDC5 in vitro, Journal of Bone and Mineral Research 12(8) (1997) 1174-1188.
[51] F. Mwale, G. Yao, J.A. Ouellet, A. Petit, J. Antoniou, Effect of parathyroid hormone on type X and type II collagen expression in mesenchymal stem cells from osteoarthritic patients, Tissue engineering Part A 16(11) (2010) 3449-3455.
[52] V. Nelea, L. Luo, C.N. Demers, J. Antoniou, A. Petit, S. Lerouge, M. R. Wertheimer, F. Mwale, Selective inhibition of type X collagen expression in human mesenchymal stem cell differentiation on polymer substrates surface-modified by glow discharge plasma, Journal of Biomedical Materials Research Part A: An Official Journal of The Society for Biomaterials, The Japanese Society for Biomaterials, and The Australian Society for Biomaterials and the Korean Society for Biomaterials 75(1) (2005) 216-223.
[53] S. Camarero-Espinosa, A. Calore, A. Wilbers, J. Harings, L. Moroni, Additive manufacturing of an elastic poly (ester) urethane for cartilage tissue engineering, Acta biomaterialia 102 (2020) 192-204.
[54] C.N. Salinas, K.S. Anseth, The enhancement of chondrogenic differentiation of human mesenchymal stem cells by enzymatically regulated RGD functionalities, Biomaterials 29(15) (2008) 2370-2377.
[55] S.D. Waldman, C.G. Spiteri, M.D. Grynpas, R.M. Pilliar, R.A. Kandel, Long-term intermittent compressive stimulation improves the composition and mechanical properties of tissue-engineered cartilage, Tissue engineering 10(9-10) (2004) 1323-1331.
[56] C. Gaut, K. Sugaya, Critical review on the physical and mechanical factors involved in tissue engineering of cartilage, Regenerative medicine 10(5) (2015) 665-679.
[57] V.V. Meretoja, R.L. Dahlin, S. Wright, F.K. Kasper, A.G. Mikos, The effect of hypoxia on the chondrogenic differentiation of co-cultured articular chondrocytes and mesenchymal stem cells in scaffolds, Biomaterials 34(17) (2013) 4266-4273.
[58] D. Bosnakovski, M. Mizuno, G. Kim, S. Takagi, M. Okumura, T. Fujinaga, Chondrogenic differentiation of bovine bone marrow mesenchymal stem cells (MSCs) in different hydrogels: influence of collagen type II extracellular matrix on MSC chondrogenesis, Biotechnology and bioengineering 93(6) (2006) 1152-1163.
[59] D. MacKenna, S. Vaplon, A.D. McCULLOCH, Microstructural model of perimysial collagen fibers for resting myocardial mechanics during ventricular filling, American Journal of Physiology-Heart and Circulatory Physiology 273(3) (1997) H1576-H1586.
[60] M. Kääb, I. Ap Gwynn, H. Nötzli, Collagen fibre arrangement in the tibial plateau articular cartilage of man and other mammalian species, The Journal of Anatomy 193(1) (1998) 23-34.
[61] M.G. Patino, M.E. Neiders, S. Andreana, B. Noble, R.E. Cohen, Collagen: an overview, Implant dentistry 11(3) (2002) 280-285.

[62] J. Riegger, R.E. Brenner, Pathomechanisms of posttraumatic osteoarthritis: chondrocyte behavior and fate in a precarious environment, International journal of molecular sciences 21(5) (2020) 1560.
[63] J.P. Armstrong, E. Pchelintseva, S. Treumuth, C. Campanella, C. Meinert, T.J. Klein, D.W. Hutmacher, B.W. Drinkwater, M.M. Stevens, Tissue Engineering Cartilage with Deep Zone Cytoarchitecture by High-Resolution Acoustic Cell Patterning, Advanced healthcare materials (2022) 2200481.
[64] G. Hochleitner, E. Fürsattel, R. Giesa, J. Groll, H.W. Schmidt, P.D. Dalton, Melt electrowriting of thermoplastic elastomers, Macromolecular rapid communications 39(10) (2018) 1800055.
[65] V.I. Sikavitsas, J.S. Temenoff, A.G. Mikos, Biomaterials and bone mechanotransduction, Biomaterials 22(19) (2001) 2581-2593.
[66] Q. Fu, E. Saiz, A.P. Tomsia, Direct ink writing of highly porous and strong glass scaffolds for load-bearing bone defects repair and regeneration, Acta Biomaterialia 7(10) (2011) 3547-3554.

Supplementary material

Table S1. *Volumetric micro-CT data of the r=0.17 and 0-90 design. Each condition contained n=3 samples. Values represent average ± standard deviation.*

Sample	Pore volume full scaffold (mm^3)	Pore volume superficial zone (mm^3)	Pore volume middle zone (mm^3)	Pore volume deep zone (mm^3)
r=0.17	109.2 ± 7.7	10.9 ± 2.3	69.0 ± 4.6	31.6 ± 4.7
0-90	125.0 ± 2.7	16.5 ± 0.7	76.0 ± 1.5	32.5 ± 0.8

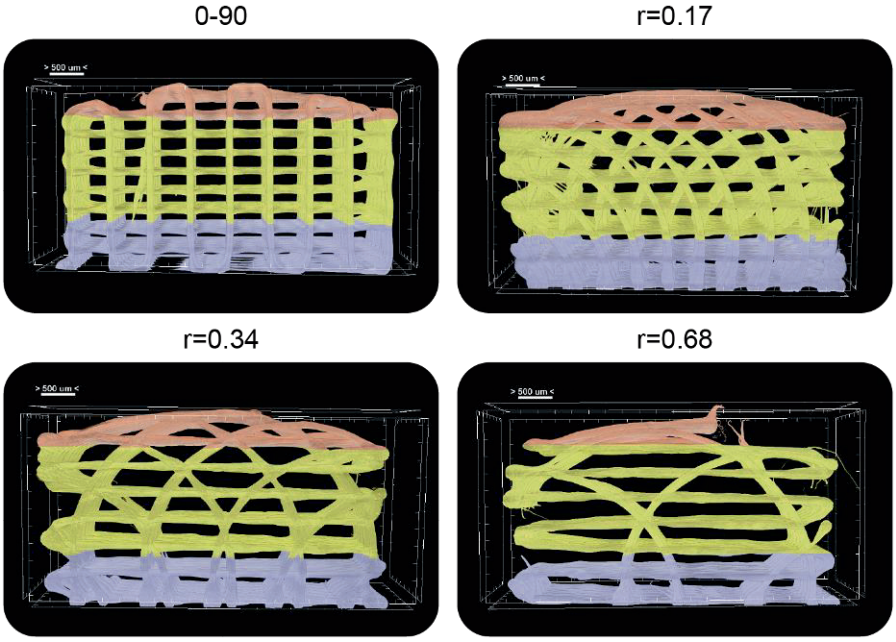

Figure S1. *Division of the different scaffold designs into the three zones. The deep zone in blue, middle zone in yellow and superficial zone in red. Scale bar represents 500 µm.*

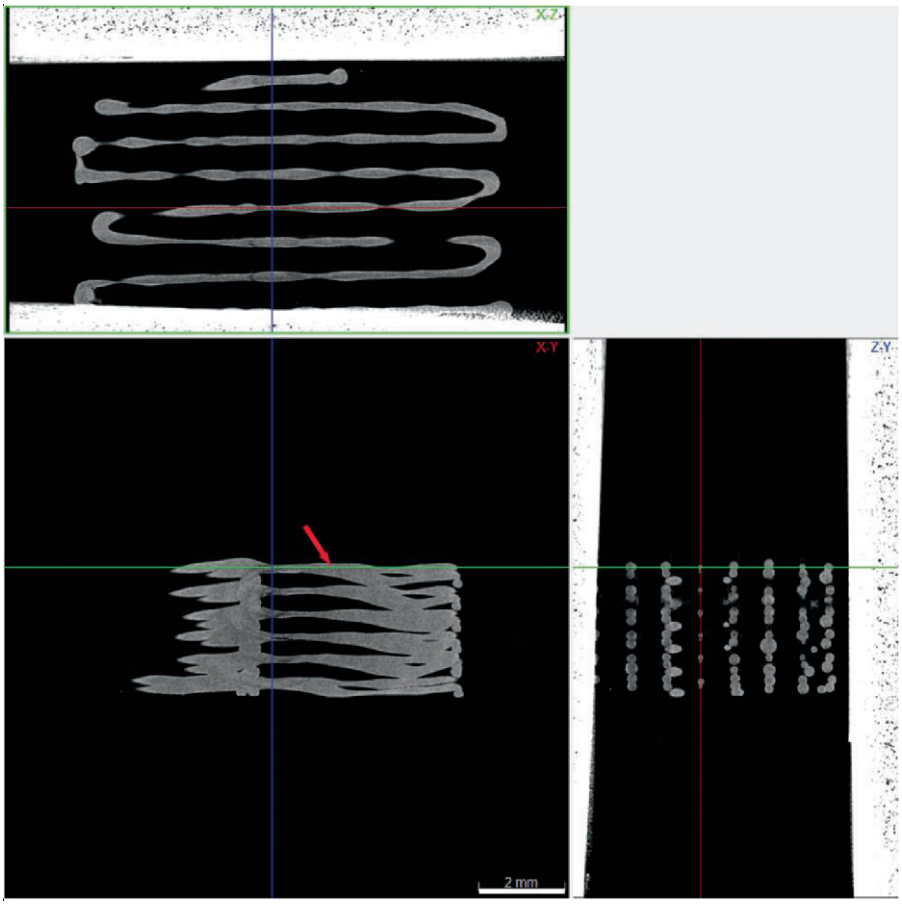

Figure S2. *Fiber collapse in the r=0.68 hypotrochoidal design. Top panel displays the frontal view, the bottom left panel top view and the bottom right panel the cross sectional view. The red arrow indicates the collapse of the fiber. The scale bar represents 2 mm.*

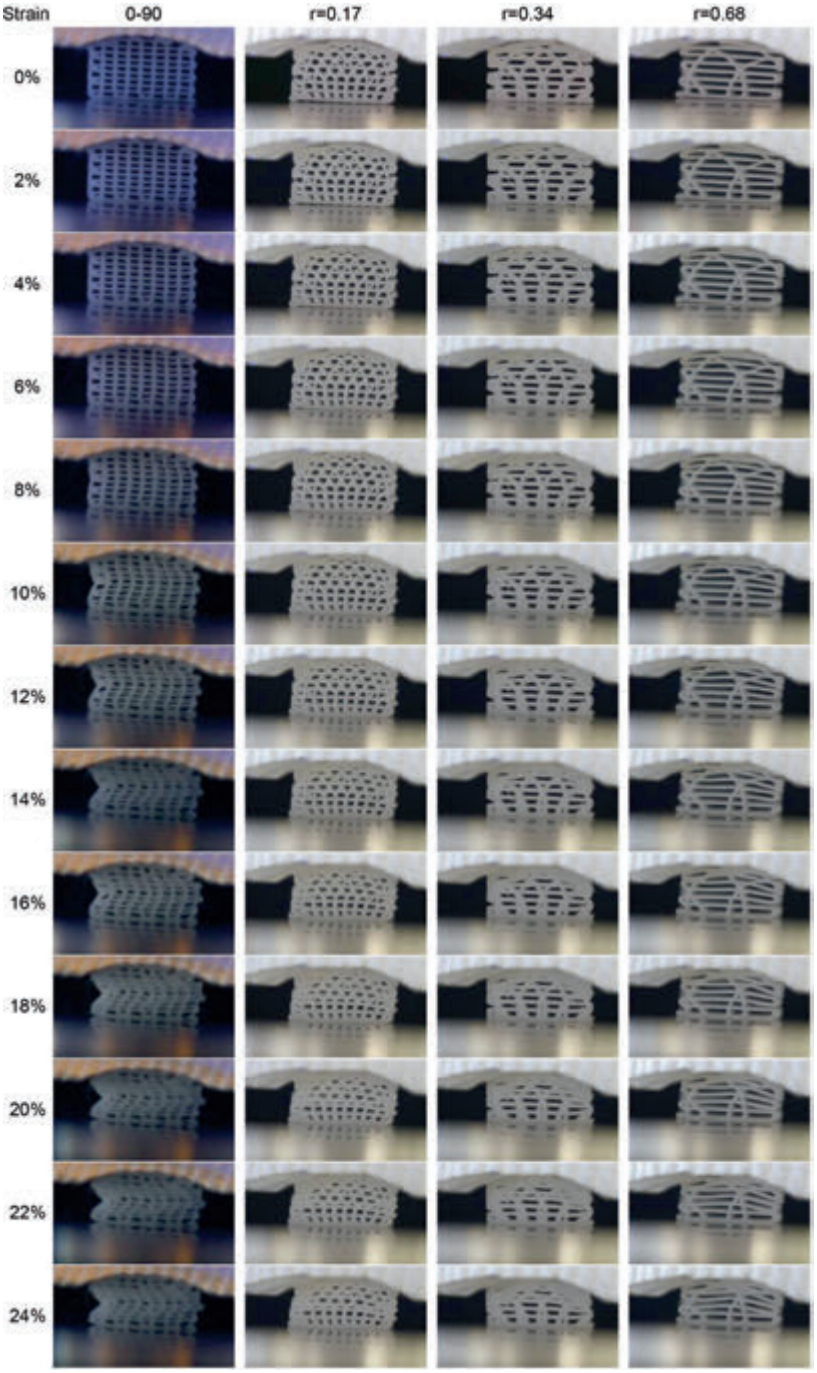

Figure S3. *Time-lapsed snapshots during the compression test of the different tested designs.*

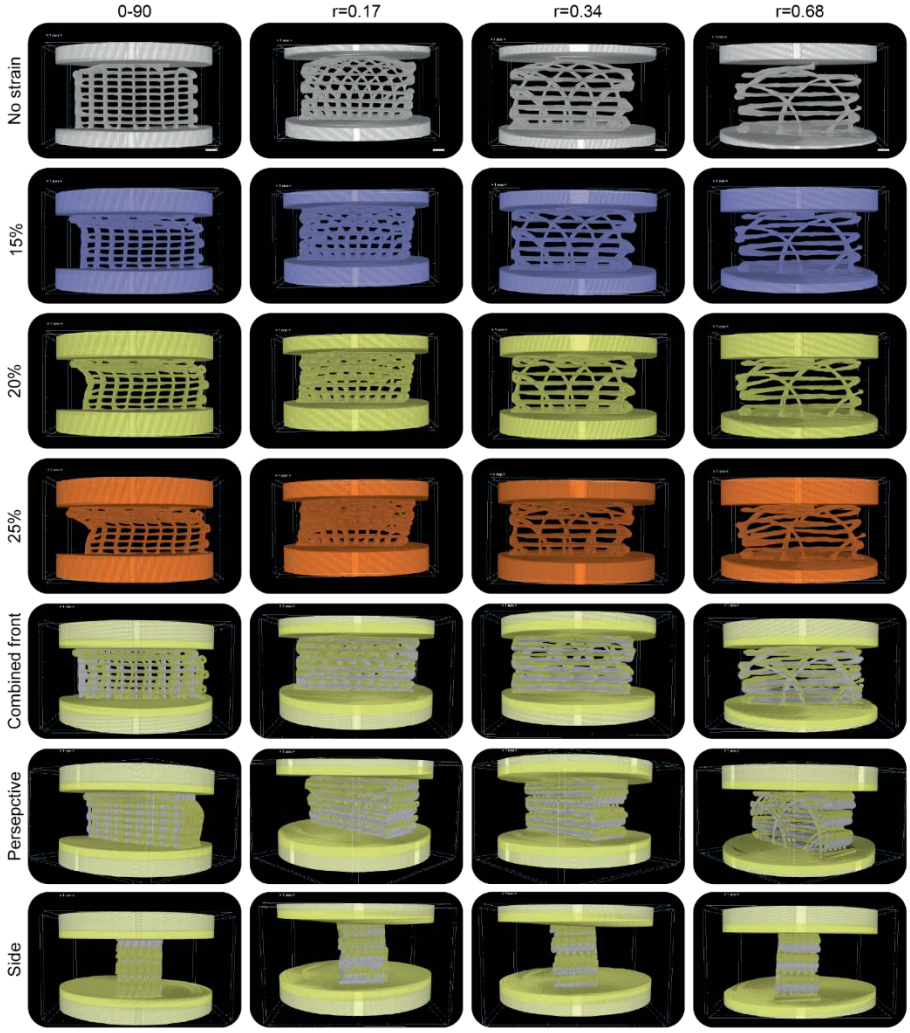

Figure S4. *Micro-CT in combination with a compression test on the different tested designs. Images were taken at 15%, 20% and 25% strain. Panels from the bottom three rows are superimposed. Scale bar represents 500 µm.*

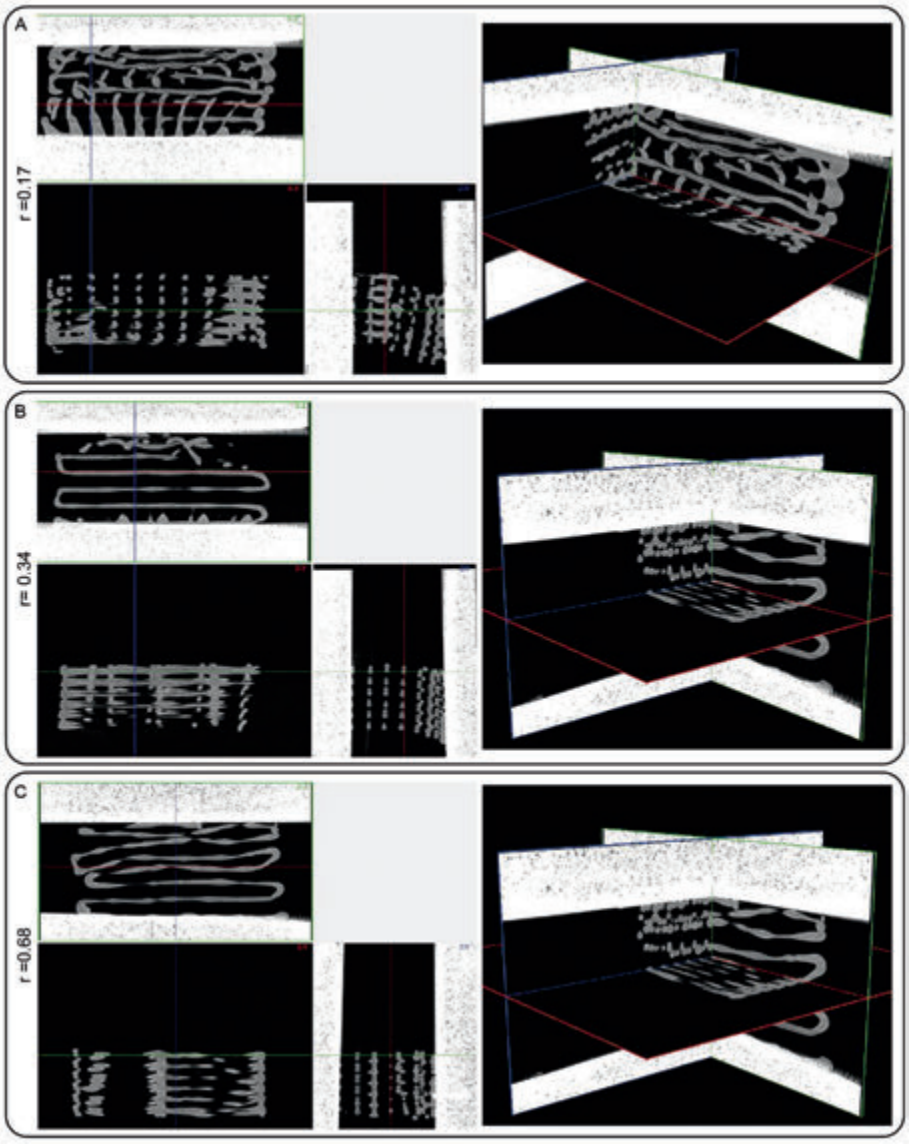

Figure S5. *Micro-CT images after a compression test at 25% strain. Left panels reveal the cross-sections from different planes and the right panels reveal the 3D assembly of each plane. (A) r=0.17 design, (B) r=0.34 design and (C) the r=0.68 design.*

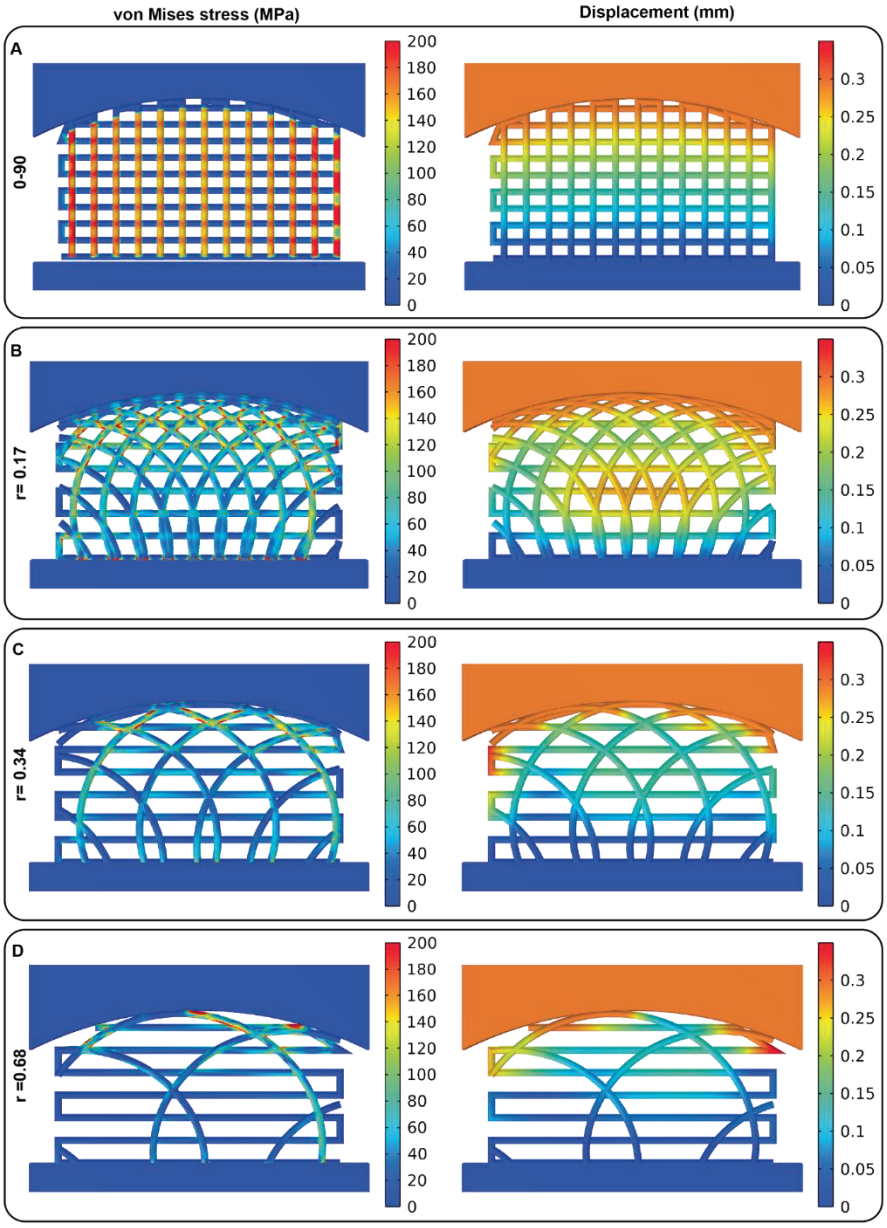

Figure S6. *Finite element model of a compression test of the different designs, (A) the 0-90, (B) r=0.17, (C) r=0.34 and (D) r=0.68 design. The bottom fixture was fixed while a displacement of 0.6 mm was simulated on the curved top fixture (10% strain). The left hand panel show the von Mises stress and the right hand panel show the displacement.*

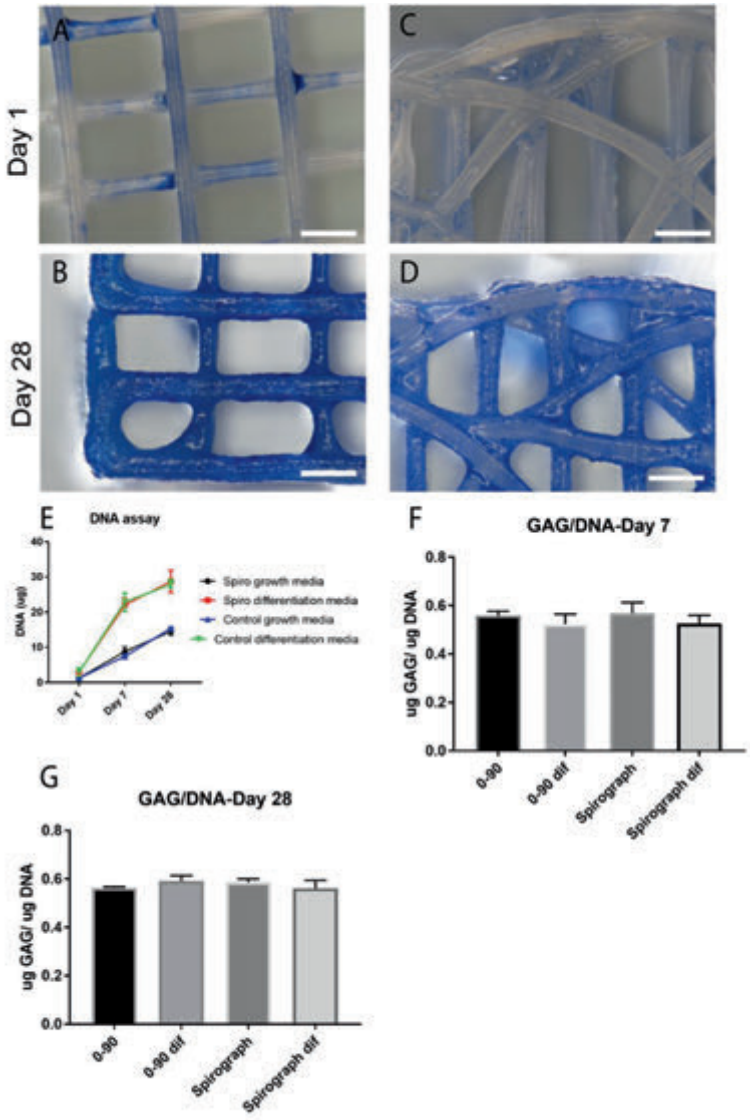

Figure S7. *Cells after 28 days in static culture stained by methylene blue. (A) 0-90 woodpile design after 1 day of culture. (B) 0-90 woodpile design after 28 days of culture. (C) r=0.34 design after 1 day of culture. (D) r-0.34 design after 28 days of culture. (E) DNA quantification of 0-90 and r=0.34 designs over 28 days of culture; and GAG quantification after 7 (F) and 28 (G) days. Scale bar represents 1 mm.*

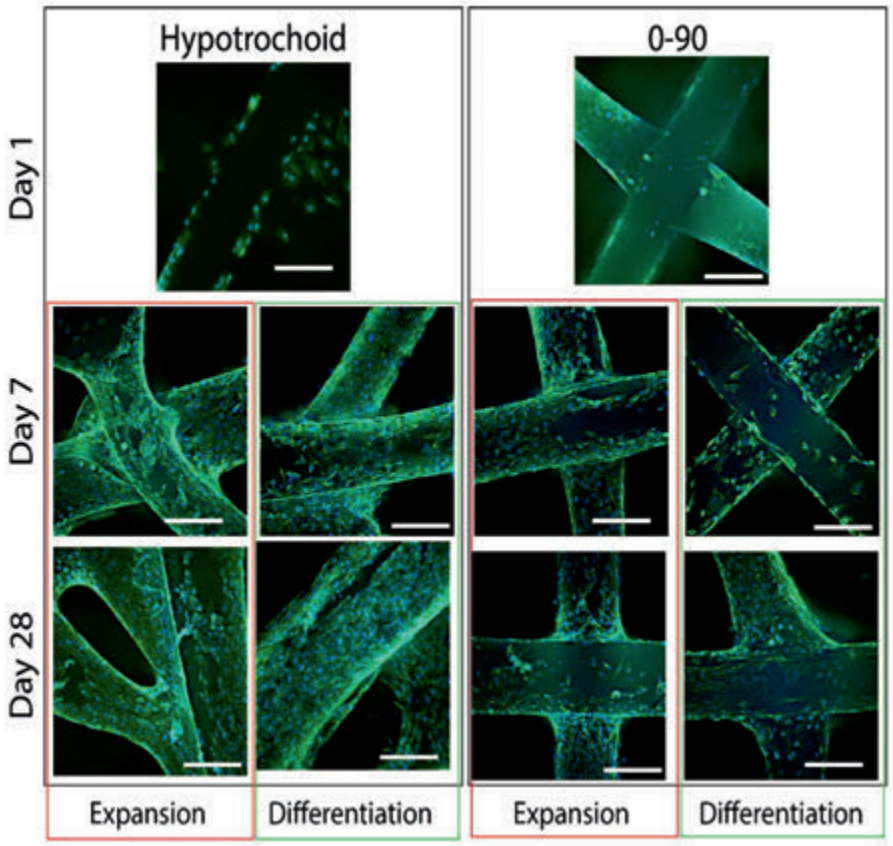

Figure S8. *Cell adhesion on 0-90 and hypotrochoidal scaffolds in basic (expansion) and differentiation media, quantified by phalloidin (green) and DAPI (blue) staining. Scale bar: represents 500 µm.*

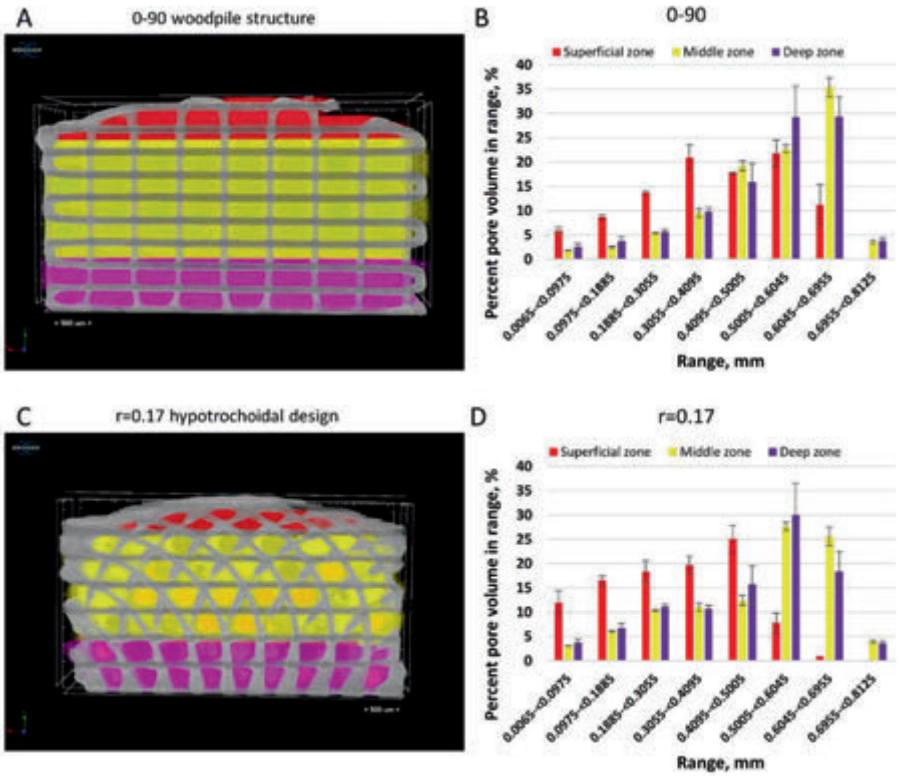

Figure S9. *Pore distribution for the 0-90 woodpile (A,B) and r=0.17 hypotrochoidal design (C,D). Representative images from micro-CT showing the porosity in the 3 zones: in red the pores of the superficial zone, in yellow the pores from the middle zone and in magenta the pores of the deep zone (A,C). Pore distribution as a percent of pore volume in different range intervals for the 3 zones: red- the superficial zone, yellow-the middle zone and purple –the deep zone (B,D).*

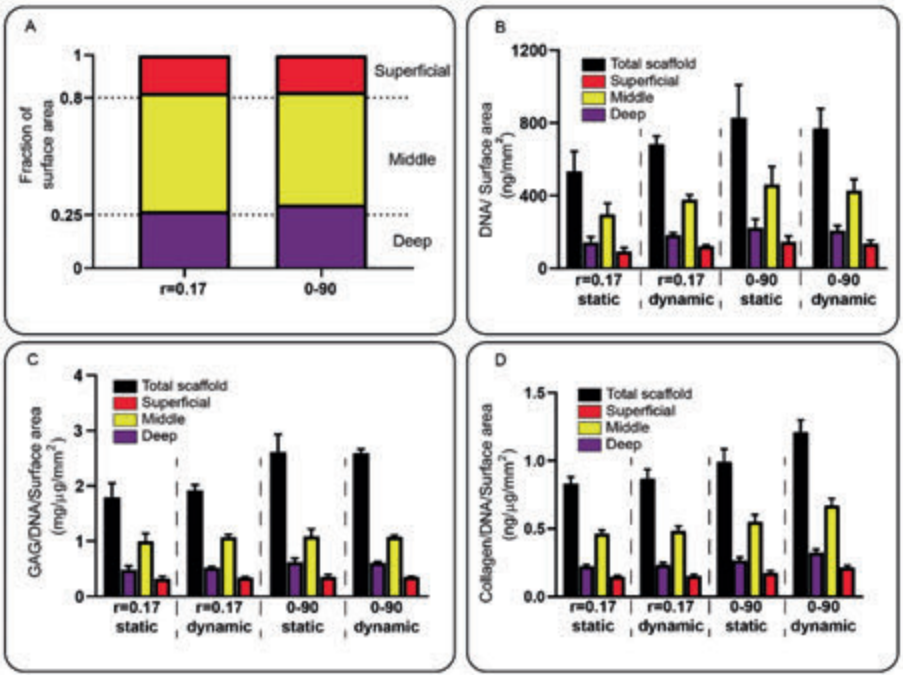

Figure S10. *DNA, GAG and collagen analyses of the tested scaffolds after 28 days of culture. (A) Micro-CT analyses of the surface area in fraction of the surface area. (B) DNA content normalized against the surface area. (C) GAG per DNA content normalized against the surface area. (D) Collagen per DNA content normalized against the pore surface area. Each condition contained n=3 samples and values represent average ± standard deviation.*

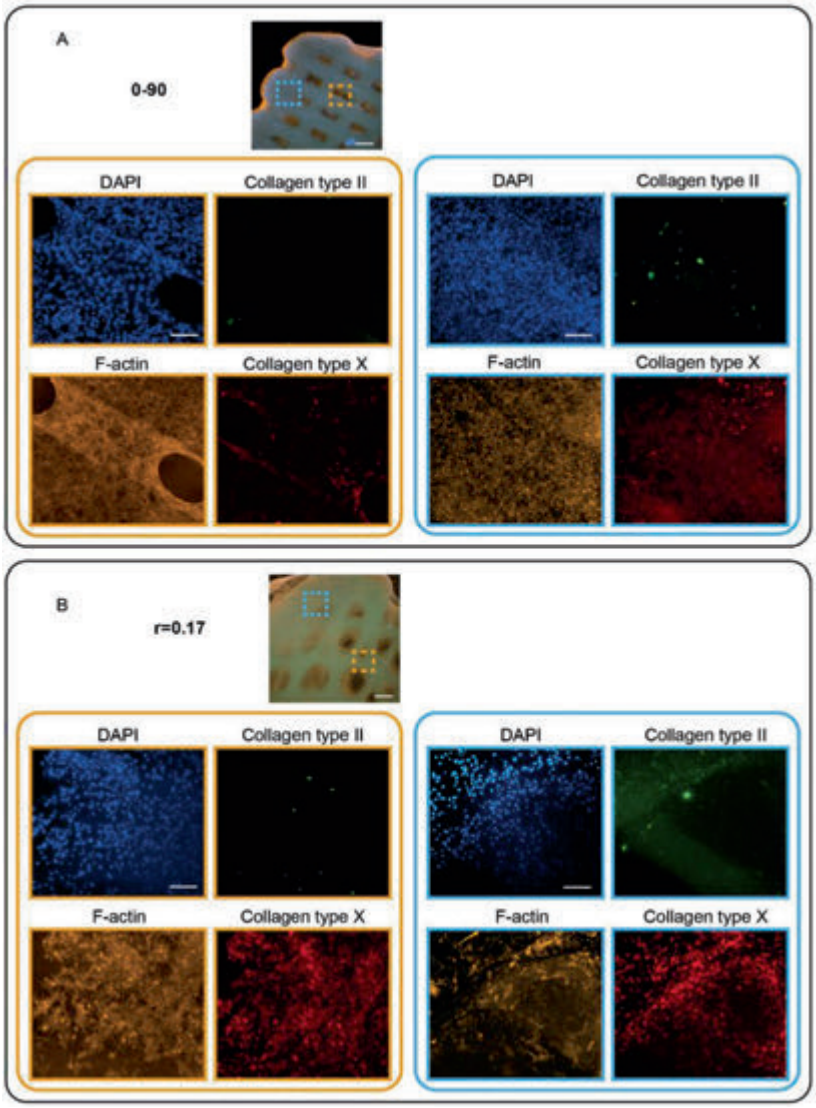

Figure S11. *Cells after 28 days in static culture. On top of the panel an overview image of the scaffold. The bottom panel sets represent different areas in the scaffold. (A) 0-90 woodpile design. (B) r=0.17 hypotrochoidal design. Scale bars represent 500 μm in the overview panel and 200 μm in the close up.*

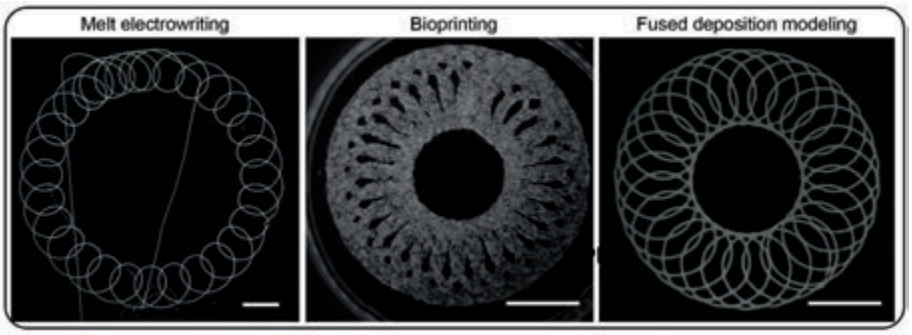

Figure S12. *Hypotrochoidal designs fabricated with various techniques and printers. From left to right, Melt electrowritting, Bioprinting and Fused deposition modeling. With PCL M_n 45,000 as material for the melt electrowritten and fused deposition modeling scaffolds and Xanthan gum (7% w/v) as material for the bioprinted scaffolds. Scale bar represents 1000 µm.*

Chapter 5

Controllable four axis extrusion based additive manufacturing system for vascular tissue regeneration

Controllable four axis extrusion based additive manufacturing system for vascular tissue regeneration*

Kenny A. van Kampen[1], Elena Olaret[2], Izabela-Cristina Stancu[2], Lorenzo Moroni[1], Carlos Mota[1]

[1]Department of Complex Tissue Regeneration, MERLN Institute for Technology-Inspired Regenerative Medicine, Maastricht University, Universiteitssingel 40, 6229ER Maastricht, The Netherlands

[2]Advanced Polymer Materials Group, University Politehnica of Bucharest, 1-7 Gh. Polizu Street, 011061, Bucharest, Romania

***Chapter published in Materials Science and Engineering C 2020, DOI: 10.1016/j.msec.2020.111472**

Abstract

Many tubular tissues such as blood vessels and trachea can suffer long-segmental defects through trauma and disease. With current limitations in the use of autologous grafts, the need for a synthetic substitute is of continuous interest as possible alternatives. Fabrication of these tubular organs is commonly done with techniques such as electrospinning and melt electrowriting using a rotational collector. Current additive manufacturing (AM) systems do not commonly implement the use of a rotational axis, which limits their application for the fabrication of tubular scaffolds. In this study, a four axis extrusion-based AM system similar to fused deposition modelling (FDM) has been developed to create tubular hollow scaffolds. A rectangular and a diamond pore design were further investigated for mechanical characterization, as a standard and a biomimicry pore geometry respectively. We demonstrated that in the radial compression mode the diamond pore design had a higher Young's modulus (19,8 ± 0,7 MPa compared to 2,8 ± 0,5

MPa), while in the longitudinal tensile mode the rectangular pore design had a higher Young's modulus (5,8 ± 0,2 MPa compared to 0,1 ± 0,01 MPa). Three point bending analyses revealed that the diamond pore design is more resistant to luminal collapse compared to the rectangular design. This data showed that a wide range of mechanical properties can be obtained with the four axis extrusion-based system. Furthermore, with this technique a full control over scaffold design and geometry can be achieved, which has not been reported with other techniques. This flexibility can allow the manufacturing of scaffolds for diverse tubular tissue regeneration applications by designing suitable deposition patterns to match their mechanical pre-requisites.

1. Introduction

Peripheral and coronary vascular substitutes have been increasing in demand [1]. Due to trauma and diseases, long-segmental defects are generated and a remedy is required. With larger diameter (6> mm) vasculature, if the defect becomes too large for end-to-end anastomosis a replacement in the form of clinical grade woven polyethylene terephthalate is used [2-4]. The main limitation with using polyethylene terephthalate is calcification that can occur in long term implantation cases, Mehta *et al*. [4] reported that after 87 months of implantation 68% of the patients showed evidence of calcification. In the smaller diameter grafts autologous tissue is harvested which is restricted by the limited availability of the tissue and require a second surgical site [5]. Due to these limitations, scaffold fabrication technologies may offer a promising alternative for creating tubular scaffolds as a template for tissue regeneration.

Currently most vascular scaffold fabrication techniques rely on methods such as electrospinning and melt electrowriting [6-8]. The main advantage of these methods is the fiber diameter size which can range from tens of nanometers to tens of micrometers [9]. The disadvantage of these technologies is that it is

still difficult to create longitudinal porosity and the mechanical properties of the scaffolds produced are often weak, and therefore more prone to luminal collapse when implanted *in vivo* [10-12]. In addition the scaffold itself can also get damaged during implantation when not carefully handled [13]. On the other hand, having a stiff scaffold can also cause mechanical mismatch and will also lead to graft failure [14]. Using a different material, changing design or fabrication technique could help to improve the mechanical properties and reduce the probability of collapse and mechanical mismatch [15, 16].

Techniques in AM such as fused deposition modeling (FDM), bioplotting and other extrusion based techniques are suitable for increasing the mechanical integrity of a scaffold by manufacturing fibres with hundreds of micrometers [17]. The main limitation in creating a tubular construct with current extrusion based setups is the designs and geometries that can be manufactured, since for these overhanging and hollow structures a support material is required [18]. This limitation is mainly caused by the fact that most systems use a layer-by-layer fabrication approach by subsequently depositing fibers to form an infill of each layer within the object contour and this process is repeated until the full 3D object is obtained. This deposition normally occurs in a flat substrate that moves in relation to the printhead in the X-Y plane and Z direction [19]. The implementation of a fourth axis allows the possibility to create more complex tubular scaffold designs such as been described in the field of prosthetic implants [20, 21]. Other groups focusing on biomedical research have implemented a fourth axis in their FDM system [22], however often without a communication between the rotational axis and the main system, which results in the creation of only helical designs [17, 23, 24]. In addition to that, tubular scaffolds are generally not completely characterized and understood for their mechanical properties and behaviour for axial, radial and bending deformations.

The aim of this study was to show an extrusion-based AM technique similar to FDM with a synchronized fourth rotational axis that allows the fabrication of complex tubular geometries. In addition, the role of geometry in scaffold design on mechanical properties such as radial compression, tensile strength and three point bending was further studied.

2. Methods

2.1 Four axis extrusion based system

A Roland EGX-360 with fully controllable fourth axis was adapted by replacing the engraving head with a custom-made heated pressure-driven dispensing cartridge. This cartridge made of stainless steel is encased in a heating aluminium block with an electrical resistance of 150 W and 240V controlled by a proportional, integral derivative (PID) unit (PID500MH-1000, Tempatron, UK). The PID was set at 110 °C and the cartridge containing poly(ε-caprolactone) (PCL, Mn =45,000 g mol-1, Sigma-Aldrich, USA) was loaded in the heating block. The polymer was kept for 15 min to ensure complete molten state and extruded with pressure of 5 bar. An electromagnetic pressure valve was used to control of deposition. The molten PCL was extruded through a 260 micron nozzle diameter (25G needle). The polymer was deposited on a rotating stainless steel mandrel with a 2 mm diameter which was attached to the 4^{th} axis and controlled by the printer.

2.2 Scaffold fabrication

All scaffolds were manufactured with a travel speed of the extruder set at 2 mm/s and the distance between nozzle and the stainless steel mandrel was set at 200 μm. The total scaffold length in all tested cases was kept constant at 18 mm with an inner diameter of 2 mm. Two different scripts were written in Python 3.6 to control the printhead movements to form the diamond and the rectangular designed patterns. Within the Phyton script developed for the rectangular pattern features such as the number of rings and struts can be

varied. Rectangular pore scaffolds were labelled according to the amount of rings (R) and struts (S) in the scaffolds, for instance 6R9S contains 6 rings and 9 struts. The distance between the rings was equally divided over the whole length of the scaffold. The struts were also equally divided over the total perimeter of the scaffold. In the diamond pore design the pitch of the diamond and the amount of helices can be defined were the space between each starting helix was equally divided along the perimeter. The total amount of complete helix turns in the diamond pore scaffolds is based on the total amount of helices multiplied by the rotations per helix. The diamond pore scaffolds were labelled according to the amount of helices (H) and the pitch (P) of the diamond, for instance 4H4,5P contains 4 helices with a pitch of 4,5 mm. One additional script was written for the Hilbert curve as an example to show the complexity of the fabricated structures that can be achieved. The mandrel for this case had a diameter of 12 mm and the scaffold was a 4^{th} generation Hilbert Curve.

2.3 Scaffold characterization

Stereomicroscope (SMZ25, Nikon instruments, U.S.A.) and scanning electron microscopy (SEM, XL-30, Philips, The Netherlands) were used to visualize the scaffold structure. The diameter of the filaments was measured on the SEM micrographs from three fibres on three different scaffolds. MicroCT was used to qualitatively and quantitatively investigate the 3D structure. The obtained micrographs were reconstructed using Nrecon software (Version 1.7.1.6.,Bruker MicroCT). Pore shape was visualised using Ctvox (Version 3.3.0r1403, Bruker MicroCT) software and the volume of the scaffold (and all other quantitaive data) was analysed through Ctan software (1.18.4.0+, Bruker MicroCT). The porosity of the scaffolds was derived from Equation 1.

Equation 1. $(1 - Vsolid/Vtotal) * 100\%$

Where *Vsolid* is obtained from the Micro-CT analysis and *Vtotal* is calculated from an equivalent tube generated with computer assisted design (CAD) software (Rhino 6, Version 6.24, Robert McNeel & Associates) with the length and wall thickness of each scaffold.

2.4 Mechanical characterization

Mechanical characterization was performed on a mechanical tester (ElectroForce, TA instruments, U.S.A.). Compression tests were performed in the radial direction between two stainless steel plates at a strain rate of 1% per second. Tensile tests were performed on the scaffolds by inserting a similar diameter stainless steel rod in the part of the lumen of the scaffold were the clamps attached. A gap of 10 mm was set between the top and the bottom clamp and the tensile test was performed at a rate of 0.1 mm/s. In addition, tensile tests were performed using micro-CT scanner (SkyScan 1272, Bruker,Belgium) provided with material testing stage 2 (MTS 2) which allow the sample to be subjected to a load until a final deformation of the sample is reached. Subsequently to perform a scanning step which allow to observe the changes appeared in the microstructure of the tested scaffold. The deformation was observed in steps and set to 0, 2, 4, 6 and 8 mm, at each step a delay of 3 minutes before scanning was set to avoid any movement artifacts during the scan. The strain rate during micro-CT was set to 11 µm per second. Three-point bending was performed to assess whether the designs can bend without lumen collapse. The scaffolds were placed on two V-shaped supports with a gap distance of 10 mm. A rounded probe set in the center of the gap was used to deform the samples at a fixed rate of 1% strain per second. The whole test was captured with a camera (DMC-G3, Panasonic, The Netherlands) with a macro-lens (Panagor 90mm f2.8, Komine, Japan), images and videos were analyzed using ImageJ (Version 1.52p, NIH) and Adobe Premiere Pro (Version 12.0, Premiere Pro CC 2018).

2.5 Finite element modeling

COMSOL multiphysics (Version 5.2, Comsol B.V., the Netherlands) was used to simulate the scaffolds from the micro-CT, a 3D model of the 4H4,5P diamond pore design and the 6R9S design was recreated. During the simulation one end of the scaffold was fixed while on the other end a tensile deformation of 8 mm was simulated in steps of 0,8 mm.

2.6 Statistics

Statistical analyses were performed with GraphPad Prism 8.1.2. Significant differences were tested using a student's t-test and were considered significant when $p<0.05$.

3. Results and discussion

A schematic overview of the fabrication process is shown in Figure 1A, a picture of the setup is shown in Figure S1. Briefly, a four axis extrusion based heating printhead containing a reservoir was used to deposit molten polymer on top of a controlled rotating mandrel. This technique is compatible with thermoplastic biomaterials. As a proof-of-concept, PCL was used for the fabrication of all scaffolds in this study.

Figure 1B shows an example of the variety of designs that can be produced with the four axis extrusion-based system. Additionally, the control in all directions is shown in Video 1. Previous works have investigated the implementation of a fourth axis in AM for creating helical structures [23-25]. The advantage of our method is that the fourth rotational axis is synchronized with the X-Y and Z axis and therefore the toolpath can be directly coded which allows high precision in scaffold design and the ability to fabricate more complex designs (Figure S2). Future optimization studies will aim at decreasing the fiber size below 100 µm [26].

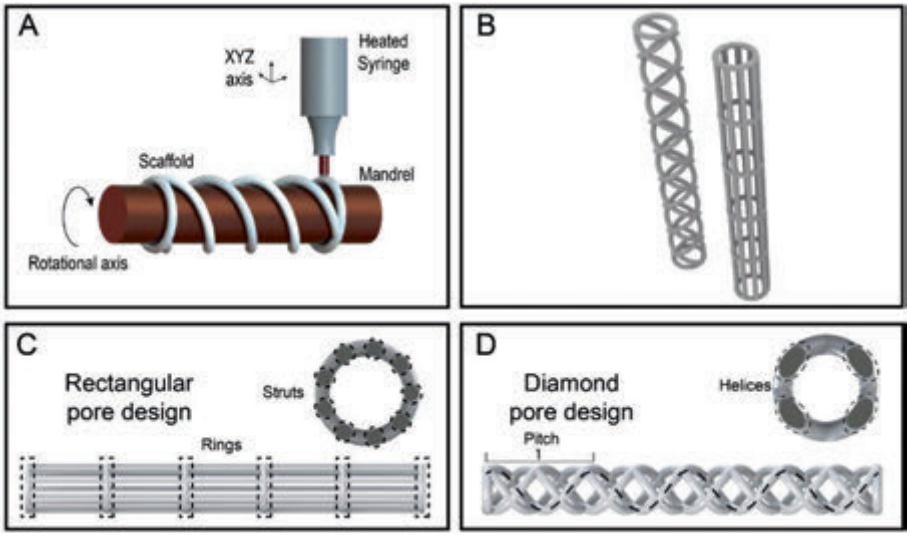

Figure 1. *Fourth axis extrusion-based system. (A) Schematic overview of the fabrication process. (B) Examples of possible designs that can be manufactured with the fourth axis FDM system. (C) Rectangular pore design with rings and struts that can be introduced. (D) Diamond pore design with the amount of helices and rotations that can be varied in the design.*

In this study two different designs were chosen, a rectangular pore design where filament rings and struts are created, and the amount in each of them can be varied (Figure 1C), which represents a standard pore design. The second design is a multiple diamond pore were the amount of helices or the pitch per helix can be varied (Figure 1D) which represents a more biomimicry pore design.

Five different variations of the rectangular pore design were successfully created and shown in Figure 2A. With the decreasing amount of rings, the distance between each rings is increased. Similarly, with the decreasing amount of struts the distance between each struts increased. In addition, the fibres in all the samples showed proper fusion, which is beneficial for the mechanical properties. Table 1 and 2 show the results obtained from micro-CT and SEM. The weight of the scaffold correlated with the porosity, by increasing the weight of the scaffold, the porosity decreases and the available

surface area increases. A variation in fiber size was observed between the rectangular pore designs, ranging from 341 ± 24 µm in the 5R9S sample to 370 ± 28 µm in the 6R7S sample (Table 1). A certain level of thickness heterogeneity was observed in micro-CT, which was in good correlation with similar features noticed in the diamond pore designs (Figure S3). An overview of the tested conditions for both scaffold types is depicted in Figure 2. In the diamond pore scaffolds, the pitch (9 mm, 6 mm and 4.5 mm) was varied while keeping 4 helices. Other two cases were also investigated by testing a 9 mm and 4.5 mm pitch with 8 and 2 helices respectively. The same as with the rectangular pore design was also observed in the diamond design, with increasing amount of weight in the scaffold there is a decreased porosity and an increased available surface area (Table 2).

Table 1. *Variations of the rectangular pore design.*

Sample	**6R5S**	**6R7S**	**6R9S**	**5R9S**	**4R9S**
Ring (Nr.)	6	6	6	5	4
Strut (Nr.)	5	7	9	9	9
Weight (mg)	14.7 ± 0.3	17.3 ± 0.5	18.2 ± 0.4	17.5 ± 0.7	17.2 ± 0.4
Fiber diameter (µm)	343 ± 17	370 ± 28	352 ± 29	341 ± 24	359 ± 34
Porosity (%)	69.7	58.2	50.8	55.7	53.8
Surface area (mm^2)	141.2	239.3	247.2	218.2	210.1

Arteries are subjected to external pressures from surrounding tissues. Luminal collapse occurs whenever the external pressure becomes higher than the internal lumen pressure [27]. Therefore, radial compression tests were performed to assess the mechanical properties of the different designs. The data of the rectangular pore designs revealed that with increasing amount of rings in the scaffold the Young's modulus increased significantly (Figure 3A), while increasing the amount of struts in the scaffold seemed to make no significant difference (Figure 3B). This indicates that the rings in the scaffolds are load bearing in radial compression while struts make no significant difference. In the case of the diamond design with higher number of helix turns

the Young's modulus increased significantly (Figure 3C). When the helices and the pitch were varied a different trend was observed (Figure 3D), the 4H4.5P design had a significantly higher Young's modulus (19,8 ± 0,7 MPa) compared to the 8H9P and 2H2.25P (13.5 ± 2.2 MPa and 6.1 ± 0.1 MPa respectively). A possible explanation for this behaviour is that with a decrease

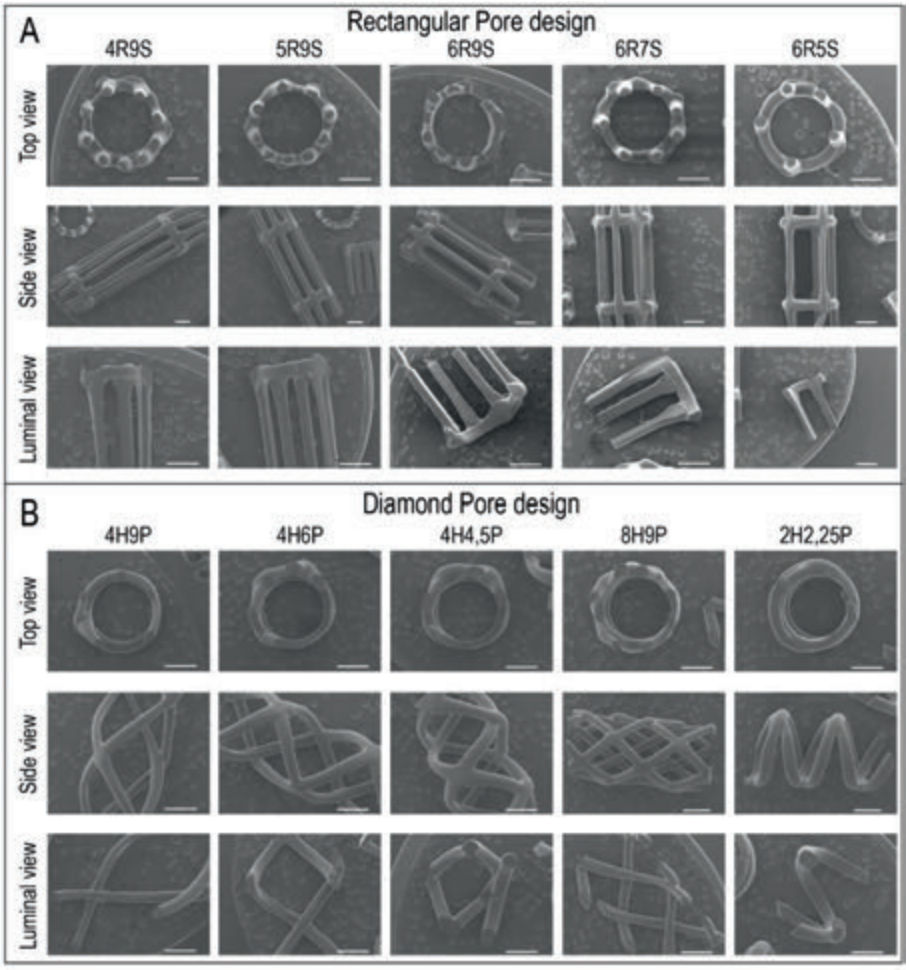

Figure 2. *Overview of the tested designs. (A) The rectangular pore design with varying amount of rings and struts in the scaffold. (B) The diamond design with varying amount of helices and rotations per diamond in the scaffold. Scale bar represents 1 mm.*

***Table 2**. Variations of the diamond pore design.*

Sample	4H9P	4H6P	4H4.5P	8H9P	2H2.25P
Pitch (mm)	9	6	4.5	9	2.25
Helix (Nr.)	4	4	4	8	2
Complete helix turn (Nr.)	8	12	16	16	16
Weight (mg)	9.3 ± 0.3	13.7 ± 0.3	17.3 ± 0.6	18.3 ± 0.3	17.3 ± 0.4
Fiber size (µm)	328 ± 25	343 ± 27	365 ± 31	343 ± 29	363 ± 34
Porosity (%)	88.4	82.8	73.5	76.4	76.4
Surface area (mm^2)	58.4	84.6	111.9	112.4	104.2

in pitch in the diamond design there are more filaments that support the load in the radial direction. In addition, the angle of those filament becomes more parallel to the load that is applied [25]. Comparing the rectangular pore design with the diamond design the main differences in radial compression is that the diamond design has a higher range in Young's modulus (9.8 ± 1.5 – 19.8 ± 0.7 MPa for the diamond and 2.8 ± 0.5 – 5.2 ± 0.2 MPa for the rectangular pore). Langewouters *et al.* found that human finger arteries collapse whenever the transmural pressure becomes less than 20 mmHg (2.7 KPa) [28]. The yield strength of the rectangular pore design ranges from 0.55 ± 0.09 MPa to 0.67 ± 0.17 MPa and 0.88 ± 0.18 MPa to 2.56 ± 0.17 MPa (Figure S4). Indicating that in this case both the diamond and the rectangular pore designs are more than capable of preventing luminal collapse.

Implants for hollow organs or end-to-end anastomosis are attached through suturing both ends together [29-31]. During their lifespan, these implants have to withstand tensile stress generated from tissue movements and the sutures which hold them in place [32], therefore longitudinal tensile properties of both designs were assessed. With the rectangular pore design an increasing amount struts introduced in the scaffold resulted in a significant increase in Young's modulus was observed (Figure 4A), while varying the amount of rings

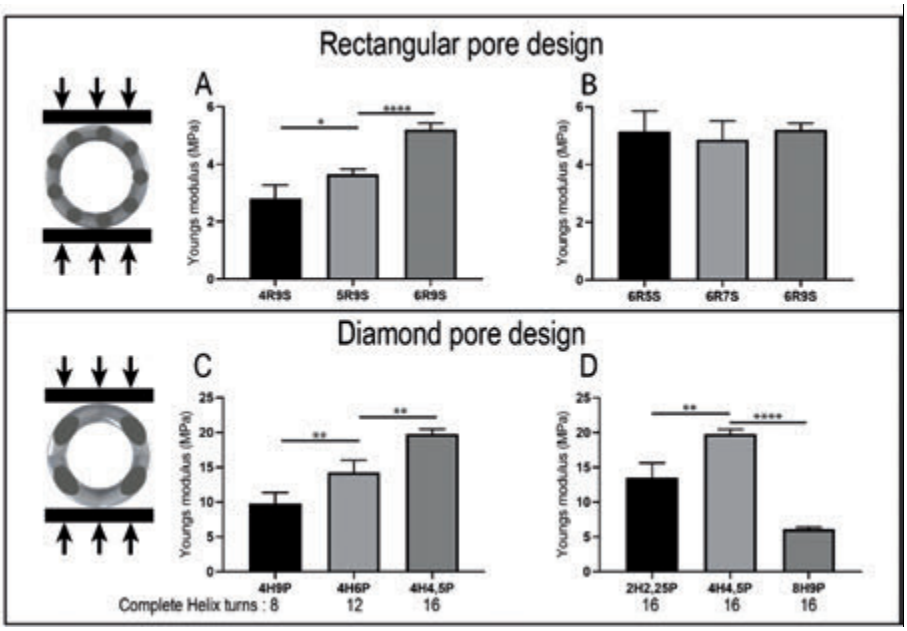

Figure 3. *Radial compression test with a strain rate of 1% per second. (A) Young's modulus in the rectangular pore design with increasing amount of rings and the same amount of struts. (B) Young's modulus in the rectangular pore design with increasing amount of struts and the same amount rings. (C) Young's modulus in the diamond design with the same amount of helices and increasing amount of rotations. (D) Young's modulus in the diamond design with increasing amount of helices and rotations and the same amount of total rotations. Statistical significance: * p<0.05, ** p<0.01, **** p<0.0001.*

in the design did not make a difference (Figure 4B).This behaviour was also confirmed with the finite element tensile model of the scaffold showing that the struts in the scaffold are load bearing while the number of rings play a minor role in longitudinal tensile (Figure 5A). In addition, micro-CT data revealed the deformation during a tensile test (Figure 6). The size of the lumen remained similar during the test, which was also confirmed by the finite element model. Another observation revealed inconsistencies in fiber diameter in the strut fibers indicating stretching of the fiber during the manufacturing process (Figure S3). During the manufacturing process if the filaments are deposited too high from the collector, then there is a chance of delamination. Conversely, a small printing distance between the nozzle and the mandrel leads to

inaccuracies of the final construct because of polymer accumulation around the nozzle [33]. The diamond design on the other hand revealed that there was no significant difference with decreasing the pitch of the scaffold (Figure 4C). Increasing the amount of helices in the scaffold resulted in a significant increase in Young's modulus (Figure 4D). This might be explained by the fact that by increasing the amount of helices there is an increased amount of filaments and filament intersections that contribute to the Young's modulus of the whole scaffold in the longitudinal direction. The finite element model of the diamond design showed that the stress distributed more on the crossing areas between two helices of the scaffold (Figure 5B). In addition, the model showed that with increasing strain the size of the lumen decreased in the diamond design, which was also observed with micro-CT analysis under mechanical testing (Figure 7). During the tensile test with micro-CT the samples were subjected up to 40% strain. At 40% strain the lumen in all samples except 2H2.25P was substantially reduced and in the case of 4H9P nearly occluded. Though in the physiological conditions the stretch in arteries in normal conditions has been reported to be up to 10% [34]. The range of Young's modulus of the diamond design was between 0.06 ± 0.01 MPa and 1.36 ± 0.24 MPa for the 2H2.25P and 8H9P design respectively. Comparing this to other similar work on helical structures showed that the value's fall in the same order of magnitude [35, 36], which is within the range compared to the native human carotid artery (0.20 ± 0.06 MPa) [37]. Furthermore a change in the material could bring these values in the same range as Jeong and Hollister [38] demonstrated by testing PCL, Poly (Glycerol-co-Sebacate) and Poly (Octanediol-co-Citrate) scaffolds of the same shape. Alternatively, changing design from helical to a rectangular pore shape, the tensile modulus can be increased by an order of magnitude with similar amount of material (Table 1). In general, the rectangular pore design has a higher Young's modulus in tensile when compared to the diamond design (5.8 ± 0.2 MPa – 8.6 ± 0.5 MPa and 0.1 ± 0.01 MPa – 1.3 ± 0.2 MPa respectively).

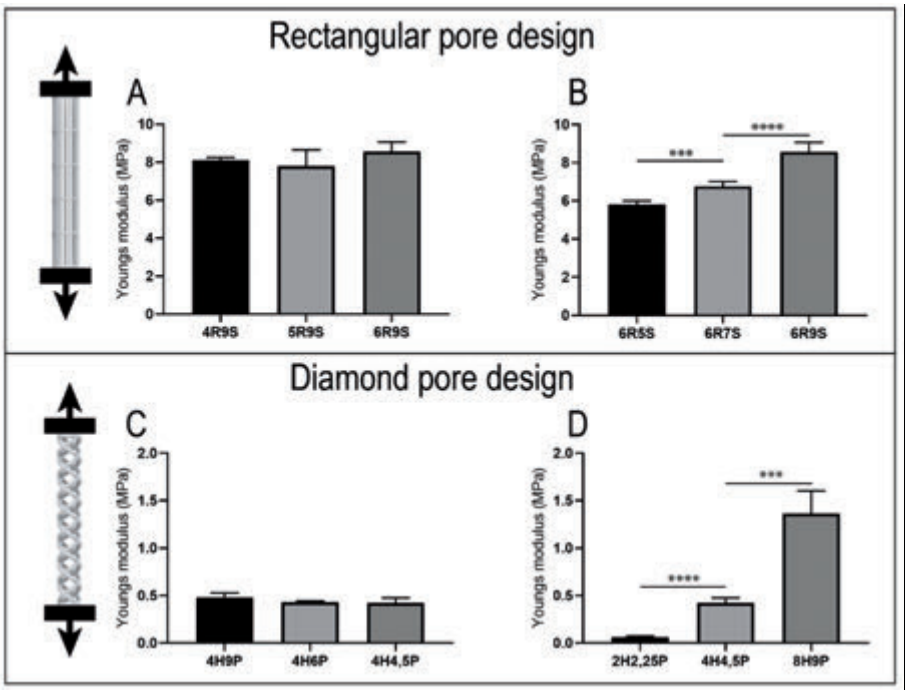

Figure 4. *Longitudinal tensile tests with a strain rate of 1% per second. (A) Young's modulus in the rectangular pore design with increasing amount of rings and the same amount of struts. (B) Young's modulus in the rectangular pore design with increasing amount of struts and the same amount rings. (C) Young's modulus in the diamond design with the same amount of helices and increasing amount of rotations. (D) Young's modulus in the diamond design with increasing amount of helices and rotations and the same amount of total rotations. Statistical significance: *** p<0.001, **** p<0.0001.*

To assess if the scaffolds were flexible enough to bend without the lumen collapsing a three-point bending was performed and captured using a camera (Video 2 and 3). Images of the video of the lumen size at 40% deformation were made and plotted in Figure 8. Analysis revealed that for the rectangular pore design the lumen size remained significantly higher with increasing amount of rings in the design (Figure 8A). The positioning of the scaffold had a significant influence on the retention of the lumen size. When the probe was centered between two rings the lumen collapsed while if the probe was centered on top of a ring then the lumen remained open (Figure S5). With

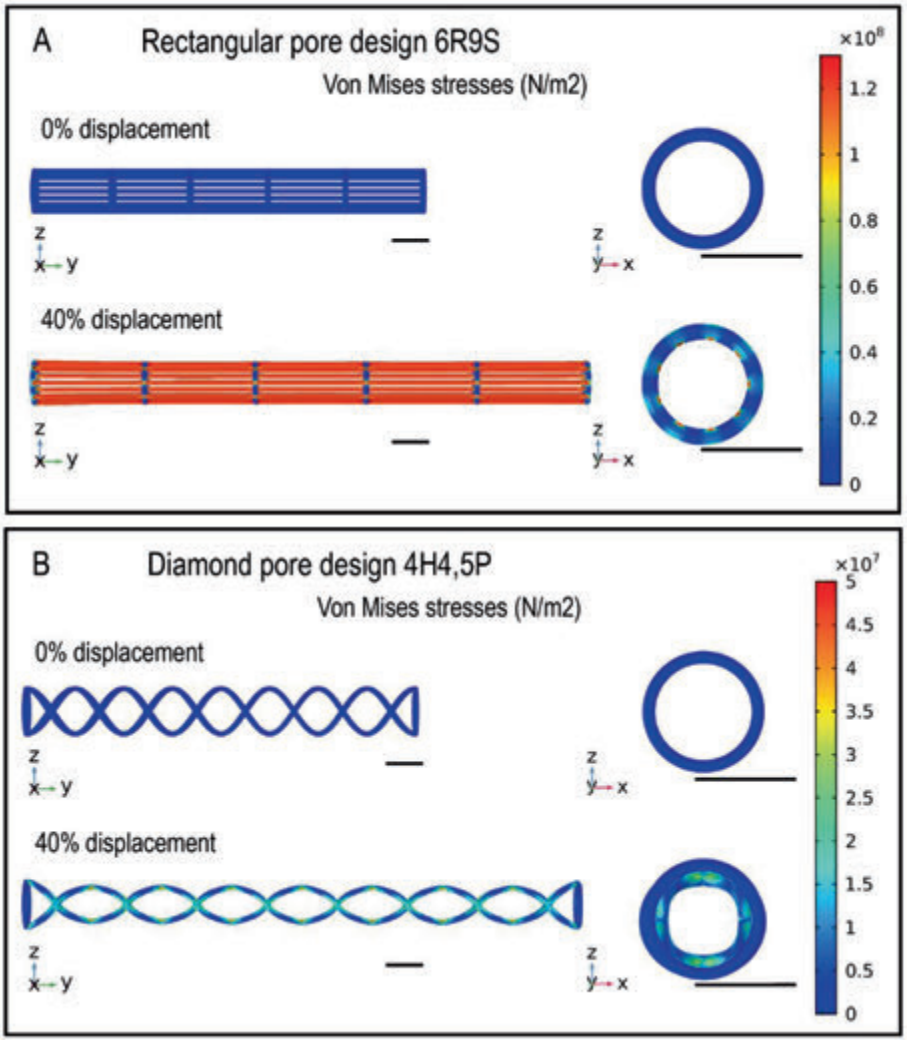

***Figure 5**. Finite element model of a tensile test in both designs. One end of the scaffold was fixated while a 40% tensile displacement applied. (A) The model for the rectangular pore sample with 6 rings and 9 struts, on the left side a side view and on the right side a top view of the scaffold. (B) The model for the diamond design with 4 helices and 4 rotations, on the left side a side view and on the right side a top view of the scaffold. Scale bar = 2mm*

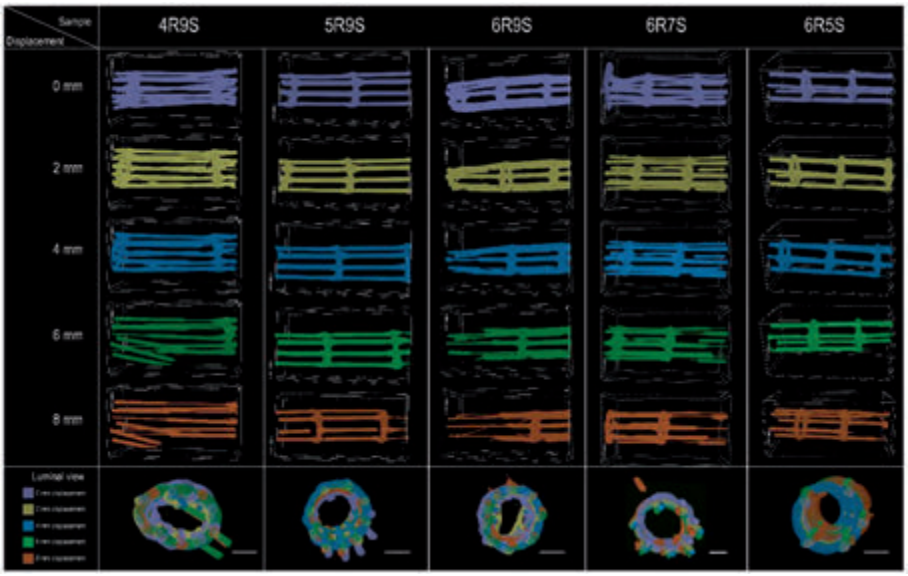

Figure 6. *Micro-CT in combination with longitudinal tensile test data on the rectangular pore design. Images were taken at 0, 2, 4, 6 and 8 mm of strain. Scale bar = 500 µm*

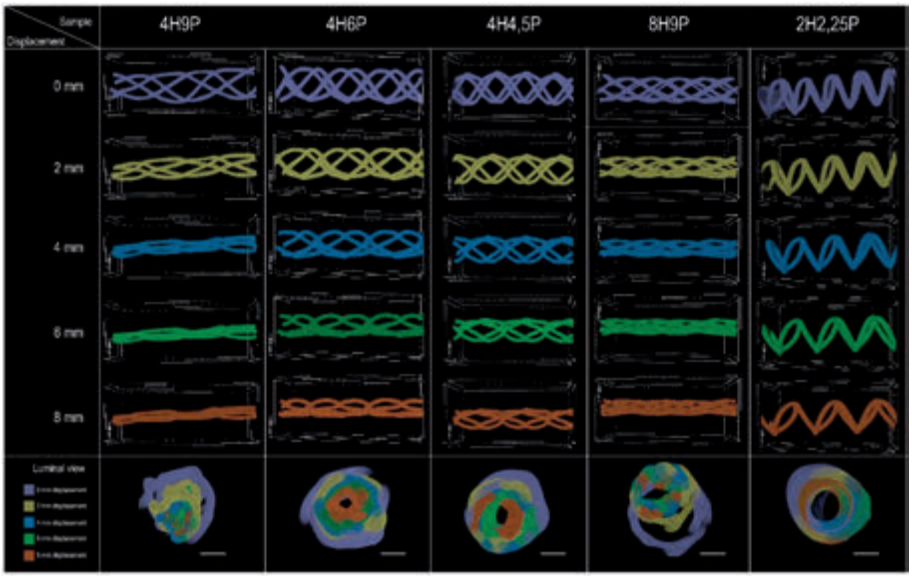

Figure 7. *Micro-CT in combination with longitudinal tensile test data on the diamond pore design. Images were taken at 0, 2, 4, 6 and 8 mm of strain. Scale bar = 500 µm*

decreasing the amount of rings in a design the distance between them increases, therefore the center of the strut would have less support in the radial direction. This explains the fact that with a decreased amount of rings the lumen tend to collapse more. In addition, when having the same amount of rings in the scaffold while reducing the amount of struts revealed no significant difference between the samples (Figure 8B). Comparing the pitch in the diamond design revealed that with a 9 mm pitch per diamond, a significant decrease in lumen size was observed while for a decrease in pitch there was no significant difference (Figure 8C). Data from Figure 8D showed that the lumen size decreases significantly with increasing amount of helices and pitch. Three point bending for hollow tubular structures is not reported often in literature [25]. One limitation of the currently applied method is that it does not calculate the actual lumen size but rather the lumen with the size of luminal wall. In general, the diamond designs have a bigger lumen size compared to the rectangular pore design, indicating that the diamond designs are more resistant to luminal collapse during bending. Therefore, relatively flexible tubular organs such as the carotid artery would benefit from a more helical design rather than a rectangular pore design [39].

The right compliance for vasculature is important in order to ensure its proper function and maintain graft patency [14, 40, 41]. Future studies will aim at matching the compliance of the carotid artery by using the different geometrical designs on the scaffold. For the designs studied here, the hypothesis is that the compliance in the rectangular pore designs might be higher due to the rings present that cannot expand any further without deforming, while the diamond design in general can expand in the radial direction to some extent. The lumen of the scaffold should be completely covered, since the scaffolds are too porous to let a liquid flow through.

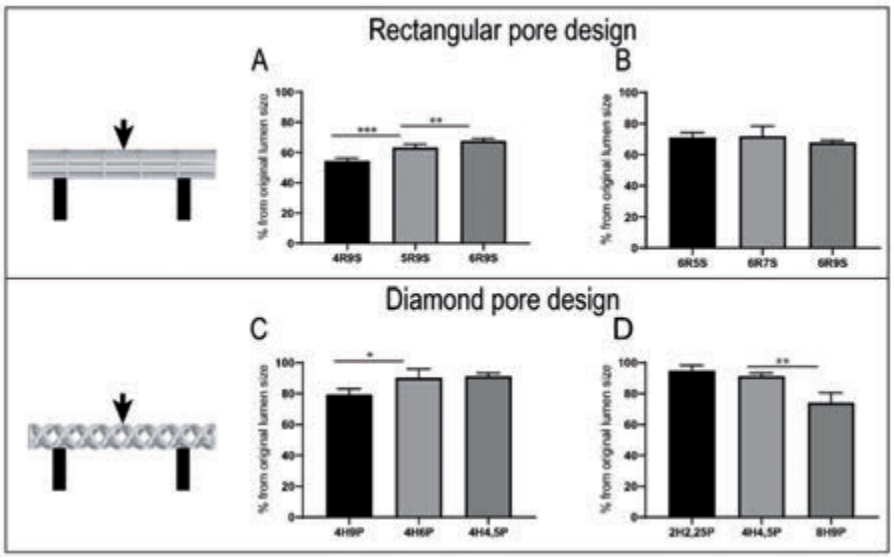

Figure 8. *Image analyses of the lumen at 40% strain during three point bending. (A) The rectangular pore design with increasing amount of rings and the same amount of struts. (B) The rectangular pore design with increasing amount of struts and the same amount rings. (C) The diamond design with the same amount of helices and increasing amount of rotations. (D) The diamond design with increasing amount of helices and rotations and the same amount of total rotations. *p<0.05, ** p<0.01, *** p<0.001.*

A balance needs to be made of having a porous structure while maintaining mechanical properties [42, 43]. Having a highly porous scaffold often means the mechanical properties are weak and vice versa often results in no room for cells to populate the scaffold or risk of mechanical mismatch [44, 45]. In bulk form PCL has a tensile modulus of 363.4 ± 71.6 MPa and a compression modulus of 297.8 ± 7.1 MPa [46]. Here, we highlighted a method to superimpose a range of different mechanical properties for PCL in bulk form that can even decrease the modulus by a factor 1000 in both tensile and compression for both designs. Furthermore, we showed that by having a more porous design such as the helical design the radial compression modulus was often higher to that of the rectangular pore designs. However, on the other hand the tensile modulus was lower in the case of the helical design. Depending on the final application, an appropriate design can be made with this system to tailor the mechanical needs of the scaffold.

Controllable four axis extrusion based additive manufacturing system for vascular tissue regeneration

The main function of vasculature is transport of nutrients and waste disposal, having barrier vital to fulfil that function [47]. A challenge remains to create a barrier function while maintaining porosity with this system. However, a barrier function can be manufactured by combining this with other techniques such as electrospinning [48, 49]. The main problem is that often these barriers are difficult to handle due to collapse or weak mechanical properties [10, 11]. Future studies can aim at combining the techniques in making vasculature with a barrier function that can be handled and with matching mechanical properties.

In this study, the main aim was to create scaffolds for small diameter vessels such as the carotid or coronary artery. The tensile properties of these small diameter vessels are within the range of the diamond pore design (Table 3) [37, 50]. For larger vessels such as the aorta the tensile properties are higher in the range of 2.6 MPa ± 0.3 MPa [51]. The data from this study suggests that the addition of more helices in the diamond pore design could increase the Young's modulus to that of the human aorta. In addition to small and larger diameter vessels, this technique can also be applied to other applications such as the trachea, intestinal system, urogenital system and long bones [52-54]. The mechanical properties of the small intestine for example are within the range the diamond pore design scaffolds [55]. In addition, data from the three point bending test also suggests that this design is capable of bending without a luminal collapse, which is beneficial for the tortuous duodenum. For stiffer tissues such as the trachea and the ureter the rectangular pore design is more suitable since the Young's modulus is within the required properties [56, 57]. Especially when considering that the rings from the rectangular pore design biomimics the tracheal cartilage rings [58, 59]. The mechanical properties of cortical bone are currently stiffer from the designs that were explored here [60]. Multiple layers to the tubular scaffold can be a further strategy to increase the tensile modulus while still maintaining interconnectivity and longitudinal

porosity, which is still not possible to create using other techniques such as melt electrowriting [12].

Table 3. *Tensile properties of various tubular organs and scaffolds.*

Type of tissue	Young's Modulus tensile
Carotid artery	0.7 ± 0.1 MPa [37]
Coronary artery	1.5 ± 0.2 MPa [50]
Aorta	2.6 ± 0.3 MPa [51]
Trachea	13.6 ± 1.5 MPa [56]
Small intestine	0.7 ± 0.2 MPa [55]
Ureter	9.0 ± 1.2 MPa [57]
Cortical bone	18.6 ± 3.5 GPa [60]
Diamond pore design	0.1 ± 0.0 MPa to 1.3 ± 0.2 MPa
Rectangular pore design	5.8 ± 0.2 MPa to 8.6 ± 0.5 MPa

4. Conclusion

In conclusion, we showed a four axis fiber extrusion-based AM technique with full control over design and geometry. Two different designs were chosen and studied further, the rectangular pore and the diamond design. Radial compression data revealed that in general the diamond design had a higher Young's modulus compared to the rectangular pore design. The tensile tests showed that the rectangular pore shape had a higher Young's modulus, in addition to that the lumen size of the diamond reduced with increased strain. Finally analyses from the three-point bending revealed the rectangular pore design is more prone to luminal collapse when bend. With this technique systematic changes in design can be made to alter the mechanical properties for the targeted organ.

Acknowledgements

This work was supported by H2020 FAST (NMP-7, GA n. 685825), and the ERC Cell Hybridge (GA n. 637308). The microCT analyses was supported by the European Regional Development Fund(6695072), through Competitiveness Operational Program 2014-2020, Priority axis 1, ID P_36_611, MySMIS code 107066, INOVABIOMED, Romania

References

[1] M. Nichols, N. Townsend, P. Scarborough, M. Rayner, Cardiovascular disease in Europe: epidemiological update, European heart journal 34(39) (2013) 3028-3034.
[2] Z. Cao, Q. Ye, X. Qian, X. Gu, E. Liang, J. Tang, J. Tang, End-to-End Anastomosis After Segmental Esophagectomy for Early Stage Cervical Esophageal Carcinoma, The Annals of Thoracic Surgery 95(5) (2013) 1815-1817.
[3] J.M. Alsac, E. Fadel, D. Fabre, S. Mussot, J.M. Maury, P. Dartevelle, Resection of Popliteal Artery Aneurysm with End-to-End Anastomosis, EJVES Extra 10(2) (2005) 41-44.
[4] R.I. Mehta, A.K. Mukherjee, T.D. Patterson, M.C. Fishbein, Pathology of explanted polytetrafluoroethylene vascular grafts, Cardiovascular Pathology 20(4) (2011) 213-221.
[5] J. Chlupáč, E. Filova, L. Bačáková, Blood vessel replacement: 50 years of development and tissue engineering paradigms in vascular surgery, Physiological Research 58(Suppl 2) (2009) S119-S139.
[6] T.D. Brown, A. Slotosch, L. Thibaudeau, A. Taubenberger, D. Loessner, C. Vaquette, P.D. Dalton, D.W. Hutmacher, Design and fabrication of tubular scaffolds via direct writing in a melt electrospinning mode, Biointerphases 7(1) (2012) 13.
[7] X. Jing, H.-Y. Mi, M.R. Salick, T.M. Cordie, X.-F. Peng, L.-S. Turng, Electrospinning thermoplastic polyurethane/graphene oxide scaffolds for small diameter vascular graft applications, Materials Science and Engineering: C 49 (2015) 40-50.
[8] H. Du, L. Tao, W. Wang, D. Liu, Q. Zhang, P. Sun, S. Yang, C. He, Enhanced biocompatibility of poly(l-lactide-co-epsilon-caprolactone) electrospun vascular grafts via self-assembly modification, Materials Science and Engineering: C 100 (2019) 845-854.
[9] W. Liu, S. Thomopoulos, Y. Xia, Electrospun nanofibers for regenerative medicine, Advanced healthcare materials 1(1) (2012) 10-25.
[10] M.R. Ladd, T.K. Hill, J.J. Yoo, S.J. Lee, Electrospun nanofibers in tissue engineering, Nanofibers-Production, Properties and Functional Applications, InTechOpen2011.
[11] H. Koh, T. Yong, W. Teo, C. Chan, M. Puhaindran, T. Tan, A. Lim, B. Lim, S. Ramakrishna, In vivo study of novel nanofibrous intra-luminal guidance channels to promote nerve regeneration, Journal of neural engineering 7(4) (2010) 046003.
[12] P.D. Dalton, Melt electrowriting with additive manufacturing principles, Current Opinion in Biomedical Engineering 2 (2017) 49-57.
[13] W. Wu, R.A. Allen, Y. Wang, Fast-degrading elastomer enables rapid remodeling of a cell-free synthetic graft into a neoartery, Nature medicine 18(7) (2012) 1148.
[14] W.M. Abbott, J. Megerman, J.E. Hasson, G. L'Italien, D.F. Warnock, Effect of compliance mismatch on vascular graft patency, Journal of vascular surgery 5(2) (1987) 376-382.
[15] A. Di Luca, I. Lorenzo-Moldero, C. Mota, A. Lepedda, D. Auhl, C. Van Blitterswijk, L. Moroni, Tuning Cell Differentiation into a 3D Scaffold Presenting a Pore Shape Gradient for Osteochondral Regeneration, Advanced healthcare materials 5(14) (2016) 1753-63.
[16] S.C. Baker, G. Rohman, J. Southgate, N.R. Cameron, The relationship between the mechanical properties and cell behaviour on PLGA and PCL scaffolds for bladder tissue engineering, Biomaterials 30(7) (2009) 1321-1328.
[17] M. Centola, A. Rainer, C. Spadaccio, S. De Porcellinis, J. Genovese, M. Trombetta, Combining electrospinning and fused deposition modeling for the fabrication of a hybrid vascular graft, Biofabrication 2(1) (2010) 014102.
[18] R. Suntornnond, J. An, C.K. Chua, Roles of support materials in 3D bioprinting, International Journal of Bioprinting 3(1) (2017) 83-86.
[19] L. Moroni, T. Boland, J.A. Burdick, C. De Maria, B. Derby, G. Forgacs, J. Groll, Q. Li, J. Malda, V.A. Mironov, Biofabrication: A Guide to Technology and Terminology, Trends in biotechnology (2017).
[20] F.B. Coulter, B.S. Coulter, J.R. Marks, A. Ianakiev, Production techniques for 3D printed inflatable elastomer structures: Part I—Fabricating air-permeable forms and coating with inflatable silicone membranes via spray deposition, 3D Printing and Additive Manufacturing 5(1) (2018) 5-16.
[21] F.B. Coulter, B.S. Coulter, E. Papastavrou, A. Ianakiev, Production techniques for 3D printed inflatable elastomer structures: part II—four-axis direct ink writing on irregular double-curved and inflatable surfaces, 3D Printing and Additive Manufacturing 5(1) (2018) 17-28.

[22] F.B. Coulter, M. Schaffner, J.A. Faber, A. Rafsanjani, R. Smith, H. Appa, P. Zilla, D. Bezuidenhout, A.R. Studart, Bioinspired heart valve prosthesis made by silicone additive manufacturing, Matter 1(1) (2019) 266-279.
[23] D. Lei, B. Luo, Y. Guo, D. Wang, H. Yang, S. Wang, H. Xuan, A. Shen, Y. Zhang, Z. Liu, 4-Axis printing microfibrous tubular scaffold and tracheal cartilage application, Science China Materials (2019) 1-11.
[24] A. Guerra, A. Roca, J. de Ciurana, A novel 3D additive manufacturing machine to biodegradable stents, Procedia Manufacturing 13 (2017) 718-723.
[25] E. McColl, J. Groll, T. Jungst, P.D. Dalton, Design and fabrication of melt electrowritten tubes using intuitive software, Materials & Design 155 (2018) 46-58.
[26] R.L. Truby, J.A. Lewis, Printing soft matter in three dimensions, Nature 540 (2016) 371.
[27] H.-C. Han, J.K.W. Chesnutt, J.R. Garcia, Q. Liu, Q. Wen, Artery buckling: new phenotypes, models, and applications, Annals of biomedical engineering 41(7) (2013) 1399-1410.
[28] G. Langewouters, A. Zwart, R. Busse, K. Wesseling, Pressure-diameter relationships of segments of human finger arteries, Clinical physics and physiological measurement 7(1) (1986) 43.
[29] R.S. Sidhu, J. Park, R. Brydges, H.M. MacRae, A. Dubrowski, Laboratory-based vascular anastomosis training: A randomized controlled trial evaluating the effects of bench model fidelity and level of training on skill acquisition, Journal of Vascular Surgery 45(2) (2007) 343-349.
[30] F. Venail, P. Sabatier, M. Mondain, F. Segniarbieux, C. Leipp, A. Uziel, Outcomes and complications of direct end-to-side facial-hypoglossal nerve anastomosis according to the modified May technique, Journal of neurosurgery 110(4) (2009) 786-791.
[31] C. Simillis, S. Purkayastha, T. Yamamoto, S.A. Strong, A.W. Darzi, P.P. Tekkis, A Meta-Analysis Comparing Conventional End-to-End Anastomosis vs. Other Anastomotic Configurations After Resection in Crohn's Disease, Diseases of the Colon & Rectum 50(10) (2007) 1674-1687.
[32] F.J. Chaparro, M.E. Matusicky, M.J. Allen, J.J. Lannutti, Biomimetic microstructural reorganization during suture retention strength evaluation of electrospun vascular scaffolds, Journal of Biomedical Materials Research Part B: Applied Biomaterials 104(8) (2016) 1525-1534.
[33] C. McIlroy, P.D. Olmsted, Disentanglement effects on welding behaviour of polymer melts during the fused-filament-fabrication method for additive manufacturing, Polymer 123 (2017) 376-391.
[34] G.B. Chapman, W. Durante, J.D. Hellums, A.I. Schafer, Physiological cyclic stretch causes cell cycle arrest in cultured vascular smooth muscle cells, American Journal of Physiology-Heart and Circulatory Physiology 278(3) (2000) H748-H754.
[35] M. Stekelenburg, M.C. Rutten, L.H. Snoeckx, F.P. Baaijens, Dynamic straining combined with fibrin gel cell seeding improves strength of tissue-engineered small-diameter vascular grafts, Tissue engineering. Part A 15(5) (2009) 1081-9.
[36] S.J. Lee, D.N. Heo, J.S. Park, S.K. Kwon, J.H. Lee, J.H. Lee, W.D. Kim, I.K. Kwon, S.A. Park, Characterization and preparation of bio-tubular scaffolds for fabricating artificial vascular grafts by combining electrospinning and a 3D printing system, Physical Chemistry Chemical Physics 17(5) (2015) 2996-2999.
[37] K.A. McKenna, M.T. Hinds, R.C. Sarao, P.-C. Wu, C.L. Maslen, R.W. Glanville, D. Babcock, K.W. Gregory, Mechanical property characterization of electrospun recombinant human tropoelastin for vascular graft biomaterials, Acta biomaterialia 8(1) (2012) 225-233.
[38] C.G. Jeong, S.J. Hollister, A comparison of the influence of material on in vitro cartilage tissue engineering with PCL, PGS, and POC 3D scaffold architecture seeded with chondrocytes, Biomaterials 31(15) (2010) 4304-4312.
[39] P. Pancera, M. Ribul, B. Presciuttini, A. Lechi, Prevalence of carotid artery kinking in 590 consecutive subjects evaluated by Echocolordoppler. Is there a correlation with arterial hypertension?, Journal of Internal Medicine 248(1) (2000) 7-12.
[40] L. Morris, F. Stefanov, N. Hynes, E.B. Diethrich, S. Sultan, An Experimental Evaluation of Device/Arterial Wall Compliance Mismatch for Four Stent-Graft Devices and a Multi-layer Flow Modulator Device for the Treatment of Abdominal Aortic Aneurysms, European Journal of Vascular and Endovascular Surgery 51(1) (2016) 44-55.
[41] W. Trubel, A. Moritz, H. Schima, F. Raderer, R. Scherer, R. Ullrich, U. Losert, P. Polterauer, Compliance and formation of distal anastomotic intimal hyperplasia in Dacron mesh tube constricted veins used as arterial bypass grafts, ASAIO J 40(3) (1994) M273-8.

[42] V. Weißmann, R. Bader, H. Hansmann, N. Laufer, Influence of the structural orientation on the mechanical properties of selective laser melted Ti6Al4V open-porous scaffolds, Materials & Design 95 (2016) 188-197.
[43] C. Torres-Sanchez, F.R.A. Al Mushref, M. Norrito, K. Yendall, Y. Liu, P.P. Conway, The effect of pore size and porosity on mechanical properties and biological response of porous titanium scaffolds, Materials Science and Engineering: C 77 (2017) 219-228.
[44] L. Xue, H.P. Greisler, Biomaterials in the development and future of vascular grafts, Journal of vascular surgery 37(2) (2003) 472-480.
[45] M.-F. Guidoin, Y. Marois, J. Bejui, N. Poddevin, M.W. King, R. Guidoin, Analysis of retrieved polymer fiber based replacements for the ACL, Biomaterials 21(23) (2000) 2461-2474.
[46] S. Eshraghi, S. Das, Mechanical and microstructural properties of polycaprolactone scaffolds with one-dimensional, two-dimensional, and three-dimensional orthogonally oriented porous architectures produced by selective laser sintering, Acta Biomaterialia 6(7) (2010) 2467-2476.
[47] N.B. Langer, N.B. Hamid, T.M. Nazif, O.K. Khalique, T.P. Vahl, J. White, J. Terre, R. Hastings, D. Leung, R.T. Hahn, Injuries to the aorta, aortic annulus, and left ventricle during transcatheter aortic valve replacement: management and outcomes, Circulation: Cardiovascular Interventions 10(1) (2017) e004735.
[48] T. Jungst, I. Pennings, M. Schmitz, A.J.W.P. Rosenberg, J. Groll, D. Gawlitta, Heterotypic Scaffold Design Orchestrates Primary Cell Organization and Phenotypes in Cocultured Small Diameter Vascular Grafts, Advanced Functional Materials 0(0) (2019) 1905987.
[49] H.P. Janke, J. Bohlin, R.M.L.M. Lomme, S.M. Mihaila, J. Hilborn, W.F.J. Feitz, E. Oosterwijk, Bioinspired coupled helical coils for soft tissue engineering of tubular structures – Improved mechanical behavior of tubular collagen type I templates, Acta Biomaterialia 59 (2017) 234-242.
[50] A. Karimi, M. Navidbakhsh, A. Shojaei, S. Faghihi, Measurement of the uniaxial mechanical properties of healthy and atherosclerotic human coronary arteries, Materials Science and Engineering: C 33(5) (2013) 2550-2554.
[51] D.A. Vorp, B.J. Schiro, M.P. Ehrlich, T.S. Juvonen, M.A. Ergin, B.P. Griffith, Effect of aneurysm on the tensile strength and biomechanical behavior of the ascending thoracic aorta, The Annals of Thoracic Surgery 75(4) (2003) 1210-1214.
[52] T. Nakamura, T. Sato, M. Araki, S. Ichihara, A. Nakada, M. Yoshitani, S.-i. Itoi, M. Yamashita, S.-i. Kanemaru, K. Omori, Y. Hori, K. Endo, Y. Inada, K. Hayakawa, In situ tissue engineering for tracheal reconstruction using a luminar remodeling type of artificial trachea, The Journal of Thoracic and Cardiovascular Surgery 138(4) (2009) 811-819.
[53] S.S. Kim, R. Penkala, P. Abrahimi, A Perfusion Bioreactor for Intestinal Tissue Engineering, Journal of Surgical Research 142(2) (2007) 327-331.
[54] M. Magnan, P. Levesque, R. Gauvin, J. Dube, D. Barrieras, A. El-Hakim, S. Bolduc, Tissue Engineering of a Genitourinary Tubular Tissue Graft Resistant to Suturing and High Internal Pressures, Tissue Engineering Part A 15(1) (2009) 197-202.
[55] V.I. Egorov, V. Schastlivtsev, R.A. Turusov, A.O. Baranov, Participation of the intestinal layers in supplying of the mechanical strength of the intact and sutured gut, European surgical research. Europaische chirurgische Forschung. Recherches chirurgicales europeennes 34(6) (2002) 425-31.
[56] C.R. Roberts, J.K. Rains, P.D. Paré, D.C. Walker, B. Wiggs, J.L. Bert, Ultrastructure and tensile properties of human tracheal cartilage, Journal of biomechanics 31(1) (1997) 81-86.
[57] Y. Shilo, J.E. Pichamuthu, T.D. Averch, D.A. Vorp, Evaluation of the tensile strength of the human ureter--preliminary results, Journal of endourology 28(12) (2014) 1470-3.
[58] S. Ley, D. Mayer, B. Brook, E. van Beek, C. Heussel, D. Rinck, R. Hose, K. Markstaller, H.-U. Kauczor, Radiological imaging as the basis for a simulation software of ventilation in the tracheo-bronchial tree, European radiology 12(9) (2002) 2218-2228.
[59] W. Wu, S. Jia, W. Chen, X. Liu, S. Zhang, Fast degrading elastomer stented fascia remodels into tough and vascularized construct for tracheal regeneration, Materials Science and Engineering: C 101 (2019) 1-14.
[60] J.Y. Rho, R.B. Ashman, C.H. Turner, Young's modulus of trabecular and cortical bone material: ultrasonic and microtensile measurements, J Biomech 26(2) (1993) 111-9.

Supplementary material

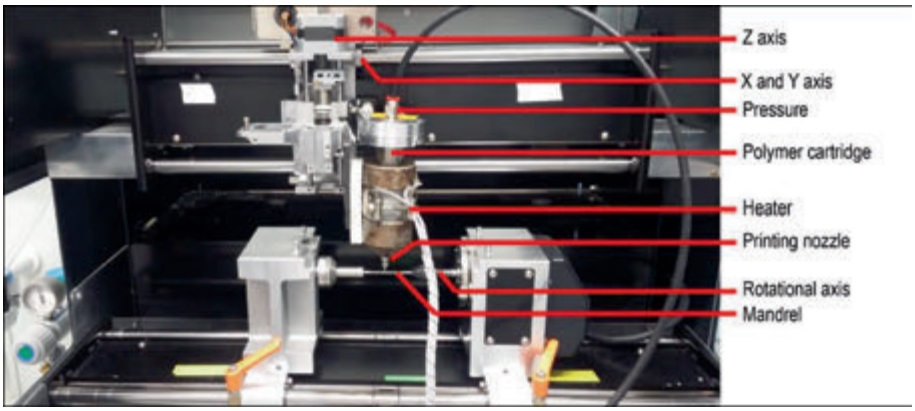

***Figure S1**. Overview of the printer and indicated parts.*

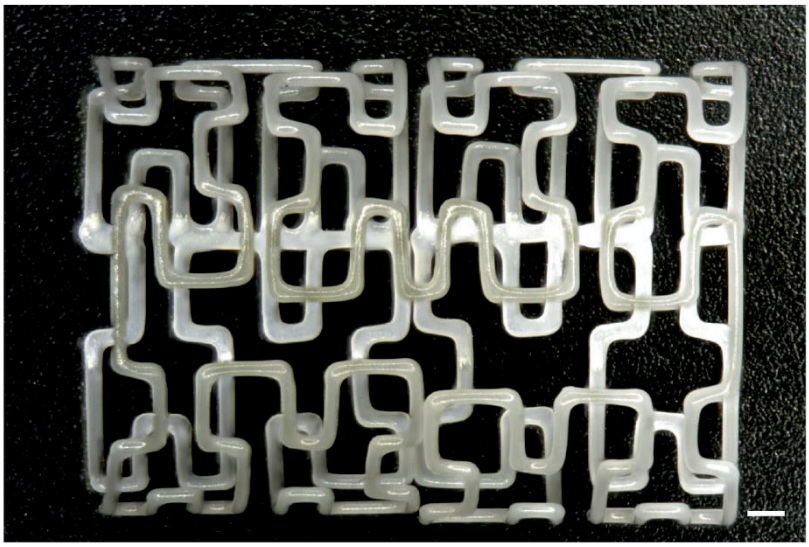

***Figure S2.** Fourth generation Hilbert curve scaffold printed on a 12 mm mandrel. Scale bar represents 1 mm.*

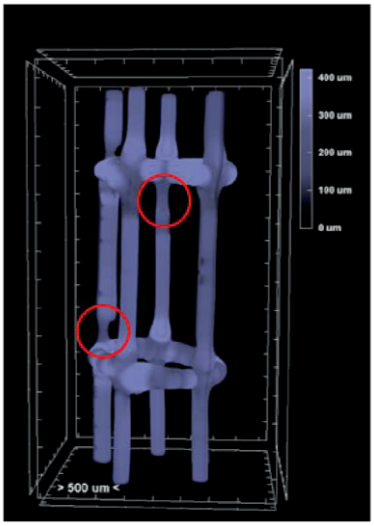

Figure S3. *Micro-CT image of the 6R5S scaffold at 0 mm displacement with inconsistencies in fiber diameter indicated by the red circles.*

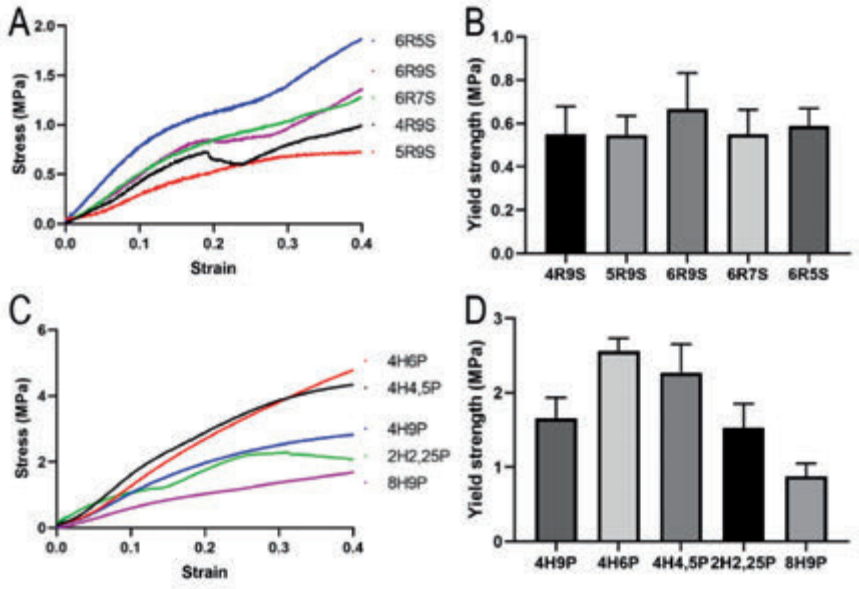

Figure S4. *Radial compression test with a strain rate of 1% per second (A) Representative stress strain curves of the rectangular pore design. (B) Yield strength of rectangular pore design. (C) Representative stress strain curves of the diamond pore design. (D) Yield strength of the diamond pore design.*

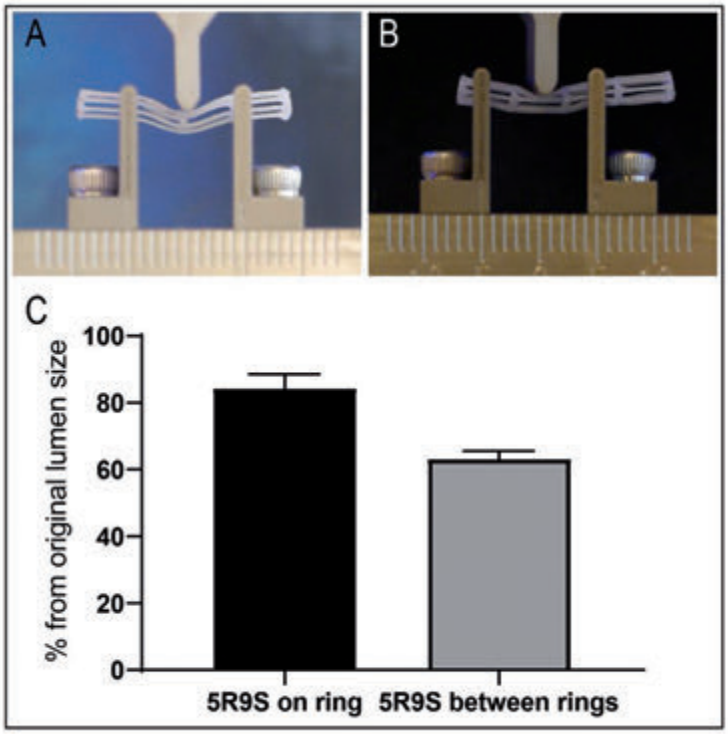

Figure S5. *Three point bending at 40% deformation on the 5R9S design. (A) Three point bending at 40% deformation on the 5R9S design when the probe is centred on top of the ring. (B) Three point bending at 40% deformation on the 5R9S design when the probe is centred between two rings. (C) Difference in luminal diameter at 40% deformation during three point bending on the 5R9S design.*

Chapter 6

Scaffolds with a tuneable non-linear elastic region using a corrugated design

Scaffolds with a tuneable non-linear elastic region using a corrugated design*

Kenny A. van Kampen[1], Tim ten Brink[1], Carlos Mota[1], Lorenzo Moroni[1]

[1]Department of Complex Tissue Regeneration, MERLN Institute for Technology-Inspired Regenerative Medicine, Maastricht University, Universiteitssingel 40, 6229ER Maastricht, The Netherlands

***Chapter published in Small structures 2024, DOI: 10.1002/sstr.202300399**

Abstract

Elastin is the main component of arteries and is responsible for their high elastic high strain capacity. The biomechanics of biological tissues typically display a stress-strain curve characterized by a sigmoidal shape that has an initial region with low stress and high strain. Studies aimed at mimicking such biomechanical behaviour focused on improving the synthesis of elastin or replicating elastin behaviour. However, this proves to be a continuous challenge. Alternatively, the design of the scaffold could potentially mimic the sigmoidal stress-strain curve of an artery. Hence, the aim of this study was to replicate the stress-strain curve of a carotid artery using a tailorable corrugated design. The results showed that the corrugated design unfolded during extension without generating significant stress and displayed a sigmoidal stress-strain curve that could be controlled depending on the corrugation features. Editing the amount of fibres resulted in a different Young's modulus, while parameters such as the amplitude of the fibres and the amount of repeating units influenced the initial non-linear region of the stress-strain curve. In addition, scaffolds made of poly(ε-caprolactone) (PCL)

and Poly(ethylene oxide terephthalate)/poly(butylene terephthalate (PEOT/PBT) were compared to determine the applicability of our design principles to different biodegradable polymers that normally do not have the same biomechanical behavior of soft tissues like arteries. Finally, the corrugated design was compared to both porcine and caprine carotid arteries. The results highlight that the corrugated design could serve as a biomimicry approach for vascular grafts. In addition, the optimized designs had a similar stress-strain curve within the physiological range as porcine arteries.

1. Introduction

Materials such as metals [1] and polymers [2], with a high elastic strain are of interest in many studies focusing on stent design, vascular and tissue engineering. High elastic strain can also naturally occur in certain proteins such as elastin and resilin [3, 4]. These elastic materials often show a stress-strain curve that is characterized with a sigmoidal shape, which has an initial region with a low stress and high strain [5]. Especially in blood vessels, elasticity is important, as it improves the pumping efficiency of the heart [6]. The overall wall thickness of each vessel varies throughout the body in order to facilitate the fluctuations in blood pressure. Each type corresponds to a unique structural composition of cell types, elastin and collagen that cumulatively define the unique stress/strain behavior of a vessel [7]. Together, this complex microenvironment is capable of withstanding physiological compliance ranging between 3-12% / 100mmHg with minimal energy loss [8]. Specifically, elastin has a pivotal role in elasticity *in vivo* [9], whereas too little elastin content can result in arterial stiffening [10]. The amount of elastin dictates the shape of the stress-strain curve. In general, arteries or veins that have less elastin content have flattened stress-strain curves and a higher Young's modulus [11, 12]. The initial part of the stress-strain curve within arteries is mainly elastin dominated and allows for a significant strain to occur on the artery whilst subjecting the tissue to minimal amounts of stress. This

region is consistent with the loading mechanics of elastin fibers and mainly serves to support physiological pressures [7, 13]. Whereas the elastin region has a low Young's moduli in the 0.2-0.6 MPa range, this range increases tenfold as the upturning region is reached and stress becomes collagen dominated (2-6 MPa) [13]. Mimicking the sigmoidal stress-strain curve with synthetic scaffolds proves to be challenging.

There are mainly two ways to obtain a sigmoidal shaped stress-strain curve. First, this is usually achieved with the inherent material properties, for example a dynamic hydrogel network with reversible crosslinks [14]. Another examples is from elastin itself that disentangles when stretched [15]. Even though this macromolecular disentanglement behavior is found *in vivo*, mimicking the complex assembly of elastin into elastic fibers proves to be challenging as well [16]. Another way to obtain a sigmoidal stress-strain curve is through design of the pore architecture of a scaffold, even with materials that inherently do not have any elastic behavior [17]. A method to mimic the elastin behavior can be achieved, for example, through a mesh of small diameter fibers that can disentangle before the individual fibers are stretched [18]. A different method for larger diameter fibers can be seen in many stent designs that can extend through fibers bending [19]. Many of these stents show some degree of flexibility, yet they are made of alloys such as cobalt-chrome or nickel-titanium [20]. The bulk properties of these materials display no sigmoidal stress-strain curve and an ultimate tensile strength in the Giga Pascal range, far too stiff for vascular grafts [21, 22]. Polymeric stents on the other hand use materials that have improved bulk properties [23, 24]. Additional benefits are that these can be made out of biodegradable polymers [25] and can be functionalized with anti-coagulants to reduce thrombosis and lower the risk of graft rejection [26, 27]. Certain polymeric stent designs are also able to compress and extend in radius, allowing them to be deployed using balloon catheters [28, 29]. Finally, the difficulty of manufacturing polymeric stents has decreased in recent years [30].

Additive manufacturing can be used to fabricate these complicated designs with high precision [31]. Specifically, manufacturing techniques that have a cylindrical collecting surface such as fused deposition modeling [23] and melt electrowriting [32] are of great interest to produce tubular structures. The combination of these techniques and a design that is minimalistic could result in a scaffold that offers tunable elastic like features. This in turn could potentially mimic the characteristic non-linear mechanical behavior of a major artery [33]. FDM-based methodologies also show high potential in on-demand printing of vascular grafts through the large range of usable materials and freedom in design orientation [34]. Although effective and highly customizable, the complex tubular design of the vasculature is often difficult to print and may therefore fall short in mechanical rigidity [23, 35].

Hence, the aim of this study is to develop a new method to create corrugated tubular scaffolds and investigate the influence of the scaffolds' architecture on the mechanical properties. This design could potentially be used for vascular tissue engineering. The correct replication of many of the mechanical properties such as compliance, diameter range, graft size and Young's modulus can have highly beneficial effects on the long-term patency of synthetic grafts. Finally, the mechanical behavior of the designs where compared to carotid arteries.

2. Materials and methods

2.1 Scaffold fabrication

A four-axis extrusion based system was used, as previously described, to fabricate the scaffolds [23]. Briefly, polymer pellets were loaded in a cartridge and heated until the polymer melted. Afterwards, the polymer melt was extruded through a 260 micron diameter nozzle (25G encapsulation needle, DL technology) using pressure and deposited on a 4 mm diameter stainless steel mandrel. For poly(ε-caprolactone) (PCL, Mn =45,000 g mol-1, Sigma-

Aldrich) the temperature was set at 110 °C, and extruded at a pressure of 4 bar. Poly(ethylene oxide terephthalate)/poly(butylene terephthalate (PEOT/PBT), comprising 1000 g/mol average molecular weight PEO and a PEOT:PBT weight ratio of 70:30, was heated until 175 °C , and extruded at a pressure of 5 bar.

2.2 Scaffold design

A script was written in Python 3.7 (64-bit) to create the corrugated pattern with both adjustable and fixed parameters. The fixed parameters used throughout the study were the length of each segment (5mm), the printing speed of 1,5 mm/s and the total amount of segments per scaffold (set at 4). The adjustable parameters consisted of changes in the amplitude, strut fiber quantity and the frequency of repeating units within one segment (Figure 1A). Each segment was closed with a ring at both ends. The scaffolds were labelled according to the maximum amplitude of the fiber in degrees (AM), the amount of units per fiber (U) and the amount of fibers per segment (F). For instance, AM100U2F7 has a maximum amplitude of 100°, with 2 units per fiber and contains 7 fibers per segment. Scaffold designs were visualized in 3D-models using the Rhinoceros 6.0 modelling software and a custom written grasshopper® graphical plugin. To visualize the damage upon stretching during the luminal fiber recovery test, a complementary microfiber lumen was created on the inner side of the corrugated scaffolds following previously established methodologies [36]. Briefly, the lumen was fabricated through melt spinning using an external DC motor with a fixed rotational speed of ~1100RPM. Fiber extrusion was set at similar parameters of the skeletal support structure whilst moving over the longitudinal (*X*) axis at 1mm/s, hereby forming a tubular lumen on which the remainder of the scaffold was printed.

2.3 Scaffold characterization

A stereomicroscope (SMZ25, Nikon instruments) with a dark field illuminator (Nikon instruments) was used to visualize the scaffold structure. The diameter

of the filaments, the angle of the fibres and the distance between each fibre were measured with the stereomicroscope. Visualization of the microfiber structures was performed through Scanning Electron Microscopy (*JOEL JSM-IT SEM*). Samples were fixed using JOEL adhesive carbon tape and sputter coated in gold (*SC7620, Quorum*), followed by SEM imaging with an SED accelerating voltage of 10-20kV (*WD. 12-14mm, Mag. 25x-30x*). The microfiber resilience to uniaxial strain was quantified using the FIJI open-source imaging software by measuring pore volume expressed in percentage of deformed luminal surface (*%*) on the varying degrees of uniaxial scaffold strain.

2.4 Mechanical testing

Mechanical characterization was performed on a mechanical tester (ElectroForce, TA instruments) with a 45 Newton load cell (4.5kg/cm^2, Electroforce). Tensile tests were performed in the longitudinal direction. A 4 mm diameter stainless steel rod was partially inserted on both sides of the scaffold so that one segment on each end was covered. After mounting the stainless steel rods, parafilm (Heathrow Scientific) was wrapped around the segment to prevent slippage during the tensile test. The samples were uniaxially stretched at a rate of 1% strain per second up to a total displacement of 400% or until break. The loading and unloading cycles were performed until 110% strain with a strain rate of 10% per second for 10 cycles. Both tensile and load and unloading tests were captured with a camera (DMC-G3, Panasonic) with a macro-lens (Panagor 90mm f2.8, Komine). Images and videos were analyzed using ImageJ (Version 1.52p, NIH) and Adobe Premiere Pro (Version 12.0, Premiere Pro CC 2018).

The obtained force displacement values from the mechanical tester were converted to stress and strain. The yield strength was obtained as the maximum force value before rupture. The Young's modulus was calculated as the slope in the linear part of the stress-strain curve before plastic deformation. The yield strain was calculated as the point when the plastic deformation

started. The toughness was calculated as the area under the stress-strain curve until plastic deformation. The toe region of the samples were calculated using three different methods. A schematic representation is shown in figure 1B. The first one was described by Freed et al. and defined as the initial linear part of the curve [37]. This was immediately followed up by a heel region, which is the non-linear transition zone between the toe region and linear elastic region. The second method was described by Vegas et al. as the nonlinear high compliance region of the stress strain curve that ends right before the start of the linear elastic region [38]. This method did not include a heel region. Finally Chandrashekar et al. calculated the toe region by approximating both the toe and linear regions as straight lines and calculate the intersection point between these two straight lines [39]. The luminal fiber recovery test under physiological strain were performed using similar settings as the tensile test. The testing limits were set at 10% strain, which represents values within physiological strain or 100% strain, which represents definite strain. The samples were carefully removed and snap-frozen in liquid nitrogen. An untested sample (0% strain) was used as control.

2.5 Finite element modeling

COMSOL multiphysics (Version 6.0, Comsol B.V.) was used to simulate the tensile test of the scaffolds. A 3D computer assisted design (CAD) model of the scaffolds was made using a custom written plug-in for Rhino Grasshopper (Rhino 6, Version 6.24, Robert McNeel & Associates) that converts the programmed X-Y-Z and Axial movements into a 3D model. During the tensile simulation one of the ends was fixed while the other end a 5 mm displacement, the equivalent to 100% strain was simulated in steps of 0.5 mm.

2.6 Carotid artery preparation

Both porcine and caprine arteries were kindly donated from the Central Animal Testing Facility (CPV) in Maastricht, right after animal sacrifice of other animal studies where arteries were not involved. Leftover carotid arteries were

excised from the animals and kept in PBS. The arteries were prepared for tensile analyses by cutting them in pieces of approximately 15 mm in length. Caprine (n=2) and porcine (n=6) arteries were obtained and further divided in 6 and 16 pieces for tensile testing respectively. The inner diameter and thickness of the wall was measured using a caliper. Comparable to the developed scaffolds, the arterial samples were fixed around stainless steel rods (*2.5 mm initial axial displacement*) and put under a controlled strain until tissue rupture occurred.

2.7 Incremental fatigue analysis

The *in-vivo* patency of a scaffold can be determined by its resilience to fatigue under physiological conditions and is tested by subjecting the sample to continuous cycles of natural strain. In this study, the cyclic resilience was quantified using mechanical loading of scaffolds at continuously increasing levels of strain. To induce incremental fatigue, software commands were set up to induce a sinusoidal waveform displacement (*Maximum Displacement - 5/5mm*), administering a 10% uniaxial strain. Each sample was subjected to a total of 100 cycles at a speed of 1Hz (*60 cycles/minute*) representative of a physiological heartbeat in resting state following previously conducted research by Chapman et al. [40] After successive exposure to 100 cycles, the waveform strain was raised by 10% for a further 100 cycles, which was repeated until sample failure or a total displacement of 100% was reached. Fatigue test data was processed in material stress (*σ, N/mm2*) over fatigue cycles (*cycles/time*).

2.8 Statistical analyses

Statistical analyses were performed with GraphPad Prism 8.1.2. Datasets were grouped according to sample design from which the population mean (μ) and standard deviations (*SD*) were calculated. Significant differences were tested using a student's t-test and were considered significant when $p < 0.05$. Statistical analyses for grouped datasets were assessed using 2-way analysis

of variance (*ANOVA*) with multiple comparison (*mixed model*), followed by either Tukey honestly significant difference (*HSD*) or Šidák correction post-hoc analysis to confirm significance between variables.

3. Results

The nomenclature used to classify the scaffolds developed herein is shown in figure 1. Briefly, scaffolds were fabricated with a four axis extrusion based system in a corrugated pattern. In this study, various parameters in the pattern were changed to investigate the influence on the mechanical properties.

3.1 The effect of amplitude variation on the mechanical properties

Various PCL scaffolds with different amplitudes were fabricated. The amount of repeating units per segment and fibers were kept constant at 2 and 7 respectively (U2F7). Table 1 shows the fiber size and angle between the samples. There was a minor variation observed in fiber size between the samples ranging from 434 µm up to 508 µm in the AM0 and AM150 respectively. In addition, the angle of the fiber between the units decreased with the increase in amplitude. Figure 2A depicts an overview of the samples.

Table 1. *Overview of the tested corrugated patterns with varying amplitude.*

Sample	**AM0**	**AM100**	**AM150**	**AM200**
Fiber size (µm)	434 ± 20	501 ± 25	508 ± 30	439 ± 23
Fiber angle (°)	N/A	55.7 ± 0.9	63.2 ± 1.1	70.0 ± 1.0
Toe region method 1 (strain %)	N/A	29.9 ± 6.0	40.1 ± 7.8	69.1 ± 6.3
Toe region method 2 (strain %)	N/A	78.6 ± 1.0	127.3 ± 10.2	182.1 ± 5.5
Toe region method 3 (strain %)	N/A	63.1 ± 2.8	103.7 ± 3.7	158.7 ± 9.7

Analyses of the stress-strain curves revealed that the increase in amplitude caused an extension in the non-linear region (Figure 2B). The Young's modulus decreased significantly with the introduction of the corrugated pattern

from 1043.0 ± 42.1 KPa to 100.7 ± 13.8 KPa in the AM0 and AM150 samples respectively. However, with the corrugated pattern the Young's modulus remained similar (Figure 2C). In addition, the yield strength of the scaffold decreased significantly from 13.2 ± 0.8 N to 8.0 ± 1.3 N in the AM0 and AM200 samples respectively (Figure 2D). While the yield strain increased significantly from 20.7 ± 2.2% to 225.2 ± 19.8% strain in the AM0 and AM200 samples respectively (Figure 2E). The toughness seemed to increase from 189.3 ± 30.4 $N*mm^2$ to 556.2 ± 95.9 $N*mm^2$ in the AM0 and AM200 samples respectively (Figure 2F).

Comparing the three different methods for calculating the toe region revealed that method 1 gave the smallest toe region, method 3 an intermediate and method 2 the largest toe region. In all three methods, the toe region increased with the increasing amplitude. Interesting to note was that the samples in the first part of the nonlinear region twisted to the inside and constricted the lumen of the scaffold while it widened again in the second part of the nonlinear region (Figure S1, Video S1). This constricting effect was more evident with an increase in amplitude. Finite element modelling showed this similar effect (Figure 3). The corrugated pattern caused a better stress distribution when stretched compared to a scaffold with straight fibers. In addition, it was noted that in the corrugated pattern the stress builds up at the edges of the fiber rather than the middle of the fiber. The results also showed that it was impossible to increase the strain up to 100% in the AM0 samples without breaking the samples.

3.2 The effect of multiple repeating units on the mechanical properties

Various PCL scaffolds with different amount of repeating units were printed as shown in figure 4A. The amplitude was reduced with increasing amount of repeating units to keep the non-linear part similar between designs. The

Scaffolds with a tuneable non-linear elastic region using a corrugated design

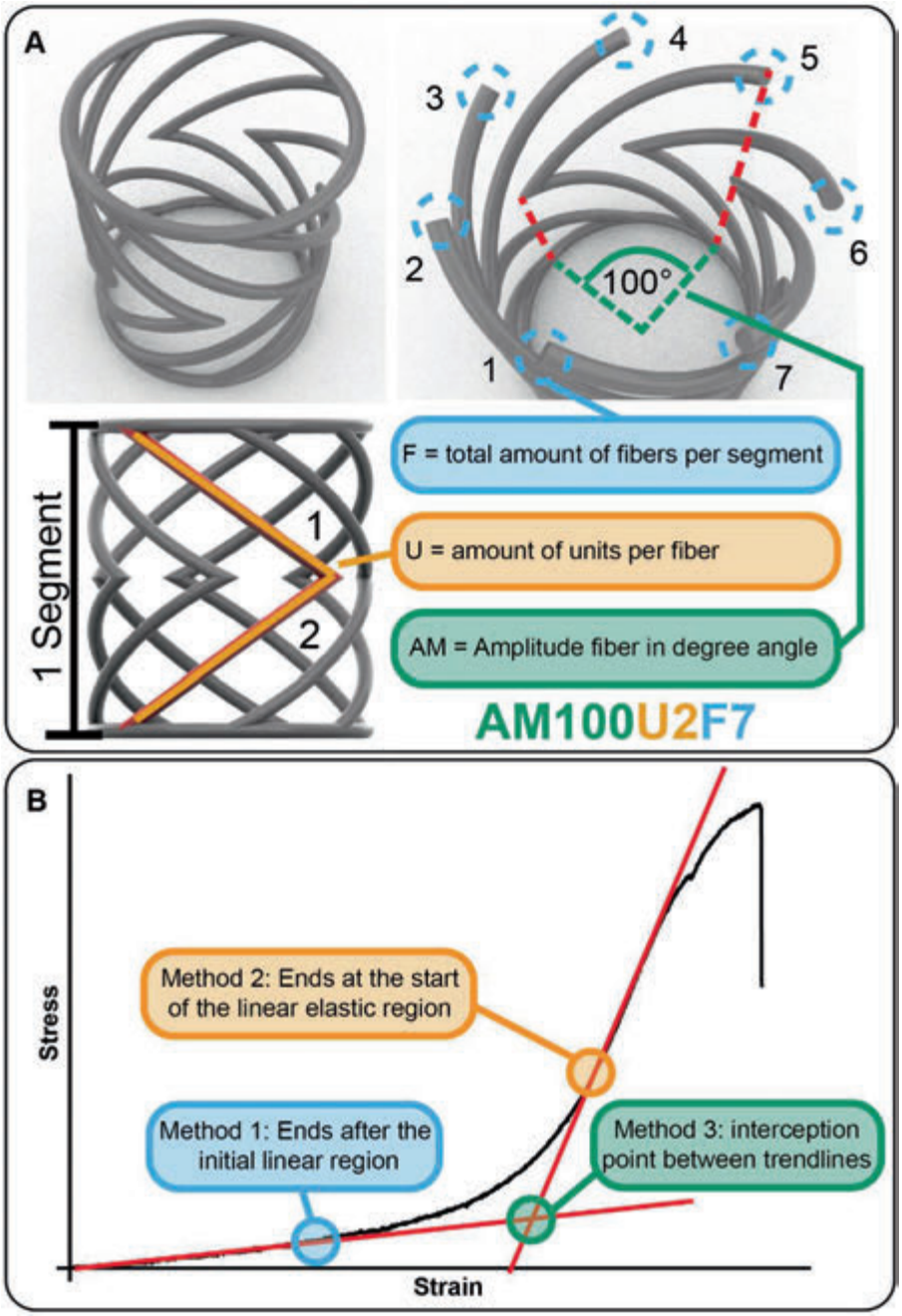

Figure 1. *Corrugated scaffold pattern. (A) Nomenclature of the corrugated pattern with the AM100U2F7 as example. (B) Example stress-strain curve with the different methods to calculate the toe region.*

amount of fibers per segment was kept constant at seven (F7). Table 2 shows an overview of the tested parameters. The fiber size between designs were similar with the smallest fiber diameter in the AM133U3 samples and the largest fiber in the AM80U5 fiber at 471 and 499 μm respectively. The fiber angle also remained similar even though the amplitude in every fiber of each sample was different. The representative stress-strain curves showed that there was an additional inflection point observed with the increasing amount of repeating units (Figure 4B). This overall resulted in a flattening of the stress-strain curve. After a closer inspection on the video data, it was observed that this initial inflection points corresponded to the corners of the fibers in the units tearing up while extending (Figure S2). After 40% strain, when the AM80U5 kept stretching until the fibers broke at around 210% strain. Figure 4C shows that the Young's modulus decreased with the increasing amount of units repeating per segment from 128.1 KPa to 54.9 KPa at 2 and 5 units per fiber respectively. Whereas the other values such as the yield strength, yield strain and the toughness remained similar between the designs, assuming that the yield point was reached right before the scaffold broke. The calculation for the toe region using method 1 showed that the toe region increased with the amount of units per fibers from 74.6% to 83.8%.

However, the second method showed an opposite trend with the largest toe region at 180.8% in AM200U2 samples and the smallest at 161.7% in the AM133U3 samples. The toe region for both the AM100U4 and AM80U5 samples could not be calculated, since the stress-strain curve was no longer sigmoidal shaped. To validate whether the scaffolds were operating in the elastic region, multiple loading and unloading cycles were performed until 110% strain. Figure 5A showed full recovery of the AM200U2 while the AM80U5 samples did not recover while the corners showed signs of tearing upon extension until 110% strain (Figure5B). This resulted in the scaffold buckling after the unloading cycle at 0%.

Scaffolds with a tuneable non-linear elastic region using a corrugated design

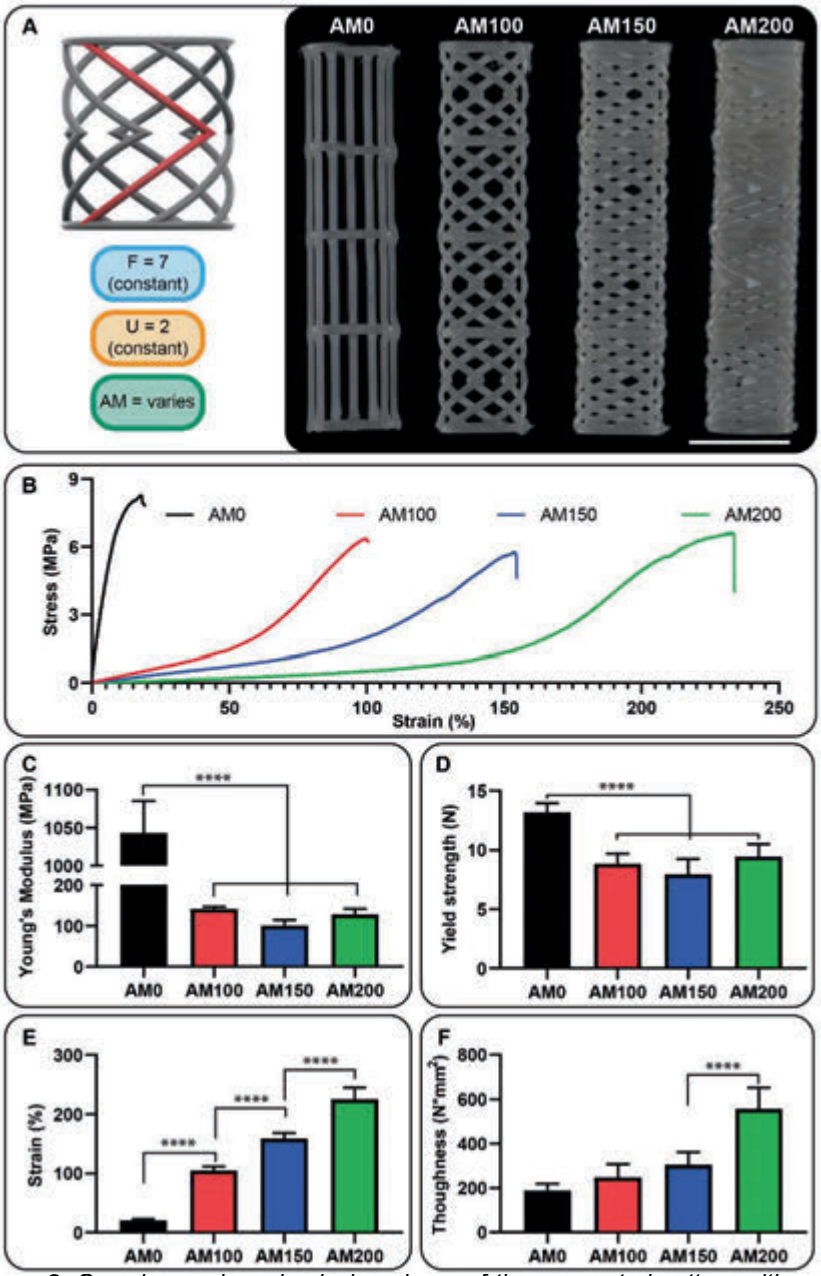

Figure 2. *Overview and mechanical analyses of the corrugated pattern with varying amplitude. (A) Stereomicroscopy images of the tested scaffolds. (B) Representative stress-strain curve of the tested designs. (C) Young's modulus, (D) Yield strength, (E) Yield strain, and (F) Toughness of the tested designs. Each condition contained n=5. Scale bar represents 5 mm. **** p<0.0001.*

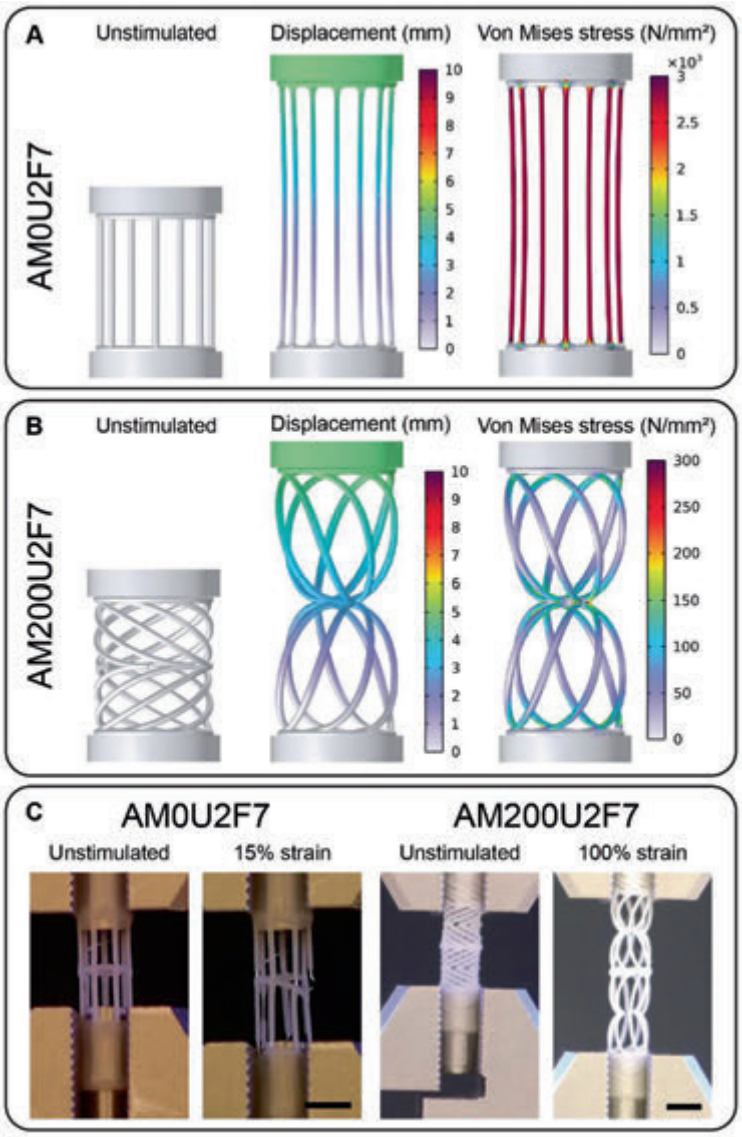

Figure 3. *Finite element model of a tensile test with the AM0U2F7 and the AM200U2F7 design compared to the mechanical test. One end was fixated while the other end was displaced 5 mm (100% strain). (A) AM0U2F7 model, in the left side the unstimulated scaffold. The middle and right side show the scaffold after 100% strain displayed as displacement and von Mises stress respectively. (B) AM200U2F7 model, in the left side the unstimulated scaffold. The middle and right side show the scaffold after 100% strain displayed as displacement and von Mises stress respectively. (C) tensile test of the AM0U2F7 and AM200U2F7 samples until break or until 100% displacement respectively. Scale bar represents 4 mm.*

Table 2. *Overview of the tested corrugated patterns with varying units and amplitude. *Toe region is calculated after the initial inflection point.*

Sample	**AM200U2**	**AM133U3**	**AM100U4**	**AM80U5**
Fiber size (µm)	485 ± 16	471 ± 17	487 ± 21	499 ± 26
Fiber angle (°)	68.5 ± 1.6	68.9 ± 1.4	70.4 ± 1.4	69.9 ± 1.0
Toe region method 1* (%)	74.6 ± 8.9	83.8 ± 5.2	Unable to calculate	Unable to calculate
Toe region method 2 (%)	180.8 ± 8.8	161.7 ± 9.0	Unable to calculate	Unable to calculate
Toe region method 3 (%)	174.7 ± 11.6	142.4 ± 24.5	Unable to calculate	Unable to calculate

Finite element modeling showed that by increasing the amount of units per fiber also increased the amount of stress buildup, specifically at the edges of the fibers (Figure 6). The model also showed that the lumen constriction was less with the increasing amount of units per fiber, which was also observed in the mechanical test (Figure S3, Video S2).

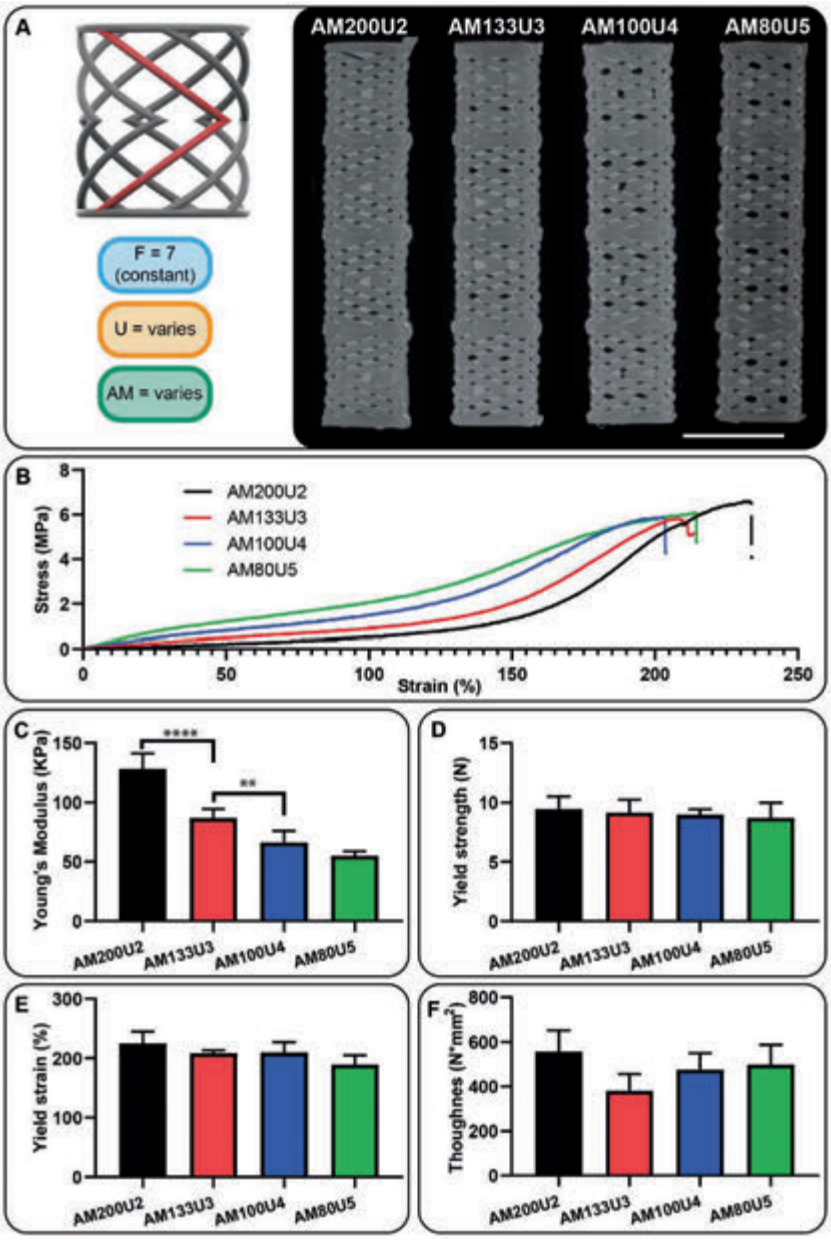

Figure 4. *Overview and mechanical analyses of the corrugated pattern with varying amount of units and amplitude. (A) Stereomicroscopy images of the tested scaffolds. (B) Representative stress-strain curve, (C) Young's modulus, (D) Yield strength, (E) Yield strain, and (F) Toughness of the tested designs. Each condition contained n=5. Scale bar represents 5 mm. ** p<0.01, **** p<0.0001.*

Scaffolds with a tuneable non-linear elastic region using a corrugated design

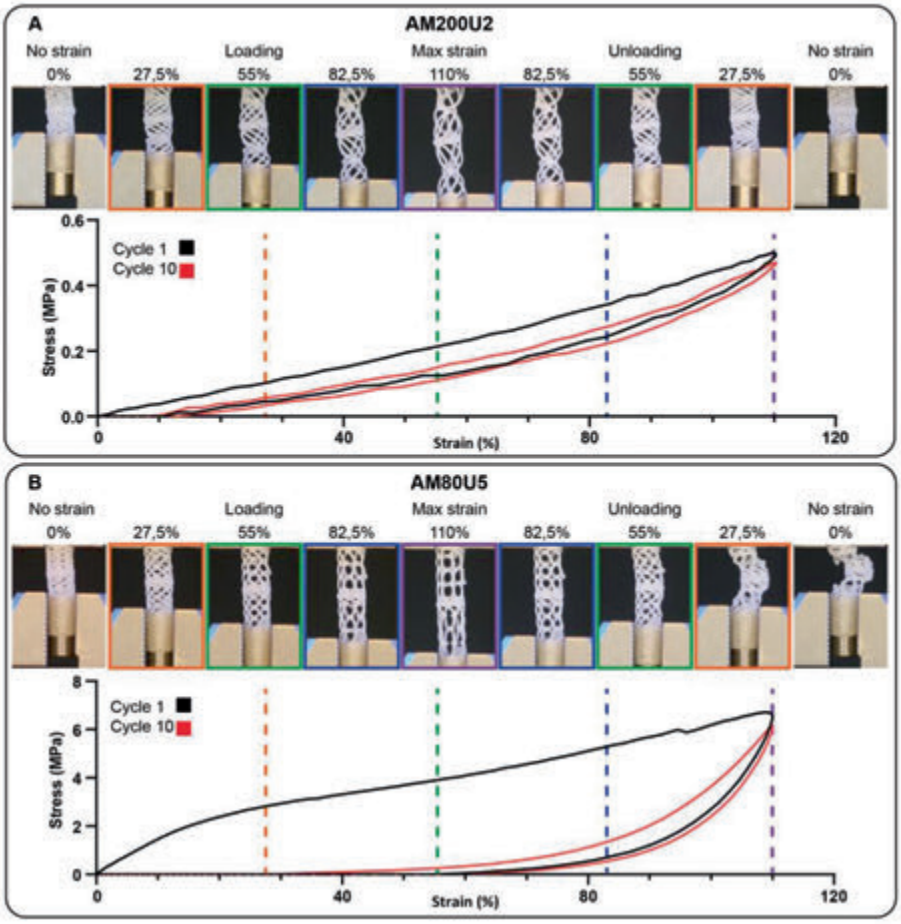

Figure 5. *Loading and unloading cycles of the AM200U2 (A) and AM80U5 (B) designs. The top panel depicts the scaffolds at various strains during the first loading cycle. The bottom panel shows the stress strain curve during the cycle with in black the first cycle and in red the second loading and unloading cycle.*

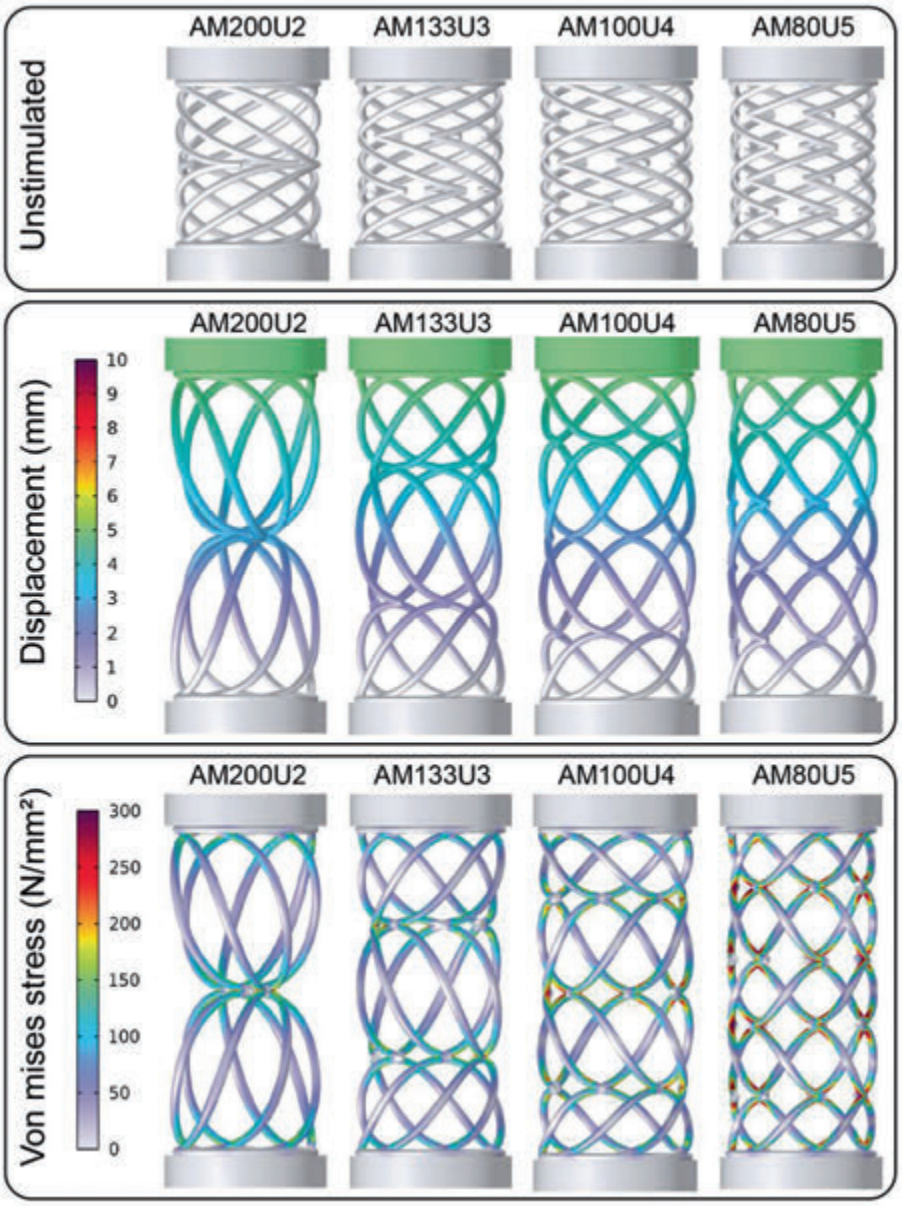

Figure 6. *Finite element model of a tensile test on the corrugated designs with varying units and amplitude. One end was fixated while the other end was displaced 5 mm (100% strain). Upper panel are the unstimulated samples. Middle panel are the samples after stimulation shown in displacement. Lower panel are the samples after stimulation shown in von Mises stress.*

3.3 The effect of material choice and the mechanical properties

Scaffolds of the same design as previously discussed with the changing amplitude and constant unit and fiber amount of 2 and 7, respectively, were fabricated with PEOT/PBT. These conditions had the best sigmoidal shaped stress-strain curve. Both materials have different bulk properties with PCL being stiffer compared to PEOT/PBT (86.1 ± 7.4 MPa and 16.9 ± 0.4 MPa respectively). This is reflected in the stress-strain curves as in all the tested conditions the PCL scaffolds have a higher Young's modulus, Yield strength and toughness. However, the shape of the stress-strain curve remained similar regardless of the material. The stress-strain curve did not contain any initial non-linear region in the AM0 designs. While the corrugated pattern did contain an extended non-linear region that increased with the increase in amplitude. The calculations of the toe region revealed that there was a notable difference between the PEOT/PBT and PCL samples using method 1. The toe region in the AM100 design was 14.4% and 29.9%; in the AM200 design 40.1 and 69.1% for PCL and PEOT/PBT respectively. The differences between the other methods were less notable. The yield strain seemed mainly influenced by the design of the scaffold rather than the material, with both materials having similar yield strains throughout all the different designs.

3.4 Microfiber lumen

An intraluminal microfiber layer was added to three PCL and PEOT/PBT scaffold types: AM0U0 (control), AM100U4 and AM200U2 (N=5 per condition). All scaffold types were exposed to a uniaxial strain of either 0% (control), 10% (*within physiological strain*) or 100% (*definite strain*) after which they were snap-frozen, sectioned and visualized using SEM. The luminal fibers were measured at an average width of 43 ± 5µm for all scaffolds. Visually, both PCL and PEOT/PBT scaffolds displayed no major distortion at 10% strain compared to their respective controls (*Figure8A*). In contrast, while

PCL scaffolds exposed to 100% strain showed significant plastic deformation of both luminal fibers as well as the skeletal support structure, PEOT/PBT scaffolds displayed only minor dilation of the intraluminal space without major dysregulation of the structure or inherent damage to the individual fibers.

Table 3. *Overview of the tested PCL and PEOT/PBT corrugated patterns with varying amplitude.*

Sample	PEOT/PBT AM0	PCL AM0	PEOT/PBT AM100	PCL AM100	PEOT/PBT AM200	PCL AM200
Fiber size (µm)	517 ± 14	434 ± 20	479 ± 20	508 ± 30	524 ± 17	439 ± 23
Fiber angle (°)	N/A	N/A	54.6 ± 1.5	55.7 ± 0.9	68.9 ± 1.4	70.0 ± 1.0
Toe region method 1 (strain %)	N/A	N/A	14.4 ± 4.0	29.9 ± 6.0	40.1 ± 12.0	69.1 ± 6.3
Toe region method 2 (strain %)	N/A	N/A	78.4 ± 8.8	78.6 ± 1.0	204.7 ± 9.9	182.1 ± 5.5
Toe region method 3 (strain %)	N/A	N/A	54.7 ± 8.0	63.1 ± 2.8	182.8 ± 9.6	158.7 ± 9.7

Figure 8B-C display the luminal deformation per uniaxial deformation of PCL and PEOT/PBT scaffolds. The intraluminal deformation within the PCL scaffolds was 4.6 ± 1.8% at 0% strain and 5.8 ± 1.1% at 10% strain, showing a limited overall increase compared to 15.8 ± 0.9% deformation when subjected to 100% strain. The increase in strain was expected to result in an increase in the total area of deformation. The exact amount of deformation however, does not necessarily follow a linear trend, since the scaffold is capable of elastic recovery at lower strain values. This was indicated by the negligible difference in deformation between the control and 10% strain (4.6 ± 1.8% and 5.8 ± 1.1% respectively). When comparing the deformation of PCL to PEOT/PBT (Figure 8C), interesting differences were found specifically in

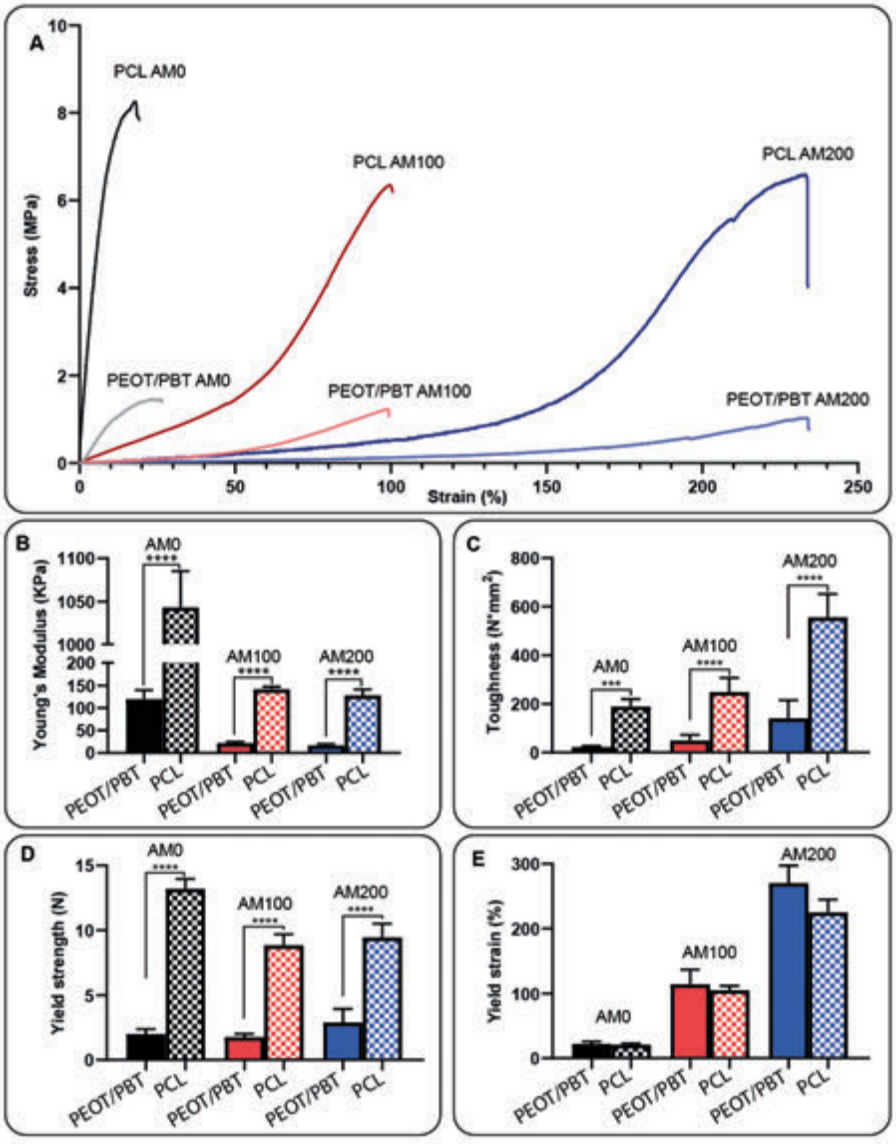

Figure 7. *Comparison between PCL and PEOT/PBT corrugated patterns with varying amplitude. (A) Representative stress-strain curve, (B) Young's modulus, (C) Yield strength, (D) Yield strain, and (E) Toughness of the tested designs. Each condition contained n=5. *** p<0.001, **** p<0.0001.*

the designs subjected to 100% strain. Although significant differences were found between 0-10% and 100% strain deformation, no structural damage of the microfiber lumen was observed in the SEM visualization of PEOT/PBT scaffolds, which did occur in PCL-based scaffolds at 100% deformation (Figure 8A). The quantified luminal deformation area at 100% also decreased in PEOT/PBT compared to PCL in all design conditions.

Comparing the variation between design structures, clear differences were found between the overall deformed area of the control (*AM0*) and the two optimized corrugated scaffold designs (*AM100, AM200*). Larger deformation was noticed in all strain areas of the control (AM0) compared to AM100 and AM200, although it must be noted that this may have occurred due to the skeletal structure being quantified as filled area in the threshold analysis.

3.5 Comparison of the corrugated design and primary animal tissue

The designs with the largest amplitude (AM200U2) from both PCL and PEOT/PBT were compared to porcine and caprine carotid arteries. Table 4 shows an overview of the carotid arteries tested. The inner diameter between goat and pig carotid arteries was 2.8 ± 0.4 mm and 2.3 ± 0.4 mm, respectively.

The wall thickness in the porcine samples was thicker compared to the caprine samples (1.0 ± 0.1 mm and 0.4 ± 0.1 mm respectively) The tested scaffolds had a comparable wall thickness as the caprine samples. The tensile test revealed that the both the caprine and porcine carotid artery had an initial linear region followed by an increase in slope at higher strain that extended beyond any of the tested designs (Figure 9B) However, when focusing on the initial 20% of the stress-strain curve, all the samples overlap except for the AM200 design made of PCL. The Young's modulus of the PCL samples was significantly different compared to both the caprine and porcine arteries (128.1 ± 13.0 KPa, 35.3 ± 14.0 KPa and 23.1 ± 6.7 KPa respectively).

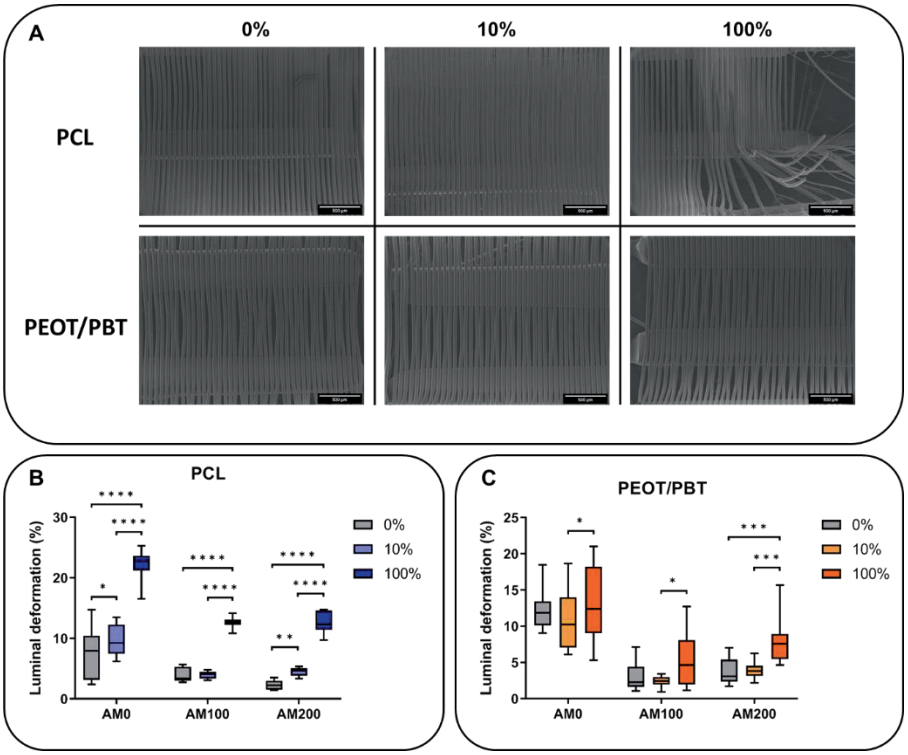

Figure 8. Visualization and quantification of luminal microfiber resilience to strain. A) SEM microscopy of PCL and PEOT/PBT scaffolds after subjection to either 0%, 10% or 100% strain (Scale: 500µm). B-C) Luminal deformation expressed in special deformation between fibers (%) for PCL and PEOT/PBT at either 0%, 10% or 100% strain. *Each condition contained n=5. *** p<0.001, **** p<0.0001.*

Table 4. *Overview of the tested carotid arteries.*

Animal source	Inner diameter (mm)	Wall thickness (mm)	Amount of arteries
Goat	2.8 ± 0.4	0.4 ± 0.1	2
Pig	2.3 ± 0.4	1.0 ± 0.1	6

3.6 Cyclic fatigue analysis

To evaluate the resistance to continuous, fluctuating stresses, the scaffolds were exposed to an incremental fatigue model, where a continuous increase in strain was applied to assess the resilience to fatigue. The cyclic stress-

strain response for most of the fatigue life can be satisfactorily described by the cyclic stress-strain curve of the material under physiological conditions [41]. Under natural conditions, the inflation-extension rate of the carotid artery determines the physiological axial strain and typically have a natural strain rate of ~10% in human carotid arteries, whilst for porcine carotids this was estimated around 50% [42]. Figure 10A shows a single block of 100 cycles at 10% strain deformation where, for the first number of cycles, scaffolds displayed stress saturation and further stabilization over the remaining cycles. Figure 10B displays the incremental fatigue cycle as the induced stress (σ, MPa) over the number of waveform cycles as a factor of time. Each loading block is indicated by a 10% increase in strain (ε +10%) causing a subsequent increase in the peak stress. Neither the PCL nor PEOT/PBT control designs (AM0U0) were able to withstand a cyclic strain rate of over 10% (100 cycles, ε=10%). The PCL samples displayed a sharp decline in stress, indicating continuous plastic deformation of the sample and eventual material failure at 45 and 85 cycles. Interestingly, PEOT/PBT AM0U0 scaffolds were able to recover in the first waveform block (ε=10%, T=100), but showed a gradual decrease in stress over the four following blocks, eventually failing at 444 cycles (ε=50%, T=444). All tested corrugated designs were able to stabilize in stress values up to the maximally tested strain rate of ε=100%. PCL AM100U4 scaffolds did display an overall higher stress compared to AM200U2 and all PEOT/PBT corrugated scaffolds (PCL AM100U4: 2.5 ± 0.2 MPa compared to PCL AM200U2: 1.1 ± 0.3 MPa; PEOT/PBT AM100U4: 0.6 ± 0.2 MPa and PEOT/PBT AM200U2: 0.2 ± 0.1 MPa respectively).

As a follow up, stress/strain values that have showed stabilization in stress during each block were plotted in a cyclic stress-strain (CSS) curve (Figure 10C) [43]. Permanent plastic deformation of a sample was confirmed through either full failure of the samples (PCL AM0U0, PEOT/PBT AM0U0) or by a decrease in overall stress whilst increasing stretch (PCL AM100U4). All other

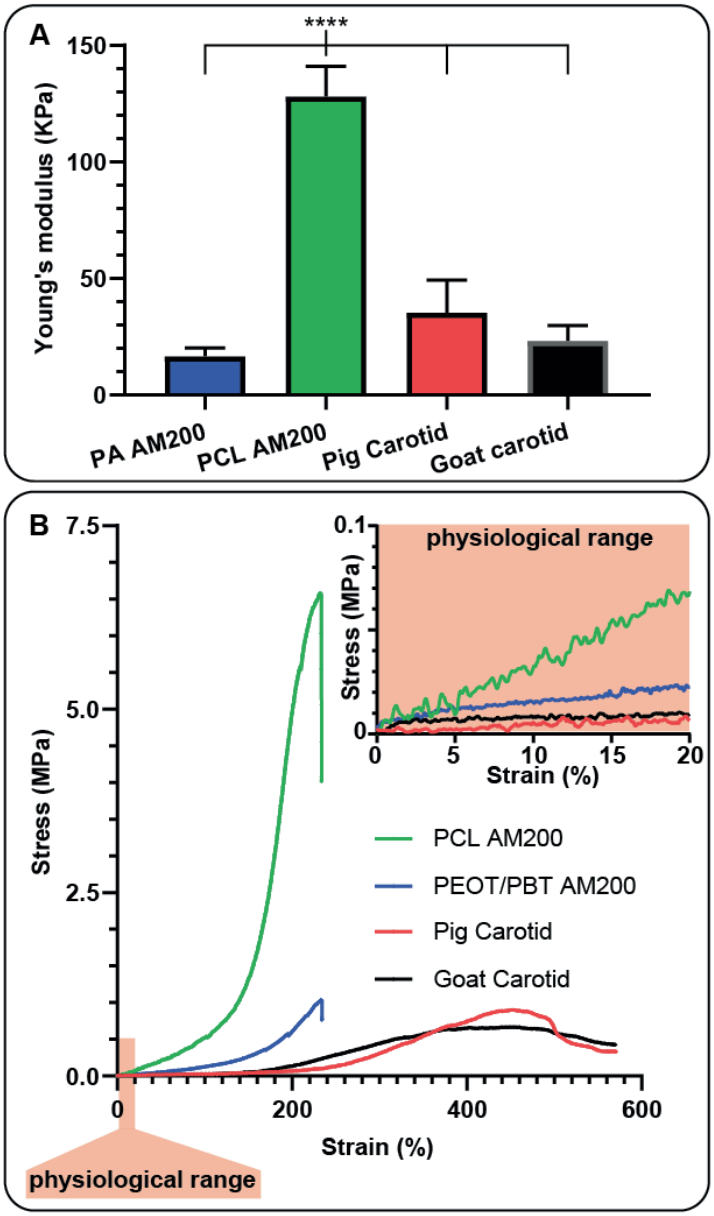

Figure 9. *Comparison between the corrugated pattern and carotid arteries from porcine and caprine. (A) Young's modulus and (B) representative stress-strain curve the physiological strain range is highlighted and the insert in the top right corner represents the physiological range. Each condition contained n=5 for the polymer samples, n= 6 for the caprine samples and n = 16 for the porcine samples. **** p<0.0001.*

samples showed proper recovery up to the maximally tested rate of ε=100%. Furthermore, the physiological stretch ranges of both human and porcine carotid arteries (Human ε=20%, Porcine ε=50%) were compared to the fatigue values and displayed in green (Figure 10C). All design models except for PCL AM0U0 were able to meet or exceed the maximal human passive strain rate (ε>10%). Additionally, both PCL and PEOT/PBT designs with corrugated patterns exceeded the porcine models with regards to strain rate (*ε>50%*).

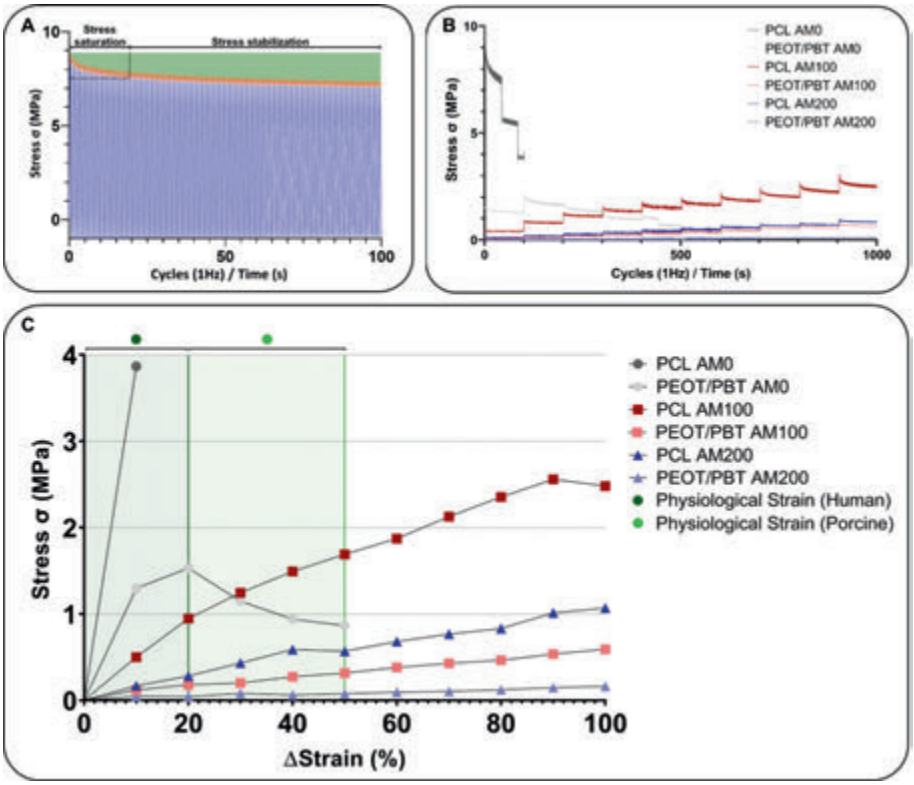

Figure. 10. *Representative incremental fatigue plots of various corrugated designs (N=5). A) Single waveform fatigue cycle displaying stress stabilization of the scaffolds. Data is plotted as the peak stress (MPa) over each cycle (1hz, 60 cycles/minute). B) Total incremental fatigue graph. The peak stress of each cycle was plotted. Scaffolds were exposed to a total of 1000 cycles with a 10% increase in strain per 100 cycles. Fatigue propagation occurs whenever a sample is not able to recover from an increase in strain. C) CSS curve of the incremental fatigue model. Physiological strain ranges of both human and porcine carotid arteries are displayed in green.*

4. Discussion

This study highlighted the use of a corrugated pattern and the influence of different design parameters on the mechanical properties of tubular scaffolds. The effect of the corrugated pattern was shown in the stress-strain curves where the non-linear region was significantly extended by the introduction of the pattern. This also introduced a sigmoidal behavior represented by the J-shaped stress/strain relationship as observed in natural vessels [44]. By varying the length of the amplitude, it was shown that the non-linear region and the yield strain could be controlled. An additional step can be taken to change the mechanical properties by introducing multiple units per segment of the corrugated pattern. This led to a decreased Young's modulus while the other parameters such as the yield strength, yield strain and the toughness remained similar. The corrugated pattern was fabricated out of different materials to explore the effect of material properties. It was shown that changing the material did not affect the yield strain and the length of the non-linear region. However, other properties such as the Young's modulus, toughness and yield strength were affected. Finally, the design with the longest non-linear region was compared to pig and goat carotid arteries. While the non-linear region in the native carotid arteries was larger compared to the tested designs, the initial part of the stress-strain curve was similar, thus demonstrating that the corrugated pattern could have potential for flexible and extendable tubular organs such as arteries.

The stress-strain curves in the corrugated samples were considerably different compared to the AM0 samples that had a straight fiber arrangement. The Young's modulus of the straight fiber samples was significantly higher, while the differences between the other samples remained similar. This is also confirmed by modelling, where the von Mises stress were a ten-fold higher compared to the samples with the longest amplitude. In addition, the yield strain of the designs was increased with the corrugated pattern. While the

yield strain of a straight PCL fiber was 21%, this was increased tenfold up to 225% strain in the samples with the largest amplitude. Fleischer *et al.* showed in a similar study that curled spring-like electrospun PCL fibers also had a decreased Young's modulus and increased yield strain compared to straight fibers [45]. The only difference is that the corrugated design extended the non-linear region while the curled spring-like fibers did not show an extended non-linear region. A different study performed by Hochleitner *et al.* showed that sinusoidal shaped melt electrowritten poly(L-lactide-co-e-caprolactone-co-acryloyl carbonate) fibers had a decreased Young's modulus and a sigmoidal stress strain curve [46], which was explained as the unfolding of the sinusoidal meanders giving rise to a non-linear behavior. This was also shown in this study with the corrugated pattern that can unfold to become a straight fiber before the plastic deformation starts. However, not all spring-like structures show this initial non-linear region. Chen et al. revealed that a wave pattern can be created after electrospinning PEOT/PBT on a Polylactic acid thermoshrinkable film [47]. The introduced wave patterns did only have an initial non-linear region of 1% strain. The yield strain in the wave patterns, however, was 100% or greater in all of the tested conditions.

Further increasing the amplitude in the corrugated pattern would result in the fusion of the fibers due to the limited space between the fibers. To avoid this, the amount of repeating units was increased while correcting for the amplitude. Increasing the amount of repeating units resulted in more space between the fibers, allowing to potentially further increase the amplitude. Another benefit of increasing the amount of units was that there was less constriction of the lumen, as shown by the mechanical tests (Figure S2). This was also confirmed by the finite element model, where less constriction was observed when increasing the amount of units. Specifically, scaffolds with only 2 repeating units showed almost a full constriction at 100% strain, while the other scaffolds showed barely any constriction at the same amount of strain. The constriction in the lumen is undesirable especially for vascular

applications where it could cause hypertension [48]. Yet, the constriction in the samples was noticeable at strain values higher than 20% strain, which is still beyond what is physiologically relevant [42]. This constrictive behavior, however, can be found in other tubular organs such as sphincters [49, 50]. An interesting approach could be to combine this structural scaffold design approach with a technique that covers the lumen of the scaffold to investigate the constrictive behavior [36], as the corrugated pattern were too porous to withhold liquid.

Another mechanical consideration to note was that increasing the amount of units caused an additional inflection point in the stress strain curve. Most likely this was caused by the corners of the fiber that acted as a hinge and started to tear resulting in a buckling effect after the unloading cycle. These hinges in the scaffold correlate with the areas where the von Mises stresses were the highest. The results from the finite element model also revealed that the stress increased with the amount of units per segment. Specifically, the samples with the largest amount of units per segment were torn as they unfolded. Once the hinges were torn, the slope of the stress-strain curve decreased, indicating that the biggest contributor of stress was the resistance caused by the unfolding of the hinges. After this additional inflection point the main contributor of stress were the fibers that were pulled during the tensile test until the scaffold broke completely. Another reason why the samples with the longest amplitude and the smallest amount of units did not show this initial inflection point is that these require more force to bend the shorter fibers with an equivalent fiber diameter [51]. The obtained stress-strain curve showed two different yield points, the first one that represents the hinges tearing but fibers in the scaffold still remain connected. The second yield point is where the fibers of the scaffolds start to tear and rupture of the scaffold soon follows after. Future studies could investigate if this tearing effect could be avoided by using a sinusoidal pattern instead of a corrugated pattern. As the generated fibers from the sinusoidal pattern should not have sharp corners that could act

as a hinge. Other studies have conducted similar investigations using sinusoidal patterns and did not observe tearing at the corners of the scaffolds; however, the mechanical testing was performed radially instead of longitudinally [28, 52].

The different methods of calculating the toe region were compared here. The Freed method, which ends after the initial linear region and includes a heel region [37]. In comparison to the other two methods described herein, this method consistently exhibits the smallest toe region.. The reason being that the heel region, which is still considered a toe region by both the Vegas and Chandrashekar methods, is included in this. The endpoint of this heel region is the end point of the toe region used in the Vegas method. This method ends at the start of the linear elastic region [38]. Of all the methods described here the Vegas method has consistently the largest toe region and from a practical point of view it is also a simpler method that could still be used to calculate samples with a very small toe region. The Chandrashekar method uses the tangents of the two trend lines [39]. This method gave a toe region that was between the Freed and Vegas method, however it can be challenging to calculate the toe region if the region is small and if the initial part of the stress-strain curve is not linear (Figure S4). It is important to consider that these methods have originally been developed to assess the material properties and not structural properties of scaffolds. Specifically, scaffolds that have complicated designs make calculating mechanical properties more complex [53, 54]. Therefore, it is recommended to supplement the mechanical tests with additional observations, such as videos during the tensile test, to better understand the complex mechanical behavior of the scaffolds.

Fabricating the scaffolds with different materials resulted in stress-strain curves that followed a similar trend. The mechanical properties of the scaffolds are based on a combination of material properties and structural design [23, 55]. Scaffolds were fabricated with different materials to differentiate between

design and material properties. The stress-strain curves of both the PCL and PEOT/PBT scaffolds followed a similar trend. For example, the Young's modulus, toughness and yield strength were more influenced by the mechanical properties rather than the design, with these parameters having at least a 5-fold difference between the PCL and PEOT/PBT scaffolds throughout the tested designs. Interestingly, the difference in yield strain was nearly the same in both PCL and PEOT/PBT samples except at larger amplitudes, indicating that the corrugated design had a greater influence on the yield strain than the material properties.

The reasoning behind an internal microfiber lumen was based on previous literature, in which microfiber lumens and meshes are able to provide improved endothelial cell adhesion, proliferation, uniformly distributed cell alignment and overall compliance of the graft [56-58]. Additionally, results from our previous study on these melt-spun microfiber scaffolds revealed a successful circumferential alignment of smooth muscle cells within the lumen when co-cultured with vascular endothelial cells [36, 59].

Within this study, the mechanical extent of luminal resilience under strain was further quantified, where no major structural deformation was found at passive physiological strain. Furthermore, the source material also appears to affect the total deformation at higher levels of strain, where a clear significant difference was found in total deformation of PCL scaffolds, whilst this was less apparent in PEOT/PBT scaffolds. These observations propose that the flexibility of PEOT/PBT serves as a major contributing factor in upholding fiber arrangement and preventing luminal collapse. The results support the hypothesis that the formation of a microfiber lumen is sufficiently resilient to the natural 20% strain of the human vasculature, only displaying deformation when high levels of strain ($\varepsilon >= 100\%$) are exerted upon the scaffolds.

The carotid arteries from both pigs and goats had a long toe region of up to 200% strain. The main differences between the corrugated design and the carotid arteries was that there was almost no stress generated with the increasing strain before the linear region. Whereas the corrugated design did generate stress even with a more flexible material such as PEOT/PBT. In the corrugated design there was a sharp drop when the scaffolds ruptured while the arteries had a more gradual decline in stress. This could be the result of the artery consisting of multiple components such as collagen and elastin, each with their own yield points [60]. Comparing the toe region between the corrugated design and the arteries revealed that the toe region was smaller in the corrugated design. The applied strain that is required to reach that toe region is, however, far beyond the physiological situation of around 10% [42]. Focusing on the initial 20% strain it was noted that the corrugated PEOT/PBT samples with the largest amplitude has a similar stress-strain curve to that of both a pig and goat carotid artery, indicating that they could be used as a biomimicking artificial graft alternative for vascular tissue engineering.

Exposure to continuous homeostatic strain can positively affect the shape and orientation of vascular cell types, increase proliferation rate, migration behavior and synthesis of contractile and regulatory proteins [61]. The proper reproduction of natural mechanical behavior in scaffolds is therefore not only critical for proper tissue arrangement, but may also contribute to the formation and proper alignment of extracellular protein sheets such as the internal elastic lamina or the adventitial type I and III collagen bundles [62]. For this reason, all optimized corrugated scaffolds were assessed for their compliance to continuous incremental strain for their resilience to continuous exposure to mechanical stressors representative of the passive forces occurring in a live host.

As discussed in the results section, all designs exceeded the maximum human passive strain (ε=20%). The radial strain rates in healthy humans often

falls even lower than this benchmark, where the strain per pulse was found to average out around 2.81 ± 0.91% [63]. Additionally, the passive carotid strain of the used porcine arteries was higher at ε=50%, which is also easily matched by all optimized corrugated scaffolds [42, 64]. Interestingly, none of the control samples (AM0U0) were able to meet these passive strain values, with PCL failing at a 10% strain rate and PEOT/PBT at 20%, indicating that the corrugated design of the scaffold has a significant influence on the overall resilience to continuous strain. Three out of the four optimized TEVGs also showed proper recovery up to the maximally tested rate of 100% (PCL AM200U2, PEOT/PBT AM200U2, PEOT/PBT AM100U4), with only PCL AM100U4 showing permanent plastic deformation in the CSS curve at 90% (Figure 10C). Studies on the average stress on the intact human carotid wall established the average stress in a range between 0.16 ± 0.04 MPa and 0.9 ± 0.25 MPa, which also corresponds with the ranges of the previously mentioned corrugated designs [65].

Elastin is the key component for elastic behavior in the human body. It is found in many organs such as the lungs [66], skin [67], tendons [68] and vasculature [69]. Together with as many as 30 other proteins, it forms a complex elastic fiber [9]. The presence of these elastic fibers allows these tissues to expand or stretch without too much force required at low strain. Similarly, the corrugated pattern presented here also requires little force to stretch. However, the way it stretches is different compared to elastin. Whereas elastin forms a network of elastic fibers that can extend and recoil and the stretch is uniform throughout the tissue [70]; the corrugated pattern extends only locally at the bending points as shown in the models. Nonetheless, it is known that elastin synthesis only occurs at the embryonic development with no *de novo* elastin production in adults [71, 72]. In combination with the complex structure of elastic fibers, this makes the corrugated pattern an easier off-the shelf approach for potential vascular tissue engineering.

5. Conclusion

We demonstrated a corrugated pattern with a tunable non-linear elastic region. Varying the amplitude of the corrugated pattern led to an increase in yield strain up to 200% compared to 15% without the pattern. The shape of the stress-strain curve became sigmoidal with the introduction of the corrugated pattern mimicking major arteries. Increasing the amount of repeating units led to an additional inflection point in the stress-strain curves generating two different yield points. In addition, mechanical data showed the corrugated pattern had a bigger influence on the yield strain than the material properties. Finally, the corrugated pattern was compared to different carotid arteries and revealed that the stress-strain curves were similar and had similar mechanical properties. These results highlight how the corrugated patterns studied here could be used as a biomechanical biomimicry approach in the fabrication of a vascular grafts.

Acknowledgements

We are grateful to the European Research Council starting grant “Cell Hybridge” for financial support under the Horizon2020 framework program (Grant #637308). We are grateful to H2020-NMP-PILOTS2015 (GA no. 685825) for financial .support.

References

[1] M.R. Dal Bó, C.A. Salvador, M.G. Mello, D.D. Lima, G.A. Faria, A.J. Ramirez, R. Caram, The effect of Zr and Sn additions on the microstructure of Ti-Nb-Fe gum metals with high elastic admissible strain, Materials & Design 160 (2018) 1186-1195.
[2] T. Sakai, Y. Akagi, T. Matsunaga, M. Kurakazu, U.i. Chung, M. Shibayama, Highly Elastic and Deformable Hydrogel Formed from Tetra-arm Polymers, Macromolecular rapid communications 31(22) (2010) 1954-1959.
[3] J. Gosline, M. Lillie, E. Carrington, P. Guerette, C. Ortlepp, K. Savage, Elastic proteins: biological roles and mechanical properties, Philosophical Transactions of the Royal Society of London. Series B: Biological Sciences 357(1418) (2002) 121-132.
[4] G. Qin, X. Hu, P. Cebe, D.L. Kaplan, Mechanism of resilin elasticity, Nature communications 3(1) (2012) 1-9.
[5] A. Pedicini, R.J. Farris, Mechanical behavior of electrospun polyurethane, Polymer 44(22) (2003) 6857-6862.
[6] M.F. O'rourke, J. Hashimoto, Mechanical factors in arterial aging: a clinical perspective, Journal of the American College of Cardiology 50(1) (2007) 1-13.
[7] C. Singh, C.S. Wong, X. Wang, Medical textiles as vascular implants and their success to mimic natural arteries, Journal of functional biomaterials 6(3) (2015) 500-525.
[8] M.J. McClure, D.G. Simpson, G.L. Bowlin, Tri-layered vascular grafts composed of polycaprolactone, elastin, collagen, and silk: Optimization of graft properties, Journal of the mechanical behavior of biomedical materials 10 (2012) 48-61.
[9] A.J. Cocciolone, J.Z. Hawes, M.C. Staiculescu, E.O. Johnson, M. Murshed, J.E. Wagenseil, Elastin, arterial mechanics, and cardiovascular disease, American Journal of Physiology-Heart and Circulatory Physiology 315(2) (2018) H189-H205.
[10] E.L. Schiffrin, Vascular stiffening and arterial compliance: implications for systolic blood pressure, American journal of hypertension 17(S3) (2004) 39S-48S.
[11] H.K. Graham, R. Akhtar, C. Kridiotis, B. Derby, T. Kundu, A.W. Trafford, M.J. Sherratt, Localised micro-mechanical stiffening in the ageing aorta, Mechanisms of ageing and development 132(10) (2011) 459-467.
[12] F.H. Silver, P.B. Snowhill, D.J. Foran, Mechanical behavior of vessel wall: a comparative study of aorta, vena cava, and carotid artery, Annals of biomedical engineering 31(7) (2003) 793-803.
[13] A.P. Ebrahimi, Mechanical properties of normal and diseased cerebrovascular system, Journal of vascular and interventional neurology 2(2) (2009) 155.
[14] W. Wang, L. Xiang, D. Diaz-Dussan, J. Zhang, W. Yang, L. Gong, J. Chen, R. Narain, H. Zeng, Dynamic flexible hydrogel network with biological tissue-like self-protective functions, Chemistry of Materials 32(24) (2020) 10545-10555.
[15] B. Li, V. Daggett, Molecular basis for the extensibility of elastin, Journal of Muscle Research & Cell Motility 23(5) (2002) 561-573.
[16] J.E. Wagenseil, R.P. Mecham, New insights into elastic fiber assembly, Birth Defects Research Part C: Embryo Today: Reviews 81(4) (2007) 229-240.
[17] E. Shady, Y. Gowayed, Effect of nanotube geometry on the elastic properties of nanocomposites, Composites Science and Technology 70(10) (2010) 1476-1481.
[18] T. Stylianopoulos, M. Kokonou, S. Michael, A. Tryfonos, C. Rebholz, A.D. Odysseos, C. Doumanidis, Tensile mechanical properties and hydraulic permeabilities of electrospun cellulose acetate fiber meshes, Journal of Biomedical Materials Research Part B: Applied Biomaterials 100(8) (2012) 2222-2230.
[19] D.B. Kim, H. Choi, S.M. Joo, H.K. Kim, J.H. Shin, M.H. Hwang, J. Choi, D.G. Kim, K.H. Lee, C.H. Lim, A comparative reliability and performance study of different stent designs in terms of mechanical properties: foreshortening, recoil, radial force, and flexibility, Artificial organs 37(4) (2013) 368-379.
[20] D. Stoeckel, A. Pelton, T. Duerig, Self-expanding nitinol stents: material and design considerations, European radiology 14(2) (2004) 292-301.
[21] A.R. Pelton, S.M. Russell, J. DiCello, The physical metallurgy of nitinol for medical applications, Jom 55(5) (2003) 33-37.

[22] K. Ueki, K. Ueda, T. Narushima, Microstructure and mechanical properties of heat-treated Co-20Cr-15W-10Ni alloy for biomedical application, Metallurgical and Materials Transactions A 47(6) (2016) 2773-2782.
[23] K.A. van Kampen, E. Olaret, I.-C. Stancu, L. Moroni, C. Mota, Controllable four axis extrusion-based additive manufacturing system for the fabrication of tubular scaffolds with tailorable mechanical properties, Materials Science and Engineering: C 119 (2021) 111472.
[24] Y. Shen, X. Yu, J. Cui, F. Yu, M. Liu, Y. Chen, J. Wu, B. Sun, X. Mo, Development of biodegradable polymeric stents for the treatment of cardiovascular diseases, Biomolecules 12(9) (2022) 1245.
[25] N. Grabow, D.P. Martin, K.P. Schmitz, K. Sternberg, Absorbable polymer stent technologies for vascular regeneration, Journal of Chemical Technology & Biotechnology 85(6) (2010) 744-751.
[26] T. Sharkawi, F. Cornhill, A. Lafont, P. Sabaria, M. Vert, Intravascular bioresorbable polymeric stents: a potential alternative to current drug eluting metal stents, Journal of pharmaceutical sciences 96(11) (2007) 2829-2837.
[27] N. Hibino, D. Mejias, N. Pietris, E. Dean, T. Yi, C. Best, T. Shinoka, C. Breuer, The innate immune system contributes to tissue-engineered vascular graft performance, The FASEB Journal 29(6) (2015) 2431.
[28] N. Debusschere, P. Segers, P. Dubruel, B. Verhegghe, M. De Beule, A finite element strategy to investigate the free expansion behaviour of a biodegradable polymeric stent, Journal of biomechanics 48(10) (2015) 2012-2018.
[29] Y. Wei, M. Wang, D. Zhao, H. Li, Y. Jin, Structural design of mechanical property for biodegradable polymeric stent, Advances in Materials Science and Engineering 2019 (2019) 1-14.
[30] D. Zhao, R. Zhou, J. Sun, H. Li, Y. Jin, Experimental study of polymeric stent fabrication using homemade 3D printing system, Polymer Engineering & Science 59(6) (2019) 1122-1131.
[31] A. Di Luca, A. Longoni, G. Criscenti, C. Mota, C. van Blitterswijk, L. Moroni, Toward mimicking the bone structure: design of novel hierarchical scaffolds with a tailored radial porosity gradient, Biofabrication 8(4) (2016) 045007.
[32] I. Pennings, E.E. van Haaften, T. Jungst, J.A. Bulsink, A.J. Rosenberg, J. Groll, C.V. Bouten, N.A. Kurniawan, A.I. Smits, D. Gawlitta, Layer-specific cell differentiation in bi-layered vascular grafts under flow perfusion, Biofabrication 12(1) (2019) 015009.
[33] A.V. Kamenskiy, Y.A. Dzenis, J.N. MacTaggart, T.G. Lynch, S.A.J. Kazmi, I.I. Pipinos, Nonlinear mechanical behavior of the human common, external, and internal carotid arteries in vivo, Journal of Surgical Research 176(1) (2012) 329-336.
[34] P.K. Penumakala, J. Santo, A. Thomas, A critical review on the fused deposition modeling of thermoplastic polymer composites, Composites Part B: Engineering 201 (2020) 108336.
[35] Z. Wang, S.M. Mithieux, A.S. Weiss, Fabrication techniques for vascular and vascularized tissue engineering, Advanced healthcare materials 8(19) (2019) 1900742.
[36] K.A. van Kampen, J. Fernández-Pérez, M. Baker, C. Mota, L. Moroni, Fabrication of a mimetic vascular graft using melt spinning with tailorable fiber parameters, Biomaterials Advances (2022) 212972.
[37] A.D. Freed, K. Rajagopal, A promising approach for modeling biological fibers, Acta Mechanica 227(6) (2016) 1609-1619.
[38] M.R. Vegas, J.L. Martin del Yerro, Stiffness, compliance, resilience, and creep deformation: understanding implant-soft tissue dynamics in the augmented breast: fundamentals based on materials science, Aesthetic plastic surgery 37(5) (2013) 922-930.
[39] N. Chandrashekar, J. Hashemi, J. Slauterbeck, B.D. Beynnon, Low-load behaviour of the patellar tendon graft and its relevance to the biomechanics of the reconstructed knee, Clinical Biomechanics 23(7) (2008) 918-925.
[40] G.B. Chapman, W. Durante, J.D. Hellums, A.I. Schafer, Physiological cyclic stretch causes cell cycle arrest in cultured vascular smooth muscle cells, American Journal of Physiology-Heart and Circulatory Physiology 278(3) (2000) H748-H754.
[41] J. Polák, M. Hájek, Cyclic stress-strain curve evaluation using incremental step test procedure, International journal of fatigue 13(3) (1991) 216-222.
[42] R.A. Macrae, K. Miller, B.J. Doyle, Methods in mechanical testing of arterial tissue: a review, Strain 52(5) (2016) 380-399.

[43] S.G.S. Raman, K. Padmanabhan, Some studies on the incremental step (fatigue) test, Materials Science and Engineering: A 188(1-2) (1994) 141-146.
[44] R.E. Shadwick, Mechanical design in arteries, Journal of Experimental Biology 202(23) (1999) 3305-3313.
[45] S. Fleischer, R. Feiner, A. Shapira, J. Ji, X. Sui, H.D. Wagner, T. Dvir, Spring-like fibers for cardiac tissue engineering, Biomaterials 34(34) (2013) 8599-8606.
[46] G. Hochleitner, F. Chen, C. Blum, P.D. Dalton, B. Amsden, J. Groll, Melt electrowriting below the critical translation speed to fabricate crimped elastomer scaffolds with non-linear extension behaviour mimicking that of ligaments and tendons, Acta biomaterialia 72 (2018) 110-120.
[47] H. Chen, D.F. Baptista, G. Criscenti, J. Crispim, H. Fernandes, C. Van Blitterswijk, R. Truckenmüller, L. Moroni, From fiber curls to mesh waves: A platform for the fabrication of hierarchically structured nanofibers mimicking natural tissue formation, Nanoscale 11(30) (2019) 14312-14321.
[48] A.M. Heagerty, E.H. Heerkens, A.S. Izzard, Small artery structure and function in hypertension, Journal of cellular and molecular medicine 14(5) (2010) 1037-1043.
[49] A. Babaei, V. Bhargava, H. Korsapati, W.H. Zheng, R.K. Mittal, A unique longitudinal muscle contraction pattern associated with transient lower esophageal sphincter relaxation, Gastroenterology 134(5) (2008) 1322-1331.
[50] G.S. Bergh, J.A. Layne, A demonstration of the independent contraction of the sphincter of the common bile duct in human subjects, American Journal of Physiology-Legacy Content 128(4) (1940) 690-694.
[51] W.J. Fischer, C. Lorbach, M. Jajcinovic, U. Hirn, W. Bauer, Measured and calculated bending stiffness of individual fibers, Proceedings, Progress in Paper Physics Seminar 2014, 2014.
[52] H. Jiang, H. Ziegler, Z. Zhang, H. Zhang, L. Le Barbenchon, S. Atre, Y. Chen, 3D printed tubular lattice metamaterials for mechanically robust stents, Composites Part B: Engineering 236 (2022) 109809.
[53] G. Flamourakis, I. Spanos, Z. Vangelatos, P. Manganas, L. Papadimitriou, C. Grigoropoulos, A. Ranella, M. Farsari, Laser-made 3D auxetic metamaterial scaffolds for tissue engineering applications, Macromolecular Materials and Engineering 305(7) (2020) 2000238.
[54] S.J. Callens, C.H. Arns, A. Kuliesh, A.A. Zadpoor, Decoupling Minimal Surface Metamaterial Properties Through Multi-Material Hyperbolic Tilings, Advanced Functional Materials 31(30) (2021) 2101373.
[55] L. Wang, C. Wang, S. Wu, Y. Fan, X. Li, Influence of the mechanical properties of biomaterials on degradability, cell behaviors and signaling pathways: current progress and challenges, Biomaterials Science 8(10) (2020) 2714-2733.
[56] P. Uttayarat, A. Perets, M. Li, P. Pimton, S.J. Stachelek, I. Alferiev, R.J. Composto, R.J. Levy, P.I. Lelkes, Micropatterning of three-dimensional electrospun polyurethane vascular grafts, Acta biomaterialia 6(11) (2010) 4229-4237.
[57] T. Matsuda, M. Ihara, H. Inoguchi, I.K. Kwon, K. Takamizawa, S. Kidoaki, Mechano-active scaffold design of small-diameter artificial graft made of electrospun segmented polyurethane fabrics, Journal of Biomedical Materials Research Part A: An Official Journal of The Society for Biomaterials, The Japanese Society for Biomaterials, and The Australian Society for Biomaterials and the Korean Society for Biomaterials 73(1) (2005) 125-131.
[58] P. Uttayarat, M. Chen, M. Li, F.D. Allen, R.J. Composto, P.I. Lelkes, Microtopography and flow modulate the direction of endothelial cell migration, American Journal of Physiology-Heart and Circulatory Physiology 294(2) (2008) H1027-H1035.
[59] J. Fernández-Pérez, K.A. van Kampen, C. Mota, M. Baker, L. Moroni, Flexible, Suturable, and Leak-free Scaffolds for Vascular Tissue Engineering Using Melt Spinning, ACS Biomaterials Science & Engineering (2023).
[60] A. Alfonso-Garcia, A.K. Haudenschild, L. Marcu, Label-free assessment of carotid artery biochemical composition using fiber-based fluorescence lifetime imaging, Biomedical Optics Express 9(9) (2018) 4064-4076.
[61] J.L. Balestrini, J.K. Skorinko, A. Hera, G.R. Gaudette, K.L. Billiar, Applying controlled non-uniform deformation for in vitro studies of cell mechanobiology, Biomechanics and modeling in mechanobiology 9 (2010) 329-344.

[62] M.-J. Chow, R. Turcotte, C.P. Lin, Y. Zhang, Arterial extracellular matrix: a mechanobiological study of the contributions and interactions of elastin and collagen, Biophysical journal 106(12) (2014) 2684-2692.
[63] S.-A. Kim, S.-M. Park, M.-N. Kim, Y.-H. Kim, D.-H. Cho, C.-M. Ahn, S.J. Hong, D.-S. Lim, W.J. Shim, The relationship between mechanical properties of carotid artery and coronary artery disease, European Heart Journal–Cardiovascular Imaging 13(7) (2012) 568-573.
[64] J.A.G. Rhodin, Architecture of the Vessel Wall, Comprehensive Physiology (1980) 1-31.
[65] T. Khamdaeng, J. Luo, J. Vappou, P. Terdtoon, E. Konofagou, Arterial stiffness identification of the human carotid artery using the stress–strain relationship in vivo, Ultrasonics 52(3) (2012) 402-411.
[66] B. Starcher, Elastin and the lung, Thorax 41(8) (1986) 577.
[67] G.C. Sephel, J.M. Davidson, Elastin production in human skin fibroblast cultures and its decline with age, Journal of investigative dermatology 86(3) (1986) 279-285.
[68] T.M. Ritty, K. Ditsios, B.C. Starcher, Distribution of the elastic fiber and associated proteins in flexor tendon reflects function, The Anatomical Record: An Official Publication of the American Association of Anatomists 268(4) (2002) 430-440.
[69] A. Tsamis, J.T. Krawiec, D.A. Vorp, Elastin and collagen fibre microstructure of the human aorta in ageing and disease: a review, Journal of the Royal Society Interface 10(83) (2013) 20121004.
[70] L. Baumann, E.F. Bernstein, A.S. Weiss, D. Bates, S. Humphrey, M. Silberberg, R. Daniels, Clinical relevance of elastin in the structure and function of skin, Aesthetic Surgery Journal Open Forum, Oxford University Press US, 2021, p. ojab019.
[71] W.C. Parks, H. Secrist, L.C. Wu, R. Mecham, Developmental regulation of tropoelastin isoforms, Journal of Biological Chemistry 263(9) (1988) 4416-4423.
[72] S. Ritz-Timme, I. Laumeier, M.J. Collins, Aspartic acid racemization: evidence for marked longevity of elastin in human skin, British Journal of Dermatology 149(5) (2003) 951-959.

Scaffolds with a tuneable non-linear elastic region using a corrugated design

Supplementary Information

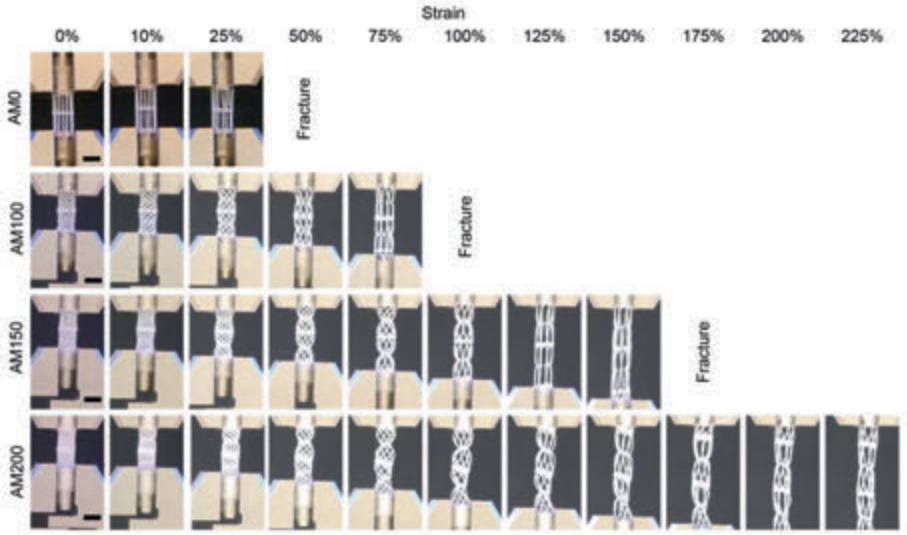

Figure S1. *Video images from tensile test with a strain rate of 1% per second of 4 different designs. Video stopped after sample fracture. Scale bar represents 4 mm.*

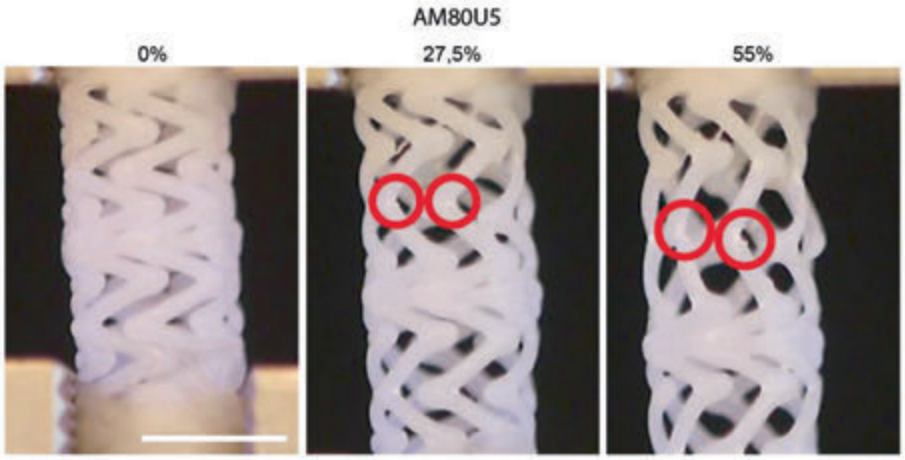

Figure S2. *Tensile test of the AM80U5 sample at various strains. Red circle indicate the fiber tearing. Scale bar represents 4 mm.*

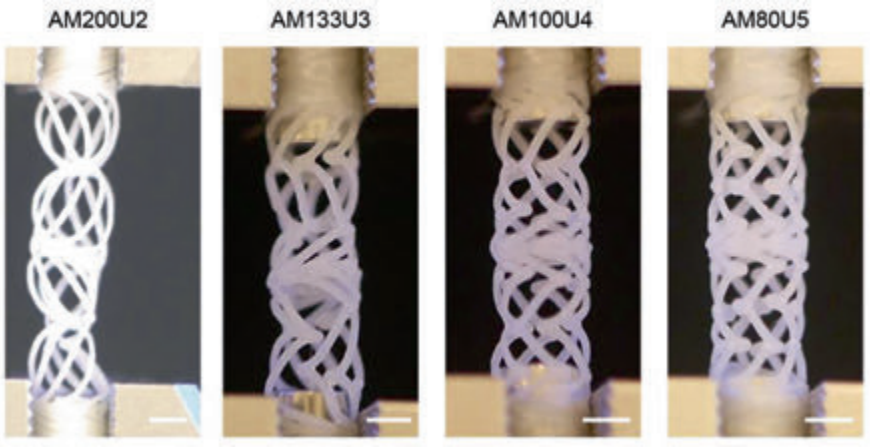

Figure S3. *Luminal deformation of different designs at 125% strain. Scale bar represents 2 mm.*

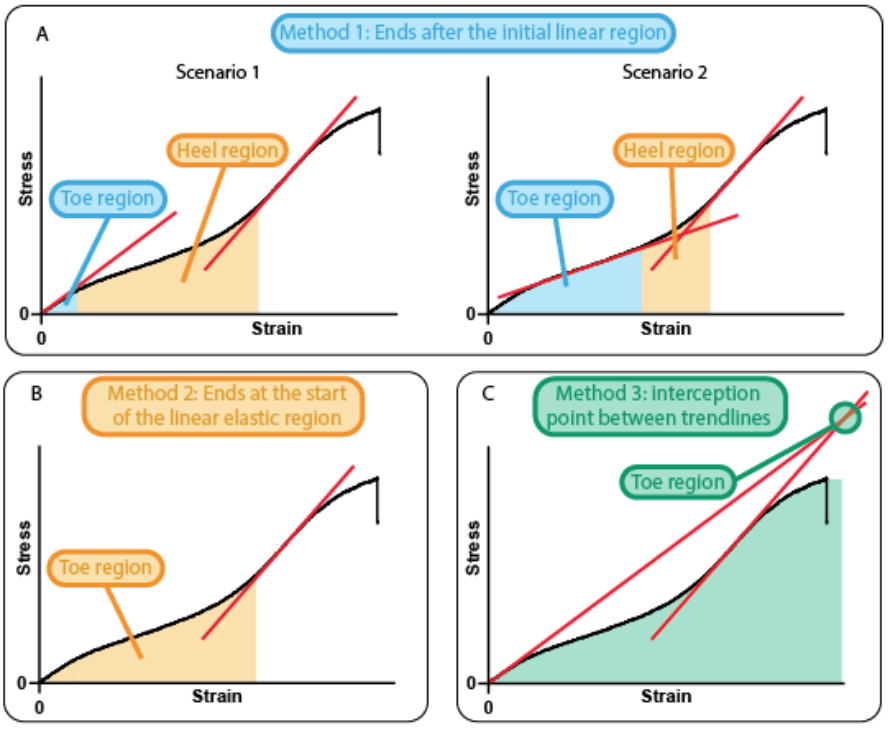

Figure S4. *Different methods for calculating the toe region of a representative AM80U5 design stress-strain curve. (A) Method 1 for calculating the toe region displayed in two different scenarios. In scenario 1 the trend line is taken from the start of the stress-strain curve. In scenario 2 the trend line is taken from the second linear part of the stress-strain curve (B) Method 2 for calculating the toe region. (C) Method 3 for calculating the toe region.*

Chapter 7

Fabrication of a mimetic vascular graft using melt spinning with tailorable fibre parameters

Fabrication of a mimetic vascular graft using melt spinning with tailorable fibre parameters*

Kenny A. van Kampen[1], Julia Fernández-Pérez[1], Matthew Baker[1], Carlos Mota[1], Lorenzo Moroni[1]

[1]Department of Complex Tissue Regeneration, MERLN Institute for Technology-Inspired Regenerative Medicine, Maastricht University, Universiteitssingel 40, 6229ER Maastricht, The Netherlands

***Chapter published in Biomaterials Advances 2022, DOI: 10.1016/j.bioadv.2022.212972**

Abstract

Smooth muscle cells play a pivotal role in maintaining blood pressure and remodeling of the extracellular matrix. These cells have a characteristic spindle shape and are aligned in the radial direction to aid in the constriction of any artery. Tissue engineered grafts have the potential to recreate this alignment and offer a viable alternative to the non-resorbable or autologous grafts. Specifically, with melt spinning small diameter fibers can be created that can align circumferentially on the scaffolds. In this study, a set of simplified equations were formulated to predict the final fiber parameters. Smooth muscle cell alignment was monitored on the fabricated scaffolds. Finally, a co-culture of smooth muscle cells in direct contact with endothelial cells was performed to assess the influence of the smooth muscle cell alignment on the morphology of the endothelial cells. The results show that the equations were able to accurately predict the fiber diameter, distance and angle. Primary vascular smooth muscle cells aligned according to the fiber direction

mimicking the native orientation. The co-culture with endothelial cells showed that the aligned smooth muscle cells did not have an influence on the morphology of the endothelial cells. In conclusion, we formulated a series of equations that can predict the fiber parameters during melt spinning. Furthermore, the method described here can create a vascular graft with smooth muscle cells aligned circumferentially that morphologically mimics the native orientation.

1. Introduction

Long-segmental vascular replacements due to bypass grafting or hemodialysis procedures are in clinical demand [1]. Gold standard treatment consists of an autologous graft. However, these grafts have restrictions such as limited donor availability, an additional surgical procedure, lower mechanical properties, and potential site morbidity [2]. Therefore, synthetic substitutes in the form of clinical grade woven polyethylene terephthalate are being used in the clinic [3]. Nevertheless, smaller diameter grafts (< 6 mm) cannot be replaced by these synthetic substitutes as a result of calcification issues [4], intimal hyperplasia [5] and acute thrombosis [6]. Due to this limitation, fabrication techniques capable of producing smaller diameter grafts may offer a viable alternative.

Electrospinning is one of the fabrication techniques frequently used to create small diameter vascular substitutes [7, 8]. With this technique small diameter fibers of less than 10 µm can be deposited, which helps creating a barrier layer necessary to generate a luminal coverage of cells [9]. Further developments led to the possibility to align the fibers along the circumference of the tubular vascular scaffold, which aids in the alignment of the cells through contact guidance and substrate curvature [10, 11]. This radial alignment of smooth muscle cells mimics the native disposition in the tunica media of any artery [12]. The main population of the tunica media consist of smooth muscle

cells. These cells have a pivotal role in maintaining blood pressure and remodeling of the extracellular matrix (ECM) [13]. Smooth muscle cells have a spindle shaped morphology that assists in the constriction of the artery [14]. However, smooth muscle cells can also adopt a more pancake-like morphology and possess a higher proliferative capacity. This phenotype has lost important contractile markers such as α-SMA and smoothelin, which stresses the importance to maintain a spindle-shaped morphology [15].

Even though electrospinning is capable of producing aligned small diameter fibers for tubular scaffolds, full control and prediction over the final outcome is somewhat limited. Especially with solution electrospinning (SES), where a whole range of controllable parameters such as the applied voltage, the nozzle-to-ground setup, the used solvent and solvent concentration have an influence on the outcome of the fiber morphology [16]. In turn, these parameters are also influenced by other factors that are less controllable, such as the humidity during spinning and electrostatic buildup from the deposited fibers [17, 18]. Melt electrowriting (MEW) is more controllable, but still influenced by electrostatic buildup and changes in the electric field [19].

Melt spinning allows the possibility to create thin fibers around a mandrel without the need for an electric field by melting a polymer and depositing it directly on a spinning mandrel [20, 21]. The resulting fibers are highly aligned and reproducible with little variations in fiber dimensions. Recent advances in the technique led to the fabrication of core-shell fibers with enhanced mechanical properties [22]. Without the need of an electric field, the controllable and uncontrollable parameters of the manufacturing process are no longer a limitation. Consequently, it could be summed up in simplified equations to predict the fiber parameters in terms of fiber dimensions, angle of the fibers and resulting spacing. This could result in a more reproducible barrier layer. Much like SES, these microfibers require a mechanical support.

A four axis melt extrusion based system could provide this support by creating larger macrofibers around the smaller microfibers [23].

The aim of the study was to further develop a spinning technique that is able to align smooth muscle cells in a small diameter vascular graft. In addition, simplified mathematical equations were formulated, based on the obtained results to predict the fiber diameter, distance between fibers and deposition angle. Primary smooth muscle cells were cultured on the scaffolds to assess whether the cells would morphologically mimic the tunica media of an artery. Finally, a co-culture with endothelial cells was done to assess whether the aligned primary smooth muscle cells influenced the morphology of the endothelial cells.

2. Materials and methods

2.1 Melt spinning method

A four-axis melt extrusion-based system was used, as described before, to fabricate the scaffolds [23]. Briefly, a cartridge containing poly(ε-caprolactone) (PCL, M_n =45,000 g mol^{-1}, Sigma-Aldrich) was loaded in the heating cartridge. The temperature was set at 130°C and extruded at a pressure of 5 bar through a 260 micron diameter nozzle (25G encapsulation needle, DL technology). A DC-motor (Unimat 12 Volt DC) with a maximum rotation of 20,000 RPM with a gear ratio of 6:1 and a collet grip was placed inside the four axis printer. The DC-motor was powered through a power-supply (Voltcraft LPS1153, Conrad) to control the RPM. The RPM of the mandrel was measured at various voltages using a stroboscope tachometer (Voltcraft DT-10L, Conrad). Data obtained from the tachometer was used to set up an equation to convert the voltage applied to RPM (Equation 1).

Equation 1 $RPM(Mandrel) = 226 * Voltage - 296$

A 2 mm diameter stainless steel mandrel was attached to the collet of the DC-motor. The distance between the nozzle of the four-axis extrusion based system and the mandrel was set at 1 cm. A low current was applied to start the rotation of the mandrel; while it was rotating the pressure of the four axis system was turned on. Once the polymer started to wrap around the mandrel, the RPM was increased to a set value ranging between 800 and 2400 RPM. A script was written to move the printhead of the four axis in the X-axis at a set speed between 1 and 30 mm/s with an excess length of 30 mm to compensate for the initial fiber deposition to settle. The extruder of the four-axis melt extrusion-based system moved while the mandrel was rotating. This created a single layer of aligned microfibers each time the extruder moved along the direction of the mandrel.

2.2 Scaffold fabrication

Once a thin layer of closely packed circumferentially aligned microfibers was created the mandrel was removed from the DC-motor and transferred to the collet of the four-axis extrusion based system to fabricate the macrofibers. There, the same script as described before was used to fabricate a diamond pore scaffold with 4 helices and a pitch of 4.5 mm to mimic the mechanical properties of a carotid artery [23]. Excess microfibers where cut with a scalpel blade and the total length of the scaffold was 10 mm for the morphological characterization and 20 mm in length for cell culture. The scaffolds used for mechanical characterization and cell culture were manufactured with 1300 RPM, with an extruder speed of 1 mm/s and 2 layers of fibers. This resulted in a scaffold with the smallest microfiber diameter and a small gap between each microfiber.

2.3 Scaffold characterization

Stereomicroscopy (SMZ25, Nikon instruments) was used to assess the morphology of the scaffold. The scaffolds were gold sputtered (SC7620, Quorum Technologies) before analyzed with scanning electron microscopy

(SEM, XL-30, Philips) to visualize and measure the fiber diameter, distance between the fiber and the angle of the deposited fibers.

2.4 Mechanical characterization

Mechanical characterization was performed on a mechanical tester (ElectroForce, TA instruments) with a 45 N load cell (ElectroForce). Tensile tests were performed in the longitudinal direction. A 5 mm long and 2 mm diameter stainless steel rod was inserted at the end of both sides of the scaffold. After the stainless steel rods were inserted, Parafilm® M (Heathrow Scientific) was wrapped around the part of the scaffold that contained the stainless steel mandrel to prevent slippage during the test. The samples were mounted in titanium clamps and stretched at a rate of 1% strain per second up to a total strain of 40% or until break. Scaffolds were sutured with polypropylene (Prolene monofil 5-0, Ethicon) at both ends of the scaffold for the suture retention test. The sutures were wrapped in Parafilm® M to prevent slippage and afterwards mounted using titanium clamps in the mechanical tester. The scaffolds were stretched at a rate of 1% strain per second up to a total of 40% or until break. Both the tensile and the suture retention test were captured with a camera (DMC-G3, Panasonic, The Netherlands) with a macro-lens (Panagor 90mm f2.8, Komine, Japan). Images and videos were analyzed using ImageJ (Version 1.52p, NIH) and Adobe Premiere Pro (Version 12.0, Premiere Pro CC 2018). The obtained force displacement values from the mechanical tester were converted to stress and strain. The Young's modulus was calculated as the slope in the linear part of the stress strain curve.

2.5 Cell culture

A10 (rat aortic smooth muscle cells) were used in the preliminary experiments to quantify the DNA content and seeding efficiency (Figure S1A-B). The A10 cells were cultured in DMEM (Sigma-Aldrich) supplemented with 10% fetal bovine serum (FBS) (Sigma-Aldrich). A10 cells were substituted for primary

smooth muscle cells (isolated from human aortas and kindly provided by Prof. Schurgers from the Department of Biochemistry at Maastricht University) after the seeding protocol was optimized. The primary vascular smooth muscle cells were cultured in DMEM, supplemented with 10% heat inactivated FBS. Human umbilical vein endothelial cells (HUVEC) (Thermo Fisher Scientific Inc.) were used as a source for endothelial cells. HUVECs were cultured in EGM-2 media (PromoCell).

2.6 Cell culture experiments

The luminal side of the scaffolds was coated using a protocol adapted from Gamboa-Martínez et al. [24]. Briefly, a solution of 20 mg/ml fibrinogen (Sigma-Aldrich) in tris-buffered saline (TBS) solution was injected in the lumen of the scaffolds. After 1 minute, the solution was removed using Whatman filter paper and a solution of 0.3 Units/ml thrombin (Sigma-Aldrich) with 20 mM $CaCl_2$ in TBS was added in the lumen. The thrombin solution was removed after 1 minute and the scaffolds were kept overnight in an oven at 37°C. The volume of fibrin and thrombin solution depends on the size of the scaffold and was calculated according to Equation 2 and rounded down to avoid liquid spilling over the scaffold. The scaffolds were disinfected with 70% ethanol for 30 minutes and dried under the laminar flow hood.

Equation 2 $Volume = \pi * radius^2 * length\ scaffold$

The luminal surface area was calculated in Equation 3 assuming the surface of the scaffold is smooth. The seeding density was based on a trial experiment using A10. The same volume used to coat the scaffolds was used to seed the cells in the lumen of the scaffolds (Equation 2). The cells were trypsinized (Thermo Fisher Scientific Inc., USA) from the culture flasks and brought to a concentration of 100,000 cells/cm^2.

Equation 3 $Luminal\ surface\ area = 2\pi * radius * length\ scaffold$

The scaffolds were transferred to a 0.65 ml microcentrifuge tube (Figure S2) for seeding to avoid cell sedimentation and attachment to one side of the scaffold. This Eppendorf was placed sideways in an empty pipette tip box and rotated 90 degrees every 15 minutes for 3 hours. After the 3 hours the scaffolds were transferred into an empty 12-well plate filled with 2 ml of media and was replaced every other day afterwards. For the coculture after 2 days the scaffolds were transferred to a 0.65 ml Eppendorf and a similar seeding procedure was performed for 3 hours with HUVECs with a seeding density of 100,000 cells/cm^2. After the seeding of the HUVECs was done, the media was changed to EGM-2 for the rest of the culture period.

2.7 Fluorescent microscopy and cell analysis

Cells were stained with 0.23 µg/ml DAPI (Sigma-Aldrich) and 0.5 µM Phalloidin (Thermo Fisher Scientific Inc.) for the alignment quantification. Fluorescent images were taken (Nikon Eclipse Ti-e) and the quantification done with a plugin for FIJI (OrentationJ) [25], which was based on the direction of the F-actin fibers stained by Phalloidin. For the coculture experiments the images were taken using confocal microscopy (Leica TCS SP8) and the cells were additionally stained against 2.5 µg/ml CD31 (Anti-CD31, Ab24590, Abcam) and 0.59 µg/ml alpha smooth muscle actin (Anti alpha smooth muscle actin, ab124964, Abcam) to visualize endothelial cells and the smooth muscle cells respectively. DNA quantification was performed using a cell proliferation assay according to the manufacturer's protocol (CyQUANT® Cell Proliferation Assay, Thermo Fisher Scientific Inc.). Nitric oxide (NO) production was measured using a nitrate nitrite fluorometric assay according to the manufacturer's protocol (nitrate nitrite fluorometric assay kit, Cayman Chemical).

2.8 Statistics

Statistical analyses were performed with GraphPad Prism 8.1.2. Significant differences were tested using an ANOVA test with a Šídák multiple comparisons test and were considered significant when $p<0.05$. All the values represented are in average ± standard deviation.

3. Results

3.1 Scaffold fabrication and characterization

A schematic overview of the fabrication process is shown in Figure 1A and 1B. Briefly, the molten polymer was deposited on top of a rotating mandrel capable of reaching speeds of 2400 RPM at maximum voltage, which resulted in an aligned thin layer of fibers (Figure 1C-F). After this process the mandrel was moved to the four axis system and a mechanical support based on a helical design to mimic the mechanical properties of an artery was printed around the thin layer of fibers.

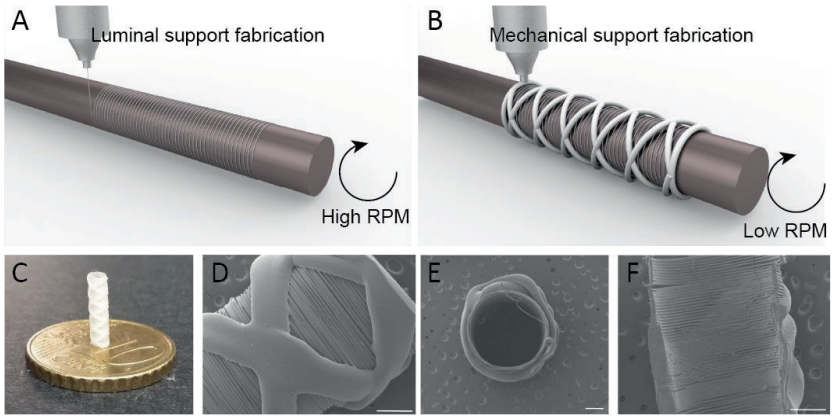

***Figure. 1**. Fabrication process of a vascular construct. (A) Schematic overview of the fabrication of the luminal support. (B) Schematic overview of the fabrication of the mechanical support. (C) Macroscopic image of the scaffold. SEM images from different perspectives. (D) Side view of the scaffold. (E) Top view of the scaffold. (F) Luminal view of the scaffold. Scale bar represents 500 µm.*

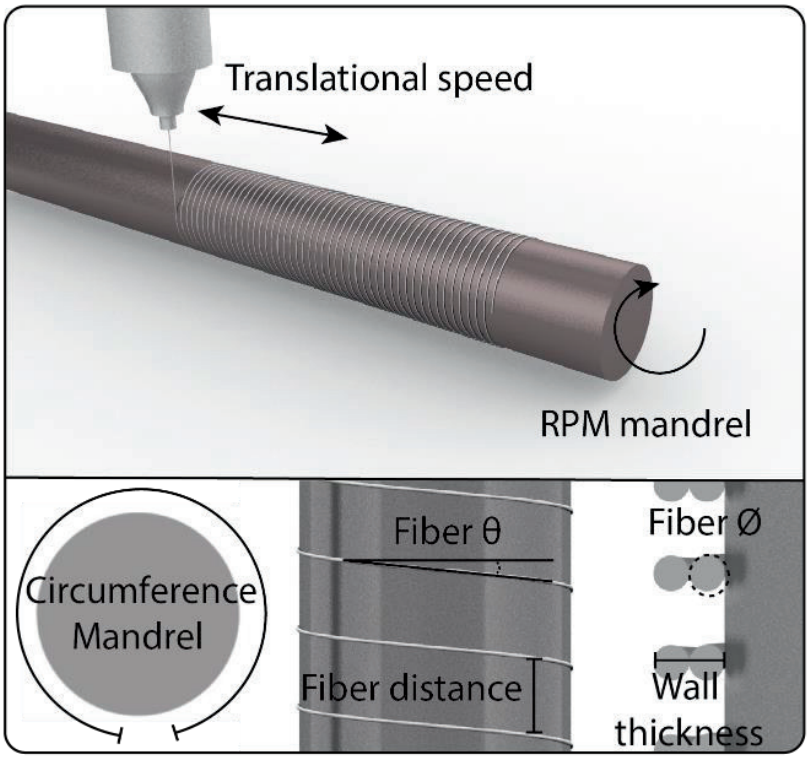

Figure. 2. *Schematic overview of the parameters used to fabricate and describe the microfibers.*

An overview of the fabrication parameters is shown in Figure 2. Various thin fiber scaffolds were fabricated by changing the RPM of the rotating mandrel (Figure 3A-B), the translational speed of the extruder and the amount of layers deposited on the mandrel. With a fixed translational speed of 1 mm/s, the RPM of the mandrel controlled the distance between the fiber. We observed that beyond 1400 RPM the fiber deposition became irregular and tend to break resulting in uneven distribution of polymer deposition and high variability in fiber distance (Figure S3A). The distances ranged from 70.2 µm ± 3.6 µm at 800 RPM to 34.0 µm ± 18.9 µm at 2400 RPM (Figure 2C). The theoretical distance between each fiber from center to center can be calculated with a known translational speed in mm/min and rotational speed in RPM (Equation 4). There was only a minor difference between the theoretical values and the actual measured values up until 1400 RPM.

Equation 4 $Fiber\ distance = \frac{translational\ speed}{RPM\ (Mandrel)}$

A correlation was observed between the angle at which the fiber is oriented, the circumference dimension of the mandrel and the distance between each fiber (Figure 3D). The faster the extruder traveled, the bigger the angle of the fiber was, ranging from 0.38° ± 0.24° at 1 mm/s to 15.67° ± 1.30° at the maximum speed of 30 mm/s with 1400 RPM. An equation was set up where the angle of the fiber (θ) can be calculated after knowing the circumference of the mandrel (C) and the distance of the fibers (Equation 5). The differences between the theoretical values and the actual values were negligible until 1400 RPM. At faster traveling speed (> 2000 RPM), the difference between theoretical and the measured values became more noticeable.

Equation 5 $Fiber\ \theta = \tan^{-1}(\frac{C}{Distance\ fiber})$

A trend between the diameter of the luminal support fibers and the RPM of the mandrel was observed. The diameter of the fibers decreased at faster RPM ranging from 55.6 µm ± 2.8 µm to 34.7 µm ± 30.6 µm at speeds of 800 RPM and 2400 RPM respectively (Figure 3E). As mentioned earlier, beyond 1400 RPM the fiber deposition became irregular and tended to break. The theoretical fiber diameter can be calculated by knowing the polymer volume being extruded (V) in mm^3 per minute and the total length of the fiber being deposited in mm per minute (Equation 6). Similar to the values for the fiber distance, the theoretical values were comparable to the actual values until 1400 RPM. At faster RPM (> 2000 RPM) the difference became more apparent.

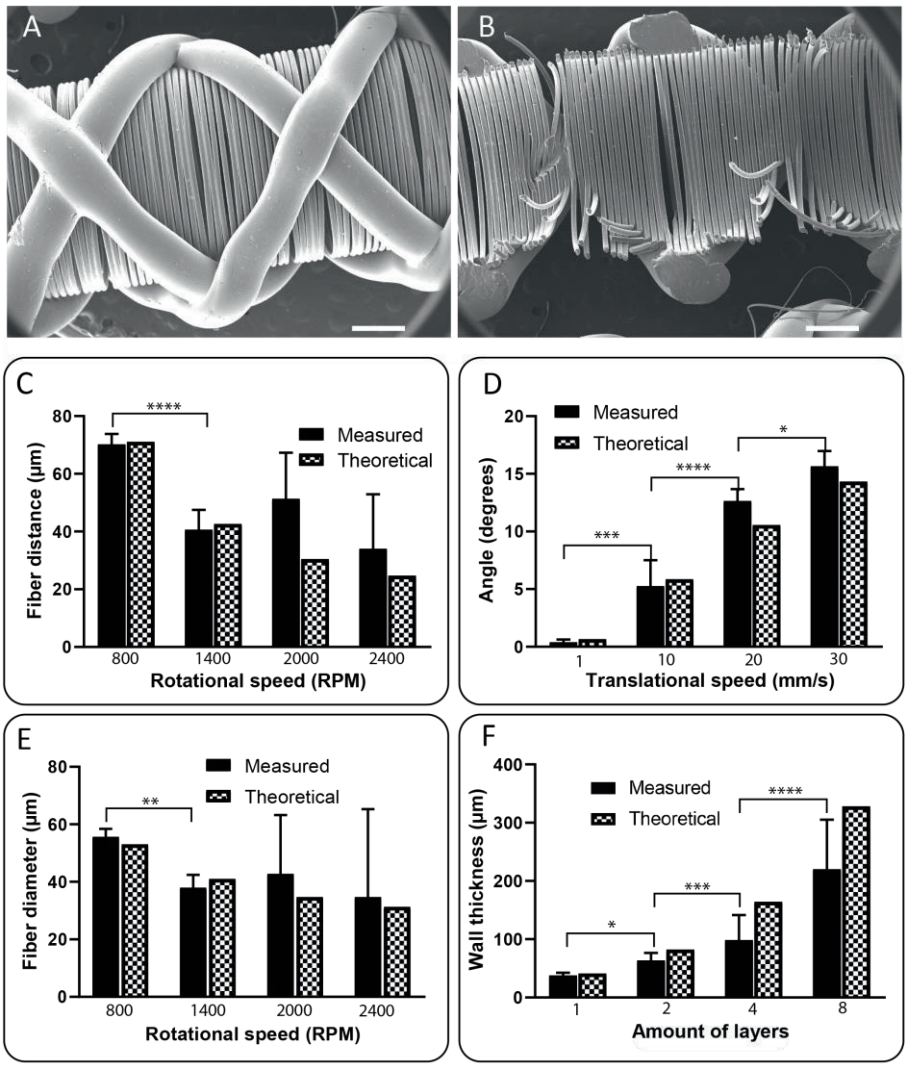

Figure. 3. *Parameters influencing the fibers of the luminal support. (A) Side view of a scaffold created at 1400 RPM with an extruder speed of 1 mm/s. (B) Luminal view of a scaffold created at 1400 RPM with an extruder speed of 1 mm/s. (C) Fiber distance measured from the center of each fiber at increasing rotational speed. (D) The angle of the fiber at increasing translational speed. (E) Fiber diameter at increasing rotational speed. (F) Wall thickness at multiple layers. Each condition contained n=5 with 6 measured fibers each. Scale bar represents 500 µm. * p<0.05, ** p<0.005, *** p<0.0005, **** p<0.0001.*

Equation 6 $Fiber\ \emptyset = 2 * \sqrt{\frac{V\ (extruded\ per\ minute)}{RPM(mandrel) * C * translational\ speed}}$

The thickness of the fiber wall depended on how many layers of fibers were deposited by the printhead each time it traversed over the whole length of the mandrel. The results showed that the thickness ranged from a single layer at 38.0 µm ± 4.4 µm up to 8 layers at 220.1 µm ± 85.1 µm, the thickness was directly correlated to the amount of times the extruder deposited a new layer (Figure 3D). The wall thickness can be expressed in an equation knowing the fiber diameter and total amount of layers deposited (Equation 7). With the increasing amount of layers, the size of the wall became irregular resulting in a notable difference with the theoretical values (Figure S3B).

Equation 7 $Fiber\ wall\ thickness = fiber\ \emptyset * layers\ deposited$

3.2 Mechanical properties of the scaffold

The effect of the luminal support on the mechanical properties was investigated via tensile testing of constructs with and without the small melt spun fibers. Scaffolds for the mechanical characterization were produced based on the previous results and equations. We selected the following parameters for further testing; 1300 RPM, with an extruder speed of 1 mm/s and 2 layers of fibers. The aim was to have a scaffold with the smallest diameter microfiber that also had a gap between each microfiber to facilitate cellular communication. The tensile test revealed that the luminal support significantly increases the Young's modulus from 1.4 ± 0.1 MPa to 5.6 ± 1.4 MPa, the test also showed some defects at larger strains (Figure 4A-B). In addition, the shape of the stress-strain curve was also different with an inflection point that was more pronounced compared to without lumen (Figure 4C). The suture retention test showed that the scaffolds with luminal support were able to hold the sutures without tearing through the mechanical support (Figure 4D). Similar to the tensile test it was shown that defects in the luminal support start to appear at higher strain. This was further quantified by video

analyses and showed that especially after 15% strain all of the tested samples showed a visible defects in the lumen (Figure 4E).

3.3 Smooth muscle cell alignment and coculture

Similar scaffolds as in the previous section have been produced for the cell experiments. A trial experiment was performed using A10 cells to determine the optimal seeding density (Figure S1B). The results showed that a seeding density of 100,000 cells/cm^2 resulted in a similar amount of DNA after both 4 hours and 3 days as compared to the 400,000 cells/ cm^2 leading to a higher seeding efficiency. After these initial trial tests, the A10 cells were replaced with primary human smooth muscle cells. Primary smooth muscle cells were seeded on the scaffolds and their alignment was observed for 2 days post-seeding. The alignment was assessed by evaluating the F-actin fibers using the orientationJ plugin from FIJI. The results showed that 4 hours post-seeding, there was no clear alignment towards the direction of the fibers. The cells imaged after 4 hours had a round morphology (Figure 5A). After 1 day of culture there was a peak observed around the direction of the fibers. In addition, the morphology changed from round to spindle shaped in the direction of the fibers (Figure 5B). This observation became more apparent at 2 days post-seeding and the cells formed a confluent layer on the luminal side of the scaffold (Figure 5C).

The inner layer of an artery is lined with endothelial cells. HUVECs were seeded in the lumen of the scaffold after 2 days to mimic this situation. The total culture time was 14 days and the morphology was assessed through microscopy. After 7 days of culture both the presence of HUVECs and smooth muscle cells was observed as indicated by the positive staining for CD31 and alpha smooth muscle actin, respectively (Figure 6). The smooth muscle cells maintained a confluent layer directly attached to the luminal side of the fibers (Figure 6A). In addition, smooth muscle cells settled between the fibers of the

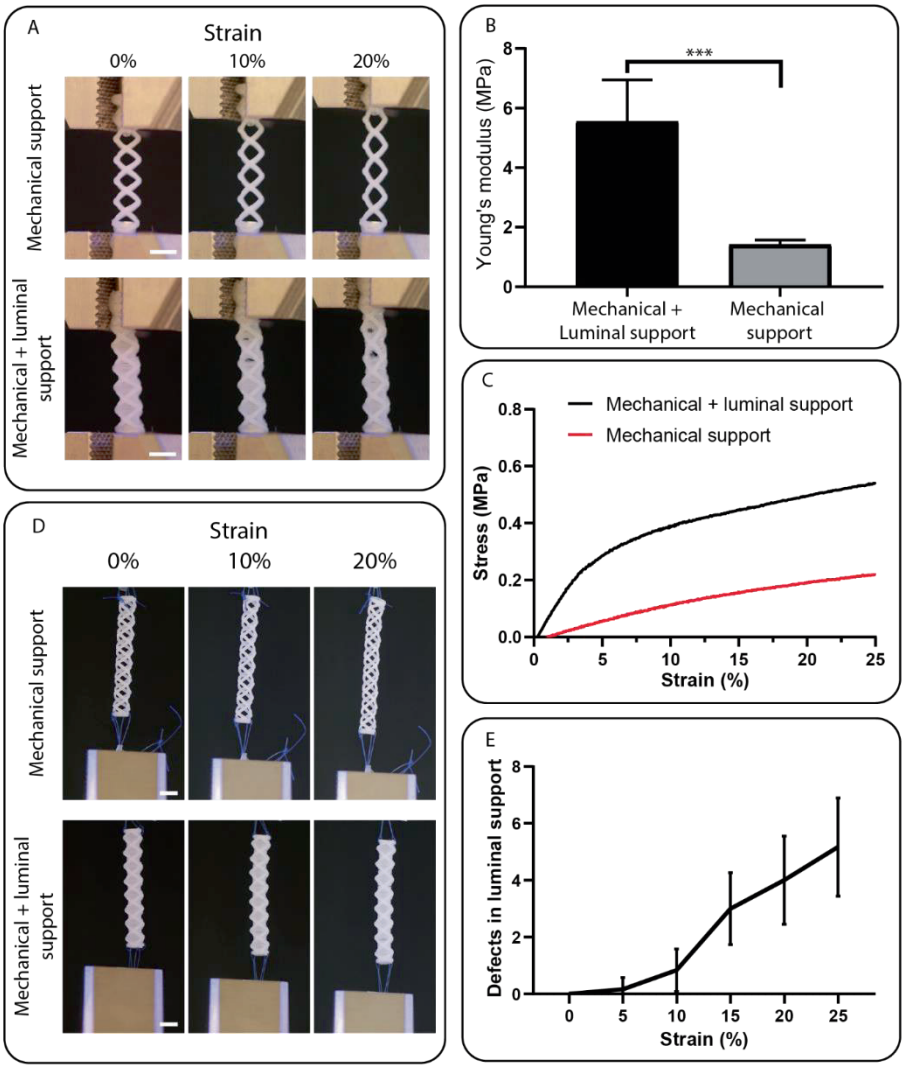

Figure. 4. *Mechanical characterization of the scaffold with and without luminal support. (A) Time-lapsed snapshots during the tensile test of the tested scaffolds. (B) Young's modulus and (C) representative stress-strain curve of the tested scaffolds. (D) Video snapshots during the suture retention test of the tested scaffolds. (E) Amount of visible defects in the luminal support during the suture retention test. Each condition contained n=5 samples. Scale bar represents 2 mm. *** p<0.0005*

scaffold indicating that the wall was still permeable enough to facilitate cell migration (Figure 6B). The morphology of the smooth muscle cells remained the same with an alignment in the direction of the fibers. The HUVECs directly

on top of the smooth muscle cells formed a monolayer, indicated by the presence of CD31 throughout the lumen of the scaffold (Figure 6C). In addition, HUVECs displayed no particular alignment and displayed a cobblestone morphology. Similar results were shown at day 14 (Figure 7A), where the smooth muscle cells retained their spindle shaped morphology in between the fibers of the scaffold (Figure 7B). The endothelial cells on the luminal side of the scaffold formed a monolayer as seen by the presence of CD31 and showed a cobblestone morphology (Figure 7C). The production of NO increased after day 3 of culture and after 7 days remained stable until day 14 (Figure S5).

4. Discussion

This study highlighted the ability to create a tubular scaffold with a luminal support through melt spinning for cells to attach. This in turn caused the smooth muscle cells to align in the circumference of the scaffold mimicking the tunica media of an artery. The theoretical fiber diameter, distance and angle can be calculated through the equations set up in this study since melt spinning relies on a few controllable parameters, making this approach reproducible and predictable for other researchers. The cultured vascular smooth muscle cells covered the luminal wall after 2 days of culture and aligned according to the direction of the fibers for the duration of the culture period, indicating that this technique is capable of creating a scaffold that aids in the alignment of cells. The morphology of both cell types after coculture in the scaffolds mimicked the native conditions, having a cobblestone and spindle shaped morphology for endothelial cells and smooth muscle cells respectively, despite being in direct contact with each other. This demonstrates that this technique is able to create a morphologically mimicking small diameter vascular graft.

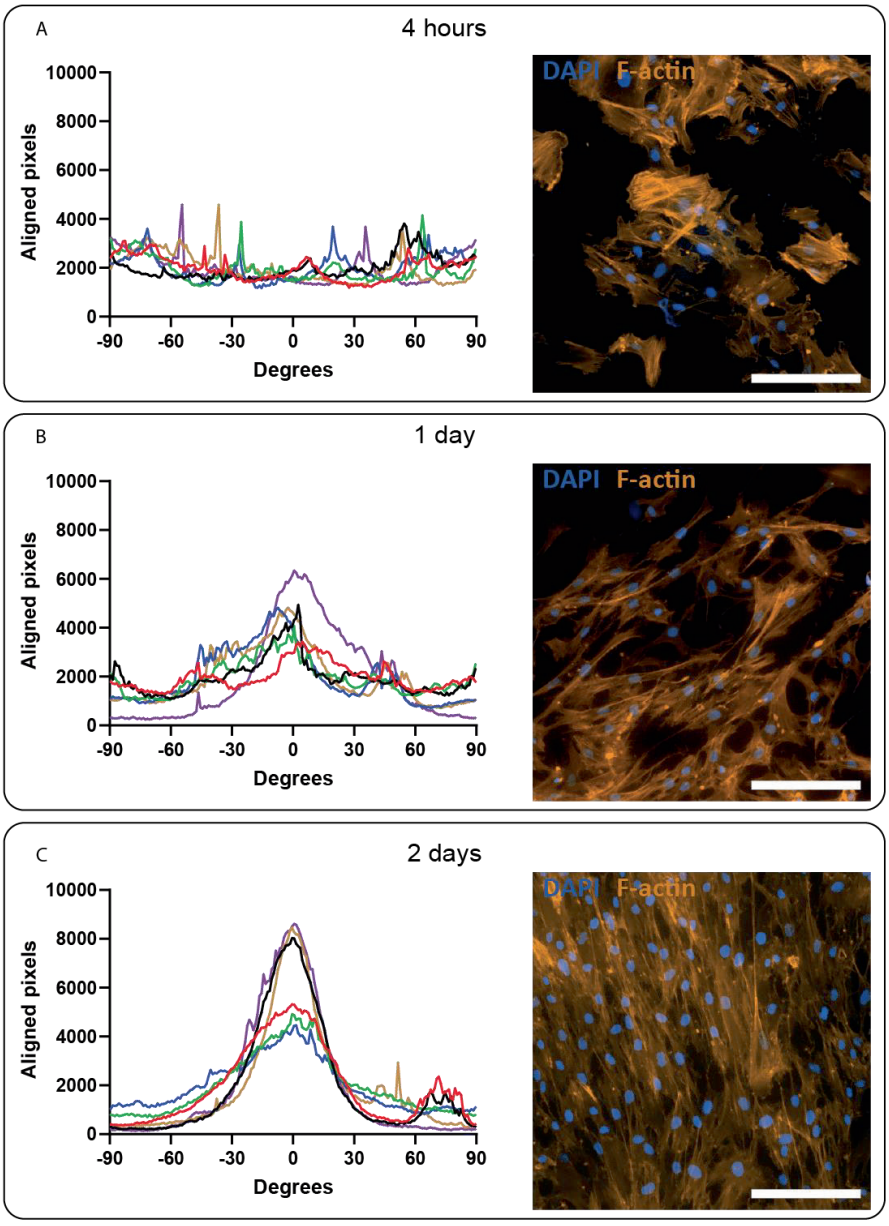

Figure. 5. *Smooth muscle cell alignment over time on the scaffolds. (A) Aligned pixels and representative image 4 hours post-seeding. (B) Aligned pixels and representative image 1 day post-seeding. (C) Aligned pixels and representative image 2 days post-seeding. Each colored line in the graphs represent one region of interest per sample n=6. Scale bar represents 50 µm.*

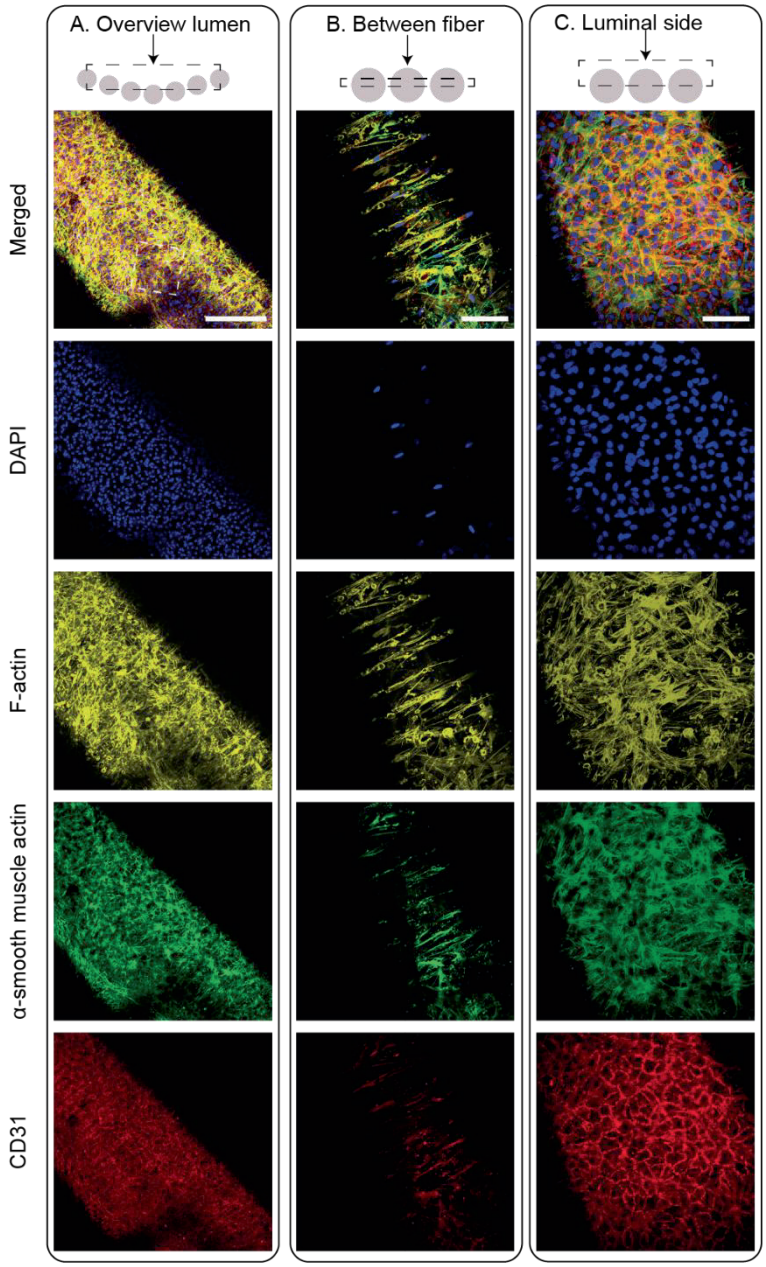

Figure. 6. *Coculture of primary smooth muscle cells and HUVECs after 7 days of culture. (A) Overview image at lower magnification. (B) Image of the smooth muscle cells in the wall of the scaffold. (C) Image of both cell types in the lumen of the scaffold. Scale bar represents 500 µm in panel A and 100 µm in panel B and C.*

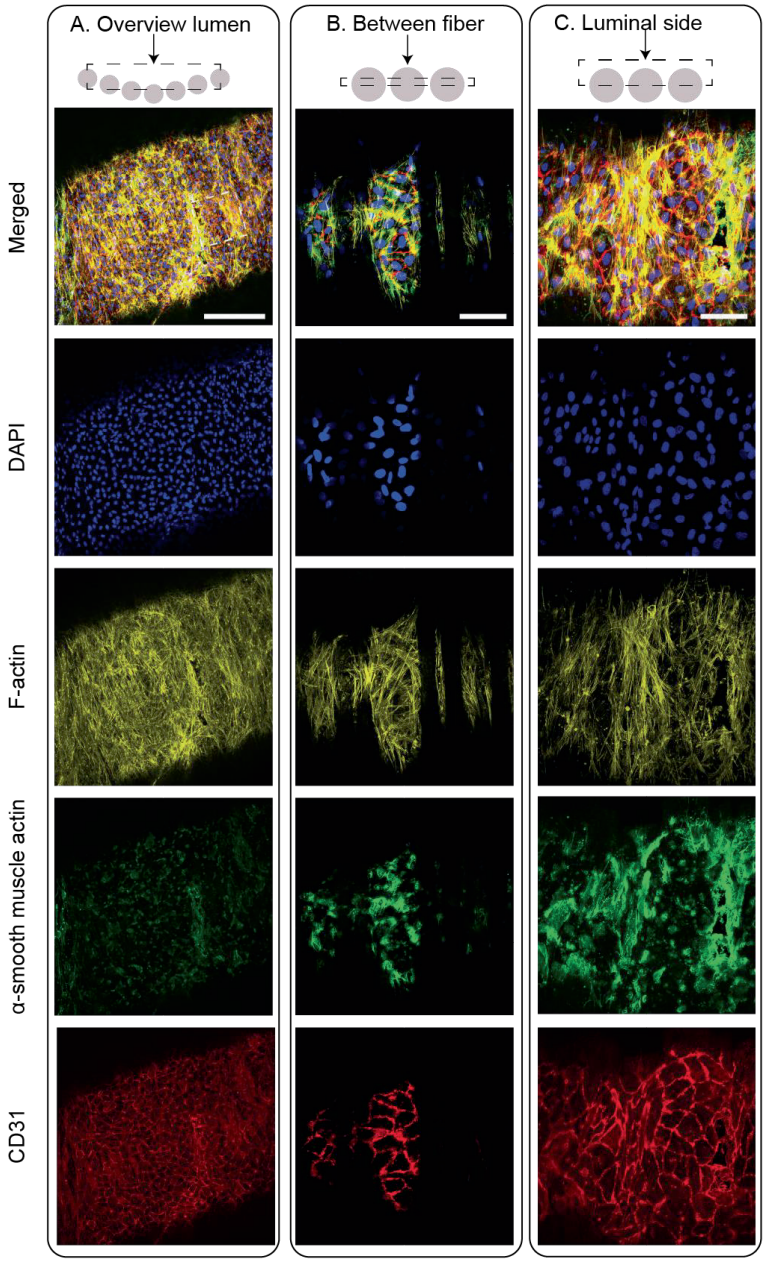

Figure. 7. *Coculture of primary smooth muscle cells and HUVECs after 14 days of culture. (A) Overview image at lower magnification. (B) Image of the smooth muscle cells in the wall of the scaffold. (C) Image of both cell types in the lumen of the scaffold. Scale bar represents 500 µm in panel A and 100 µm in panel B and C.*

Smooth muscle cell alignment is vital for a functioning artery, their morphology helps the cells in their contractile function [26]. Creating a template that mimics this morphology can improve the final function of a constructed artery. Therefore prior work to create a luminal support layer focused on either using MEW or SES [27, 28]. A thin mesh can be created with SES, which allows certain alignment. However, there is still a significant part of the fibers that do not follow the same circumferential alignment especially at small diameter grafts [29]. In addition, the mesh that is created is often dense and is difficult for cells to penetrate through [30]. This might not be beneficial since there is interaction between the inner and outer layers of an artery [31]. Moreover, the mechanical properties of a SES mesh are often too weak to carry its own weight. Therefore, SES is often combined with MEW [10]. With MEW, the alignment of the fibers is improved, although the fibers stacking next to each other is limited due to the electric repulsion [32]. This makes melt spinning a viable option to create a supporting lumen with aligned small diameter fibers. Further development, such as using different materials and optimization of the fabrication process could reduce the diameter of the fibers. A different possibility to explore is the effect of fiber stacking in different configurations or surfaces on cellular and mechanical behavior.

The equations that are formulated in this study have shown to accurately predict the actual values for the scaffold. The initial parameters that are required such as the mandrel size, volume extruded per minute and RPM of the mandrel can easily be obtained. In addition, the equations themselves are relatively simple to solve. However, one of the limitations of the calculations presented here is that there is no theoretical limit to the fiber diameter. Our data shows that with PCL (M_n 45,000) the limit for stable fibers is around 35 µm with 1400 RPM. A higher RPM would result in the fiber becoming unstable and depositing unevenly which also reduces the accuracy of the equations. Further investigations using different materials could give insight to what role the mechanical properties of the bulk material play in the minimum microfiber

diameter limit. Another limitation is that the calculations presented here are simplified. The equation to obtain the fiber diameter is overestimated due the assumption that the circumference is equal to the mandrel size. In practice, the final diameter should be equal to the diameter of the mandrel plus the produced fiber. However including this into the formula would result into a differential equation that is more difficult to solve. Furthermore, the increase in circumference is negligible due to the large size of the mandrel compared to the produced microfibers.

The stacking of multiple layers on the scaffold resulted in a less accurate prediction of the wall thickness. This can be explained by a sagging effect when there is no support underneath the deposited fiber resulting in a collapse of the fibers. This effect is also seen with other techniques such as melt extrusion and MEW and can be solved by reducing the distance between the fibers [33, 34]. The objective is to keep some degree of porosity between the fibers that facilitates cell migration. This is essential not only to create the adventitia layer of a blood vessel, but also to communicate between the three layers of an artery [35, 36].

The addition of the luminal support had a significant influence in the Young's modulus of the scaffold. This makes the scaffold with a luminal support stiffer than a healthy human carotid artery [37]. A cytocompatible material that is less stiff could result in a lower Young's modulus that matches the native tissue. The alternative is to study the effect of the angle of the fiber on the mechanical properties. This in combination with the a different material could bring the mechanical properties in the right range to avoid any mechanical mismatch [38]. The rings on the mechanical support made the suturing of the scaffolds more accessible. In addition, the thick fibers prevented the suture from tearing through the entire wall of the scaffolds when pulled in the retention test. Visible defects were noted in the scaffolds at strains bigger than 10%. All of the scaffolds showed defects after 15% strain. This could cause ruptures when

implanting the scaffolds and result in disturbed flow and risk of thrombosis [39]. However it is important to note that most of the defects happen at strain values that are beyond what is physiologically relevant [40]. A key point of vascular grafts is the ability to withstand arterial pressure [41]. A method to measure this ability in scaffolds is through a burst pressure test [42]. However one of the requirements is that the sample is hermetically sealed. With our scaffold geometry, we chose not to investigate this due the small gaps present between the fibers as a result of the fabrication process Therefore, studies that used electrospun meshes or other semipermeable grafts use a balloon catheter or other non-permeable membrane on the luminal side of the scaffold [43, 44]. The catheter however, also prevents the ability to detect small defects in a scaffold that could either tear open when pressurized and result in an overestimation in burst pressure [45].

Smooth muscle cells can be divided in two different phenotypes, a synthetic type that has a flat and pancake shaped morphology that deposits ECM, and a contractile type that is spindle-shaped and contains more contractile filaments [46]. The cells observed after 2 days of culture shared a similar morphology of the contractile phenotype [14]. Moreover, after 2 days of culture the smooth muscle cells showed a similar alignment as to the native vascular environment [47]. Albeit at a decreased presence of α-smooth muscle actin. Cell alignment has been well studied and similar results showed that having small fiber diameter improves alignment [48]. In addition, the spacing between the fibers that is created causes the cells to align through contact guidance [48, 49]. Other studies demonstrated the possibility to keep this alignment for at least 7 days in culture [10]. Our results on the other hand showed that this can be extended to at least 14 days of culture with multiple cell layers. Smooth muscle cells are known to lose their α-smooth muscle actin when there is a lack of mechanical stimuli [50]. This could explain why the presence of α-smooth muscle actin seemed to decrease and did not follow a similar alignment as the F-actin after 14 days. Another aspect to note is that the

amount of cell layers presented here does not compare to the native situation where the tunica media of a coronary artery is around 200 µm [51]. Images taken from the adventitial side of the scaffold revealed that the cells after 7 days are migrated through the scaffold and were starting to form a monolayer (Figure S4). Future studies could aim at adding multiple layers in combination with longer culture periods to mimic the thickness of the tunica media.

A coculture not only represents the physiological situation better, but can also improve the α-smooth muscle actin organization [52]. Other studies have performed cocultures on scaffolds, however these cells had a physical barrier between them and direct cell-cell contact was limited [10, 53, 54]. Facilitating direct cell-cell contact between the two cell types is vital for the inhibition of chronic inflammation of the endothelial cells and the differentiation of smooth muscle cells from undifferentiated mesenchymal cells [55-58]. In this study, the endothelial cells were seeded directly on top of the cultured smooth muscle cells to improve the direct cell-cell contact in the scaffold. This was reflected by the increase in NO production after the start of the coculture (Figure S5). NO is a vasodilating agent that is released by the endothelial cells and acts on the smooth muscle cells [59]. However, the observed increase was stabilized after 7 days. A possible explanation is that in this study the scaffolds were cultured statically, whereas NO synthesis is known to be increased upon shear stress and could be stimulated when the scaffolds are cultured under flow conditions [60].

The culture time for smooth muscle cells and when to introduce the endothelial cells are important. In our study, we showed that after 2 days of culture the smooth muscle cells populated the entire luminal wall of the scaffold. This was one of the requirements before seeding the endothelial cells. A study by Williams et al. showed that the duration of the smooth muscle cell culture should be increased for a uniform distribution of the cells [61]. In addition, smooth muscle cells showed a more contractile phenotype over long-term

coculture periods. However, ECM deposition and smooth muscle cell proliferation is reduced when the endothelial cells are introduced at an early time point. For this study, the duration of 2 days might be too early for smooth muscle cells to deposit enough ECM for firm attachment. This could result in the detachment of the cells after longer culture periods, especially when subjected to flow [62]. This effect was sporadically observed in some of the samples even under static conditions after 14 days (Figure S6).

Interesting to note is that the endothelial cells did not align to the direction of the fibers, unlike smooth muscle cells directly underneath them. The morphology of the endothelial cells remained a cobblestone shaped. Other research showed that endothelial cells do align in the direction of small fibers [63]. An explanation for this could be that the smooth muscle cells filled up the gaps between the fibers after the first two days of culture. The filled up gaps results in the smoothening of the luminal wall (Figure 8). This is confirmed by the fact that between the fibers the cells stain positive for α-smooth muscle actin while negative for CD31. Another observation is that the method of seeding the smooth muscle cells before the endothelial cells does not reflect the native regeneration process [64]. The scaffolds are coated with fibrin on the luminal side, however this coating is thin enough for cells to pass through as shown in the results (Figure 6, Figure S4). If there was a thicker coating, this could act as a barrier for both the endothelial and smooth muscle cells to migrate through, giving them both the opportunity to populate the area between the fibers and luminal side respectively. Future studies could investigate whether the thickness of the fibrin coating and the simultaneously seeding of both cell types would still result in a similar alignment.

Although we have shown here that combining melt spinning with 4-axis additive manufacturing leads to the fabrication of a scaffold able to direct cell alignment, future research could investigate other biomaterials. This could give insight to the minimal fiber diameter possible with this technique and the

influence of the material properties, which can also be beneficial for smooth muscle cells, known to dedifferentiate towards a macrophage like phenotype when cultured on stiff materials [65]. In addition, the elastic behavior of an artery can be recreated with other polymers [66, 67]. This emphasizes the need to explore this technique with different materials. Furthermore, these scaffolds should also be validated under dynamic culture conditions, which was shown to improve the outcome of the engineered vascular tissue [68]. Future studies can aim at the fabrication of the adventitia layer, which is often overlooked though vitally important [69, 70].

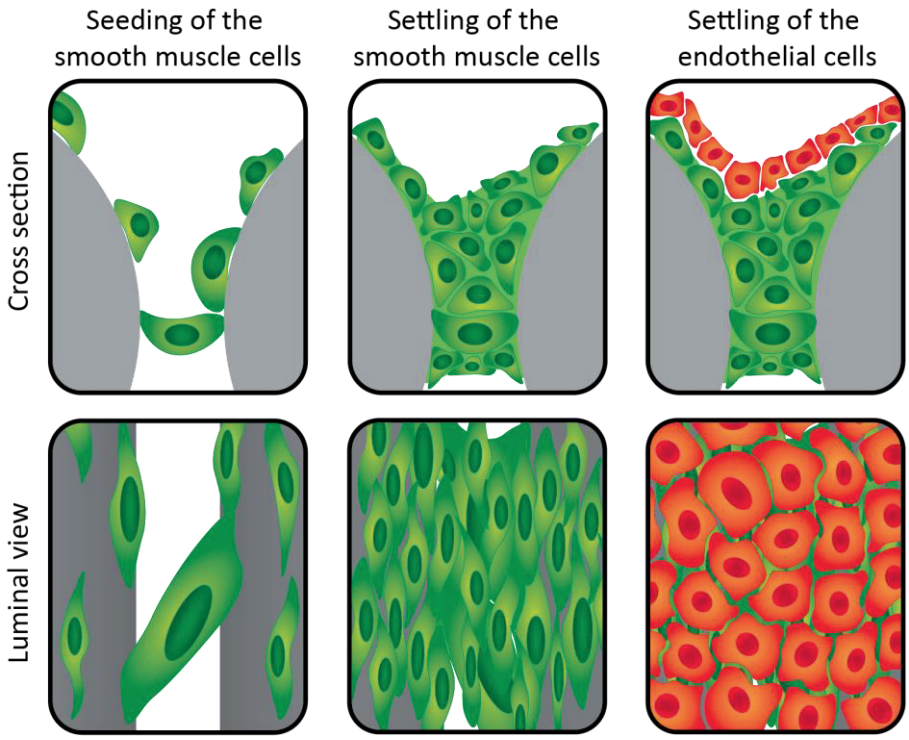

Figure. 8. *Proposed explanation of the smooth muscle cell alignment and the rounded endothelial cell morphology.*

5. Conclusion

In conclusion, we demonstrated a melt spinning technique that is capable of both supporting and aligning smooth muscle cells. The dimensions of the produced fibers can be accurately predicted through the equations set up in this study. Using the equations described here as a template for other more complex fabrication techniques can help understand the parameters that influence the microfiber dimensions of a scaffold. Aligned deposited microfibers helped align the smooth muscle cells. In addition, cell alignment was maintained after 14 days of culture even in direct contact with endothelial cells. Finally, the alignment of the smooth muscle cells did not influence alignment of the endothelial cells. With this technique a predictable mesh of highly aligned fibers can be created that can aid in the development of a coronary artery graft.

Acknowledgements

This work was supported by H2020 FAST (NMP-7, GA n. 685825), the ERC Cell Hybridge (GA n. 637308); the partners of Regenerative Medicine Crossing Borders and Health Holland. We also gratefully acknowledge the donation of the primary smooth muscle cells by Prof. Schurgers and Dr. Jaminon.

References

[1] H. Haruguchi, S. Teraoka, Intimal hyperplasia and hemodynamic factors in arterial bypass and arteriovenous grafts: a review, Journal of Artificial Organs 6(4) (2003) 227-235.
[2] J. Chlupáč, E. Filova, L. Bačáková, Blood vessel replacement: 50 years of development and tissue engineering paradigms in vascular surgery, Physiological Research 58(Suppl 2) (2009) S119-S139.
[3] K.-M. Park, Y.W. Kim, S.-S. Yang, D.-I. Kim, Comparisons between prosthetic vascular graft and saphenous vein graft in femoro-popliteal bypass, Annals of Surgical Treatment and Research 87(1) (2014) 35-40.
[4] R.I. Mehta, A.K. Mukherjee, T.D. Patterson, M.C. Fishbein, Pathology of explanted polytetrafluoroethylene vascular grafts, Cardiovascular Pathology 20(4) (2011) 213-221.
[5] Y. Jeong, Y. Yao, E.K. Yim, Current understanding of intimal hyperplasia and effect of compliance in synthetic small diameter vascular grafts, Biomaterials science 8(16) (2020) 4383-4395.
[6] J. Al Shakarchi, G. Houston, N. Inston, Early cannulation grafts for haemodialysis: a systematic review, The Journal of Vascular Access 16(6) (2015) 493-497.
[7] Y. Pan, X. Zhou, Y. Wei, Q. Zhang, T. Wang, M. Zhu, W. Li, R. Huang, R. Liu, J. Chen, Small-diameter hybrid vascular grafts composed of polycaprolactone and polydioxanone fibers, Scientific reports 7(1) (2017) 1-11.
[8] P. Davoudi, S. Assadpour, M.A. Derakhshan, J. Ai, A. Solouk, H. Ghanbari, Biomimetic modification of polyurethane-based nanofibrous vascular grafts: A promising approach towards stable endothelial lining, Materials Science and Engineering: C 80 (2017) 213-221.
[9] Y. Wang, H. Shi, J. Qiao, Y. Tian, M. Wu, W. Zhang, Y. Lin, Z. Niu, Y. Huang, Electrospun tubular scaffold with circumferentially aligned nanofibers for regulating smooth muscle cell growth, ACS applied materials & interfaces 6(4) (2014) 2958-2962.
[10] I. Pennings, E.E. van Haaften, T. Jungst, J.A. Bulsink, A.J. Rosenberg, J. Groll, C.V. Bouten, N.A. Kurniawan, A.I. Smits, D. Gawlitta, Layer-specific cell differentiation in bi-layered vascular grafts under flow perfusion, Biofabrication 12(1) (2019) 015009.
[11] A.M. van Genderen, K. Jansen, M. Kristen, J. Van Duijn, Y. Li, C.C. Schuurmans, J. Malda, T. Vermonden, J. Jansen, R. Masereeuw, Topographic Guidance in Melt-Electrowritten Tubular Scaffolds Enhances Engineered Kidney Tubule Performance, Frontiers in bioengineering and biotechnology 8 (2021) 1542.
[12] J. Walmsley, M. Campling, H. Chertkow, Interrelationships among wall structure, smooth muscle orientation, and contraction in human major cerebral arteries, Stroke 14(5) (1983) 781-790.
[13] A.L. Durham, M.Y. Speer, M. Scatena, C.M. Giachelli, C.M. Shanahan, Role of smooth muscle cells in vascular calcification: implications in atherosclerosis and arterial stiffness, Cardiovascular research 114(4) (2018) 590-600.
[14] S. Rensen, P. Doevendans, G. Van Eys, Regulation and characteristics of vascular smooth muscle cell phenotypic diversity, Netherlands Heart Journal 15(3) (2007) 100-108.
[15] R.T. Johnson, R. Solanki, D.T. Warren, Mechanical programming of arterial smooth muscle cells in health and ageing, Biophysical Reviews (2021) 1-12.
[16] M.K. Leach, Z.-Q. Feng, S.J. Tuck, J.M. Corey, Electrospinning fundamentals: optimizing solution and apparatus parameters, JoVE (Journal of Visualized Experiments) (47) (2011) e2494.
[17] S. Theron, E. Zussman, A. Yarin, Experimental investigation of the governing parameters in the electrospinning of polymer solutions, Polymer 45(6) (2004) 2017-2030.
[18] V. Beachley, X. Wen, Effect of electrospinning parameters on the nanofiber diameter and length, Materials Science and Engineering: C 29(3) (2009) 663-668.
[19] F.M. Wunner, P. Mieszczanek, O. Bas, S. Eggert, J. Maartens, P.D. Dalton, E.M. De-Juan-Pardo, D.W. Hutmacher, Printomics: the high-throughput analysis of printing parameters applied to melt electrowriting, Biofabrication 11(2) (2019) 025004.
[20] P. Wu, L. Wang, W. Li, Y. Zhang, Y. Wu, D. Zhi, H. Wang, L. Wang, D. Kong, M. Zhu, Construction of vascular graft with circumferentially oriented microchannels for improving artery regeneration, Biomaterials 242 (2020) 119922.

[21] S. Chung, N.P. Ingle, G.A. Montero, S.H. Kim, M.W. King, Bioresorbable elastomeric vascular tissue engineering scaffolds via melt spinning and electrospinning, Acta Biomaterialia 6(6) (2010) 1958-1967.
[22] C. Cherif, N. Tran, M. Kirsten, H. Bruenig, R. Vogel, Environmentally friendly and highly productive bi-component melt spinning of thermoregulated smart polymer fibres with high latent heat capacity, Express Polymer Letters 12(3) (2018) 203-214.
[23] K.A. van Kampen, E. Olaret, I.-C. Stancu, L. Moroni, C. Mota, Controllable four axis extrusion-based additive manufacturing system for the fabrication of tubular scaffolds with tailorable mechanical properties, Materials Science and Engineering: C 119 (2021) 111472.
[24] T.C. Gamboa-Martínez, J.L. Gómez Ribelles, G. Gallego Ferrer, Fibrin coating on poly (L-lactide) scaffolds for tissue engineering, Journal of Bioactive and Compatible Polymers 26(5) (2011) 464-477.
[25] R. Rezakhaniha, A. Agianniotis, J.T.C. Schrauwen, A. Griffa, D. Sage, C.v. Bouten, F. Van De Vosse, M. Unser, N. Stergiopulos, Experimental investigation of collagen waviness and orientation in the arterial adventitia using confocal laser scanning microscopy, Biomechanics and modeling in mechanobiology 11(3) (2012) 461-473.
[26] P. Lacolley, V. Regnault, A. Nicoletti, Z. Li, J.-B. Michel, The vascular smooth muscle cell in arterial pathology: a cell that can take on multiple roles, Cardiovascular research 95(2) (2012) 194-204.
[27] N.T. Saidy, T. Shabab, O. Bas, D.M. Rojas-González, M. Menne, T. Henry, D.W. Hutmacher, P. Mela, E.M. De-Juan-Pardo, Melt Electrowriting of Complex 3D Anatomically Relevant Scaffolds, Frontiers in bioengineering and biotechnology 8 (2020) 793.
[28] C. Grasl, M. Stoiber, M. Röhrich, F. Moscato, H. Bergmeister, H. Schima, Electrospinning of small diameter vascular grafts with preferential fiber directions and comparison of their mechanical behavior with native rat aortas, Materials Science and Engineering: C 124 (2021) 112085.
[29] S. Park, J. Kim, M.-K. Lee, C. Park, H.-D. Jung, H.-E. Kim, T.-S. Jang, Fabrication of strong, bioactive vascular grafts with PCL/collagen and PCL/silica bilayers for small-diameter vascular applications, Materials & Design 181 (2019) 108079.
[30] G.Z. Tan, Y. Zhou, Electrospinning of biomimetic fibrous scaffolds for tissue engineering: a review, International Journal of Polymeric Materials and Polymeric Biomaterials 69(15) (2020) 947-960.
[31] L. Chang, H. Milton, D.T. Eitzman, Y.E. Chen, Paradoxical roles of perivascular adipose tissue in atherosclerosis and hypertension, Circulation Journal (2012) CJ-12-1393.
[32] C.D. O'Connell, O. Bridges, C. Everett, N. Antill-O'Brien, C. Onofrillo, C. Di Bella, Electrostatic Distortion of Melt-Electrowritten Patterns by 3D Objects: Quantification, Modeling, and Toolpath Correction, Advanced Materials Technologies (2021) 2100345.
[33] N.T. Nguyen, J.H. Kim, Y.H. Jeong, Identification of sagging in melt-electrospinning of microfiber scaffolds, Materials Science and Engineering: C 103 (2019) 109785.
[34] A.R. Calore, R. Sinha, J. Harings, K.V. Bernaerts, C. Mota, L. Moroni, Additive Manufacturing Using Melt Extruded Thermoplastics for Tissue Engineering, Computer-Aided Tissue Engineering, Springer2021, pp. 75-99.
[35] A. Loesch, M.R. Dashwood, Vasa vasorum inside out/outside in communication: a potential role in the patency of saphenous vein coronary artery bypass grafts, Journal of cell communication and signaling 12(4) (2018) 631-643.
[36] P. Martinez-Quinones, C.G. McCarthy, S.W. Watts, N.S. Klee, A. Komic, F.B. Calmasini, F. Priviero, A. Warner, Y. Chenghao, C.F. Wenceslau, Hypertension induced morphological and physiological changes in cells of the arterial wall, American journal of hypertension 31(10) (2018) 1067-1078.
[37] A. Karimi, M. Navidbakhsh, A. Shojaei, S. Faghihi, Measurement of the uniaxial mechanical properties of healthy and atherosclerotic human coronary arteries, Materials Science and Engineering: C 33(5) (2013) 2550-2554.
[38] S. Sarkar, H. Salacinski, G. Hamilton, A. Seifalian, The mechanical properties of infrainguinal vascular bypass grafts: their role in influencing patency, European journal of vascular and endovascular surgery 31(6) (2006) 627-636.
[39] M. Lesiak, A. Araszkiewicz, “Leaving nothing behind”: is the bioresorbable vascular scaffold a new hope for patients with coronary artery disease?, Postępy w Kardiologii Interwencyjnej= Advances in Interventional Cardiology 10(4) (2014) 283.

[40] R.A. Macrae, K. Miller, B.J. Doyle, Methods in mechanical testing of arterial tissue: a review, Strain 52(5) (2016) 380-399.
[41] S. Pashneh-Tala, S. MacNeil, F. Claeyssens, The tissue-engineered vascular graft—past, present, and future, Tissue Engineering Part B: Reviews 22(1) (2016) 68-100.
[42] D. Camasão, D. Mantovani, The mechanical characterization of blood vessels and their substitutes in the continuous quest for physiological-relevant performances. A critical review, Materials Today Bio 10 (2021) 100106.
[43] A. Aussel, A. Montembault, S. Malaise, M.P. Foulc, W. Faure, S. Cornet, R. Aid, M. Chaouat, T. Delair, D. Letourneur, In vitro mechanical property evaluation of chitosan-based hydrogels intended for vascular graft development, Journal of cardiovascular translational research 10(5) (2017) 480-488.
[44] S.J. Lee, J. Liu, S.H. Oh, S. Soker, A. Atala, J.J. Yoo, Development of a composite vascular scaffolding system that withstands physiological vascular conditions, Biomaterials 29(19) (2008) 2891-2898.
[45] W.J. Geelhoed, R.A. Lalai, J.H. Sinnige, P.J. Jongeleen, C. Storm, J.I. Rotmans, Indirect burst pressure measurements for the mechanical assessment of biological vessels, Tissue Engineering Part C: Methods 25(8) (2019) 472-478.
[46] H. Hao, G. Gabbiani, M.-L. Bochaton-Piallat, Arterial smooth muscle cell heterogeneity: implications for atherosclerosis and restenosis development, Arteriosclerosis, thrombosis, and vascular biology 23(9) (2003) 1510-1520.
[47] C.G. Cordoba, C.J. Daly, The organisation of vascular smooth muscle cells; a quantitative fast Fourier transform (FFT) based assessment, Translational Research in Anatomy 16 (2019) 100047.
[48] M. Werner, N.A. Kurniawan, G. Korus, C.V. Bouten, A. Petersen, Mesoscale substrate curvature overrules nanoscale contact guidance to direct bone marrow stromal cell migration, Journal of The Royal Society Interface 15(145) (2018) 20180162.
[49] J.A. Nuhn, A.M. Perez, I.C. Schneider, Contact guidance diversity in rotationally aligned collagen matrices, Acta biomaterialia 66 (2018) 248-257.
[50] J. Wang, R. Zohar, C.A. McCulloch, Multiple roles of α-smooth muscle actin in mechanotransduction, Experimental cell research 312(3) (2006) 205-214.
[51] I. Ozolanta, G. Tetere, B. Purinya, V. Kasyanov, Changes in the mechanical properties, biochemical contents and wall structure of the human coronary arteries with age and sex, Medical engineering & physics 20(7) (1998) 523-533.
[52] S.L. Rose, J.E. Babensee, Complimentary endothelial cell/smooth muscle cell co-culture systems with alternate smooth muscle cell phenotypes, Annals of biomedical engineering 35(8) (2007) 1382-1390.
[53] L. Xu, M. Varkey, A. Jorgensen, J. Ju, Q. Jin, J.H. Park, Y. Fu, G. Zhang, D. Ke, W. Zhao, Bioprinting small diameter blood vessel constructs with an endothelial and smooth muscle cell bilayer in a single step, Biofabrication 12(4) (2020) 045012.
[54] J. Liu, Y. Qin, Y. Wu, Z. Sun, B. Li, H. Jing, C. Zhang, C. Li, X. Leng, Z. Wang, The surrounding tissue contributes to smooth muscle cells' regeneration and vascularization of small diameter vascular grafts, Biomaterials science 7(3) (2019) 914-925.
[55] K.K. Hirschi, S.A. Rohovsky, P.A. D'Amore, PDGF, TGF-β, and heterotypic cell–cell interactions mediate endothelial cell–induced recruitment of 10T1/2 cells and their differentiation to a smooth muscle fate, The Journal of cell biology 141(3) (1998) 805-814.
[56] G.A. Truskey, Endothelial cell vascular smooth muscle cell co-culture assay for high throughput screening assays for discovery of anti-angiogenesis agents and other therapeutic molecules, International journal of high throughput screening 2010(1) (2010) 171.
[57] C.S. Wallace, G.A. Truskey, Direct-contact co-culture between smooth muscle and endothelial cells inhibits TNF-α-mediated endothelial cell activation, American Journal of Physiology-Heart and Circulatory Physiology 299(2) (2010) H338-H346.
[58] B. Lilly, We have contact: endothelial cell-smooth muscle cell interactions, Physiology 29(4) (2014) 234-241.
[59] K. Ghimire, H.M. Altmann, A.C. Straub, J.S. Isenberg, Nitric oxide: what's new to NO?, American Journal of Physiology-Cell Physiology 312(3) (2017) C254-C262.
[60] M. Noris, M. Morigi, R. Donadelli, S. Aiello, M. Foppolo, M. Todeschini, S. Orisio, G. Remuzzi, A. Remuzzi, Nitric oxide synthesis by cultured endothelial cells is modulated by flow conditions, Circulation research 76(4) (1995) 536-543.

[61] C. Williams, T.M. Wick, Endothelial cell–smooth muscle cell co-culture in a perfusion bioreactor system, Annals of biomedical engineering 33(7) (2005) 920-928.
[62] J.H. Lee, S.J. Lee, G. Khang, H.B. Lee, The effect of fluid shear stress on endothelial cell adhesiveness to polymer surfaces with wettability gradient, Journal of colloid and interface science 230(1) (2000) 84-90.
[63] M.-X. Li, L. Li, S.-Y. Zhou, J.-H. Cao, W.-H. Liang, Y. Tian, X.-T. Shi, X.-B. Yang, D.-Y. Wu, A biomimetic orthogonal-bilayer tubular scaffold for the co-culture of endothelial cells and smooth muscle cells, RSC Advances 11(50) (2021) 31783-31790.
[64] C.E. Evans, M.L. Iruela-Arispe, Y.-Y. Zhao, Mechanisms of endothelial regeneration and vascular repair and their application to regenerative medicine, The American journal of pathology 191(1) (2021) 52-65.
[65] B. Yi, Y. Shen, H. Tang, X. Wang, B. Li, Y. Zhang, Stiffness of aligned fibers regulates the phenotypic expression of vascular smooth muscle cells, ACS applied materials & interfaces 11(7) (2019) 6867-6880.
[66] M. Zhu, Y. Wu, W. Li, X. Dong, H. Chang, K. Wang, P. Wu, J. Zhang, G. Fan, L. Wang, Biodegradable and elastomeric vascular grafts enable vascular remodeling, Biomaterials 183 (2018) 306-318.
[67] M. Wong, L. Toh, A. Wilson, K. Rowley, C. Karschimkus, D. Prior, E. Romas, L. Clemens, G. Dragicevic, H. Harianto, Reduced arterial elasticity in rheumatoid arthritis and the relationship to vascular disease risk factors and inflammation, Arthritis & Rheumatism 48(1) (2003) 81-89.
[68] H. Inoguchi, T. Tanaka, Y. Maehara, T. Matsuda, The effect of gradually graded shear stress on the morphological integrity of a huvec-seeded compliant small-diameter vascular graft, Biomaterials 28(3) (2007) 486-495.
[69] M. Gonzalez, S. Arribas, F. Molero, M. Fernandez-Alfonso, Effect of removal of adventitia on vascular smooth muscle contraction and relaxation, American Journal of Physiology-Heart and Circulatory Physiology 280(6) (2001) H2876-H2881.
[70] M.W. Majesky, X.R. Dong, V. Hoglund, W.M. Mahoney Jr, G. Daum, The adventitia: a dynamic interface containing resident progenitor cells, Arteriosclerosis, thrombosis, and vascular biology 31(7) (2011) 1530-1539.

-

Supplementary material

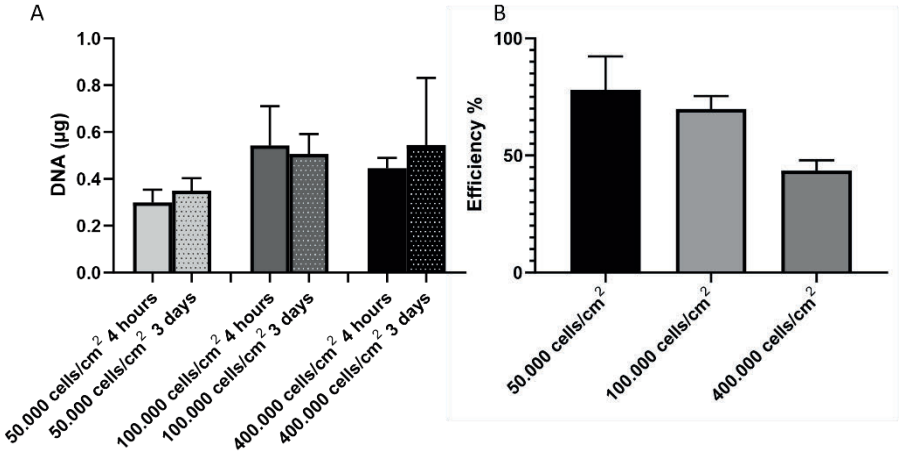

Figure S1. *A10 optimization experiments after 3 days of culture following different seeding densities. (A) DNA quantification after 3 days of culture. (B) Seeding efficiency after 4 hours post seeding. Each condition contained n=5 samples.*

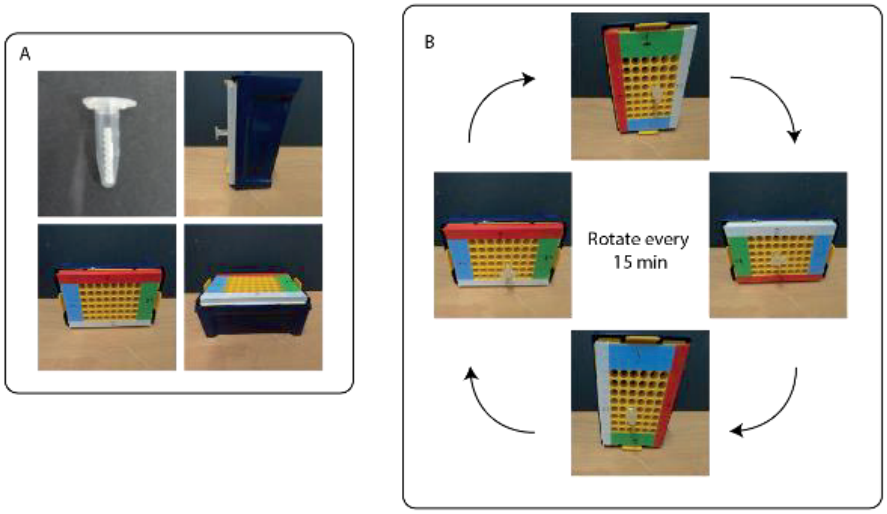

Figure S2. *Seeding method for the vascular grafts. (A) Images of a scaffold in an Eppendorf and an empty P-1000 pipette tip-box for seeding. (B) Procedure of turning the pipette tip-box with the scaffold every 15 minutes.*

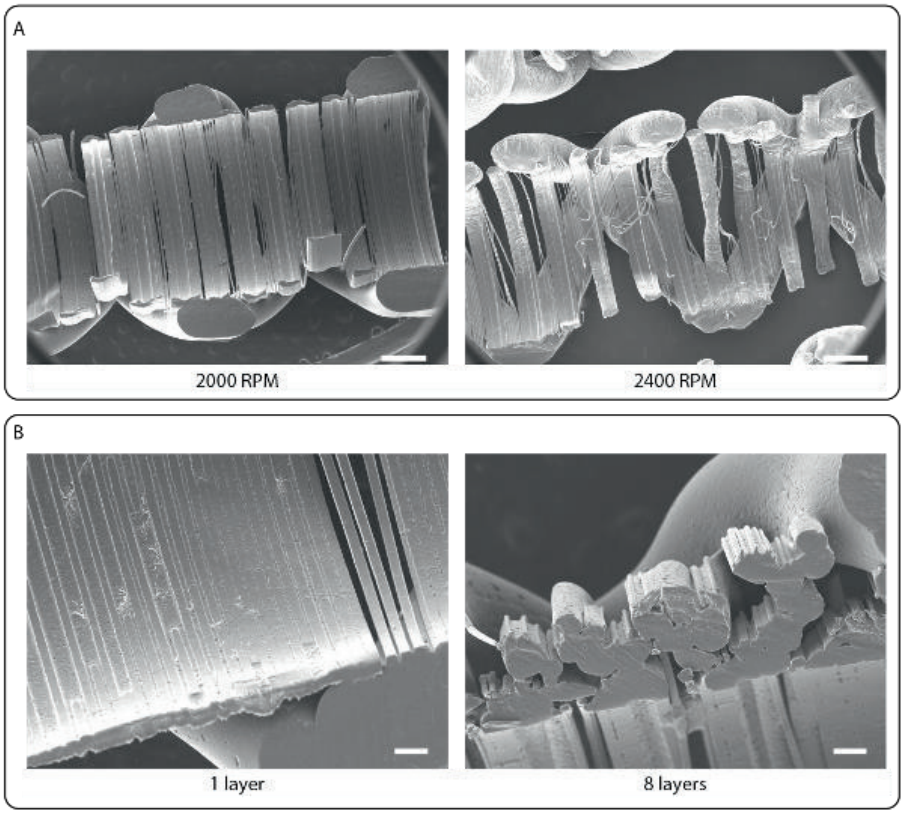

Figure S3. *SEM images of the luminal support. (A) Cross section of the luminal wall created at 2000 and 2400 RPM. (B) Cross section of the luminal wall with 1 layer and 8 layers. Scale bar represents 500 µm for panel A and 100 µm for panel B.*

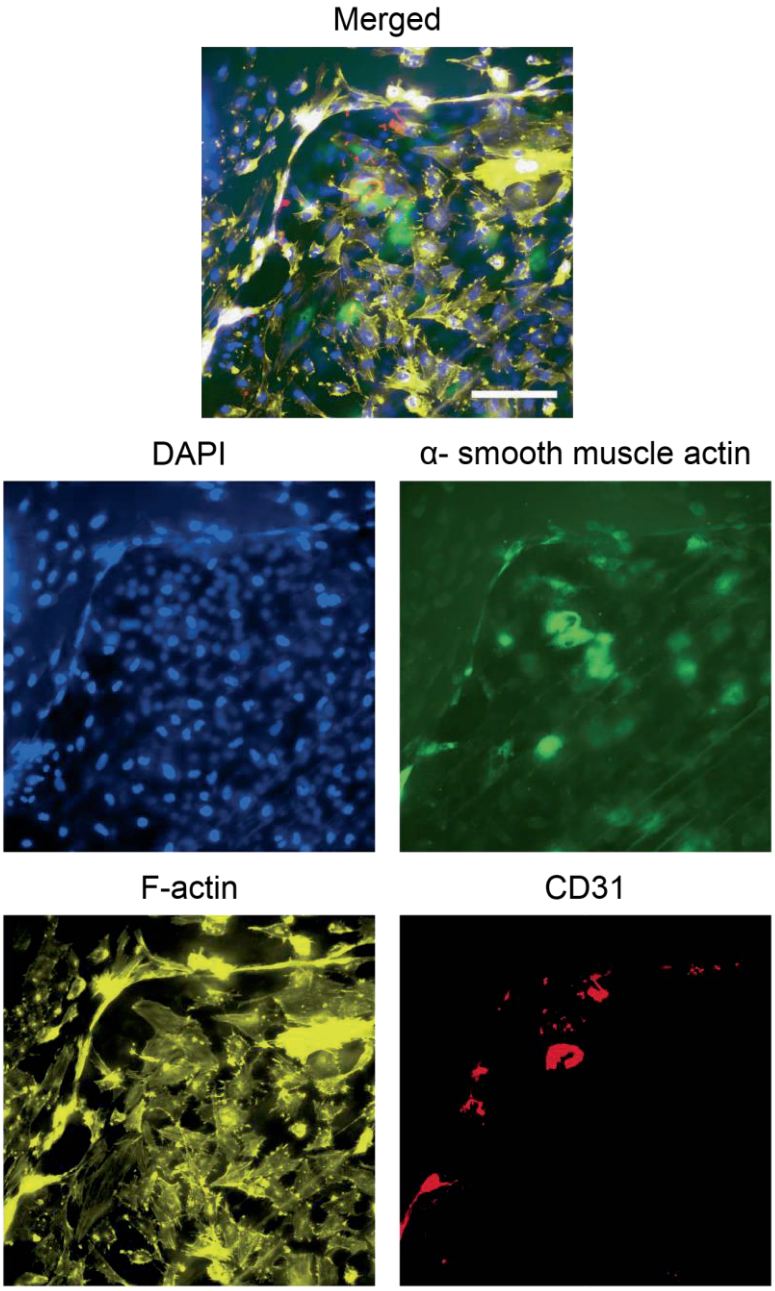

Figure S4. *Coculture of primary smooth muscle cells and HUVECs after 7 days of culture. Images were taken from the adventitial side of the scaffold. Scale bar represent 50 µm.*

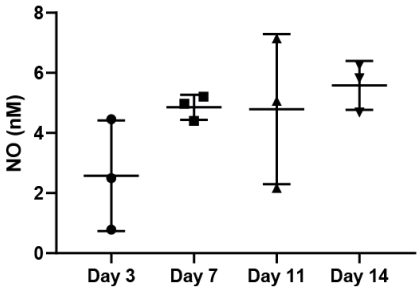

***Figure S5**. NO release in the culture medium from the coculture. Each condition contained n=3 samples.*

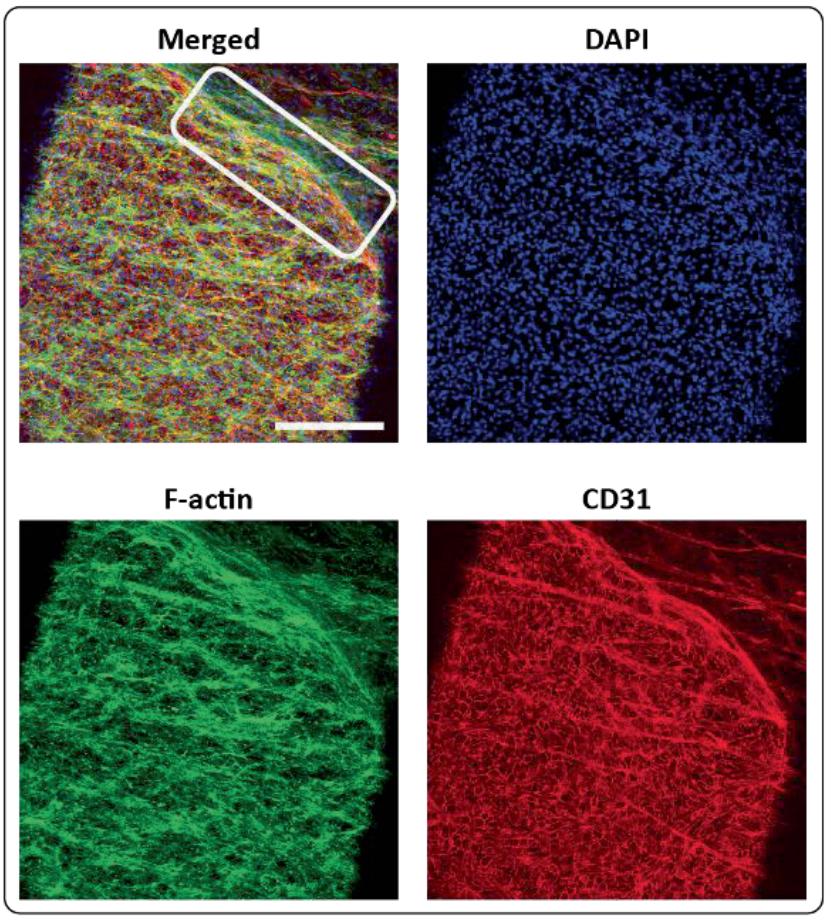

***Figure S6.** Coculture of primary smooth muscle cells and HUVECs after 14 days of culture. White box indicate the detachment of the endothelial cell layer. Scale bar represents 500 µm.*

Chapter 8

General discussion

The work presented in this thesis aimed at designing and creating 3D scaffolds with alternative patterns defining pore architecture. These scaffolds could be fabricated through fused deposition modeling (FDM) and were studied for cartilage and cardiovascular regenerative medicine applications, but could potentially be used for a multitude of other applications as well. Hereafter, I discuss the results of the thesis divided into 6 main topics: 1) the ultimate goal of biomimicry, 2) picking the right pattern, 3) mimicking collagen type II organization, 4) FDM produced hollow tubular scaffolds, 5) mimicking the mechanical properties of an artery, and 6) from mechanical to combined mechanical-morphological mimicry. Finally, a perspective on how this knowledge could be used in the future to design more complex and biomimicking scaffolds for regenerative medicine (RM) application is provided.

The ultimate goal of biomimicry

The ultimate goal in RM is to replace or repair damaged tissues with a new engineered or endogenously developed tissue equivalent [1]. The mimicking approach that researchers use for this purpose is called biomimicry [2]. However, biomimicry is often a broadly used term and does not specify which aspect of the tissue the researcher aims at replicating. Therefore, **Chapter 2** clarifies the different strategies that tissue engineers may follow when developing a new RM strategy and divides biomimicry into mechanical, morphological and biological biomimicry. In this chapter, we also discussed what can be done to improve biomimicry of scaffolds. The focus of mechanical biomimicry is to obtain mechanical properties similar to those of the target tissue. This can be obtained through various methods, such as choosing the right material, varying the scaffold design, changing the crosslinkers or using fillers to create composite materials. Morphological biomimicry aims at creating scaffolds that are morphologically similar to the native counterpart. The strategies applied here can vary from mimicking the interfaces between tissues, to recreating similar porosity, size and shape, using decellularized tissue or through templating techniques. Biological biomimicry aims at

recreating the biological environment that is found in the specific targeted tissue. Methods to obtain this can range from mimicking cellular anchoring points, to conditioning scaffolds by placing them in a more mimicking environment such as tissue-specific biomechanical loading regimes during culture [3], adding growth factors to promote rapid growth or using decellularized tissues as a base material for creating scaffolds.

The findings in this review identified that studies often focused on a single aspect of biomimicry while neglecting other aspects. Examples were studies that focused on matching mechanical properties, but studied the biological response of the fabricated scaffolds to a limited extent [4]. Similarly, the morphology of a tissue was exactly replicated by the scaffold design strategy, but with weaker mechanical properties [5]. *In-vivo* research has shown that scaffolds can have negative results for mechanical [6], morphological [7] or biological [8] reasons even though the studies did mimic one of the other aspects. This indicates that every aspect of biomimicry is important and none should be neglected. In addition, a single change made in the scaffold can influence multiple aspects of biomimicry: for example, changing the bulk material will not only change the mechanical properties, but also the cell-material interactions [9]. The first steps in a biomimicry strategy should already be taken in the material development stage. This should include studying both mechanical and biological response of a material. **Chapter 2** could serve as an example of this strategy where a library of patterns was screened for their mechanical properties. Afterwards, the right morphology, which is scalable for larger clinically relevant constructs and can steer vascularization and innervation processes, has to be chosen. To further close the gap between *in vitro* and *in vivo*, the dynamic environment of the tissue should be recreated as close as possible *in vitro*.

Picking the right pattern

One of the most commonly used techniques to fabricate 3D printed scaffolds in RM is FDM. This technique extrudes molten polymers through a nozzle that solidifies upon extrusion. It is suitable for personalized medicine as 3D data from medical imaging techniques can be converted into a 3D model and fabricated into a scaffold [10]. However, the limitation is that the infill pattern of these 3D models is often a meandering set of lines. As discussed in **Chapter 2,** the differences between tissues can be enormous and using a single design might not be the best for all of the applications. Therefore, **Chapter 3** was focused on showcasing a methodology for creating alternative patterns for RM applications. Among different possibilities to create alternative scaffolds' pore architecture patterns, we used three different methods aiming at increasing the degree of biomimicry of the resulting scaffolds: 1) space filling fractal based patterns, which are generated through an L-system; 2) Tiling based patterns, which are generated by having a set of tiles that create a pattern on a plane; 3) Cartesian based scaffolds, which are generated through Cartesian coordinate equations. In addition, the effect of different loading regimes on the scaffolds was studied to replicate the potential suturing positions for the scaffold.

The results from **Chapter 3** revealed the possibility to create a variety of different patterns. The material for all of these patterns was the same, yet the differences in Young's modulus between the scaffolds could vary two orders of magnitude, which is roughly the difference between cortical bone [11] and tracheal cartilage [12]. The loading regimes represents potential suturing positions as the majority of the scaffolds are fixated through sutures [13]. Even within the same design, major influences in mechanical properties were observed with a different loading regime. Therefore, the design matters as much as the loading regimes on a scaffold. This also highlights that a recommendation for what is the most suitable pattern is dependent on the final application. In addition, this also emphasizes that a suitable pattern can

potentially be tailored for a specific tissue. For softer tissues that require high deformations, such as skin [14], a more open design that has poorly interconnected fibers such as the Gosper curve could be more suitable. Rigid patterns such as the woodpile design or the Penrose tiling with well-connected fibers could be more suitable for stiffer tissues such as bone [15]. Other patterns with more unique mechanical properties such as the Peano curve could serve to understand what happens to the cells on the scaffolds locally when subjected to mechanical stress. Previous work mainly focused on two different approaches. The first one involves investigating infill patterns either by varying the infill density [16] or changing the angle of each layer [17]. The infill pattern is not fundamentally altered by these parameters, as they are default settings from the software generating the pattern. In addition, the differences in mechanical properties within these tested designs is less than 2-fold. Making this approach more suitable in the final stages of scaffold design where only small changes in mechanical properties are required. The second approach is to use a different infill pattern altogether. Other studies have investigated other infill patterns and showcased that they are able to create density gradients using sinusoidal patterns [18] or radial gradients using fractal trees [19]. However, the variety of patterns presented in **Chapter 3** is unique to this study. The ability to create more versatile scaffold designs allows other researchers to use materials that were previously deemed unsuitable due to a mismatch in mechanical properties [20]. The study highlights that no advanced software or skill in mathematics is required to create new patterns. This could inspire other researchers to explore the infinite amount of designs available instead of reusing the same woodpile pattern [21, 22]. In addition, the resulting scaffold could be more biomimicking, for example by implementing fractal patterns, as some studies have attempted to achieve biomimicry through scaffold design [18, 23].

Mimicking collagen type II organization

Articular cartilage is an avascular tissue, which provides a low friction surface to protect the underlying subchondral bone. The extracellular matrix (ECM) composition of articular cartilage mainly consists of collagen type II and glycosaminoglycans. Articular cartilage is characterized by three distinct zones with each of them having a different composition in ECM and cell density [24]. The organization of collagen type II fibers could be mathematically described with an arch-like structure. Hence, one of the main objectives of **Chapter 4** was to implement the methodology developed in Chapter 3 and use a hypotrochoidal curve to define scaffolds that mimics this arch-like orientation of collagen type II. Our hypothesis was that the hypotrochoidal scaffold design would not only mimic morphologically, but also mechanically articular cartilage. Consequently, this should result in a better biological biomimicry as well. These designed scaffolds were assessed mechanically and biologically in both static and dynamic culture conditions.

The findings from **Chapter 4** revealed that the hypotrochoidal design could be successfully printed. The amount of arches introduced in the scaffold can be varied by changing the input parameters in the mathematical equations defining the hypotrochoidal design. The Young's modulus was significantly lower, while the Yield strength and strain and the toughness were significantly higher in the hypotrochoidal design compared to woodpile patterns. The mechanical properties of the hypotrochoidal design (14.1MPa) was within the range of native cartilage tissue (10.6 - 18.6 MPa) [25]. In addition, multiphysics modeling showed that the stress was equally distributed throughout the hypotrochoidal scaffolds. This was reflected in the dynamic cultured conditions where the hypotrochoidal samples had an improved collagen type II deposition, specifically in the areas that were correlated with less stress in the scaffolds, thus indicating that the hypotrochoidal scaffold design is superior compared to the woodpile structure for cartilage regeneration. Most studies that use FDM scaffolds for cartilage regeneration still use a woodpile

design [26-28]. Therefore the hypotrochoidal design can be a major improvement for cartilage regeneration because this design is easy to implement and can be shared with other labs.

Another study that focus on the design part of the scaffold also showcased that geometry is a key parameter for cell differentiation [29]. Evidence from literature demonstrated that cells respond to their microenvironment via mechanotransduction [30]. A recent review has demonstrated that scaffold geometry or design can have a significant influence on mechanotransduction, as the scaffold provides physical stimuli to the cells [31]. In addition, this is a prime example, which was highlighted in **Chapter 2,** demonstrating that the design can make the difference. Even with a material such as PCL, which is generally regarded as too stiff for cartilage regeneration [32]. The ATDC5 cells that were used in this study are known to be hypertrophic [33] showing that it might be possible to revert the phenotype to a hyaline phenotype only through design.

FDM produced tubular hollow scaffolds

Traditional FDM systems are limited in creating structures that are not planar, due to the use of a flat collecting plate combined with a conventional layer-by-layer fabrication approach [34]. Therefore, **Chapter 5** is focused on introducing a fourth axis in a classical FDM system that replaces the flat collecting surface with a controllable cylindrical one. This allows the fabrication of more complicated structures that are not possible with “classical” FDM systems. A diamond and a rectangular pore design that could not be fabricated with the classical systems were mechanically characterized and compared with each other and to native tissues, such as the coronary and carotid artery, trachea and small intestine.

The results showed that both patterns could be successfully printed in the four axis system. The diamond pore design had a lower Young’s modulus, which

was comparable to a carotid artery [35]. On the other hand, the rectangular pore design was stiffer and had a comparable Young's modulus to tracheal tissue [12]. Three point bending tests revealed that the lumen remained open in the diamond pore design. This chapter highlights that a completely new set of patterns can be created for tubular hollow tissues. Even within the cardiovascular network the range in mechanical properties is significant ranging from a saphenous vein at 0.1 MPa [36] to 2.6 MPa in the aorta [37]. Either different materials or designs have to be used to capture this range in mechanical properties. The four axis system allows the user to change both these parameters. Even though the majority of the materials have been characterized, the designs for these tubular patterns have not been explored yet. With minor alterations, the methods described in **Chapter 3** can potentially be used to create a whole new array of patterns for the four axis system.

Mimicking the mechanical properties of an artery

The stress-strain curve of a small diameter artery has unique elastic properties [38]. The curve follows a sigmoidal shape that has an initial region, which has a low stress and high strain. This elasticity improves the pumping efficiency of the heart. Mimicking this behavior requires the starting material to be elastic [39] or the scaffold design to mimic elastic-like behavior. In **Chapter 6,** a corrugated pattern is explored that has elastic-like behavior to mimic the mechanical behavior of small diameter arteries. Various versions of the corrugated patterns were compared with porcine carotid arteries.

The data revealed that a sigmoidal stress-strain curve could be obtained through the corrugated design. Thanks to the parametric approach, the design and consequently the stress-strain behavior can be tuned. Which is something that only has been achieved with wavy and tangled electrospun fibers using polycaprolactone as material [40]. Although the entire stress-strain curve of a porcine carotid artery could not be matched with the corrugated design, the

initial 20% of strain, which is the physiological range, was nearly identical. This suggested that even with a stiff material such as polycaprolactone elastic-like properties can be introduced on the scaffold macrostructural level. In addition, it was showcased here that in certain cases the scaffold's architecture has a larger influence on mechanical properties compared to the material. Other studies have demonstrated that varying the scaffold architecture influences the mechanical properties [41]. However, there was limited control over the entire stress-strain curve.

From mechanical mimicry to combined morphological mimicry

The tunica media of any small diameter artery contains smooth muscle cells that are radially aligned [42]. This specific morphology enhances the contractility of arteries. Placing a highly aligned mesh of thin fibers should trigger smooth muscle cells to align in that direction through contact guidance [43]. **Chapter 7** explored how a thin fiber mesh could be created through melt spinning. Melt spinning is a technique that creates a highly aligned mesh of thin fibers by depositing a molten polymer on a fast rotating mandrel. Equations were set up to predict the fiber dimensions during melt spinning. The effect of these thin fibers on cell morphology was measured to mimic the tunica media by adding smooth muscle cells in the walls of the scaffold. In addition, a co-culture with endothelial cells was performed to create a barrier function and to mimic the tunica intima of a carotid artery.

The findings from **Chapter 7** revealed that the equations formulated in this study were accurate to predict the fiber dimensions. This could serve as an alternative to melt electrowriting as the fibers that are produced are within the same order of magnitude, but the process was more predictable [44]. In addition, the process was compatible with any thermoplastics. This could be further studied with other materials that either improve mechanical properties or are functionalized to improve cell adhesion [45]. Furthermore, the melt

spinning technique produced a highly aligned mesh where smooth muscle cells aligned within 2 days of culture. The co-culture revealed that the alignment of the smooth muscle cells did not influence the alignment of the endothelial cells even though there was direct contact with the cells. The direct contact is important as it stimulates the smooth muscle cells to produce fibrillary fibronectin, which improves endothelial cell adhesion [46]. The effect of direct cell contact has been broadly studied in other fields of medicine, however it is not widely applied within cardiovascular RM [47].This study showcased the possibility to have this direct contact between the different cell types. In addition, the results of this study demonstrate that with melt spinning a predictable mesh of highly aligned fibers can be created that can aid in the development of a coronary artery graft. The equations presented in **Chapter 7** can be beneficial for other researchers that use melt spinning to accurately predict the fiber geometry [48, 49]. Other more complex biofabrication techniques such as melt electrowriting and solution electrospinning could potentially also benefit from these equations as this method could be applied to help understand the parameters that influence the fabrication process [50-53].

Future Perspectives

As discussed in **Chapter 2,** there is a broad variability between tissue properties. Therefore, using a single pattern and resulting periodic scaffold for all of the different tissues of our body is not logical. The tissue should be investigated before a final pattern and scaffold architecture can be chosen. Some tissues have complex mechanical behavior [54] that could potentially be replicated with a pattern. The amount of patterns that can be designed are limitless and some of the methods to generate such patterns have been used in **Chapter 3.** These generated patterns are simplified and can be used without the need for a background in programming, mathematics or engineering. Similarly, the possibility to draw an own custom pattern and convert it directly to G-code is today also available with the same approach.

The creation of custom-designed patterns can also be used to mimic cell alignment or certain ECM components in a tissue, as demonstrated in **Chapter 7**. **Chapter 4** showed a combination of the two previously mentioned approaches, where the collagen type II organization was mimicked using a hypotrochoidal design, but the scaffolds designed with these patterns had also improved mechanical properties. This chapter can serve as a blueprint of how to investigate and apply a new pattern for a specific tissue. Some potential tissue that could be investigated are the fractal organization of bone [55], the type I and type II collagen organization of the annulus fibroses [56] or the muscle band organization in the myocardium (Figure 1) [57].

The four axis FDM system from in **Chapter 5** revealed that a whole new set of patterns can be produced that previously were not possible to create with a regular FDM system. There is no limit to the number of tubular patterns that can be made using this additional axis, and **Chapters 5 and 6** only highlight a small subset of possible tubular patterns; the vast majority is yet undiscovered. These patterns can be based on the same principles as described in **Chapter 3**. Future development in an FDM system with a robotic arm, which can replicate multiple degrees of freedom similar to the human arm, will allow a broad set of patterns that previously were not possible to create with Cartesian controlled systems [61, 62]. While this approach offers “endless” pattern possibilities, a better understanding of the printing materials melt rheology is required to exploit printing without a support, as the material solidification needs to occur directly after extrusion [63]. Another future direction could couple medical imaging data with patient specific requirements to create a personalized scaffold pattern. Finite element models can already convert medical imaging data into a model [64] and future development could also include scaffolds with unique patterns in this model.

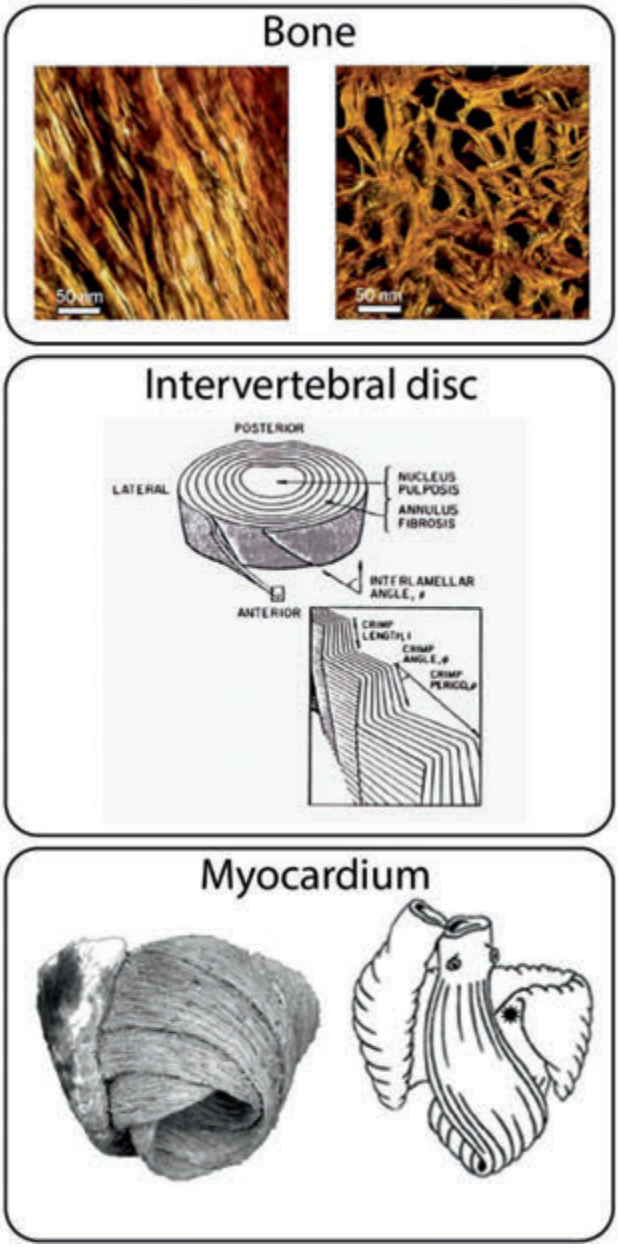

Figure 1. *Potential tissues were new patterns can be applied. The mineral organization of bone (top panel), the collagen type I and II organization of the annulus fibroses (middle panel). The muscle band organization of the myocardium, left part an anatomical specimen and the right part a cartoon version (bottom panel). Images were adapted from Reznikov et al. [58], Gruber et al. [59] and Kocica et al. [60].*

The four axis FDM system from **Chapter 5** is able to produce tubular structures for the regeneration of cardiovascular scaffolds, which we have further explored in both **Chapters 6 and 7**. However, the four-axis system is not limited to only cardiovascular scaffolds. Some examples that could be replicated with this system are the C-shaped rings found in the trachea [65], the circular folds in the lumen of the small intestine [66] using a corrugated design similar to the one described in **Chapter 6**, the folded star-shaped lumen of the urethra [67] or the density gradient found in the cross section of long-bones [68].

Bulk material properties are often one of the main reason to pick an ideal material to make a scaffold for tissue regeneration. PCL is known to be a stiff polymer, especially for soft tissues such as cartilage and vascular tissue [69, 70], yet a common biodegradable polymer used in many studies for its processing stability and biocompatibility. However, **Chapter 6** proved that even materials that have been regarded as non-elastic can have elastic-like behavior through scaffold design. Another example is showecased in **Chapter 3,** where we were able to achieve a 100 fold difference between the Young's modulus in the fabricated scaffolds even when the fibers of these designs have the same diameter and the material is identical. Therefore, having a focus on the bulk properties can make researchers forget that a material could be suitable given the right scaffold design. It would be possible that multiple materials are suitable for a single application. However, the design of the scaffolds is dependent on both the final application and the chosen material. Future studies should also elucidate if cell-material interactions known to occur at bulk level are altered by such different architecture-dependent mechanical behavior. For example, PCL is known to show calcification initiation in vascular grafts [71, 72]. Yet, it would be amusing to evaluate if such calcification onset could be abated by biomimicked architecture-dependent mechanical properties.

It is well known that the choice of a material has an influence on cellular response [73]. The surface roughness [74], the ability to interact with the material [75] or substrate rigidity [76] can be triggered by this response. However, the impact of dynamic load on the cells and materials remains poorly understood. Especially dynamic loading conditions can have a major effect on cell behavior [3]. This was already explored in the different loading regimes in **Chapter 3**, where certain patterns that have similar porosity, such as the Hilbert curve and the 0-90 woodpile design, have uniquely different mechanical properties. These differences could translate to a different outcome in cellular behavior when culturing under mechanical stimulation [77]. This was also observed in **Chapter 4**, where differences in collagen type II deposition was only found in the hypotrochoidal design. Future studies could explore or include dynamic loading during cell culture to study cellular behavior. Previous studies that have been published, but did not involve dynamic loading with cells, could have a different outcome. This is showcased in **Chapter 4** where the static culture condition did not show differences in cell behavior. Other examples of dynamic loading can exploit fluid flow mimicking the physiological conditions. Example of these are the pulsatile flow that arteries and veins are continuously subjected to. The scaffolds produced in **Chapter 7** could be ideal candidates to evaluate whether the cell morphology is retained during pulsatile flow perfusion. Although this would allow relevant validation *in vitro* prior to pre-clinical translation, most of the commercially available bioreactors cannot mimic such physiological conditions. This will require a constant evolution not only of the scaffolds, but also of the *in vitro* culturing conditions to emulate the *in vivo* scenario as close as possible. In doing so, one would expect to shorten eventually the research and development needed to bring these solutions to the patient.

References

[1] F. Berthiaume, T.J. Maguire, M.L. Yarmush, Tissue engineering and regenerative medicine: history, progress, and challenges, Annual review of chemical and biomolecular engineering 2 (2011) 403-430.
[2] G. Zhang, Biomimicry in biomedical research, Taylor & Francis, 2012.
[3] N. Mahmoudifar, P.M. Doran, Chondrogenic differentiation of human adipose-derived stem cells in polyglycolic acid mesh scaffolds under dynamic culture conditions, Biomaterials 31(14) (2010) 3858-3867.
[4] Z.P. Rad, J. Mokhtari, M. Abbasi, Fabrication and characterization of PCL/zein/gum arabic electrospun nanocomposite scaffold for skin tissue engineering, Materials Science and Engineering: C 93 (2018) 356-366.
[5] D.M. Casali, R.M. Handleton, T. Shazly, M.A. Matthews, A novel supercritical CO2-based decellularization method for maintaining scaffold hydration and mechanical properties, The Journal of Supercritical Fluids 131 (2018) 72-81.
[6] R. Hosseinzadeh, B. Mirani, E. Pagan, S. Mirzaaghaei, A. Nasimian, P. Kawalec, S.C. da Silva Rosa, D. Hamdi, N.P. Fernandez, B.D. Toyota, A drug-eluting 3D-printed mesh (GlioMesh) for management of glioblastoma, Advanced Therapeutics 2(11) (2019) 1900113.
[7] M. Hallman, J.A. Driscoll, R. Lubbe, S. Jeong, K. Chang, M. Haleem, A. Jakus, R. Pahapill, C. Yun, R. Shah, Influence of geometry and architecture on the in vivo success of 3D-printed scaffolds for spinal fusion, Tissue Engineering Part A 27(1-2) (2021) 26-36.
[8] B.M. Sicari, S.A. Johnson, B.F. Siu, P.M. Crapo, K.A. Daly, H. Jiang, C.J. Medberry, S. Tottey, N.J. Turner, S.F. Badylak, The effect of source animal age upon the in vivo remodeling characteristics of an extracellular matrix scaffold, Biomaterials 33(22) (2012) 5524-5533.
[9] L. Di Silvio, Cellular response to biomaterials, Elsevier2008.
[10] F. Rengier, A. Mehndiratta, H. Von Tengg-Kobligk, C.M. Zechmann, R. Unterhinninghofen, H.-U. Kauczor, F.L. Giesel, 3D printing based on imaging data: review of medical applications, International journal of computer assisted radiology and surgery 5(4) (2010) 335-341.
[11] F. Bini, A. Marinozzi, F. Marinozzi, F. Patanè, Microtensile measurements of single trabeculae stiffness in human femur, Journal of biomechanics 35(11) (2002) 1515-1519.
[12] C.R. Roberts, J.K. Rains, P.D. Paré, D.C. Walker, B. Wiggs, J.L. Bert, Ultrastructure and tensile properties of human tracheal cartilage, Journal of biomechanics 31(1) (1997) 81-86.
[13] L. Ruiz-Cantu, A. Gleadall, C. Faris, J. Segal, K. Shakesheff, J. Yang, Characterisation of the surface structure of 3D printed scaffolds for cell infiltration and surgical suturing, Biofabrication 8(1) (2016) 015016.
[14] M. Aragona, A. Sifrim, M. Malfait, Y. Song, J. Van Herck, S. Dekoninck, S. Gargouri, G. Lapouge, B. Swedlund, C. Dubois, Mechanisms of stretch-mediated skin expansion at single-cell resolution, Nature 584(7820) (2020) 268-273.
[15] B.E. Grottkau, Z. Hui, Y. Yao, Y. Pang, Rapid fabrication of anatomically-shaped bone scaffolds using indirect 3D printing and perfusion techniques, International Journal of Molecular Sciences 21(1) (2020) 315.
[16] T. Abbas, F.M. Othman, H.B. Ali, Effect of infill Parameter on compression property in FDM Process, dimensions 12(7) (2017) 25-4.
[17] B. Aloyaydi, S. Sivasankaran, A. Mustafa, Investigation of infill-patterns on mechanical response of 3D printed poly-lactic-acid, Polymer Testing 87 (2020) 106557.
[18] D. Kilian, S. Holtzhausen, W. Groh, P. Sembdner, C. Czichy, A. Lode, R. Stelzer, M. Gelinsky, 3D extrusion printing of density gradients by variation of sinusoidal printing paths for tissue engineering and beyond, Acta Biomaterialia 158 (2023) 308-323.
[19] H. Qu, Z. Han, Z. Chen, L. Tang, C. Gao, K. Liu, H. Pan, H. Fu, C. Ruan, Fractal design boosts extrusion-based 3D printing of bone-mimicking radial-gradient scaffolds, Research 2021 (2021).
[20] S. Gross, E. Abel, A finite element analysis of hollow stemmed hip prostheses as a means of reducing stress shielding of the femur, Journal of Biomechanics 34(8) (2001) 995-1003.
[21] J. Choi, S. Koo, I. Sakellari, H. Kim, Z. Su, K.R. Carter, M. Farsari, C.P. Grigoropoulos, T.P. Russell, Guided assembly of block copolymers in three-dimensional woodpile scaffolds, ACS Applied Materials & Interfaces 10(49) (2018) 42933-42940.
[22] M. Alksne, E. Simoliunas, M. Kalvaityte, E. Skliutas, I. Rinkunaite, I. Gendviliene, D. Baltriukiene, V. Rutkunas, V. Bukelskiene, The effect of larger than cell diameter polylactic acid

surface patterns on osteogenic differentiation of rat dental pulp stem cells, Journal of biomedical materials research Part A 107(1) (2019) 174-186.
[23] W. Wojnicz, M. Augustyniak, P. Borzyszkowski, Mathematical approach to design 3D scaffolds for the 3D printable bone implant, Biocybernetics and Biomedical Engineering 41(2) (2021) 667-678.
[24] T.J. Klein, B.L. Schumacher, T.A. Schmidt, K.W. Li, M.S. Voegtline, K. Masuda, E.J.M.A. Thonar, R.L. Sah, Tissue engineering of stratified articular cartilage from chondrocyte subpopulations, Osteoarthritis and cartilage 11(8) (2003) 595-602.
[25] D.E. Shepherd, B.B. Seedhom, The 'instantaneous' compressive modulus of human articular cartilage in joints of the lower limb, Rheumatology (Oxford, England) 38(2) (1999) 124-32.
[26] A. Sadeghianmaryan, S. Naghieh, H.A. Sardroud, Z. Yazdanpanah, Y.A. Soltani, J. Sernaglia, X. Chen, Extrusion-based printing of chitosan scaffolds and their in vitro characterization for cartilage tissue engineering, International Journal of Biological Macromolecules 164 (2020) 3179-3192.
[27] Y.-T. Wen, N.-T. Dai, S.-h. Hsu, Biodegradable water-based polyurethane scaffolds with a sequential release function for cell-free cartilage tissue engineering, Acta biomaterialia 88 (2019) 301-313.
[28] K. Flégeau, A. Puiggali-Jou, M. Zenobi-Wong, Cartilage tissue engineering by extrusion bioprinting utilizing porous hyaluronic acid microgel bioinks, Biofabrication 14(3) (2022) 034105.
[29] D. Martínez-Moreno, G. Jiménez, C. Chocarro-Wrona, E. Carrillo, E. Montañez, C. Galocha-León, B. Clares-Naveros, P. Gálvez-Martín, G. Rus, J. de Vicente, Pore geometry influences growth and cell adhesion of infrapatellar mesenchymal stem cells in biofabricated 3D thermoplastic scaffolds useful for cartilage tissue engineering, Materials Science and Engineering: C 122 (2021) 111933.
[30] A. Saraswathibhatla, D. Indana, O. Chaudhuri, Cell–extracellular matrix mechanotransduction in 3D, Nature Reviews Molecular Cell Biology (2023) 1-22.
[31] P. Han, G.A. Gomez, G.N. Duda, S. Ivanovski, P.S. Poh, Scaffold geometry modulation of mechanotransduction and its influence on epigenetics, Acta Biomaterialia (2022).
[32] C.G. Jeong, S.J. Hollister, A comparison of the influence of material on in vitro cartilage tissue engineering with PCL, PGS, and POC 3D scaffold architecture seeded with chondrocytes, Biomaterials 31(15) (2010) 4304-4312.
[33] H. Akiyama, C. Shukunami, T. Nakamura, Y. Hiraki, Differential expressions of BMP family genes during chondrogenic differentiation of mouse ATDC5 cells, Cell structure and function 25(3) (2000) 195-204.
[34] W. Kosorn, M. Sakulsumbat, P. Uppanan, P. Kaewkong, S. Chantaweroad, J. Jitsaard, K. Sitthiseripratip, W. Janvikul, PCL/PHBV blended three dimensional scaffolds fabricated by fused deposition modeling and responses of chondrocytes to the scaffolds, Journal of Biomedical Materials Research Part B: Applied Biomaterials 105(5) (2017) 1141-1150.
[35] K.A. McKenna, M.T. Hinds, R.C. Sarao, P.-C. Wu, C.L. Maslen, R.W. Glanville, D. Babcock, K.W. Gregory, Mechanical property characterization of electrospun recombinant human tropoelastin for vascular graft biomaterials, Acta biomaterialia 8(1) (2012) 225-233.
[36] G.E. Smith, R. Barnes, M. Fagan, I.C. Chetter, The impact of vein mechanical compliance on arteriovenous fistula outcomes, Annals of Vascular Surgery 32 (2016) 9-14.
[37] D.A. Vorp, B.J. Schiro, M.P. Ehrlich, T.S. Juvonen, M.A. Ergin, B.P. Griffith, Effect of aneurysm on the tensile strength and biomechanical behavior of the ascending thoracic aorta, The Annals of Thoracic Surgery 75(4) (2003) 1210-1214.
[38] M.F. O'rourke, J. Hashimoto, Mechanical factors in arterial aging: a clinical perspective, Journal of the American College of Cardiology 50(1) (2007) 1-13.
[39] J.E. Wagenseil, R.P. Mecham, New insights into elastic fiber assembly, Birth Defects Research Part C: Embryo Today: Reviews 81(4) (2007) 229-240.
[40] H.-Y. Mi, X. Jing, E. Yu, X. Wang, Q. Li, L.-S. Turng, Manipulating the structure and mechanical properties of thermoplastic polyurethane/polycaprolactone hybrid small diameter vascular scaffolds fabricated via electrospinning using an assembled rotating collector, Journal of the Mechanical Behavior of Biomedical Materials 78 (2018) 433-441.
[41] J.M. Sobral, S.G. Caridade, R.A. Sousa, J.F. Mano, R.L. Reis, Three-dimensional plotted scaffolds with controlled pore size gradients: effect of scaffold geometry on mechanical performance and cell seeding efficiency, Acta biomaterialia 7(3) (2011) 1009-1018.

[42] J. Walmsley, M. Campling, H. Chertkow, Interrelationships among wall structure, smooth muscle orientation, and contraction in human major cerebral arteries, Stroke 14(5) (1983) 781-790.
[43] A.M. van Genderen, K. Jansen, M. Kristen, J. Van Duijn, Y. Li, C.C. Schuurmans, J. Malda, T. Vermonden, J. Jansen, R. Masereeuw, Topographic Guidance in Melt-Electrowritten Tubular Scaffolds Enhances Engineered Kidney Tubule Performance, Frontiers in bioengineering and biotechnology 8 (2021) 1542.
[44] C.D. O'Connell, O. Bridges, C. Everett, N. Antill-O'Brien, C. Onofrillo, C. Di Bella, Electrostatic Distortion of Melt-Electrowritten Patterns by 3D Objects: Quantification, Modeling, and Toolpath Correction, Advanced Materials Technologies (2021) 2100345.
[45] F. Xu, Z. Wang, W. Yang, Surface functionalization of polycaprolactone films via surface-initiated atom transfer radical polymerization for covalently coupling cell-adhesive biomolecules, Biomaterials 31(12) (2010) 3139-3147.
[46] C.S. Wallace, G.A. Truskey, Direct-contact co-culture between smooth muscle and endothelial cells inhibits TNF-α-mediated endothelial cell activation, American Journal of Physiology-Heart and Circulatory Physiology 299(2) (2010) H338-H346.
[47] G.A. Truskey, Endothelial cell vascular smooth muscle cell co-culture assay for high throughput screening assays for discovery of anti-angiogenesis agents and other therapeutic molecules, International journal of high throughput screening 2010(1) (2010) 171.
[48] P. Wu, L. Wang, W. Li, Y. Zhang, Y. Wu, D. Zhi, H. Wang, L. Wang, D. Kong, M. Zhu, Construction of vascular graft with circumferentially oriented microchannels for improving artery regeneration, Biomaterials 242 (2020) 119922.
[49] S. Chung, N.P. Ingle, G.A. Montero, S.H. Kim, M.W. King, Bioresorbable elastomeric vascular tissue engineering scaffolds via melt spinning and electrospinning, Acta Biomaterialia 6(6) (2010) 1958-1967.
[50] W.E. King III, G.L. Bowlin, Near-field electrospinning and melt electrowriting of biomedical polymers—Progress and limitations, Polymers 13(7) (2021) 1097.
[51] F.M. Wunner, P. Mieszczanek, O. Bas, S. Eggert, J. Maartens, P.D. Dalton, E.M. De-Juan-Pardo, D.W. Hutmacher, Printomics: the high-throughput analysis of printing parameters applied to melt electrowriting, Biofabrication 11(2) (2019) 025004.
[52] M.M. Nazemi, A. Khodabandeh, A. Hadjizadeh, Near-field electrospinning: crucial parameters, challenges, and applications, ACS Applied Bio Materials 5(2) (2022) 394-412.
[53] N. Angel, L. Guo, F. Yan, H. Wang, L. Kong, Effect of processing parameters on the electrospinning of cellulose acetate studied by response surface methodology, Journal of Agriculture and Food Research 2 (2020) 100015.
[54] A. Sharir, M.M. Barak, R. Shahar, Whole bone mechanics and mechanical testing, The Veterinary Journal 177(1) (2008) 8-17.
[55] W. Geraets, P. Van Der Stelt, Fractal properties of bone, Dentomaxillofacial Radiology 29(3) (2000) 144-153.
[56] L.M. Benneker, P.F. Heini, S.E. Anderson, M. Alini, K. Ito, Correlation of radiographic and MRI parameters to morphological and biochemical assessment of intervertebral disc degeneration, European spine journal 14(1) (2005) 27-35.
[57] B. Marino, A.F. Corno, Spiral pattern: universe, normal heart, and complex congenital defects, The Journal of Thoracic and Cardiovascular Surgery 126(4) (2003) 1225-1226.
[58] N. Reznikov, M. Bilton, L. Lari, M.M. Stevens, R. Kröger, Fractal-like hierarchical organization of bone begins at the nanoscale, Science 360(6388) (2018) eaao2189.
[59] H.E. Gruber, E.N. Hanley, Observations on morphologic changes in the aging and degenerating human disc: secondary collagen alterations, BMC Musculoskeletal Disorders 3(1) (2002) 1-6.
[60] M.J. Kocica, A.F. Corno, F. Carreras-Costa, M. Ballester-Rodes, M.C. Moghbel, C.N. Cueva, V. Lackovic, V.I. Kanjuh, F. Torrent-Guasp, The helical ventricular myocardial band: global, three-dimensional, functional architecture of the ventricular myocardium, European journal of cardio-thoracic surgery 29(Supplement_1) (2006) S21-S40.
[61] I. Ishak, J. Fisher, P. Larochelle, Robot arm platform for additive manufacturing: Multi-plane printing, Proceedings of the 2016 Florida conference on recent advances in robotics (FCRAR 2016), 2016.

[62] P. Fucile, V.C. David, M. Kalogeropoulou, A. Gloria, L. Moroni, RAVEN: development of a novel volumetric extrusion-based system for small-scale Additive Manufacturing, bioRxiv (2023) 2023.03. 30.534759.
[63] M. Gelber, G. Hurst, T. Comi, R. Bhargava, Model-guided design and characterization of a high-precision 3D printing process for carbohydrate glass, Additive Manufacturing 22 (2018) 38-50.
[64] M. Caragiuli, M. Mandolini, D. Landi, G. Bruno, A. De Stefani, A. Gracco, I. Toniolo, A finite element analysis for evaluating mandibular advancement devices, Journal of Biomechanics 119 (2021) 110298.
[65] D. Iber, M. Mederacke, Tracheal Ring Formation, Frontiers in Cell and Developmental Biology 10 (2022) 900447.
[66] J. Zha, S. Zou, J. Hao, X. Liu, G. Delaplace, R. Jeantet, D. Dupont, P. Wu, X.D. Chen, J. Xiao, The role of circular folds in mixing intensification in the small intestine: A numerical study, Chemical Engineering Science 229 (2021) 116079.
[67] L.R. Versteegden, K.A. Van Kampen, H.P. Janke, D.M. Tiemessen, H.R. Hoogenkamp, T.G. Hafmans, E.A. Roozen, R.M. Lomme, H. van Goor, E. Oosterwijk, Tubular collagen scaffolds with radial elasticity for hollow organ regeneration, Acta Biomaterialia 52 (2017) 1-8.
[68] S. Prevrhal, T. Fuerst, B. Fan, C. Njeh, D. Hans, M. Uffmann, S. Srivastav, H. Genant, Quantitative ultrasound of the tibia depends on both cortical density and thickness, Osteoporosis international 12 (2001) 28-34.
[69] C.J. Little, N.K. Bawolin, X. Chen, Mechanical properties of natural cartilage and tissue-engineered constructs, Tissue Engineering Part B: Reviews 17(4) (2011) 213-227.
[70] S.-A. Kim, S.-M. Park, M.-N. Kim, Y.-H. Kim, D.-H. Cho, C.-M. Ahn, S.J. Hong, D.-S. Lim, W.J. Shim, The relationship between mechanical properties of carotid artery and coronary artery disease, European Heart Journal–Cardiovascular Imaging 13(7) (2012) 568-573.
[71] S. de Valence, J.-C. Tille, D. Mugnai, W. Mrowczynski, R. Gurny, M. Möller, B.H. Walpoth, Long term performance of polycaprolactone vascular grafts in a rat abdominal aorta replacement model, Biomaterials 33(1) (2012) 38-47.
[72] R. Khosravi, C.A. Best, R.A. Allen, C.E. Stowell, E. Onwuka, J.J. Zhuang, Y.-U. Lee, T. Yi, M.R. Bersi, T. Shinoka, Long-term functional efficacy of a novel electrospun poly (glycerol sebacate)-based arterial graft in mice, Annals of biomedical engineering 44 (2016) 2402-2416.
[73] W.M. Saltzman, T.R. Kyriakides, Cell interactions with polymers, Principles of tissue engineering (2020) 275-293.
[74] T. Jacobs, R. Morent, N. De Geyter, P. Dubruel, C. Leys, Plasma surface modification of biomedical polymers: influence on cell-material interaction, Plasma chemistry and plasma processing 32 (2012) 1039-1073.
[75] P. Wysotzki, A. Sancho, J. Gimsa, J. Groll, A comparative analysis of detachment forces and energies in initial and mature cell-material interaction, Colloids and Surfaces B: Biointerfaces 190 (2020) 110894.
[76] S. Nemir, J.L. West, Synthetic materials in the study of cell response to substrate rigidity, Annals of biomedical engineering 38 (2010) 2-20.
[77] G.H. Altman, R.L. Horan, I. Martin, J. Farhadi, P.R. Stark, V. Volloch, J.C. Richmond, G. Vunjak-Novakovic, D.L. Kaplan, Cell differentiation by mechanical stress, The FASEB Journal 16(2) (2002) 1-13.

Chapter 9

Societal impact

There is a shortage of tissues and organs for transplantation. Patients who have not received a heart transplant after 5 years on the waiting list have a survival rate of 40% [1]. This has led to a need to create tissues within a lab and was the foundation of regenerative medicine (RM). The global RM market size reached 22.24 billion dollar in 2022 and is expected to grow until 125.54 billion dollar in 2030, according to a market analyses report by Precedence Research [2]. The majority of cell therapy studies performed their research in 2D before RM became a specialization within medicine. RM promoted the investigations and creation of 3D tissues and substrates to grow cells. These substrates are better known as scaffolds. Several fabrication techniques have been applied within RM to construct 3D scaffolds. Specifically, additive manufacturing techniques such as fused deposition modeling (FDM) are commonly used in RM for this purpose. Recently, implants fabricated with FDM or FDM-derived technologies have been used for critical bone defects and articular cartilage [3][4]. Therefore, further improvements in additive manufacturing technologies can bring additional benefits to the entire RM community and ultimately to the patient.

The findings in **Chapter 3** provide a setup to create a library of patterns for other researchers to use. This could allow to design and engineer tissue specific patterns that can be used for scaffold fabrication aiming at mimicking a broad range of tissues. These patterns could also be used to guide cells to mimic specific tissue functions. One of the examples from **Chapter 4** revealed that using a hypotrochoidal design improved not only the mechanical, but also the biological outcome when envisioning scaffolds for cartilage regeneration. The only difference between the conditions was the design of the scaffold, thus highlighting how with the design of tailored scaffold structural properties it is possible to influence cell activity and tissue formation by architected biomaterials. Therefore, frequently studied biomaterials can offer additional enhanced tissue regeneration when appropriately combined with advanced architectures. The work in **Chapter 4** can serve as a biomimetic approach

blueprint for the research community. Future work could lead to a workflow that starts with a tissue of interest to then test a selection of patterns to assess the best outcome, for instance to determine which load is required for the targeted tissue of interest (e.g. bone, articular cartilage), and use the conceptual framework here developed to match loading with the correspondent architecture pattern. The next step in this endeavor is to fine-tune the chosen pattern to the patients' needs. As every patient provides a different biomechanical and tissue architecture signature, this strategy has the potential to contribute to personalized medicine. The required scaffolds can be fabricated based on medical imaging techniques and manufactured using an appropriate pattern that matches the mechanical and biological requirements.

Designing and validating a pattern for a specific tissue is potentially time-consuming. However, once the design is finalized it can be easily shared without rewriting the entire source code besides some printer specific commands. The universality of G-code allows the code to be transferred to almost any additive manufacturing equipment. This was highlighted in **Chapter 4,** where the code to create a hypotrochoidal pattern was used with FDM, bioprinting and melt electrowriting (MEW). As G-codes can be shared and transferred digitally, the proposed approach can be easily transferred to any printing facility. This is beneficial, since the production of a personalized scaffold can be done locally while specialized personnel can design the scaffolds centrally, making additive manufacturing a more cost effective process for the improvement of RM therapies, especially when applied on a global scale.

In 2019 insurance companies in the Netherlands had to pay for the cardiovascular-, urogenital, intestinal- and respiratory- system a combined 19.8 billion Euro, which translates to 1,142 Euro per inhabitant [5]. This does not reveal to total cost of these healthcare sectors, as not everything is

covered by the insurance, but any relieve for this economic burden is welcome. Currently, FDM systems are not able to reach these healthcare sectors, as tubular structures are impossible to create with classical FDM techniques. Therefore, **Chapter 5** focused on creating a system that is capable of creating scaffolds for these healthcare sectors and potentially reducing the costs. The freedom of the system allows the user to create a variety of different patterns with different mechanical properties that could mimic various tubular tissues.

Chapter 6 highlighted that it is possible to mimic the elastic properties of a coronary artery using a stiff material such as PCL [6]. This finding can have broader implications for material sciences and RM, as some materials are not deemed suitable due to their bulk material properties. **Chapter 6** contributed to the increasing know-how over architected materials, showing an example in the vascular field where mechanical properties of scaffolds can be tunable by varying the scaffolds' architecture, independently from the bulk properties of the selected biomaterials.

Chapter 7 demonstrates how a complex process such as melt spinning can be simplified to make it understandable for everyday users. As a consequence of this simplification, melt spinning can be more broadly adopted within the biofabrication community without necessarily applying electrostatic fields as in the case of melt electrowriting (MEW). In addition, the formulated equations in this chapter are universal and improve the reproducibility by already predicting what the fiber outcome will be. Also, this approach will help researchers by providing more control over the fabrication technique and reducing the time needed to optimize processing parameters, which can require a substantial amount of wasted material during optimization [7]. The developed parametric mathematical method can be applied to other more complicated techniques such as MEW, further increasing the standardization of scaffold fabrication within the RM field.

A future outlook on the impact of this thesis is already briefly discussed in **Chapter 2**, where I postulated that research should focus more on multiple aspects of biomimicry. Instead of focusing on a single pattern, **Chapter 3** and **Chapter 5** highlighted the importance to further investigate the role of architected material patterns, which can be easily available to manufacture. The expansion of such patterns can inspire fellow researchers to use them to discover new fundamental biological processes that can be triggered by more unconventional scaffolds' structural properties. The path from bench to bedside for scaffolds should also include defining a pattern for production, as shown in **Chapter 4**. More studies are required before these scaffolds will become available in the clinic, which shall aim at investigating the effect of, in this case, the hypotrochoidal architecture *in vivo*.

References

[1] S.S. Bakhtiyar, E.L. Godfrey, S. Ahmed, H. Lamba, J. Morgan, G. Loor, A. Civitello, F.H. Cheema, W.B. Etheridge, J. Goss, Survival on the heart transplant waiting list, JAMA cardiology 5(11) (2020) 1227-1235.
[2] P. Research, Regenerative medicine market, Precedence research, 2022, p. 150.
[3] M. Laubach, S. Suresh, B. Herath, M.-L. Wille, H. Delbrück, H. Alabdulrahman, D.W. Hutmacher, F. Hildebrand, Clinical translation of a patient-specific scaffold-guided bone regeneration concept in four cases with large long bone defects, Journal of Orthopaedic Translation 34 (2022) 73-84.
[4] K. Słynarski, W.C. de Jong, M. Snow, J.A.A. Hendriks, C.E. Wilson, P. Verdonk, Single-Stage Autologous Chondrocyte-Based Treatment for the Repair of Knee Cartilage Lesions: Two-Year Follow-up of a Prospective Single-Arm Multicenter Study, The American Journal of Sports Medicine 48(6) (2020) 1327-1337.
[5] RIVM, Kosten van Ziekten 2019, 2022.
[6] V. Guarino, F. Causa, L. Ambrosio, Porosity and mechanical properties relationship in PCL porous scaffolds, Journal of Applied Biomaterials and Biomechanics 5(3) (2007) 149-157.
[7] G. Hochleitner, E. Fürsattel, R. Giesa, J. Groll, H.W. Schmidt, P.D. Dalton, Melt electrowriting of thermoplastic elastomers, Macromolecular rapid communications 39(10) (2018) 1800055.

Appendix

Summary

Every tissue in the human body is composed of a unique mixture of cells and extracellular matrix (ECM) components. A mixture, which is specifically arranged and is often related to the function of the tissue. The ultimate goal of tissue engineering is to replace damaged or diseases tissues with engineered biological analogues that can restore their original functionality until the tissue would be again fully recovered. Researchers are trying to imitate or recreate a tissue through a process defined as biomimicry or “the imitation of life and nature”. The term biomimicry itself is still rather vague as it is broadly used in tissue engineering and regenerative medicine, since it does not specify what exactly is being mimicked. Therefore, **Chapter 2** is focused on what biomimicry encompasses within the scope of regenerative medicine. This chapter first describes that biomimicry can be used in three different forms: mechanical biomimicry, morphological biomimicry and biological biomimicry. Using current biofabrication techniques, this chapter explores how each form of biomimicry is achieved within regenerative medicine. One of these commonly used biofabrication techniques is fused deposition modeling (FDM). This technique is an extrusion-based technique that allows a material to be extruded through a nozzle in a molten form that solidifies directly after extrusion to form a filament. With FDM, any 3D design is possible to recreate, but only limited infill patterns can be generated with current software. This thesis aimed at investigating alternative patterns that can be fabricated through extrusion-based techniques, taking FDM as a testbed. These patterns were used to create scaffolds with enhanced biomimicry, which were further explored for different tissue engineering applications, namely vascular and skeletal regeneration. A methodology to generate patterns was established to create a foundation of patterns to investigate in **Chapter 3**. By expanding the available patterns to use, this chapter makes unconventional patterns more accessible and easier to understand. These patterns are based on various mathematical curves. The results revealed that the differences in Young’s

modulus between the patterns can have a factor of 100 using the same material. In addition, the study found that the mechanical behavior of the scaffolds was significantly changed when a different loading regime was applied. One of the patterns that was further investigated in **Chapter 4** is based on the hypotrochoidal curve. This curve mimics the organization of collagen type II bundles in articular cartilage. Here, we investigated the mechanical properties of the scaffolds designed with the hypotrochoidal pattern compared to a classical woodpile 0-90 scaffold design. We studied what was the influence of the scaffold architecture on collagen type II deposition when cultured in static and dynamic conditions. The research showed that the hypotrochoidal pattern had improved mechanical properties over the conventional 0-90 woodpile structure. In addition, it revealed an improved collagen type II deposition and reduced type X collagen when cultured in dynamic conditions, indicating that the hypotrochoidal pattern could be better used for cartilage regeneration.

An additional application investigated in this thesis was vascular regeneration. In spite of many efforts, scaffolds used for vascular regeneration still do not correspond to the vessel's biomechanics or its structural design. The reason for this is that there is a limitation in creating hollow tubular structures using traditional FDM platforms. This is caused by the lack of support during fabrication and the possibility to crash into previously deposited filaments. **Chapter 5** introduces a solution to this by replacing the flat collecting surface of the traditional FDM system and introducing a cylindrical 4^{th} axis, which is controllable. A variety of new patterns for tubular scaffolds could be created using this system for the regeneration of hollow tubular tissues such as blood vessels. This chapter showcases the technology and compares two different patterns, which cannot be created using a traditional FDM platform. The results showed that small variations within the patterns can be made to change the mechanical behavior. These pattern changes can be used to mimic the mechanical properties for a targeted tissue. Tissues such as large

diameter arteries have unique mechanical properties. The stress-strain curve of a carotid artery can be described with a sigmoidal shape when tensile forces are applied. **Chapter 6** is focused on using a corrugated pattern to mimic the stress-strain curve of large arteries. The corrugations within the pattern allowed the scaffold to extend during tensile testing before the stress increased mimicking the mechanical behavior of a large artery. This behavior could be controlled by varying the corrugation amount. It was found that the stress-strain curves and mechanical properties of the corrugated patterns were similar to those of carotid arteries. The downside of the patterns that were used is that the gaps between the fibers is too big to fully populate with cells and to maintain a barrier function. To solve this limitation, a technique that is further explored in **Chapter 7** is called melt spinning. With melt spinning a thin fiber is being drawn around a mandrel to create highly aligned fibers in the circumferential direction. The resulting fibers mimic the orientation of the tunica media of an artery. This study used melt spinning in combination with the four axis FDM described in **Chapter 5** to create a scaffold that had mechanical biomimicry from the large supporting fibers, but also morphological biomimicry from the melt spun fibers. The results showed that the process of melt spinning was reliable enough, hence could be described with equations predicting the fiber outcome. The process could be controlled to such an extent that gaps just small enough for cells to pass through could be created facilitating cells growth while still maintaining a barrier function when seeded with cells. The co-culture with endothelial and smooth muscle cells revealed that the endothelial cells had a cobblestone morphology forming a barrier in the luminal side of the scaffold and the smooth muscle cells populated directly underneath between the melt spun fibers.

In **Chapter 8**, all the above results are discussed and placed into a state-of-the-art context, in addition to providing future perspectives. In **Chapter 9**, we conclude by reviewing the scientific and societal impact of the research presented in this thesis.

Samenvatting

Elk weefsel in het menselijk lichaam is opgebouwd uit een unieke mix van cellen en extracellulaire matrix (ECM) componenten. Een mengsel dat specifiek gerangschikt is en vaak gerelateerd is aan de functie van het weefsel. Het ultieme doel van tissue engineering is om beschadigde of zieke weefsels te vervangen door gefabriceerde biologische analogen die hun oorspronkelijke functionaliteit kunnen genezen tot het weefsel weer volledig hersteld is. Onderzoekers proberen menselijk weefsel te imiteren of te recreëren door middel van een proces dat wordt gedefinieerd als biomimicry of "de imitatie van het leven en de natuur". De term biomimicry zelf is nog steeds vrij vaag, aangezien het breed gebruikt wordt in tissue engineering en regeneratieve geneeskunde, omdat het niet specificeert wat er precies wordt nagebootst.

Daarom is **Hoofdstuk 2** gericht op wat biomimicry inhoudt binnen de regeneratieve geneeskunde. Dit hoofdstuk beschrijft dat biomimicry in drie verschillende vormen kan worden gebruikt: mechanische biomimicry, morfologische biomimicry en biologische biomimicry. Aan de hand van de huidige biofabricage technieken onderzoekt dit hoofdstuk hoe elke vorm van biomimicry wordt bereikt binnen de regeneratieve geneeskunde. Een van deze veelgebruikte biofabricagetechnieken is fused deposition modeling (FDM). Deze techniek is gebaseerd op extrusie, waarbij een materiaal door een spuitmond wordt geëxtrudeerd in een gesmolten vorm die direct na extrusie stolt tot een filament. Met FDM is elk 3D ontwerp na te maken, maar met de huidige software kunnen slechts beperkte invulpatronen worden gegenereerd. Dit proefschrift was gericht op het onderzoeken van alternatieve patronen die gemaakt kunnen worden door middel van extrusietechnieken, met FDM als proefbank. Deze patronen werden gebruikt om scaffolds te maken met verbeterde biomimicry, die verder werden onderzocht voor verschillende tissue engineering toepassingen, namelijk vasculaire en

skeletregeneratie. In **Hoofdstuk 3** een methodologie om patronen te genereren werd ontwikkeld om een grondslag van patronen te creëren om te onderzoeken. Door de beschikbare patronen uit te breiden, maakt dit hoofdstuk onconventionele patronen toegankelijker en begrijpelijker. Deze patronen zijn gebaseerd op verschillende wiskundige curven. De resultaten onthulden dat de verschillen in Young's modulus tussen de patronen een factor 100 kunnen hebben bij gebruik van hetzelfde materiaal. Bovendien bleek uit het onderzoek dat het mechanische gedrag van de scaffolds significant veranderde wanneer een ander belastingregime werd toegepast. Een van de patronen die verder werd onderzocht in **Hoofdstuk 4** is gebaseerd op de hypotrochoïdale curve. Deze curve bootst de organisatie van collageen type II bundels in gewrichtskraakbeen na. Hier onderzochten we de mechanische eigenschappen van de scaffolds ontworpen met het hypotrochoïdale patroon in vergelijking met een klassiek 0-90 houtstapel scaffold ontwerp. We onderzochten wat de invloed was van de architectuur van de scaffold op de depositie van collageen type II bij het kweken in statische en dynamische omstandigheden. Het onderzoek toonde aan dat het hypotrochoïdale patroon betere mechanische eigenschappen had dan de conventionele 0-90 houtstapelstructuur. Daarnaast toonde het onderzoek een verbeterde collageen type II afzetting en een verminderd type X collageen bij het kweken in dynamische omstandigheden, wat aangeeft dat het hypotrochoïdale patroon beter gebruikt zou kunnen worden voor kraakbeenregeneratie.

Een andere toepassing die in dit proefschrift werd onderzocht was vasculaire regeneratie. Ondanks vele inspanningen komen de scaffolds die gebruikt worden voor vasculaire regeneratie nog steeds niet overeen met de biomechanica of het structurele ontwerp van het bloedvat. De reden hiervoor is dat er een beperking is bij het maken van holle buisstructuren met traditionele FDM platvormen. Dit wordt veroorzaakt door het gebrek aan ondersteuning tijdens de fabricage en de mogelijkheid om tegen eerder

gedeponeerde filamenten aan te botsen. **Hoofdstuk 5** introduceert een oplossing hiervoor door het vlakke opvangoppervlak van het traditionele FDM-systeem te vervangen door een cilindrische 4e as, die controleerbaar is. Met dit systeem kunnen verschillende nieuwe patronen voor buisvormige scaffolds worden gemaakt voor de regeneratie van hol buisvormig weefsel zoals bloedvaten. Dit hoofdstuk laat de technologie zien en vergelijkt twee verschillende patronen, die niet gemaakt kunnen worden met een traditioneel FDM platvorm. De resultaten toonden aan dat kleine variaties binnen de patronen gemaakt kunnen worden om het mechanische gedrag te veranderen. Deze patroonveranderingen kunnen worden gebruikt om de mechanische eigenschappen van een weefsel na te bootsen. Weefsels zoals slagaders met een grote diameter hebben unieke mechanische eigenschappen. De spanning-rek curve van een halsslagader kan beschreven worden met een sigmoïdale vorm wanneer trekkrachten worden uitgeoefend. **Hoofdstuk 6** richt zich op het gebruik van een gegolfd patroon om de spanning-rek curve van grote slagaders na te bootsen. Door de golven in het patroon kon de scaffold zich tijdens trektesten uitstrekken voordat de spanning toenam, waardoor het mechanische gedrag van een grote slagader werd nagebootst. Dit gedrag kon worden gecontroleerd door de hoeveelheid golven te variëren. Het bleek dat de spanning-rek curves en mechanische eigenschappen van de gegolfde patronen vergelijkbaar waren met die van halsslagaders. Het nadeel van de gebruikte patronen is dat de openingen tussen de vezels te groot zijn om ze volledig te vullen met cellen en een barrièrefunctie te behouden. Om deze beperking op te lossen, wordt een techniek gebruikt die verder wordt onderzocht in **Hoofdstuk 7**: melt spinning. Bij meltspinning wordt een dunne vezel door een naald getrokken om sterk uitgelijnde vezels in de omtrekrichting te creëren. De resulterende vezels bootsen de oriëntatie van de tunica media van een slagader na. In dit onderzoek werd meltspinning gebruikt in combinatie met FDM met vier assen, zoals beschreven in **Hoofdstuk 5**, om een scaffold te maken met mechanische biomimicry van de grote ondersteunende vezels, maar ook

morfologische biomimicry van de meltspun vezels. De resultaten toonden aan dat het meltspin proces betrouwbaar genoeg was en dus beschreven kon worden met vergelijkingen die de vezeluitkomst voorspelden. Het proces kon zo gecontroleerd worden dat er openingen ontstonden die net klein genoeg waren om cellen door te laten, waardoor cellen konden groeien terwijl de barrièrefunctie behouden bleef als er cellen in werden geplaatst. De co-cultuur met endotheelcellen en gladde spiercellen liet zien dat de endotheelcellen een keienmorfologie hadden die een barrière vormde in de luminale zijde van de scaffold en dat de gladde spiercellen zich direct eronder bevonden tussen de uitgelijnde vezels.

In **Hoofdstuk 8** worden alle bovenstaande resultaten besproken en in een state-of-the-art context geplaatst en worden toekomstperspectieven geboden. In **Hoofdstuk 9** sluiten we af met een overzicht van de wetenschappelijke en maatschappelijke impact van het in dit proefschrift gepresenteerde onderzoek.

List of Publications

Publications related to this thesis

K.A. van Kampen, C. Mota, L. Moroni, *A tissue engineering's guide to biomimicry*. (Submitted)

K.A. van Kampen, C. Mota, L. Moroni, *Scaffolds with atypical space-filling curves for tissue engineering,* (In preparation)

K.A. van Kampen, E. Olaret, I.C. Stancu, D.F. Duarte Campos, H. Fischer, C. Mota, L. Moroni, *Hypotrochoidal scaffolds for cartilage regeneration,* Materials Today Bio 2023, DOI: 10.1016/j.mtbio.2023.100830

K.A. van Kampen, E. Olaret, I.C. Stancu, L. Moroni, C. Mota, *Controllable four axis extrusion based additive manufacturing system for vascular tissue regeneration,* Materials Science and Engineering C 2020, DOI: 10.1016/j.msec.2020.111472

K.A. van Kampen, T. ten Brink, C. Mota, L. Moroni, *Scaffolds with a tuneable non-linear elastic region using a corrugated design,* Small structures 2024, DOI: 10.1002/sstr.202300399

K.A. van Kampen, J. Fernández-Pérez, M. Baker, C. Mota, L. Moroni, *Fabrication of a mimetic vascular graft using melt spinning with tailorable fibre parameters,* Biomaterials Advances 2022, DOI: 10.1016/j.bioadv.2022.212972

Other publications

L.R. Versteegden, K.A. van Kampen, H.P. Janke, D.M. Tiemessen, H.R. Hoogenkamp, T.G. Hafmans , E.A. Roozen, R.M. Lomme, H. van Goor, E. Oosterwijk, W.F. Feitz, T.H. van Kuppevelt, W.F. Daamen, *Tubular collagen scaffolds with radial elasticity for hollow organ regeneration,* Acta Biomaterialia 2017, DOI: 10.1016/j.actbio.2017.02.005

K.A. van Kampen, R.G. Scheuring, M.L. Terpstra, R. Levato, J. Groll, J. Malda, C. Mota, L. Moroni, *Biofabrication: From Additive Manufacturing to Bioprinting,* In book: Reference Module in Biomedical Sciences 2019, DOI: 10.1016/B978-0-12-801238-3.11118-3

V.A. Parfenov, V.A. Mironov, K.A. van Kampen, P.A. Karalkin, E.V. Koudan, F. DAS Pereira, S.V. Petrov, E.K. Nezhurina, O.F. Petrov, M.I. Myasnikov, F.X. Walboomers, H. Engelkamp, P. Christianen, Y.D. Khesuani, L. Moroni and C. Mota, *Scaffold-free and label-free biofabrication technology using levitational assembly in a high magnetic field,* Biofabrication 2020, DOI: 10.1088/1758-5090/ab7554

J. Chakraborty, J. Fernández-Pérez, K.A. van Kampen, S. Roy, T. ten Brink, C. Mota, S. Ghosh, L. Moroni, *Development of a biomimetic arch-like 3D bioprinted construct for cartilage regeneration using gelatin methacryloyl and silk fibroin-gelatin bioinks,* Biofabrication 2023, DOI: 10.1088/1758-5090/acc68f

J. Fernández-Pérez, K.A. van Kampen, C. Mota, M. Baker, L. Moroni, Flexible, *Suturable, and Leak-free Scaffolds for Vascular Tissue Engineering Using Melt Spinning,* ACS Biomaterials Science & Engineering 2023, DOI: 10.1021/acsbiomaterials.3c00535

J. Chakraborty, J. Fernández-Pérez, M. Takhsha Ghahfarokhi, K.A. van Kampen, T. ten Brink, J. Ramis, M. Kalogeropoulou, R. Cabassi, C. de Julián Fernández, F. Albertini, C. Mota, S. Ghosh, L. Moroni, *4D-bioprinted shape-morphing magnetic constructs for cartilage regeneration using a silk fibroin-gelatin bioink,* Cell Reports Physical Science 2024, DOI: 10.1016/j.xcrp.2024.101819

Conference Presentations

Oral presentations

Hypotrochoidal scaffold design for cartilage regeneration, International Society for Biofabrication (ISBF), 2022

Fabrication of a mimetic vascular scaffold using a four axis extrusion based system, Tissue Engineering and Regenerative Medicine International Society (TERMIS), 2021

Four Axis Additive Manufacturing Filament Deposition System for Vascular Regeneration Tissue Engineering and Regenerative Medicine International Society (TERMIS), 2019

Controllable Four Axis Fused Deposition Modeling System for Tubular Hollow Organ Regeneration, MERLN PhD Symposium, Maastricht 2018

Controllable Four Axis Fused Deposition Modeling System for Tubular Hollow Organ Regeneration, Netherlands society for Biomaterials and Tissue engineering (NBTE), 2019

Poster presentations

Mechanical stimulation of fractal based scaffolds to steer stem cell activity, Tissue Engineering and Regenerative Medicine International Society (TERMIS), 2021

Four Axis Additive Manufacturing Filament Deposition System for Vascular Regeneration, Netherlands society for Biomaterials and Tissue engineering (NBTE), 2018

Four Axis Additive Manufacturing Filament Deposition System for Vascular Regeneration, MERLN PhD Symposium, Maastricht 2018

Hypotrochoid-based scaffolds for osteochondral tissue engineering, European Society of Biomaterials (ESB), 2018

Acknowledgement

Finally, the long journey has ended. With this I would like acknowledge all the people that have helped me during this trip and made things a bit easier and more enjoyable.

First of all, thank you Lorenzo for hiring me to do a PhD in biofabrication after my internship despite me being a pathobiologist. Giving me all the freedom in creating my own project. I hope you did not lose all patience with me during the writing phase of the thesis, which I acknowledge is definitely not my strong point. You always saw the positive side of things in results, encouraged me when I needed it and triggered my curiosity. I've learned a lot from you and I will take these lessons with me.

Special thanks to Carlos, thank you again for hiring and having some faith in me for my internship on combining two different printing techniques with a person who never touched a 3D printer in his life before. You introduced me to the world of biofabrication and from that point on I knew I wanted to do something with fabrication and tinkering with equipment. Even though you were picky sometimes, your critical eye helped my work a lot. Thanks to your help and support, I managed to create half of the chapters in this thesis based on an initial Friday afternoon experiment.

My paranymphs Clarissa and Ivo, you both have been an incredible support during this journey. Clarissa, you always had the latest gossips around the lab which made the work a bit more lively. Besides that you always were a listening ear when I was stuck with some of my experiments, especially when it came to iPSC culture. Ivo, thanks for all the moments in the lab. The jokes made the experiments a bit less serious and more enjoyable during those long printing days.

Thank you OG biofabrication crew. Andrea for being the best FAST printer impersonator and your envy towards my choice of printing material. Ravi for the scientific discussions and the DIY experimental setups we made. Maria, for your time shared during printing. Sandra, for expanding my Spanish vocabulary and your tips for printing and Filipa, for your positivity and enthusiasm in everything.

Special thanks to Tim and Julia. I hope you both did not suffer too much from the four axis printer. Tim, for being a wonderful student who helped me gain another chapter in this thesis. I couldn't imagine having a better student. Julia, for your collaboration on the chapter of the four axis and being a listening ear.

I would like to thank the newer generation in the biofabrication lab, Shivesh, Maria, Pierpaolo, Vivek and Sophia. You all were very kind and helped made life in the lab more enjoyable. I hope you didn't inherit to much of my mess in the lab.

Thanks to the vascularization group, Tristan, Mirco, Gabrielle, Tianyu, Rebeca and Filipa. I enjoyed the discussions during the meetings and it really improved my experiments. In addition, I would like to thank the biofabrication group in general, I learned a lot from you and you all helped me improve my work.

To my outside collaborators Iza and Elena thank you so much. Both of you helped improve two of my chapters tremendously with the micro-CT images and analyses.

Thank you Paul for dealing with me, I know we both are a bit stubborn on certain things but I learned a lot during this time period. Thank you Jay, Adrian Kike and Amit during my time in Paul's group. I hope I was of value during this short time period.

Acknowledgement

I would like to thank the lab managers, Timo, Eva, Marloes and Denis for your help and support in the lab keeping it run. Besides that, I would like to thank the rest of MERLN for your support and help during this journey.

Thank you colleagues from ReGEN Biomedical for giving me that final push to finish the thesis.

Nu voor mijn persoonlijke kennis kring wil ik graag mijn vriendengroep uit Maas en Waal bedanken. Bedankt Coen, Ernst, Harper en Loek. De bordspel avonden gaven me altijd even de tijd om te ontspannen zodat ik niet te veel aan experimenten hoef te denken.

Bedankt familie, Pap, Mam, Jeroen, Karly en Carla jullie hebben me enorm geholpen in de afgelopen jaren. Jullie hebben mijn keuzes altijd gesteund ondanks dat ik helemaal in dat verre Limburg zat voor mijn promotie.

Finally, I come to the last person who has been the greatest support of all. Sandra, Vielen Dank für alles, du warst immer für mich da. This journey has been a rollercoaster and you always found a way to cheer me up when experiments or writing didn't went well. I hope I wasn't too difficult on you during this time. Je bent echt de beste en ik kan me niemand beter wensen als partner.

Biography

Kenny was born on 9 September 1992 in Nijmegen, Netherlands. Following his interest in Biology and Medicine, he completed his BSc. in Biomedical Sciences at the Radboud University in Nijmegen, in 2015. He started his MSc. in Biomedical Sciences with a focus in pathobiology at the Radboud University in Nijmegen. His first master thesis was focused on creating a tubular construct with shape recovery for urethral tissue engineering. This exposure in tissue engineering led to another master thesis at the MERLN institute for Technology-inspired Regenerative Medicine in Maastricht and the ZWBF group at the RWTH in Aachen. The focus was on combining two different printing techniques to create a construct for cartilage regeneration. In 2017, he stayed at the MERLN institute joining as a PhD candidate. There, he investigated alternative patterns that can be fabricated through extrusion-based additive manufacturing. Creating more complex biomimicking scaffolds which can be used for different tissue engineering applications such as vascular and skeletal regeneration. With the ultimate goal of improving tissue engineering and regenerative medicine, in the future he aims at creating new tools for tissue engineers that could help improve new biomedical products.